Stabilization and propagation of lean premixed flames in small dimensions conducts in strong thermal interaction with the walls

Amanda Pieyre

université PARIS-SACLAY

NNT : 2019SACLC053

CentraleSupélec

Stabilisation et propagation de flammes pauvres prémélangées dans des conduits de petites dimensions en interaction forte avec les parois

Thèse de doctorat de l'Université Paris-Saclay
préparée à CentraleSupélec

École doctorale n°579 : Sciences mécaniques et énergétiques, matériaux et géosciences (SMEMAG)
Spécialité de doctorat : Combustion

Thèse présentée et soutenue à Gif-sur-Yvette, le 30/04/2019, par

Amanda Pieyre

Composition du Jury :

Pascale Domingo Directrice de Recherche, CORIA – CNRS	Rapporteur
Marc Bellenoue Professeur, ENSMA, PPRIME – CNRS	Rapporteur
Carmen Jimenez Chercheuse, CIEMAT	Examinateur
Guillaume Ribert Maitre de conférence, CORIA – CNRS	Examinateur
Laurent Zimmer Chargé de recherche, EM2C – CNRS	Examinateur
Guillaume Dayma Professeur, Université d'Orléans, ICARE – CNRS	Président du jury
Franck Richecoeur Professeur, CentraleSupélec, EM2C – CNRS	Directeur de thèse
Nasser Darabiha Professeur, CentraleSupélec, EM2C – CNRS	Co-Encadrant
Luc Vervisch Professeur, INSA Rouen Normandie, CORIA – CNRS	Invité

Thèse de doctorat

Laboratoire d'Energétique
Moléculaire & Macroscopique,
Combustion
EM2C – UPR288

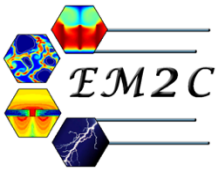

Université Paris-Saclay
Espace Technologique / Immeuble Discovery
Route de l'Orme aux Merisiers RD 128 / 91190 Saint-Aubin, France

Remerciements

De façon liminaire, je remercie tous les membres de mon jury pour avoir accepté ce rôle et évalué ma présentation orale. Je remercie plus particulièrement Pascale Domingo et Marc Bellenoue d'avoir endossé les rôles de rapporteurs de mon manuscrit et pour leurs remarques pertinentes dans les rapports et les discussions qui en ont suivi. Je remercie également Guillaume Dayma d'avoir accepté d'être le président du Jury, ainsi que Carmen Jiménez, Guillaume Ribert et Laurent Zimmer d'avoir accepté le rôle d'examinateur. Enfin je remercie Luc Vervisch d'avoir accepté d'assister à ma soutenance en tant qu'invité. Je remercie tous les membres du jury pour la qualité des échanges que l'on a pu avoir en dehors ainsi que durant les questions de la soutenance. Ils ont permis d'enrichir ce travail ainsi que d'ouvrir de nouvelles pistes pour de futurs travaux sur le sujet.

Je souhaiterai ensuite remercier mes encadrants. Mon directeur de thèse Franck Richecoeur, pour avoir su me guider dans une thèse qui avait pour vocation d'aborder de nombreux sujets, pour la prise de recul et les conseils sur la gestion et rédaction de la thèse. Je remercie mon encadrant Nasser Darabiha pour m'avoir formé sur la partie numérique notamment le code Regath. Merci pour votre gentillesse et votre disponibilité.

Je remercie les permanents du laboratoire avec qui j'ai pu échanger tout au long de ma thèse, notamment Laurent, Clément, Antoine, David et Dédit. Ceci inclus aussi l'équipe de l'atelier, thèse expérimentale oblige, je remercie grandement Erika et Yannick pour leur aide précieuse. Ensuite sur la partie calcul et informatique je remercie Sébastien et Jean-Michel. Je remercie très chaleureusement l'équipe administrative du laboratoire, Nathalie, Noï et Brigitte. Votre soutien, votre aide et votre amitié m'ont beaucoup apporté dans ce parcours d'obstacle qu'est la thèse, et vous m'en avez évité un certain nombre grâce à votre efficacité et disponibilité.

Plus globalement je remercie tous les doctorants et post doctorants que j'ai pu croiser, pour leur participation dans le maintien d'une bonne ambiance, pour leur amitié et l'entraide qui règne dans le laboratoire. Cette aventure nous permet de tisser des liens particuliers avec certaines personnes qui rendent l'exercice plus agréable, notamment mon équipe du RAID de CentraleSupélec Lívia et Quentin, mes co-bureaux et voisins des deux campus Lorella, Léo, Davy, Kevin P., Giunio, Giampaolo, Jan, Théa, Abi, Guillaume, Robin et les petits

nouveaux Suzane, Victor, Yacine, Constantin, Kevin T... Et bien d'autres que j'oublie, à qui je présente mes excuses pour ne pas les avoir cité !
Je remercie grandement mes amis d'enfance, d'école ou d'ailleurs, qui ont vécu cette thèse avec moi, et notamment ceux qui ont fait le déplacement pour ma soutenance et ceux qui ont pu venir fêter cet accomplissement avec moi, vous vous reconnaitrez, sinon ci-après une liste non exhaustive :D. Merci à Rym, Omar C., Aliae, Aida, Yousra, Ismail, Yacine B., Yacine R., Mehdi E., Inès, Anas, Bachir, Meryem, Jaza Thomas, Bako, Katia, Alix, Amine, Mehdi B.,...
Enfin je remercie infiniment toute ma famille. Tout d'abord mes parents, Ingrid et Jacky, pour leur soutien infaillible et leur force sans quoi je n'aurai pas pu poursuivre mes études si loin, et dans de si bonnes conditions. De même je remercie mon frère Alex et sa femme Camélia pour leur soutien et leur présence. Merci à mon parrain et ma tante, Claude et Jacqueline, d'être venus assister à ma soutenance et de m'avoir soutenu dans toute ma scolarité post-bac. Merci à Sam et ma petite soeur Taylit d'avoir fait ce grand voyage pour l'occasion et pour votre soutien. Merci à ma tante Geneviève pour tous ses conseils et merci d'avoir suivi ma soutenance en streaming à 5h du matin. Enfin, je remercie infiniment Omar, pour cette décennie passée ensemble, pour sa patience et son soutien indéfectible dans toutes mes entreprises.

Abstract

The main issue of premixed flame stabilization in narrow channels is the massive heat losses to the walls due to the high ratio surface on volume. In a major part of the literature, in order to reach flame stabilization, an external assistance is provided through catalytic walls, pilot flame or external heating. External heating insures isothermal heated walls, however the heating powers used are usually greater than the flame power. In such configurations, the heat exchanges go from walls to gas which prevents an arrangement to extract heat from combustion in order to generate mechanical or electrical power.
The aim of the present work is to better understand the stabilization mechanisms of flames in narrow channels without any external assistance and with natural venting generating heat loss to ambient air. To do so, a fairly simple configuration is studied, composed of a 5 mm inner diameter quartz tube inside which a lean premixture of methane and air is injected and ignited. The diameter is chosen above the quenching diameter of the premix to allow flame stabilization without external assistance. At this scale, the thermal interactions with the walls have a strong impact on flame regimes. Several originals phenomena have been experimentally observed in stationary regime (fixed position stabilization) and in propagation regime.
When stabilized at a given position in the tube, the flame heats the wall in the vicinity of the maximum heat release but soon, heat is conducted towards the unburnt gases in the walls pre-heating the reactive mixture and increasing the flame speed. A unique stable point is observed depending on the equivalence ratio. This latter shows a strong influence on the flame shape, and systematic observation of the flame has been performed depending on the tube diameter and equivalence ratio. For large equivalence and diameter, a slant flame is observed due to the combined effects of non-symmetric external heat distribution and induced inner fluid vorticity from gravity. Phosphor thermometry measurement techniques were implemented to quantify the heat fluxes at the wall. The other diagnostics used to characterize the flame front are flames spontaneous emission and chemiluminescence.
The flame ability to sit at a given location in the tube remains sensitive to any modification of the flow and/or heat exchanges. In particular, this thesis work presents an original way of controlling the flame position in the tube through the modification of heat fluxes upstream from the flame. It was shown that a small,

temporary and local heat excess (of order of magnitude of the flame power) in the fresh gas can generate an irreversible change of the flame location in the tube. This controlled flashback generates a slow transition motion from one position to another. The systematic measurements of flame positions and speeds allowed to detail the different mechanisms involved in this transition together with the existence of a threshold between two regimes of flame propagation speed.
To enrich the description and understanding of these combustion configurations, a complex chemistry one-dimensional code (REGATH) is used to compute flame speeds, considering the thermal exchanges with the walls, in a configuration close to the experiment. These simulations confirm the mechanisms leading to the flame flashback : the additional heat deposited upstream from the flame is conducted into the wall heating up the unburnt gas. The characteristic response time of the flame to this perturbation is the addition of the conduction time in the wall and the convection of the gas. In a perspective point of view, the flame was coupled with microwave plasma in order to study the capacities of this kind of plasma as an assistance to flame stabilization. The challenge here is to find a configuration allowing to discharge the excited species produced by the plasma into the fresh combustion gas close enough to the flame to have an impact.

Résumé

Le problème étudié dans ce travail de thèse concerne la stabilisation de flammes prémélangées dans des canaux étroits où les pertes de chaleur ont un effet majeur sur la flamme dû au rapport surface sur volume élevé. Dans la littérature, une assistance est généralement fournie à ces flammes via des parois catalytiques, une flamme pilote ou un chauffage externe pour parvenir à stabiliser la flamme. Bien souvent, la puissance de chauffage extérieure est supérieure à la puissance de la flamme, et les configurations étudiées ne permettent pas la récupération de la chaleur utile issue de la combustion, extraite du brûleur, en vue de générer de l'énergie mécanique ou électrique.
Le but du travail présenté est de mieux comprendre les mécanismes de stabilisation de ces flammes en canal étroit sans assistance extérieure mais avec une ventilation extérieure naturelle générant une perte de chaleur du système vers l'air ambiant. Pour ce faire, on étudie une configuration relativement simple, composée d'un tube de quartz de diamètre intérieur de 5 mm dans lequel un prémélange pauvre de méthane et d'air est injecté et allumé. Le diamètre est choisi au-dessus du diamètre d'extinction du prémélange afin de permettre la stabilisation de la flamme sans assistance extérieure. À cette échelle, les interactions thermiques avec les murs ont un impact important sur les régimes de flammes. Plusieurs phénomènes originaux ont été observés expérimentalement en régime stationnaire (stabilisation à une position fixe) et en régime de propagation.
Une fois stabilisée à une position donnée dans le tube, la flamme chauffe la paroi au voisinage du dégagement de chaleur maximal mais rapidement, la chaleur est conduite vers les gaz non brûlés dans les parois, préchauffant ainsi le mélange réactif et augmentant la vitesse de la flamme. Un point stable unique est observé par richesse. Cette dernière influence fortement la forme de la flamme et une observation systématique de la flamme a été réalisée en fonction du diamètre du tube et de la richesse. Pour une richesse et un diamètre importants, la flamme s'incline en raison des effets combinés de la distribution non symétrique de la chaleur à l'extérieur du tube et de circulations internes induites par la gravité. Des techniques de mesure de température de parois par phosphorescence sont mises en œuvre pour quantifier les flux de chaleur. De plus, l'émission spontanée de la flamme et la chimiluminescence sont utilisées afin de caractériser le front de flamme.

La capacité de la flamme à se stabiliser à une position donnée dans le tube est sensible à toute modification du débit et/ou des échanges thermiques. Ce travail de thèse présente notamment une manière originale de contrôler la position de la flamme dans le tube par la modification des flux thermiques en amont de la flamme. Il y est démontré qu'un léger excès de chaleur temporaire et local (de l'ordre de grandeur de la puissance de la flamme) dans les gaz frais peut générer un changement irréversible du point de stabilisation de la flamme dans le tube. Cette remontée de flamme reste contrôlée durant une phase transitoire depuis une position initiale vers une position finale. Les mesures systématiques des positions et des vitesses de la flamme ont permis de détailler les différents mécanismes impliqués dans cette transition et de montrer l'existence d'un seuil séparant deux régimes de vitesse de propagation de flamme.
Pour enrichir la description et la compréhension de ces configurations de combustion, un code 1D de chimie complexe (REGATH) est utilisé pour calculer les vitesses de flamme, en tenant compte des échanges thermiques avec les parois, dans une configuration proche de l'expérience. Ces simulations confirment les mécanismes de stabilisation et ceux conduisant à la remontée de flamme lorsque soumise à une perturbation extérieure : la chaleur supplémentaire déposée en amont de la flamme est conduite dans la paroi puis réchauffe les gaz non brûlé. Le temps de réponse caractéristique de la flamme à cette perturbation est la somme du temps de conduction dans la paroi et de la convection du gaz. En termes de perspectives, la flamme a été couplée à un plasma micro-ondes afin d'étudier les potentialités de ce type de plasma en tant qu'aide à la stabilisation de la flamme. Le défi consiste ici à trouver une configuration permettant de coupler le plasma et les gaz frais à proximité de la flamme.

Le manuscrit s'articule comme suit. La première partie de cette étude met en place le contexte, en présentant les configurations étudiées et les diagnostiques utilisés, et met en exergue les premières observations. Le premier chapitre s'applique à démontrer l'intérêt de la combustion dans de petits conduits. De plus l'état de l'art est présenté afin de contextualiser la présente étude, ainsi que de montrer ses enjeux et limitations. Le deuxième chapitre s'attèle à la présentation et justification de la configuration expérimentale choisie, d'une flamme pauvre de prémélange méthane et air, placée dans des tubes en quartz de petites dimensions, sans assistance extérieure. De plus, les diagnostiques utilisés sont décrits. Le troisième chapitre répond à la demande d'une mesure de température précise par la description de la méthode de phosphorescence induite par laser, et compare deux méthodes de mesure sur des tubes à grand rayon de courbure.
La seconde partie introduit les premiers résultats d'une flamme en régime stable. Le quatrième chapitre expose ainsi les domaines de stabilisation de la flamme en fonction de la vitesse de flamme et de la richesse, et montre l'évolution de la topologie de flamme. Les effets sur la topologie et points de fonctionnement dus à la variation du diamètre et du positionnement horizontal/vertical du tube

sont observés. Ce chapitre permet ainsi la caractérisation de la stabilité de la flamme sans assistance. A la suite de cette caractérisation expérimentale, le cinquième chapitre fourni une analyse théorique sur les échanges thermiques de la flamme avec l'air ambiant, ainsi qu'une simulation monodimensionnelle stable à l'aide d'un code de chimie complexe (REGATH). Cette section permet l'identification des transferts thermiques et ainsi que de quantifier leur impact sur la stabilité de flamme. En collaboration avec une équipe de recherche du CORIA, qui procèdent aux simulations bidimensionnelles DNS de la configuration étudiée, le sixième chapitre retrace l'origine de l'asymétrie de la flamme observée expérimentalement.
Enfin la troisième partie montre la réponse de flamme à deux types de perturbations. Ainsi le septième chapitre décrit expérimentalement et numériquement, à nouveau à travers le code de chimie complexe monodimensionnel, un retour de flamme de la flamme causé par un apport thermique local extérieur en amont de la flamme. Le huitième chapitre comme perspective ouvre la possibilité d'un couplage expérimental d'un plasma micro-onde en assistance à la flamme. Numériquement un modèle existant est testé dans la configuration étudiée afin d'évaluer la réponse de la flamme à un apport d'énergie vibrationnelle en amont du front de flamme.

Table des matières

Liste des tableaux

Table des figures

Nomenclature

The following file gives the nomenclature :
Latin Characters :

L	Tube length [m]
d	Internal/External tube diameter [m]
r	Internal/External tube radius [m]
S	cylindre section with a r radius [m^2]
h	convection heat loss coefficients of gas to inner solid wall/inner to outter solid wall [$W/(m^2.K^1)$]
T	Temperature [K]
k	Thermal conductivity [W/(m.K)]
p	Pressure [Pa]
$\dot{m}$	Mass flow rate [$kg.s^{-1}$]
c_p	Specific heat [J/(kg.K)]
P	Power [W]
f_s	Sampling frequency [Hz]
U	Flow velocity in the laboratory frame [$m.s^{-1}$]
V	Flame related velocity in the laboratory frame [$m.s^{-1}$]
S_L^o	Laminar adiabatic flame speed [$m.s^{-1}$]
Y_k	Mass fraction
V_k	Diffusion speed
W	Molecular mass
H	Enthalpy
g	Gravitational constant[$m^2.s^{-1}$]
Nu	Nusselt number
Gr	Grashof number
Re	Reynolds number
Pr	Prandtl number
Ri	Richardson number
L_{th}	Thermal entrance length [m]
L_{hy}	Hydrodynamic entrance length [m]
e_{vib}	Vibrationnal energy
$\dot{Q}_{cvf_g}$	Heat losses of forced convection in the gas energy equation
$\dot{Q}_{cvn}$	Heat losses of natural convection from wall ambient air
$\dot{Q}_{rad}$	Heat losses of wall radiation
$\dot{Q}_{cvf_s}$	Heat losses of forced convection in the gas solid equation
$\dot{E}^p_{vib}$	Ultra fast vibrationnal energy rate
$\dot{E}^p_{heat}$	Ultra fast heating rate
$\dot{E}^p_{chem}$	Ultra fast species dissociation rate
$\dot{R}^p_{VT}$	Relaxation of vibrationnal energy rate

d_P	Plasma end deposition coordinate [m]	$x_c d$	Plasma center discharge coordinate [m]
w_P	Plasma discharge width [m]		

Greek Characters :

ϕ	Equivalence ratio [a.u]	$\dot{\omega}$	Molar production rate by chemical reaction of the k^{th} specie by volume unity
λ	Wavelength [nm]		
α	Thermal diffusivity $[m^2.s^{-1}]$	ϵ_S	quartz emissivity
		σ	Stefan-Boltzmann constant $[W.m^{-2}.K^{-4}]$
ρ	Density $[kg.m^{-3}]$		
μ	Dynamic viscosity $[kg.m.s^{-1}]$	σ_g	Gaussian width $[m^{-1}]$
		β	isobaric coefficient of thermal expansion coefficient $[K^{-1}]$
ν	Kinematic viscosity $[m^2.s^{-1}]$		
δ	Flame thickness [m]	τ	Time constant [s]

Abbreviations :

AIT	Auto inflammation temperature
LVC	Heat release per unit mass of fuel

Subscript :

b	burning
p	propagation
i	internal
e	external
w	wall
g	gas
UG	Unburned Gas
BG	Burned Gas
k	k^{th} specie
0	Ambient air characteristic
D	Diameter based number

Première partie

Context, experimental set up and measurements strategies

Chapitre 1

Introduction

Contents

1.1 Interest in the subject

1.1.1 Interest in narrow channel combustion

Following the miniaturisation tendency of electronics, biology and biomechanics, the demand for reduced-size mechanical and electro-mechanical devices is greatly increasing. In this run to reduce devices scale, the limiting factor is usually the power source (Dunn-Rankin et al. (2005)). The commercial and technological need for reduced-size, safe and efficient power system sets a context of researches for technical solutions.
Thus, if the commonly used power source for electro-mechanical devices are batteries, they prove to be too heavy, volume/space consuming, with a short lifetime and a long recharge time. Therefore, a new generation of power sources was needed, bearing three critical characteristics : reduced size (volume), low weight and long operational lifetime. These new sources are high-specific-energy microelectromechanical power systems (MEMS).

The fabrication of these reduced-sized power systems was also a challenge. Taking advantage of the evolution of high precision microfabrication techniques (centimeter scale) in the precursor fields (bio and electronics), the creation of MEMS got fast-tracked in prototyping and manufacturing, using for instance the same materials as microchips. Also, the micro-fabrication technologies such as stereolithography, low temperature co-fired ceramic taping (LTCC) and silicon based microelectromechanical system (MEMS) fabrication techniques have been used for the design of micro-thrusters. From simple actuators to now pumps, motors, microrovers, microairplanes, unmanned air vehicles and thrusters, the MEMS fabrication is rapidly expanding (Fernandez-Pello (2002)).
In the search for heat power sources, combustion has a great potential for small mechanical devices when coupled with thermo-electric converters. In fact, so called micro and mesoscale combustion benefit from the great energy density of hydrocarbon fuels that is sixty times higher than the one for classical lithium-ion batteries with the advantage of unlimited and immediate refill. Based on a 10 % energy conversion efficiency, the energy density of a micro-combustor is six times higher than the one of a lithium battery (Maruta (2011)). With an adapted conversion system based on combustion, liquid fuel could then be used to feed MEMS in various applications as biomedical (such as drug delivery system), telecommunications or small thrusters.

1.1.2 Existing micro burners

The energy generated by micro burners can be converted into several energy types. Fig. 1.1 represents three possible paths of conversion from thermal energy created by the microburner to electrical, mechanical and chemical energy.
The conversion from thermal to mechanical (T→M) is made through a microturbine (μT) or a micropropulsion (μP) system. Thus, H_2 is produced through an endothermic reactor (T→C). To obtain electricity from the microburner, the direct conversion is done through thermoelectric elements (T→E). Electricity can be obtained from the microturbine converting mechanical energy to electrical energy, or from the created H_2 using fuel cells.
The challenge of reduced-size combustors is to ignite and maintain a combustion with increasing heat and radical losses to the walls. Thus, the materials used must resist to high temperatures and possibly elevated pressures. In the last decades, several kinds of micro-thrusters with different combustor length scales, materials, propellants, and ignition methods have been designed and tested successfully. A sum up of some of the existing meso and micro-scale thrusters and power generators using gas-phase combustion extracted from Ju and Maruta (2011) is represented in Fig. 1.2.
The variety of materials and power developed as well as the sizing of the devices show a great potential of these devices, especially of the small scale combustion as power source. Three examples extracted from the table Fig. 1.2 are represented in Fig. 1.3. Several advanced gas turbine engines were developed by

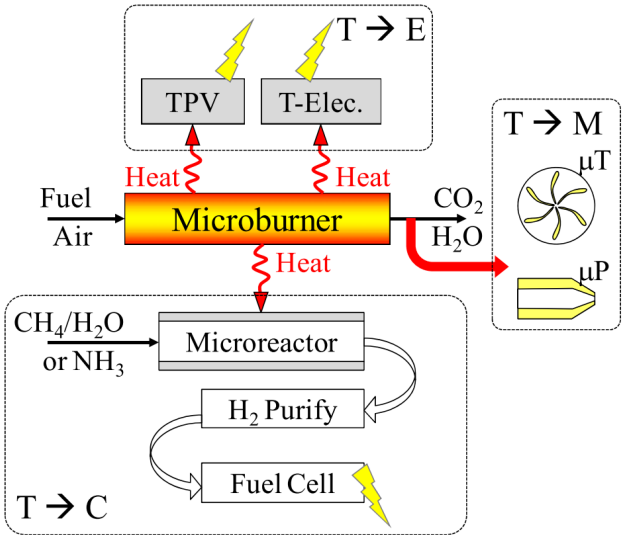

FIGURE 1.1 – *Paths of thermal energy released on microcombustion. "T / E" (thermal to electrical), "T / C" (thermal to chemical) and "T / M" (thermal to mechanical) (extracted from Kaisare and Vlachos (2012))*

Micro-thrusters & engines	Materials	Size/length scale	Thrust, Power	Propellant	Pressure	Challenges
Digital rocket chip (Caltech)	Silicon	0.5 mm^3	0.1 N 100W	$C_6H_3N_3O_8Pb$	~1atm	Large heat loss $d/\delta_f \sim O(10)$
Bi-propellant (MIT)	Silicon	705 mm^3	1N, 750 W	O_2/CH_4	12.3 atm	Low flame temperature and small $Da = t_{res}/t_c$
Staged thruster (PU)	Quarz	2000 mm^3	~500 W	Methanol, butene/air	2 atm	Strong wall-flame coupling $t_c/t_s = O(1)$
Vortex flow combustor (PSU)	Inconel	10–50 mm^3	~500 W	methane/oxygen	1 atm	Small $Da = t_{res}/t_c$
Electrolytic thruster (PSU)	ceramic	322 mm^3	197 mN	HAN	1 atm	Cracking, heat loss, $d/\delta_f \sim O(10)$
Non-premixed combustor (UIUC)	Quartz, alumina	0.1–2 mm	10–50 W	H_2, methane	1 atm	Thermal, radical quenching $Da = t_{res}/t_c \sim 1$
Micro-gas turbine (MIT, Tohoku)	Silicon	60–200 mm^3	50W	Jet fuel	1 atm	Friction, sealing
Rotary engine (UCB)	Silicon, Stainless	1–1000 mm^3	0.01–30 W	Hydrocarbon fuel	1atm	Fuel delivery, friction, sealing, $Da = t_{res}/t_c \sim 1$
Free-piston engine (Honeywell, UM, Georgia Tech)	Stainless	1 cm^3	~10W	heptane, butane, Jet fuel	1–5 atm	Mass loss, sealing, ignition, $t_{ig}/t_{res} = O(1)$

FIGURE 1.2 – *Sum up extracted from Ju and Maruta (2011) of existing/developed meso and micro-scale thrusters and power generators using gas-phase combustion.*

MIT research laboratory, for power generation, using the silicon based microfabrication technology. A schematic of the one stage, single shaft micro-gas turbine engine and the turbine blades are represented in Fig. 1.3(a). The dimensions of 4 mm diameter rotor and 200 mm airfoil height allow to reach 1.3 million rpm, producing from 10 to 20 W, with a sustainable hydrogen combustion.

A research group of Tohoku University in cooperation with IHI Corporation has achieved the creation of the world's smallest gas turbine engine, depicted in Fig. 1.3(b). The dimensions of the engines are about 10 cm diameter and 15 cm long. The compressor, turbine and dummy electromagnetic generator are represented on the right side of the figure. The rotor weights approximately 37 g. The combustor reached $3.6 \cdot 10^5$ rpm, and a temperature between 800 and 900°C, with an established Brayton cycle. This miniaturization success, opens

space for several applications.
At UC Berkeley, a research team has developed two different sizes of rotary engines, fueled by liquid hydrocarbon (hydrogen/air mixtures). Figure 1.3(c) depicts the two different sizes of rotary engines : a mesoscale rotary engine with an output about 30 W and a micro-rotary engine with an output of a few mW.

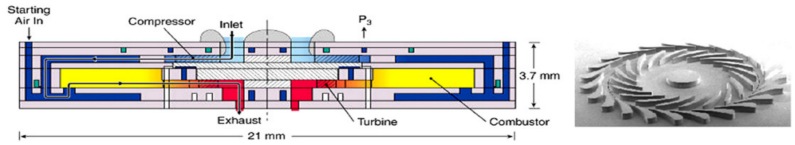

(a) Miniature gas-turbine (MIT)

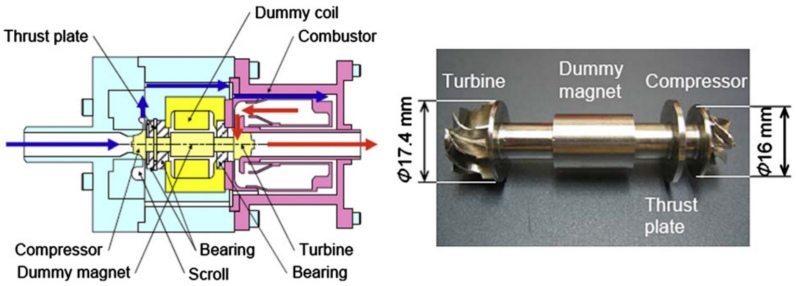

(b) Miniature gas-turbine (Tohoku)

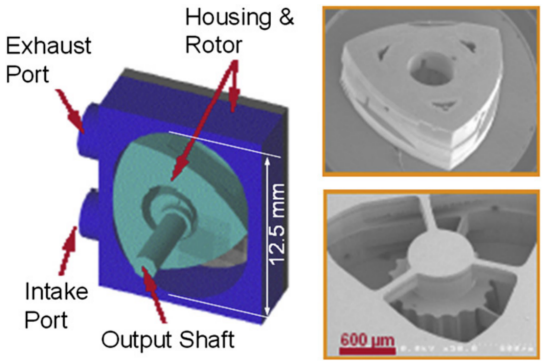

(c) Micro rotary engines (UCB)

FIGURE 1.3 – *Miniature gas-turbine developed at MIT ; Miniature gas-turbine developed at Tohoku with IHI, rotor with compressor and turbine impellers ; meso/microscale rotary engines developed at UCB ; (extracted from Maruta (2011)).*

Nonetheless, as highlighted by the "challenge" column in Fig. 1.2, the size of these micro and mesoscale devices sets some limits to overcome for a broad industrial development. In those devices the large surface to volume ratio causes massive heat loss leading to flame oscillations, quenching and setting flammability limits. Thus, to achieve a sustainable combustion with high combustion efficiency, materials' thermal stability, thermal isolation, turbine cooling and

high pressure sealing sets technical challenges to overcome. Thereby, micro and mesoscale combustion raise a great interests through the technical challenges to understand physical phenomena involved in the operation of these systems and to overcome the stability limits of such small scale devices.

1.2 Narrow channel combustion

1.2.1 Definition and limits

The narrow channel combustion is characterized by combustion in channel or conduct dimensions where a large heat loss to the walls occurs due to high surface/volume ratio. The flow is usually laminar and therefore molecular diffusion is the primary mechanism for mixing. The commonly adopted scaling is to consider micro scale combustion for characteristical burner dimensions under 1 mm, meso scale between 1 mm and 1 cm and macro scale above 1 cm. The mesoscale is often used to highlight specific features of microscale combustion using scale-up model approach.
The flammability limits of narrow channel are set by the quenching phenomenon, which is defined as the smallest dimension under which no flame can propagate in a cold flow. To overcome this limit, thermal and chemical stability managements are required to establish stable combustion in micro and mesoscale devices.

1.2.2 State of the art on flame propagation and stabilization

The multiple behaviors of flames have raised interests of research for a couple of decades. In recent studies, three different phenomena have been investigated both numerically and experimentally :

- the propagation of premixed flames in meso/micro tubes (propagation speeds, limit of propagation, weak flame...),
- the thermal, chemical and mechanical stability management of flames using external assistance (heated walls, catalytic walls, bluff body, heat recirculation, external pilot flame, flame holder...)
- the dynamic behavior of flames (FREI, oscillations, rotating flames, instabilities...)

These three categories of studies are more described in the following.

1.2.2.1 Propagation of premixed flames

Numerical, experimental and analytical studies of flame propagation and extinction limits in a narrow channel have been extensively carried out. Numerically, the stabilization of flames in the computational domain by mass flow rate adaptation was challenging, and thereby the flames propagation is often studied. Numerical computations represent a majority of the existing literature. Chronologically, the hypothesis considered were : first, neglecting gravity

effects, and then domain axisymmetry assumption in order to remove computational domain and as a consequence computational time.

Numerical studies with domain symmetry Mainly before 2008, due to the limitations on computational resources, the numerical computations were carried out with a domain symmetry hypothesis to study flames propagation in narrow channels. Thus, in the majority of these works, adiabatic or isothermal conditions were applied to the walls and mainly reduced chemistry is used (few reaction steps).
As early as 1953, Von Karman and Millan (1953) considered the propagation of two dimensional flames in stationary flows, in large diameter tubes filled with unburned gas mixture. The authors concluded that the flame shape is determined by the thermal conduction.
Less than, forty years later, using one step chemistry on a lean methane/air mixture, Lee and Tsai (1994) identified two flame shapes in adiabatic and isothermal walls. These flames are represented on Fig. 1.4. The first structure is called "tulip" shaped. The flame is concave toward the direction of propagation at the channel centerline. It is mainly existing in adiabatic wall conditions. The second shape called mushroom shaped is convex toward the unburned gas, and mainly existing in isothermal wall conditions. It is shown that the primary mode of the solution is a tulip shaped flame in adiabatic walls, and a mushroom shaped in isothermal walls.
Figure 1.4 depicts the existence of these two flames in function of the flame propagation speed with the tube radius for $\phi = 0.5275$, considering adiabatic (top) or isothermal walls (bottom). Both flame shapes can be found propagating steadily in tubes.
Following the work of Lee and Tsai (1994) and also using a one step chemistry and a two dimensional domain, Hackert et al. (1998) showed the dependance of the two flame shapes on the channel width and on the heat transfer, comparing adiabatic, isothermal and cooled walls by external natural convection and solid radiation. They concluded that the heat transfers to the walls greatly affect flame shape and propagation speed, especially solid radiation which has an impact on temperature distribution and flame propagation speed.
Few years later, Kurdyumov and Fernández-Tarrazo (2002) carried out a two and three dimensional numerical study on flame propagation in conducts with isothermal and adiabatic wall conditions. The effect of the Lewis number on the flame structure is analyzed. For unity Lewis number the mushroom flame is retrieved. For Lewis number under unity, the flame adopts a cellular structure, with two cells in a shape close to the tulip flame structure. In this case the flame almost extinguished near the tube's centerline. Therefore it is shown that the Lewis number has a strong influence on the quenching radius and on the flame shape.
In Daou and Matalon (2002) the flame propagation subjected to a Poiseuille flow is studied in a two dimensional channel and accounting for the heat losses

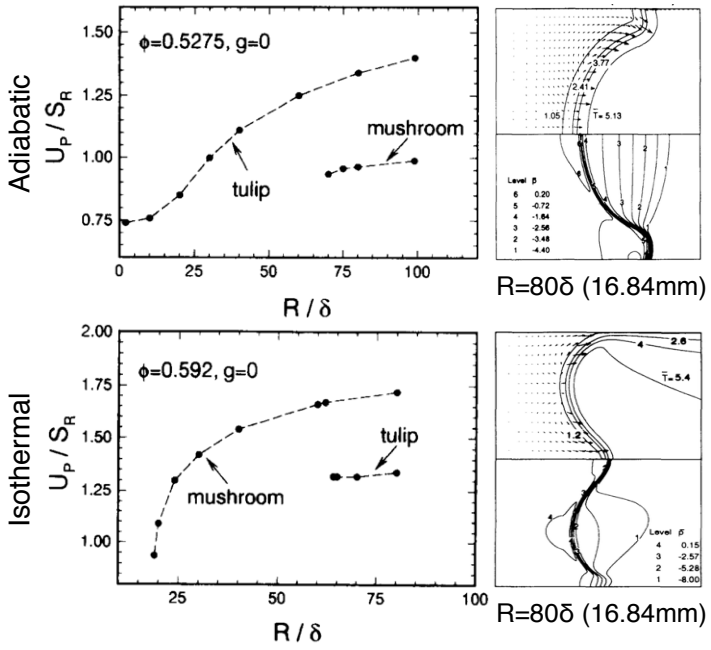

FIGURE 1.4 – ***Left :*** *Variation of the flame propagation speed with the tube radius for adiabatic (top) and isothermal (bottom) walls.* ***Right :*** *Contours of temperature (upper half) and relative pressure (lower half) showing mushroom shaped flame (top) in adiabatic walls conditions, and tulip shape flame (bottom) in isothermal wall conditions for ϕ=0.5275 and U=18 cm·s^{-1} (extracted from Lee and Tsai (1994))*

by wall conduction. It is found that the magnitude of the heat losses is proportional to the square of the channel's width, and extinction occurs at a burning rate close to 60% of the adiabatic laminar flame speed.
Kim and Maruta (2006) simulated a premixed methane/air flame in circular tubes with diameters ranging from 0.4 to 4.0 mm investigating the effect of thermal (adiabatic or isothermal) and velocity boundary conditions. Using a steady formulation and a single-step irreversible reaction, they analyzed the flame shape, the propagation velocity, and the flow velocity variations generated by the flames. As a result in isothermal wall, uniform velocity profile and no-slip wall, they showed that two flame solutions are possible depending on the propagation velocities (positive or negative flow profile) and shapes.
In the same year, the shape and propagation of unsteady premixed flames in narrow channels were numerically investigated in Song et al. (2006) with adiabatic and isothermal walls and one-step overall reaction. The two flame shapes previously illustrated of, tulip and mushroom, were retrieved according to the wall conditions. The results show that the thermal boundary conditions greatly affect the flame formation and shape.
Few of the symmetric studies used complex chemistry, among them Raimondeau et al. (2002); Ju and Xu (2005); Li et al. (2008); Li et al. (2009) studied

the propagation of flames in narrow channels. Raimondeau et al. (2002) showed that the interaction between the gas and solid is critical for flame stability. In fact, two interfacial discontinuities can possibly exist. The first discontinuity is caused by mass transfer at the wall, where the radicals are absorbed into active wall site and are therefore removed from the reactions area leading to wall termination reactions and thus a decrease in the reaction rate. The second discontinuity involves the energy transfer between the gas and the walls. The flame stability comes under the competition between heat loss, radical quenching, and heat generation.
Ju and Xu (2005) studied analytically, numerically and experimentally the propagation of a propane flame inside a 7 mm diameter tube looking at the influence of heat losses. It shows that by decreasing the channel width two types of flames can propagate at a same equivalence ratio : a fast flame and a slow flame. These multiple flame regimes are caused by the wall-flame interactions. The latter also impacts the flammability limits. They also prove a non-linear dependance of the flame speed on equivalence ratio.
Li et al. (2008) and Li et al. (2009) solved the wall temperature in symmetric assumption for two dimensional cylindrical and planar channel, showing the effects of combustor geometry on flame temperature, respectively for hydrogen and methane air mixture. The Fig. 1.5 depicts the flame temperature according to the geometry, and the inlet velocity.

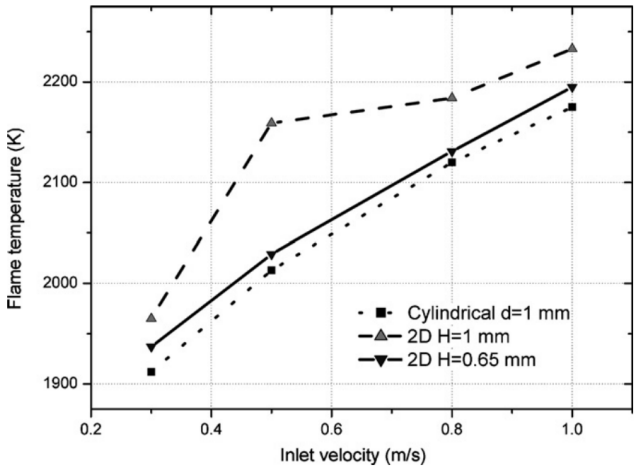

FIGURE 1.5 – *Effects of combustor geometry on the flame temperature (extracted from Li et al. (2009))*

It can be seen on Fig. 1.5 that the flame temperature is lower in cylindrical geometry burners than in planar channels.
Two main flame types are found in symmetrical computations, the tulip and mushroom shaped flames using adiabatic and isothermal wall conditions but also using wall solved temperature computations. These numerical results all

converge to the same conclusions that the wall conditions, geometry and wall-gas interface are critical to flame stability, propagation speeds and shape. However the symmetric assumption was progressively put in default starting with Pizza et al. (2007), Pizza et al. (2008) and Tsai (2008).
In these more recent studies the computation domains are solved entirely, and the tulip shape flame is not retrieved.

1.2.2.1.1 Numerical studies with and without domain symmetry

Tsai (2008) proposed the study of stoichiometric methane/air premixed flame propagation in a two dimensional channel and in a circular tube, with isothermal wall and a prescribed Poiseuille flow, using a one-step irreversible reaction. The symmetry assumption is considered and compared to the full domain computation. It is shown that without the symmetry assumption, two flame shapes are distinguished in the numerical results : a mushroom shaped and an asymmetrical slant shaped flame.

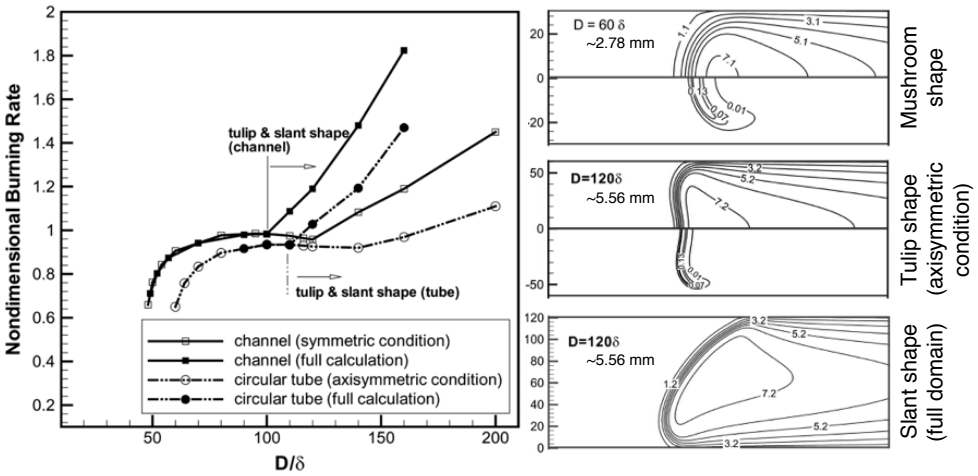

FIGURE 1.6 – ***Left :*** *Variation of the flame burning rate with the duct width for the stationary flame (V_p=0) in ducts.* ***Right :*** *from top to bottom : Mushroom-shaped flame in 2-D channel, D =60δ and V_p=0. Tulip-shaped and asymmetrical slant-shaped flame in 2-D channel, D=120δ and V_p=0. Upper half : contours of the dimensionless temperature T=T/298K. Lower half : contours of the dimensionless fuel mass reaction rate $\dot{w}_f = -\dot{w}_f/510$ (extracted from Tsai (2008)).*

The mushroom shape is preferably found in small conducts and asymmetrical shape found in larger ones. When the symmetrical assumption is considered, the tulip shaped flame is retrieved instead of the asymmetrical slant shaped flame. The asymmetrical slant shaped flame is then a more robust manifestation of the tulip flame in full domain computation.
In Pizza et al. (2007) and Pizza et al. (2008) the stabilization and dynamics of lean (ϕ=0.5) premixed hydrogen/air flame are investigated in respectively micro (height h=0.3 to 1.0 mm) and meso (heights h=2,3 and 7 mm) pla-

nar channels using direct numerical simulation with detailed chemistry. The flame regimes are mapped according to the channel height h and the inflow velocity. In microscale channel, five different burning modes are observed : periodic ignition/extinction, V-shaped steady flame, asymmetric flame, oscillatory mode between two asymmetric flames and oscillatory mode pulsating axially. In mesoscale channel, six burning modes, are identified : mild combustion, periodic ignition/extinction, closed symmetric stable flames, open symmetric stable flames, oscillating flames, and asymmetric stable flame. For mesoscale channels, cellular flame structures and chaotic behavior are also observed. By increasing the channel's height, and varying the inflow velocity, the flame dynamics becomes richer. Those two parameters are then crucial in the stabilization and propagation regimes of the flame.
Kurdyumov et al. (2009) investigated the effects of channel height, inflow velocity and wall temperature on the burning modes with a two-dimensional thermo-diffusive model, isothermal walls, single step chemistry and unity Lewis number. Again steady symmetric and asymmetric flames are observed as well as oscillatory behaviors. The wall temperature is shown to have a strong influence on the flame dynamics. A one-dimensional model is developed and is able to qualitatively reproduce some of the observed dynamics of two-dimensional flame. Using a reduced chemistry and no hydrodynamic and thermo-diffusive instabilities due to the adopted models, the source of flame instabilities is identifies as the thermal flame-wall interaction.
Later on, Kurdyumov (2011) studied the influence of the differential diffusion effect on lean flame propagation, using a constant density approximation to eliminate hydrodynamic effects and flame-fluid interactions, in adiabatic walls. Steady and oscillatory symmetrical and asymmetrical flames are observed according to the Lewis number and the flow rate. A linear stability analysis of the solutions is also provided. Finally the differential diffusion effect is not the only phenomenon which can contribute to formation of the asymmetrically propagating flames in ducts.
In following work using the same modelisation, Kurdyumov and Jiménez (2014), investigated the influence of conductive heat losses. Again, for Lewis number below unity, steady symmetrical and asymmetrical solutions are observed, and in the case of high flow rates they coexist for the same set of parameters. It is shown that for symmetrical flames in this case, conductive heat-losses produce a stabilization effect. For high Lewis numbers, the oscillatory symmetrical and asymmetrical flames are observed and the linear stability analysis shows that in this case the conductive heat losses promote the oscillatory behavior.
Later on, Kurdyumov and Jiménez (2016) proposed an analysis of a lean flame propagation in a two and three dimensional cylindrical conduct with adiabatic walls, diffusive-thermal modelisation and single step chemistry, investigating the effects of Lewis number and channel radius on the burning modes. The thermal expansion and heat loss effects are not accounted for. As for the planar channel, for Lewis number below unity, the solution are steady symmetrical or

asymmetrical. Thus, for low Lewis number the two steady solutions can co-exist for the same set of parameters. For Lewis number higher than unity, oscillation and rotation behaviors are observed. Therefore the axial symmetry commonly used is invalidated for non-unity Lewis numbers.
Jointly Dejoan and Kurdyumov (2018), using the same modelisation with single step chemistry, investigated the thermal expansion effect on the flame propagation. Therefore the flow is under variable-density and zero Mach approximation. The multiplicity of flame propagation solutions is retrieved. Thus in non axi-symmetrical assumption, the slant shape flame is observed instead of the concave flame or tulip shape flame branch, which is not observed. The thermal expansion has an effect on expanding the Lewis number range (below unity) at which the steady solutions appear. Due to the density variation, the flame structure is modified by an accelerated flow at the flame front.
Following the work of Kurdyumov and Fernández-Tarrazo (2002), Kurdyumov (2011) and Fernández-Galisteo et al. (2014), combined with complexe chemistry, transport and thermal expansion effects Jiménez et al. (2015) investigated the propagation and flashback limits of lean hydrogen-air flames in two dimensional narrow channel, with adiabatic walls using direct numerical simulation. The propagation speeds differ greatly between the symmetrical and asymmetrical flames, which also impacts flashback conditions.
Fernández-Galisteo et al. (2017) showed that both differential diffusion and preferential diffusion have influence on the stability of the symmetric flame shape. For high and low equivalence ratio, the flame behaves as dictated by the Lewis number of the deficient reactant, meaning that the flame destabilizes toward non-symmetric solutions for large mass flow rates when the mentioned Lewis number is less than one. Near stoichiometry, the symmetric solution is stable for large mass flow rates because of the difficulty found by the less diffusive reactant to reach the reactive zone of the flame.
To conclude, in numerical computations, the symmetry assumption as well as strong wall conditions (adiabatic or isothermal) were first broadly adopted because of computation limitations. Following this assumption two flame shapes were encountered : the mushroom shaped and tulip shaped flames. In the last decade, the full domain resolution results lead to a different flame shape, a symmetric mushroom shaped flame and an asymmetric slant shaped flame. The flame shape is found to depend on the equivalence ratio, the thermal-diffusion (Lewis number), the heat losses, the incoming velocity and the wall conductivity. Thus the flame stabilization is challenging and requires stability management.

1.2.2.2 Thermal, mechanical and chemical stability management

The second set of studies investigated the stabilization of a laminar flame in narrow channels with external assistance. Indeed, the micro and meso combustion suffer from massive heat loss. The strategy is to compensate heat loss by

thermal, chemical or mechanical assistance, in order to stabilize the flame, and extend the flammability limits.

Thermal combustion assistance Thermal assistance is performed either by pre-heating fresh gases (Chao et al. (2007); Ju and Xu (2006a); Ronney (2003); Federici and Vlachos (2008)), by creating a controlled temperature distribution within the tube wall (Di Stazio et al. (2015); Maruta et al. (2004); Maruta et al. (2005); Nakamura et al. (2012)), or by stabilizing a pilot flame at the tube output (Evans and Kyritsis (2009)). These methods are called assistance by excess enthalpy.

— Technically, the preheating of the fresh gas (Sánchez-Sanz (2012); Chao et al. (2007); Ju and Xu (2006a); Ronney (2003); Federici and Vlachos (2008)) can be processed by recirculation of the burned gas, or by heating systems such as heating wires, or electrical heater. Heat recirculation has been extensively studied in the past decade, especially its effect on flame speeds and flammability limit. It is based on the direct enthalpy transfer from the burned gas to the unburned cold mixture, through wall conduction. In single channel burners, an indirect enthalpy transfer from the burned gas to the fresh reactant occurs through the axial wall conduction. This indirect heat recirculation strongly depends on the wall conductivity. It is responsible for a strong coupling between the flame and the wall. To use direct enthalpy transfer, recirculation burners are considered and represented in Fig. 1.7(left).
Ju and Choi (2003) carried out a study on the (a) counter flow burner, where two parallel channels in which two equal unburned gas flow in opposite directions are ignited in a way that the burned gas of one flame preheats the unburned gas of the other one. It is shown that the flame can be maintained in leaner conditions than without heat recirculation. Ronney (2003) investigated the (b) U shaped burner, and show that the axial conduction in walls has a great effect on the operating limits of the burner, especially for low flow speeds. If the mass flow rate is sufficiently low, it leads to a higher heat recirculation and a greater time residence of the flame, possibly overcoming the heat losses, and by suppressing axial wall conduction, no extinction limit is found. However, the burner shows a high sensitivity to the wall conduction. The investigation of Federici and Vlachos (2008) on the effects of preheating the unburned gas on flame speed using a (d) burner, is depicted in Fig. 1.7(right), where the critical velocity is plotted against the wall thermal conductivity using two dimensional CFD simulation. The blowout and extinction limits are drawn for the heat recirculation burner (HR), and the single channel(SC). In-between these limits, a flame can be stabilized. It is therefore shown that the blowout limit is clearly extended by the use of heat recirculation. The height of the center HR burner channel and SC burner channel is 600 μm, while the secondary channels height of HR

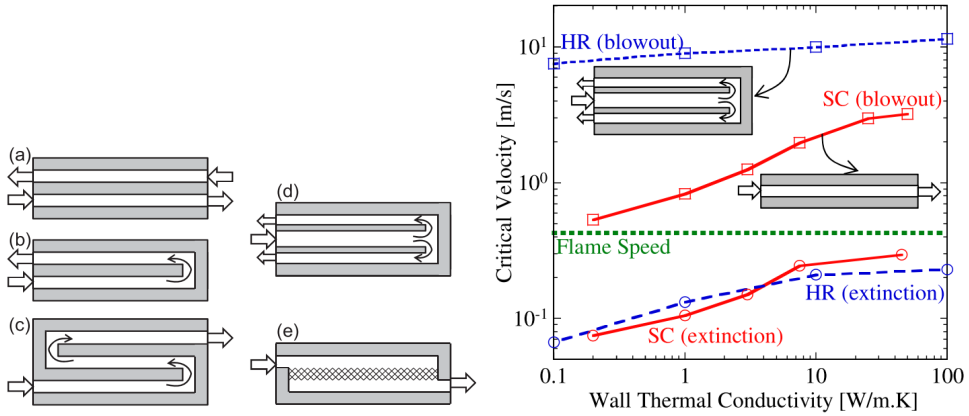

(a) Heat recirculation burners Kaisare and Vlachos (2012)

(b) Flammability limits comparison between single channel (SC) and heat recirculation burner (HR) Federici and Vlachos (2008)

FIGURE 1.7 – ***Left :*** *Heat recirculation burners (a) counter-flow burner, (b) U-shaped burner, (c) serpentine burner, (d) symmetric recirculation burner, (e) porous co-flow burner.* ***Right :*** *Effects of heat recirculation burner (HR) on flame speed, in comparison to a single channel burner (SC) (extracted from Kaisare and Vlachos (2012); Federici and Vlachos (2008)).*

burner are of 300 μm.

— The imposed temperature profiles are usually assured by external burners as shown in Fig. 1.8. According to the temperature imposed and the fuel used, auto-ignition can be triggered and several flame dynamics as well as flame stabilization can be reached.

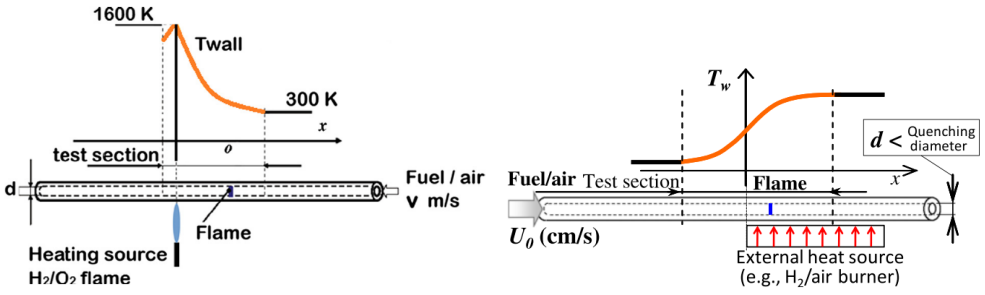

(a) Gaussian temperature profile Di Stazio et al. (2015)

(b) Step temperature profile Nakamura et al. (2012)

FIGURE 1.8 – *External burner imposing a temperature profile in the burner walls. Two types of temperature profiles.* ***Left :*** *gaussian type, using three 120° spaced H_2/O_2 burners ;* ***Right :*** *step type, using H_2/air flat burner respectively (extracted respectively from Di Stazio et al. (2015); Nakamura et al. (2012)).*

These thermal assistance create adequate conditions for the flame to stabilize at one location in the tube but the energy addition is usually over-sized and the total budget is negative, which leads to a one-way coupling where the flame position cannot modify the wall temperature.

Chemical combustion assistance Chemical assistance is mainly performed through catalytic walls that could compensate the heat losses (Dogwiler et al. (1998) ; Maruta et al. (2002) ; Smyth and Kyritsis (2012) ; Kaisare and Vlachos (2012)). The catalytic assistance takes advantages of the large surface-to-volume ratio, removing radical quenching and giving a fixed reaction area. Thus, clean emission can be achieved by using appropriate material. Kaisare and Vlachos (2012) schematically describe in Fig. 1.9 the mechanisms of catalytic combustion assistance. The diffusive mass transfer of reactants occur from bulk flow to the catalyst layer, inside which exothermic catalytic reactions take place. The products of these reactions are transferred back into the bulk flow by diffusion. Heat transfer occur from the heat produced by these exothermic reaction to the solid structure (wall) and to the bulk flow, and therefore contribute to the flame stabilization at a specific location.

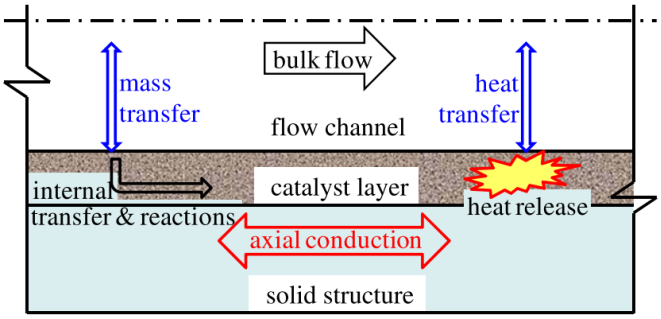

FIGURE 1.9 – *Schematic of various processes within a catalytic microburner. The mass and thermal processes are shown on left and right ends, respectively, for clarity; these processes indeed take place at the same location in a microburner.(Kaisare and Vlachos (2012))*

Using Pt-coated surfaces on a 7 mm height planar channel, Dogwiler et al. (1998) investigated numerically and experimentally the effects of catalytic walls on a lean methane/air (ϕ=0.31-0.37) flame. The incoming flow is heated around 750 K and the flow speed is set to 2 m·s^{-1}. With the catalytic walls, the authors were able to retrieve the tulip shape flame found with heat assistance or adiabatic walls, and which was replaced by the asymmetrical slant shape without the assistance.

Mechanical combustion assistance Mechanical assistance is created through flame holders to force the flame stabilization at a given point where the velocity field is adapted and flame heat is accumulated. Using a wire mesh between

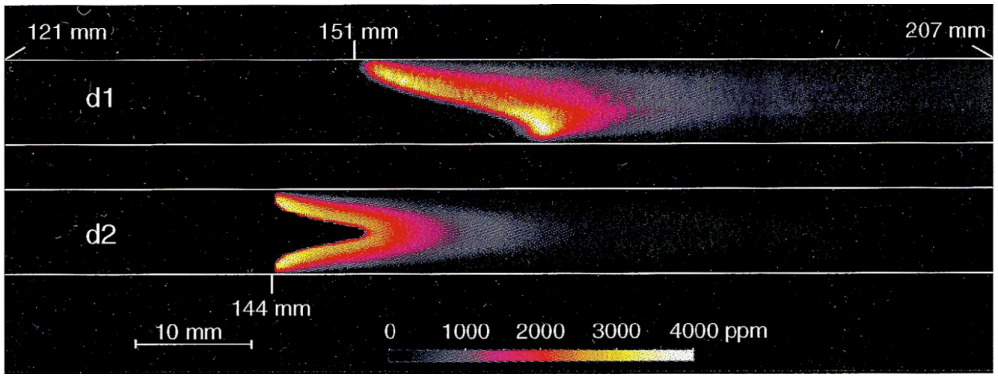

(a) Non catalytic case : ϕ=0.33, U=2.1 m·s^{-1}, T_{GF}=680 K

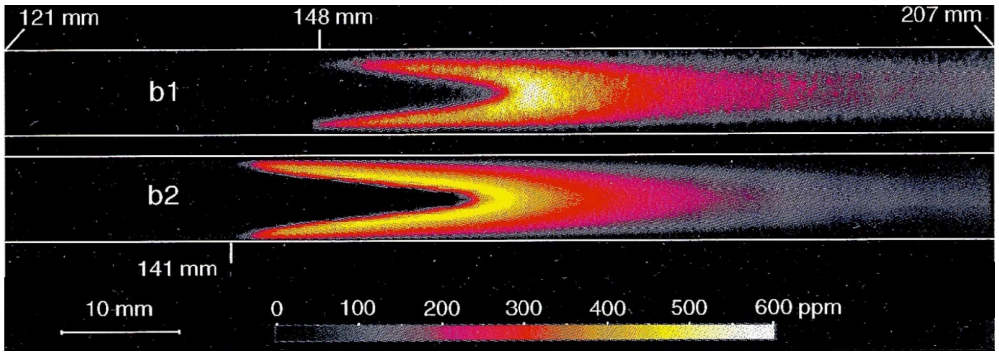

(b) Catalytic case : ϕ=0.33, U=2.1 m·s^{-1}, T_{GF}=680 K

FIGURE 1.10 – *Top : Measured (d1) and predicted (d2) OH concentration maps (in ppm) for the non catalytic case : ϕ=0.33, U=2.1 m·s^{-1}, T_{GF}=680 K. Bottom : Measured (b1) and predicted (b2) OH concentration maps (in ppm) for cases (b) (extracted from Dogwiler et al. (1998)).*

two quartz tube represented in Fig. 1.11, Mikami et al. (2013) show that the flammability limits are greatly extended as flames can be stabilized inside the tube near the mesh for tube diameter lower than the quenching diameter.
In the same way, Munir and Mikami (2015) show numerically the stabilizing effect of concentric rings.
To conclude, these three types of assistances allow to extend the flammability limits and the domain of stabilization of the flame but also to observe several flame regimes. However, they are extensively modifying or annihilating the flame-wall interactions, and the flammability domain dependence to flow characteristics, heat transfer and wall properties is not identified.

1.2.2.3 The dynamic behavior of flames

The last set of studies observed or modeled original dynamic behaviors of flames in the context of micro-combustion, in particular the case of the FREI pheno-

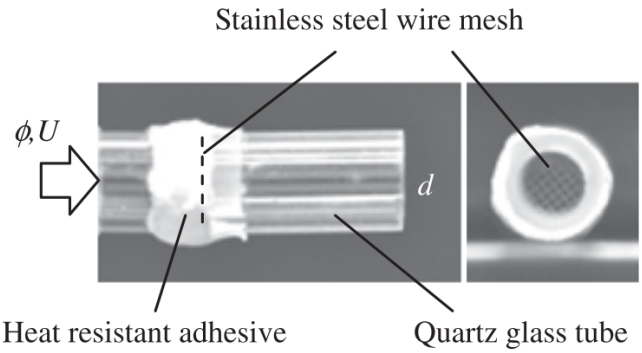

FIGURE 1.11 – *Wire mesh used as flame holder in a mechanical combustion assistance (extracted from Mikami et al. (2013))*

menon Richecoeur and Kyritsis (2005); Maruta et al. (2004); Nakamura et al. (2012) ; Maruta et al. (2005); Kurdyumov et al. (2009); Minaev et al. (2007); Di Stazio et al. (2016) or rotating flames Kumar et al. (2007). These instabilities are observed with the previously thermal or chemical stabilizing mechanisms. The temporal motions of various flames of propane/air mixtures at an average mixture velocity of U=30 cm·s^{-1} and an equivalence ratio of ϕ=0.5 are represented in Fig. 1.12. The cylindrical quartz tube has a 2 mm inner diameter which is under the quenching diameter for the mixture. A step temperature gradient is imposed to the tube's wall, and according to the maximum of temperature imposed, four different flame regimes are observed : a stable flame for T_c=1320 K, flame with repetitive extinction and ignition (FREI) for T_c=1130 K, a pulsating flame for T_c=1270 K and a flame with a combination of pulsating flame and FREI at T_c=1200 K.
The origin of these instabilities can be multiple, and the literature shows a growing interest in identifying these phenomena.

- Buoyancy forces instability leading to vortex motions of burned and unburned gases
- Hydrodynamic Darrieus-Landau instability, caused by thermal expansion, and leading to streamline deformation.
- Diffusive-Thermal mass diffusivity of the heavier species
- Saffman-Taylor instability is linked to pressure gradient induced by viscous effects
- Rayleigh-Taylor instability occur when two gases of different densities are in contact

All instabilities have an impact in terms of flame shapes and propagation rates.

1.2.3 Parametric studies and effects

In the literature the main variated parameters are the channel width (Hackert et al. (1998); Daou and Matalon (2002); Norton and Vlachos (2004); Ju and Xu

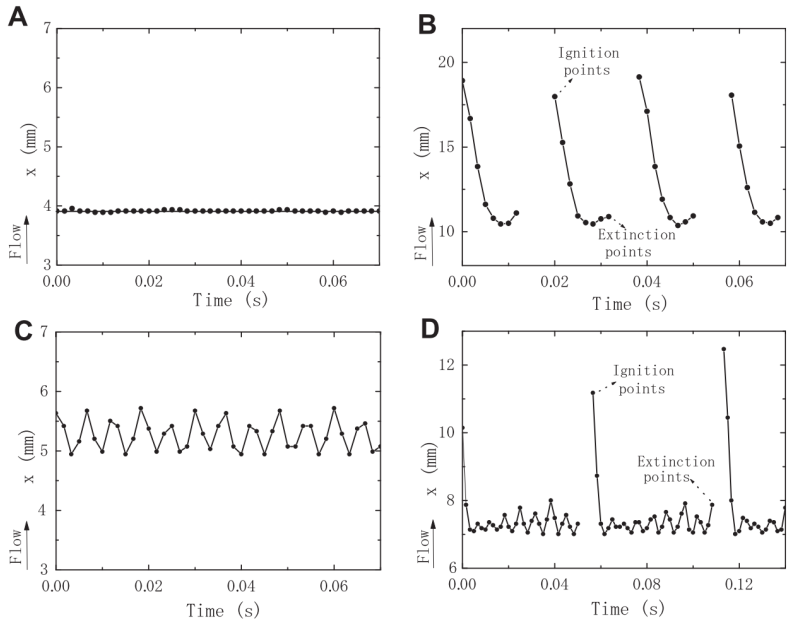

FIGURE 1.12 – *Temporal evolutions of the motions of various flames of propane/air mixtures at an average mixture velocity of 30 cm·s^{-1} and an equivalence ratio of ϕ=0.5; (A) stable flame in the case of maximum wall temperature, Tc=1320 K, (B) flame with repetitive extinction and ignition, Tc=1130 K, (C) pulsating flame, Tc=1270 K, and (D) flame with a combination of pulsating flame and FREI, Tc= 1200 K (extracted from Maruta et al. (2005))*

(2006a); Tsai (2008); Pizza et al. (2008)), the incoming velocity (Norton and Vlachos (2004); Daou and Matalon (2002); Ju and Xu (2006a); Tsai (2008); Pizza et al. (2008)), the wall heat losses (Hackert et al. (1998); Norton and Vlachos (2004); Daou and Matalon (2002); Sánchez-Sanz et al. (2014)) the Lewis number (Ju and Xu (2006a); Kurdyumov and Fernández-Tarrazo (2002); Kurdyumov (2011); Sánchez-Sanz et al. (2014)), the equivalence ratio. The effects are multiple, and these study show the sensitivity of the combustion in narrow channels.

1.2.4 Numerical studies considering gravity

Gravity was not broadly investigated in the literature, the hypothesis of no effect on the combustion is made in the great majority of the cases. One of the early investigators of gravity effects on the flame propagation Lee and Tsai (1994), take the gravity along the tube axis, with a symmetry assumption.
The direction of the gravity with respect to the flow is varied, with an interval of acceleration of gravity of -3< g/g$_0$<1.5 with g$_0$=9.8 m·s^{-2}, with adiabatic walls. The existences of both tulip and mushroom flame shape are represented in Fig. 1.13(a) in these cases.

Recently, Tsai (2008) took into consideration the gravity in the numerical computation of a two-dimensional channel. The non dimensional burning rate is represented in Fig. 1.13(b) as a function of the Froude number. The Froude number $\mathrm{Fr}^{-1} = (gd/U_a d^2)$ varies from negative values where the direction of the flow is opposite to the gravity to positive values where both have the same direction.

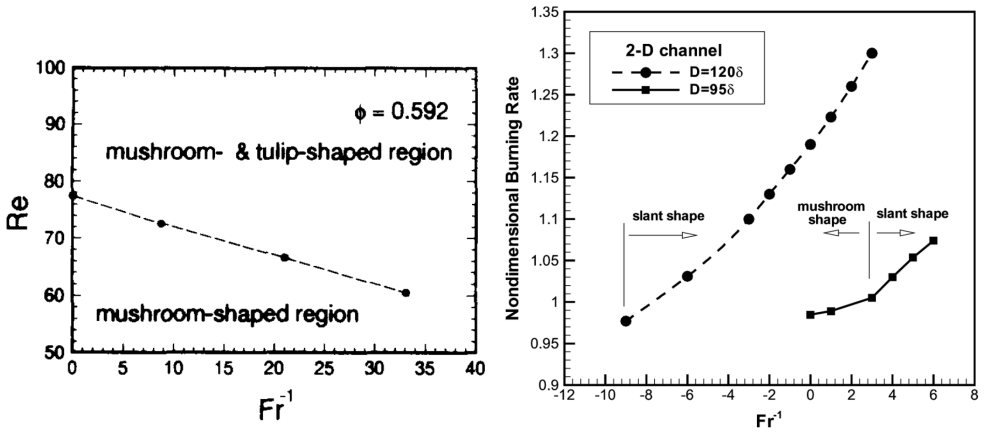

FIGURE 1.13 – ***Left :*** *Bifurcation map for ϕ=0.592 and isothermal wall, extracted from Lee and Tsai (1994)* ; ***Right :*** *Variation of the burning rate with Fr^{-1} for stationary flame in 2D channel; V_P=0, extracted from Tsai (2008).*

Fig. 1.13 highlights the threshold between the symmetric mushroom and asymmetric slant shape flame at a certain Froude number (≈3), for a R=95δ width channel. This threshold does not appear for R=120δ width channel where only the asymmetrical slant shape flame is observed. Globally, it shows that positive Froude number promotes the asymmetrical flame shape. The buoyancy forces push the heated gas of the reaction area away from the fresh gas, in the opposite direction of the gravity, leading to an increase in the flame area with the increase of g, and resulting in the increase of flame propagation speed.
The latest article on the influence of gravity on flame shape, stability and propagation in narrow channel is Fernández-Galisteo and Kurdyumov (2018). A two dimensional study of a planar flame propagating in adiabatic walls. The wall-plates are inclined with a variating angle. At a negative angles, the flame propagates downward, and inversely at positive angles the flame propagates upwards. At a zero angle the plates are horizontal. A gravity parameter is defined according to this angle and the gravity acceleration as $G = (h^2 \mid \vec{g} \mid \sin\alpha)/(12 Pr S_L^2 \delta_T)$. For downward propagation (G>0) and a Lewis number below unity, it is found that above a critical value of G_c ≈5.84, the buoyancy forces stabilize the hydrodynamic instability. For unity Lewis number, only the Darrieus-Landau hydrodynamic instability is suppressed, above a threshold of G_c ≈10.61. Above unity Lewis number, the flame oscillatory instability is shown

to have a diffusive-thermal nature. For G>0 the buoyancy forces are unable to stabilize the instability, and the most unstable modes are reached for G<0.
The impact of buoyancy forces on narrow channel combustion seems then important to account for. Further work on gravity is carried out in chapitre 6 as the orientation of the tube is varied, to explain some experimental and numerical observed phenomena.

1.3 Motivations and outline of the presented work

In most of the presented studies, the flame residence time in the channel is not long enough to interact thermally with the walls and modify the temperature distribution in the wall. Thus, numerical computations often adopt strong assumptions such as adiabatic or isothermal walls, and symmetric domain. Some of studies focused on the flame wall interactions in micro combustion without assistance (Daou and Matalon (2002); Jackson et al. (2007); Wan et al. (2015)) briefly showed the stabilization of a premixed flame in a 7 mm high rectangular tube and observed the non-symmetry of the flame. The mechanisms of stabilization of a flame without assistance are not sufficiently documented and, consequently the lack of knowledge on the interactions between the flame and the wall makes impossible a fine tuning of the flame stabilization strategy. Thus, several instabilities have been observed and studied in the cases of no thermal coupling with walls. It is the purpose of this study to show the behavior of a premixed laminar flame stabilized in a 5 mm diameter quartz tube without assistance and to expose a way to choose the flame location through an external thermal controller. The question is raised if the observed instabilities exist in such configuration, or if the wall coupling plays a role in stabilizing the flame. The choice of the experimental setup's scale is challenging. The present study uses a tube diameter slightly above the quenching diameter so that heat transfers have a significant impact on the flame, but the latter is self-maintained. If the diameter is too small, the heat losses and flow speed increase, leading to flame propagation or extinction. If the diameter is too large, thermal effects have a weaker impact on flame stabilization.
The **first part** of the present work aims to set the context, presenting the configurations studied and the diagnostics used, as well as highlighting the first observations. In chapitre 1, the interests of narrow channel combustion were pointed out. Thus the state of the art was presented to contextualize the present work, as well as its stakes and limitations. chapitre 2 presents the chosen experimental set up of a lean premixed methane/air flame, in quartz tubes, without external assistance. Furthermore, the diagnostics operated described. Thus, the justifications of the choices of the studied configurations are exposed. chapitre 3 answers a demand of precise wall temperature measurements by exposing Laser Induced Phosphorescence temperature measurements, and tests two measurements methods on high curvature radius tubes. The **second part** of the present work introduces the first results in flame steady regime. chapitre 4 exposes the stabilization domains of the flame according to flow speed and equivalence ratio as well as its shape. The effects on the flame shape and operating points due to the variation of tube diameter and positioning in horizontal or vertical configuration are observed. All together this chapter allows to characterize the flame stability without assistance. Following this experimental characterization, chapitre 5 provides a theoretical analysis on heat exchanges from the flame to the ambiant air, as well as a one-dimensional steady com-

putation using a complex chemistry code (REGATH). It allows to identify the heat transfer exchanges and quantify their impact on flame stability. Jointly with CORIA research team proceeding a two dimensional DNS simulation of the studied configuration, chapitre 6 retraces the origin of the observed flame asymmetry. Finally the **third part** of this work shows the response of the flame to two types of perturbations. The chapitre 7 describes experimentally and numerically, once again using the one-dimensional complex chemistry code REGATH, the flashback of a flame caused by a thermal input upstream from the flame. Lastly, chapitre 8 as perspectives for further work, exposes the possible experimental coupling of a microwave-plasma assistance to the flame. Numerically, an existing model is tested in the studied configuration to evaluate the flame response to vibrational energy input upstream from the flame front.

1.4 Publications

1.4.1 Journals

K. Bioche, A. Pieyre, G. Ribert, F. Richecoeur, L. Vervisch, *The role of gravity in the asymmetry of flames in narrow combustion chambers*, Combustion and Flame 203, 2019, Pages 238–246.
Another paper is in preparation based on the chapitre 7, about the response of a stabilized flame to an upstream thermal perturbation.

1.4.2 Conferences

— A. Pieyre, T. Yokomori and F. Richecoeur, *Thermal characterization of a narrow channel wall by thermographic phosphor thermometry*, in the 8^{th} European Combustion Meeting, 2017.
— A. Pieyre, T. Yokomori and F. Richecoeur, *Determination of wall temperature in a narrow channel by thermographic phosphor thermometry*, in the Fifty four Japanese Symposium on Combustion, 2016.
— A. Pieyre, N. Darabiha and F. Richecoeur, *Unsteady position control of lean premixed flames in a narrow channel*, in the Fifty Third Japanese Symposium on Combustion, 2015.

Chapitre 2

Experimental configuration : Flame in a narrow channel

Contents

2.1 Extended abstract

The main motivations for micro-combustion development is to convert efficiently and steadily liquid fuel into heat to equip portable or small-size devices. In literature, most of the studied configurations provide heat to the combustor (or at least consider adiabatic walls) or investigate the non-stationary regime of propagation. A simple experimental setup, built around a cylindrical tube, is designed to observe a stationary lean premixed flame with significant heat losses to the walls. The smaller the diameter of the tube, the larger the heat loss through the walls. At the limit, below the quenching diameter, the flame cannot stand due to excessive heat loss and/or radical quenching at the walls.

Thus the experiment runs with an internal diameter equal to 5 mm and a wall thickness equal to 1 mm. These dimensions strongly depends on the wall material. First, quartz allows to observe flame intermediate species in ultra-violet frequency band and therefore track accurately the flame shape and position. Second, quartz minimises radical quenching at the walls in the range of temperature studied. Third, the thermal conductivity provides thermal time scale of the order of tens of seconds that are small enough to observe effect on the flame but large enough not to compete directly with convection and chemical time scales. The wall conductivity also controls the length of the tube. The idea is to get an experimental setup where the excess energy from combustion is transferred to external medium through natural convection and radiative transfers. So there should not be any increase of the gaz enthalpy between the input and the output of the tube. With a twenty-centimeter long tube, the outgoing burnt gas recover the ambient temperature and do not convey residual heat. Physical considerations impose the geometry and the material. In this configuration, a steady laminar flame is stabilized within the tube at a given position without any artificial anchoring. The coupling between the flame and the wall temperature creates a favorable zone where the flame sits for a given mass flow rate and equivalence ratio. The flame can adapt to a change of mass flow rate, equivalence ratio and thermal conditions. To understand how the flame stands, direct observations of hydroxyl radicals in the flame front are performed with a filtered camera. It tracks both the position and the geometry of the flame (curvature, thickness, orientation...). Due to the importance of heat exchanges, external wall temperatures are measured. First results show a maximum temperature at 850 K for the highest equivalence ratio studied with a spatial dispersion validating the tube length (i.e. the wall temperature is equal to ambient temperature).

2.2 Flame in a narrow channel in natural environment

2.2.1 Description of the experimental setup

The experimental setup, displayed in Fig. 2.1, consists in a d_i=5 mm inner diameter and e_w=1 mm thick quartz tube placed in two configurations : horizontal or vertical position. The tube's length is L=200 mm. Inside the tube a lean methane/air premixture is injected. The mixture is ignited at the free end of the tube, the mass flow rate is then adapted for the flame to enter the tube and the flame is finally stabilized at a given position by equalizing the bulk mean speed to the burning velocity.
The quartz was chosen for its thermal and optical properties, which allow a direct visualization of the flame and its propagation. In fact, direct visualization of the flame is essential to track the flame motion and topology, but also because

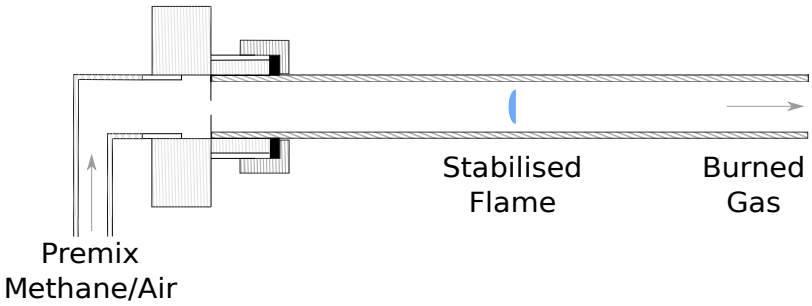

(a) Scheme of the experimental setup

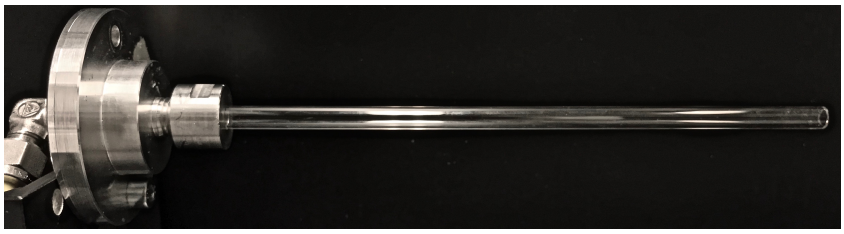

(b) Picture of the experimental setup

FIGURE 2.1 – *Schematic view (a) and picture (b) of the experimental setup composed of a quartz tube of 5 mm inner diameter and 1 mm thickness, inside which a lean methane/air mixture is injected.*

a part of the diagnostics are based on image analysis.
The diameter was chosen accordingly to the dependence of heat exchanges and flame speed to the tube diameter. It is right above the quenching diameter of the premixture ($\simeq$ 3 mm) to prevent the use of an external assistance and keep similar stabilization behavior to a microscale flame. The quenching effects on flame propagation and stabilization are exposed in the following section 2.3.2.
As abovementionned, a lean methane/air premixture is injected inside the tube illustrated in Fig. 2.1. Two mass flow controllers (EL-FLOW Bronkhorst) of range for air 0-700 Nml·min^{-1} and for methane 0-70 Nml·min^{-1} are enslaved to command the bulk velocity and the equivalence ratio of the flow. A mixture chamber is created prior to the quartz tube entrance (not shown on the figure). The maximum mean bulk velocity imposed is then U=70 cm·s^{-1} (826 ml·min^{-1} at T=300 K). With a precision of 0.35 ml·min^{-1} (0.06 cm·s^{-1} in bulk speed), the mass flow controllers allow to precisely modify the bulk velocity. The flow is laminar with a Reynolds number below 200, and is under a prescribed Poiseuille profile. When the bulk speed is equal to the burning velocity, the flame is stabilized inside the tube. These operating points are characterized by a unique couple of equivalence ratio and bulk velocity.
The interest of this fairly simple configuration is then to observe the full interaction between the inner gas, outer gas and wall, without assistance. The aim is to evaluate the heat exchanges and identify the dominant phenomena in the propagation and stabilization mechanisms of a flame in such dimensions.

2.2.2 Flame temperature domain

To evaluate the length sizing of the tube, the temperature profile of a flame in steady regime in the horizontal configuration is measured by thermocouple (see 2.4.3) for the equivalence ratio ϕ=0.80 and drawn on Fig. 2.3. The flow direction is taken as a convention all along this work from left to right. The flame front is positioned as the zero abscissa coordinate and highlighted by a black dashed line. Therefore, the negative coordinates represent the unburned gas area while the positive coordinates depict the burned gas area. This temperature profile allows to set the boundary conditions of the study, schematically represented in Fig. 2.2.

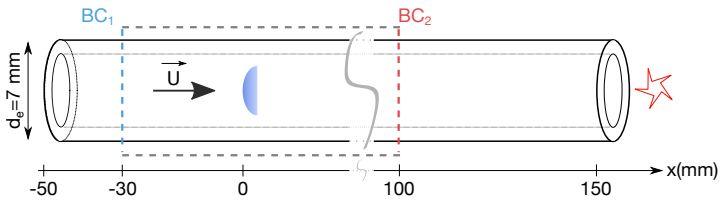

FIGURE 2.2 – *Schematic representing the boundary conditions (BC_1 and BC_2) with a flame stabilized inside the tube.*

In fact, on Fig. 2.3 thermal equilibrium is reached 30 mm upstream and 100 mm downstream the flame front. The left boundary condition is thereby set where the temperature of the unburned gas is equal to the wall temperature at ambient temperature $T_{UG} = T_{BC_1} = T_0$, 30 mm upstream from the flame. The tube's length (200 mm) is chosen to guarantee that at the output section of the tube (x=150 mm), both burned gas and wall temperatures (respectively, T_{BG} and T_{BC_2}) have the same values, and do not change with the axial direction. Thereby, the right boundary conditions of the domain are : T_{BG}=T_{BC_2} and $\partial T_{BG}/\partial x = \partial T_{BC_2}/\partial x = 0$. The outgoing boundary condition is set 100 mm downstream from the flame, where the temperature of the burned gas is equal to the temperature of the wall.
Through temperature measurements, the maximum temperature reached by the wall at the highest studied equivalence ratio (ϕ=0.95) is determined and equal to T_w=850 K, few millimeters downstream from the flame front. These limits are used as reference for further numerical computations.

2.2.3 Various type of configurations

Other configurations than the basic configuration, of different diameters and orientations were tested. The goal is to reproduce the stabilization behavior of a microscale flame while staying above the quenching diameter in order to avoid the use of external assistance. Thereby, several inner diameter above the quenching diameter are tested and summed up in table 2.1. The comparison between

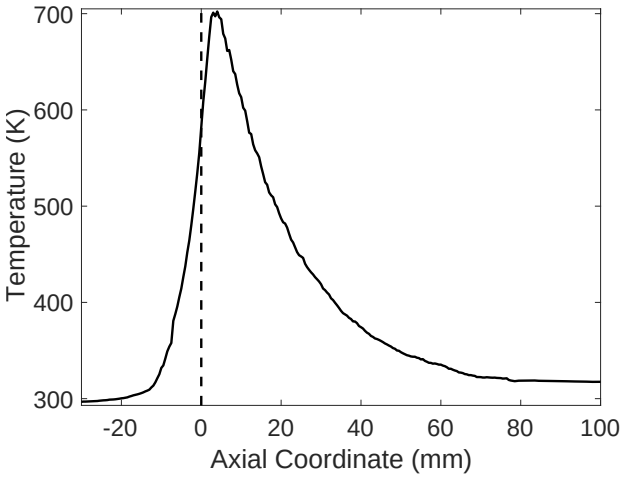

FIGURE 2.3 – *External wall temperature profile of a stabilized flame in the basic horizontal configuration at ϕ=0.80, measured by thermocouple.*

the tubes and the justification of the choice is made in chapitre 4, by comparing the operating points, the robustness of the flames and their topologies.

Configurations	Names	d_i [mm]	d_e [mm]
Under	A	4	6
Basic	B	5	7
Above	C	7	9

TABLE 2.1 – *Summary of the various quartz tubes used, with different inner and outer diameters, inside which flame propagation and stabilisation were investigated.*

Moreover, the thermal environment around the tube not being controlled, the local heating of the tube caused by the flame creates important temperature gradients in the surrounding air. These gradients lead to natural convection movement that may modify the flame stability. In order to evaluate the impact of these convective motions, experiments are repeated with the tube in horizontal and vertical positions. In vertical configuration, the flow's direction is opposite to gravity, the burned gases being located toward the exhaust section of the tube, reducing the effect of the gas expansion. All these configurations and their interests in understanding the involved phenomena in the stabilization and propagation of the flame inside a narrow channel are exposed in the steady (chapitre 4).

2.3 Characterization and limits of the system

2.3.1 Properties of the mixture

Fuel choice The methane/air is injected in lean proportions inside the narrow quartz tube. The chemical reaction is then written as :

$$\phi CH_4 + 2(O_2 + \gamma N_2) \rightarrow 2\phi H_2O + \phi CO_2 + 2\left[(1-\phi)O_2 + \gamma N_2\right] \qquad (2.1)$$

The methane is chosen as hydrocarbon fuel because it has been extensively studied which insure accurate detailed reactions mechanisms. Thus the adiabatic flame speeds for lean premixture are low enough to achieve stabilization by progressive mass flow rate adaptation. The equivalence ratio is varied between 0.7 and 0.95 according to the configurations.

Flame power scaling In order to scale the power of the studied flame, the heat release per unit mass of fuel (LCV) is multiplied by the fuel mass flow rate. The power of the flame can be expressed as :

$$P_{flame} = \dot{m}_{fuel} \times LCV$$

with $\mathrm{LCV_{CH_4}}$= 50 10^6 $\mathrm{J \cdot kg^{-1}}$ at 300 K.
For a stabilized flame at equivalence ratio ϕ=0.8 in the basic configuration, the mass flow rate is $\dot{m}$=1.69 10^{-7} $\mathrm{kg \cdot s^{-1}}$, in this configuration the flame power is then

$$P_{flame} = 50\ 10^6 \times 1.69\ 10^{-7} = 8\ W$$

This scaling allows to evaluate the ratio of possible assistance power over the combustion power.

Auto-ignition temperature (AIT) The auto-ignition temperature (AIT) of the methane air mixture has been previously studied experimentally (Kong et al. (1995)) and numerically (Ye et al. (2014)) in the literature. The auto-ignition is defined as the explosion limit of a system of initially stable chemical species exposed to an elevated temperature, at a given pressure. In Ye et al. (2014), the auto-ignition temperature is computed using complex chemistry (GRI mesh), with convective heat loss at the walls. Several convective heat coefficient h are tested from natural (10 $\mathrm{W/(m^2 \cdot K)}$) to forced convection (25-100 $\mathrm{W/(m^2 \cdot K)}$). The AIT increases with the increase of heat coefficient, and non linearly decreases with the increase of equivalence ratio. Thus, the AIT experimentally determined depends on the experimental apparatus, and can vary of hundreds of degrees between configurations.
It is established in Guirguis et al. (1981), that the reaction $CH_4 \rightarrow CH_3 + H$ plays a bottle neck role in the process of auto-ignition of methane air, because

of its large activation energy and low reaction rate at low temperatures. This explains the high value of methane/air AIT. However, H atoms can be generated through other reactions and increase the decomposition/oxidation velocity of methane, and by that decrease the AIT.
Overall in the literature, the lowest AIT of methane/air mixture is 913 K. The AIT allows to evaluate the maximum temperature of a possible assistance, in order to avoid auto-ignition of the premixture.

2.3.2 Quenching distance

A literature review on the quenching was carried out since it has a great importance in the narrow channel combustion. The coupling between a premixed combustion and a surface plays an important role in the safety analysis of reactors, the heat production, the flame stability and polluant emission. The quenching diameter allows to set the limits of the configuration and justify them.

2.3.2.1 Definition of the quenching distance

The general definition of the quenching diameter/distance is the smallest tube diameter/channel height which allows the propagation of a flame within cold wall (Spalding (1957)). It is determined by reducing progressively the diameter of a tube or the distance between two slabs, until flames can no longer propagate in the fresh gases, inside the conduct/channel. This distance depends on the equivalence ratio of the gas pre-mixture as well as pressure ($d_q \propto 1/p$) and temperature. Thus the quenching distance varies according to the combustion regime, either propagation or steady regime. Two main mechanisms are source of quenching. The first is a thermal mechanism, due to the heat loss to the wall. The second is a chemical mechanism, caused by radical absorption by the wall. Thereby, the key phenomena of microburners are interfacial phenomena between the gas and solid phases of heat loss and radical quenching. The stabilization of a flame inside these microburners is then a competition between heat generation, heat loss and radical quenching. Both interfacial mechanisms play a critical role in flame stability and propagation at micro/meso-scale (Raimondeau et al. (2002)), and could be the root of two interfacial discontinuities.

2.3.2.2 Radical quenching

A first discontinuity, caused by radical quenching, is related to mass transfer at the interface, and thereby to the individual concentrations of radicals in both phases. The radicals created as intermediate of reactions in the combustion reaction zone are absorbed in the wall where they recombine by surface reactions (Miesse et al. (2004)). Stable molecules resulting from these reactions can possibly desorb in the fluid. Therefore, those surface reactions are termination reactions. Thus an important removal of these radicals from the reaction zone

leads to flame extinction. The rate of removal is modeled in Raimondeau et al. (2002) using the flux from the kinetic theory of ideal gases reduced by the sticking coefficient. According to Aghalayam et al. (1998), the sticking coefficient is defined as the probability of an impinging molecule to stick to the surface and the probability of a radical encountering an empty active wall site. It provides a reaction rate of the surface. As a result when the sticking coefficient tends to zero, the wall is considered as inert, and on the contrary when the probability is equal to one, all radicals are absorbed by the surface and thereby the radical removal rate is at its fastest. Thus, the radical recombinaison being exothermic, it can have a stabilizing effect of flames through the heat released (Aghalayam et al. (1998)). However, Ju and Xu (2006b) established two limits of the radical quenching : a diffusion limit for large channel widths and large radical Lewis numbers and a kinetic limit for lower Lewis number, where the limiting factor is the rate of surface quenching.
Finally, radical quenching depends greatly on the surface properties, temperature and on the channel diameter. Indeed, Ju and Xu (2006b) demonstrated that radical quenching has stronger influence on flame propagation at higher wall temperature. It is demonstrated to have an impact on flame speed, structure and extinction limits, and therefore must be considered.

2.3.2.3 Thermal quenching

The difference between the close-wall gas and the wall temperature represent the second discontinuity described by Raimondeau et al. (2002). This energy transfer is the source of thermal quenching. Thermal quenching occurs when the heat loss to the walls gets too important regarding the heat generated by the combustion. Indeed, the wall act as an enthalpy sink for the combustion area since the heat loss lower the temperature on the reacting zone, slow down the kinetic reactions and lead to flame extinction. As a result, a diameter exists under which no flame can propagate. However, in the literature, several techniques such as excess enthalpy and burned gas recirculation, are adopted to decrease the thermal quenching by increasing the unburned gas temperature and by that reducing the difference of temperature between the wall and the gas, reducing in this way the heat loss (Shirsat and Gupta (2011)). The importance of this discontinuity in the flame stability process depends on the operating conditions (heat loss), the diameter and the gas molecules (Raimondeau et al. (2002)). Again, the flame stability, structure and the extinction limits are impacted by the thermal quenching and should be taken into account.

2.3.3 Parameters effects on quenching

Several operating parameters effects on quenching distance have been extensively studied in the literature, for both quenching mechanisms.

2.3.3.1 Surface temperature

First, the surface temperature plays a major role in the flame stability. Indeed, increasing the wall temperature allows to greatly extend the flammability domain of hydrocarbon combustion in narrow channels. This extension is linked to a quenching distance increase. To estimate these dependance to the wall temperature, Bai et al. (2013) defined two quantities : the radical quenching coefficient Γ, and the heat loss quenching coefficient Ω. In this definition, Γ equal zero represents an inert wall and Ω equal zero describes an adiabatic wall. The heat loss quenching coefficient is plotted against the radical quenching coefficient in Fig. 2.4 for three wall temperature normalized by the ambient temperature. The area under each plot line, which represents the flammability domain, increases with the increase in wall temperature. Bai et al. (2013) point out that the heat loss quenching limit is more extended by the increase of wall temperature then the radical quenching limit.

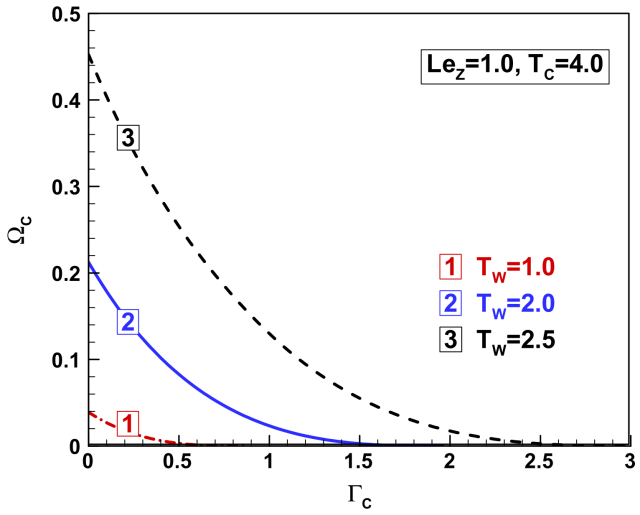

FIGURE 2.4 – *Effects of wall temperature on flame quenching limits. Flame quenching occurs when the coefficients of (Γ, Ω) are on the upper-right side of each line (extracted from Bai et al. (2013)).*

In the literature, it is established that the radical and the thermal quenching do not operate on the same range of temperatures. More precisely, Kim et al. (2006) identified three wall temperature range with a different quenching diameter evolution on a methane/air flame with a two dimensional slit burner. These regimes depicted in Fig. 2.5, are representative of three physical phenomena. In the first regime (A), under 400°C, the quenching distance decreases with the increase of temperature. In this regime, thermal quenching is dominant. The second regime (B), represents a transition between the two quenching mechanisms. In fact, the quenching distance slightly increases with the wall temperature because as the wall temperature increases, the heterogeneous

chemical reactions at the surface are enhanced, namely radical removal. The loss of radicals by wall absorption slows down the combustion reaction rate and leads to flame extinction. The third regime (C), shows a drop of the quenching distance with the increase of temperature. In this temperature range, the homogeneous chemical reactions, among which chain-branching reactions, overcome the heterogeneous reactions of radical removal by an excessive production of OH, O, and H radicals.

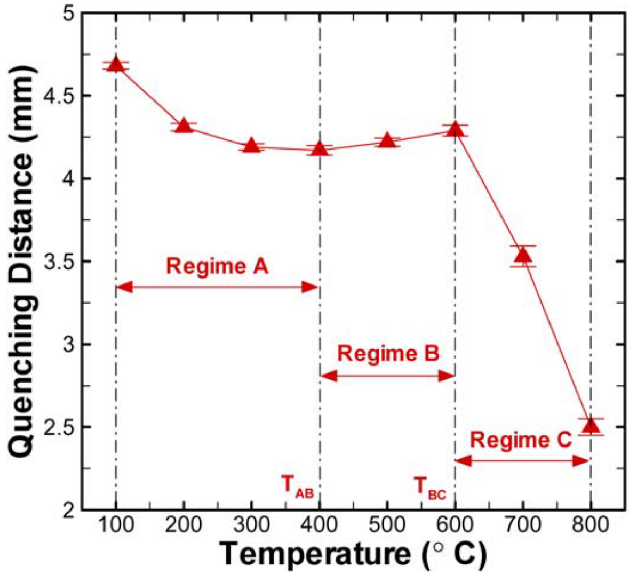

Figure 2.5 – *Three evolutions of the quenching diameter are observed according to the wall temperature (extracted from Kim et al. (2006))*

Finally, by increasing the wall temperature the quenching distance decreases. The heat loss quenching is mainly due to the fact that under a certain temperature called cross-over temperature, the chain branching reaction does not take place. By increasing the wall temperature or the fresh gas temperature, this cross-over temperature is reached and as a result more radicals are created, the combustion is enhanced and the flammability domain is extended.Thus, at higher unburned gas temperature, the radical concentration and the flame speed increase and consequently, both radical and thermal quenching limits are extended (Bai et al. (2013)).
However, the increase of wall temperature as a solution against heat loss and thermal quenching while decreasing the channel diameter has its limits (Raimondeau et al. (2002)). Indeed, Fig. 2.6 represents the dimensionless temperature (T_w/T_0) against the axial dimension of the reactor, for three different radii and for two heat exchange coefficient, 4.187 W/(m^2·K) (top) and 41.87 W/(m^2·K) (bottom). First a decrease of the temperature is observed, due to heat loss to the wall. Then, the temperature rises with the flame front, and then drops again in the burned gas area as the gas are cooled down by the

walls.

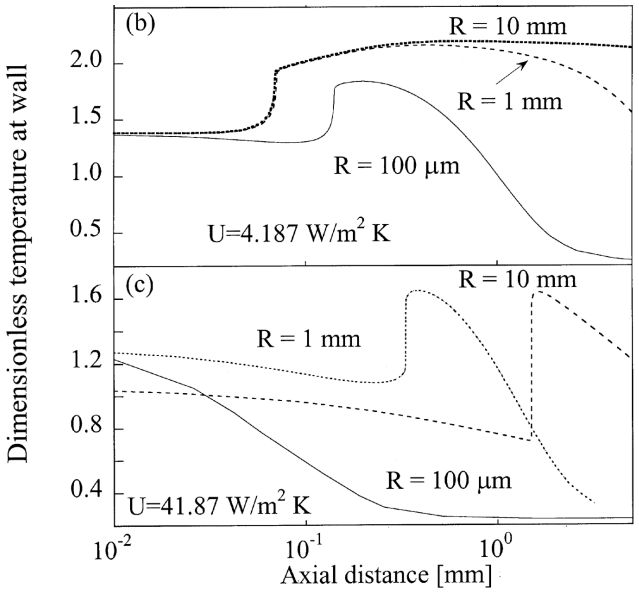

FIGURE 2.6 – *Wall dimensionless temperature profiles along the length of the reactor for three different radii indicated on the figure for two different heat exchange coefficient (top) 4.187 W/(m²·K) and (bottom) 41.87 W·m⁻²·K⁻¹ (extracted from Raimondeau et al. (2002)).*

In can be observed at a channel radius of 100 μm, with a heat exchange coefficient of 41.87 W/(m^2·K) that no flame can propagate in the channel, despite the heat assistance. This figure illustrates that the thermal properties of the wall and preheating of the reactants influence drastically the critical diameter for flame propagation, but also that this method has limits.

2.3.3.2 Surface properties

Experimentally (Saiki and Suzuki (2013); Miesse et al. (2004); Yang et al. (2011)), numerically (Saiki and Suzuki (2013)) and analytically (Bai et al. (2013); Ju and Xu (2006b)), the quenching is found to depend strongly on wall materials, especially at high temperatures. Indeed, it is established that under T_w=800 K, the quenching distances are not function of the material but only the wall temperature. Therefore, in this range of temperature the thermal quenching mechanism is dominant. Indeed, Yang et al. (2011) describe two reasons why the radical quenching cannot occur in this temperature range. The first reason is that at these temperatures, the combustion chemical reactions taking place do not produce much radicals. The second reason is because the solid surface radical traps are occupied by chemisorbed OH groups. Therefore, as the wall temperature increase (starting from 673 K) two phenomenon are added in favor of radical quenching. First, the OH groups desorb in the reaction

area, and release surface traps. Then, the combustion chemical reaction create more radicals. At high temperature (T_w=973 K), all traps are free, OH groups being completely desorbed in the gas, and the fuel oxidation reactions are more effective, extensively creating O, H and OH radicals. Thereby, from this temperature, the quenching distances become function of the surface composition, and more specifically of coverage proportions and desorption rates of OH. As a result, at high temperature, radical quenching dominates.
Indeed, Miesse et al. (2004) clearly demonstrate that the thermal processes play no role at high temperature, by measuring the quenching distances of two materials with very similar thermal conductivities (quartz and cordierite) and finding different values. Thus in Saiki and Suzuki (2013), the OH^* concentration close to the wall is measured for different materials and at wall temperatures. In fact, it has been established that the radical quenching causes the reduction of the near-wall OH^* concentration, and it is therefore used as quenching indicator. As a result, at wall temperature of T_w=873 K, the OH^* concentration close to the wall is unchanged for different wall materials whereas for higher temperatures, a discrepancy is observed revealing the actions of kinetic mechanisms. Furthermore, the quartz sticking coefficient associated with radical adsorption, is estimated and found to be non-zero at T_w=1273 K (Saiki and Suzuki (2013)), causing a decrease in radical concentration. Thereby, at high temperature the radical quenching cannot be neglected for quartz. This established fact is illustrated by Kim et al. (2006) in Fig. 2.7 drawing the quenching distance of reactive and inert quartz plates according to surface temperature. Therefore, before T_w=800 K, the quenching distances of both quartz are sensibly equal, however starting from T_w=800 K, a discrepancy between the inert and reactive material is observable.
Finally, a solution to reduce quenching distances at high temperature is to use surface preparation to eliminate radical traps. Surface treatments associated with proper thermal conditions is key to obtain a flame propagation in channels with a diameter under the standard quenching diameter (Miesse et al. (2004)).

2.3.3.3 Diameter influence on quenching

The decrease of the diameter implies an increase of the surface-to-volume ratio and thereby greater volumic loss. Thus the radicals are more in contact with the surface, since the concentration of radicals is higher. Therefore, both radical and thermal quenching increase with the decrease of the diameter (Bai et al. (2013)). Using the heat assistance as a diagnostic, it can be seen that the amount of preheating of unburned gases needed increases as the diameter decreases and as the heat transfer coefficient increases. In the other direction, when increasing the diameter (e.g. d_i=20 mm), in a propagating flame case, neither thermal nor radical quenching have an effect, because the heat and mass transfer characteristical times are lower than the residence time of the flame (Raimondeau et al. (2002)). Moreover, when the flame is stabilized away

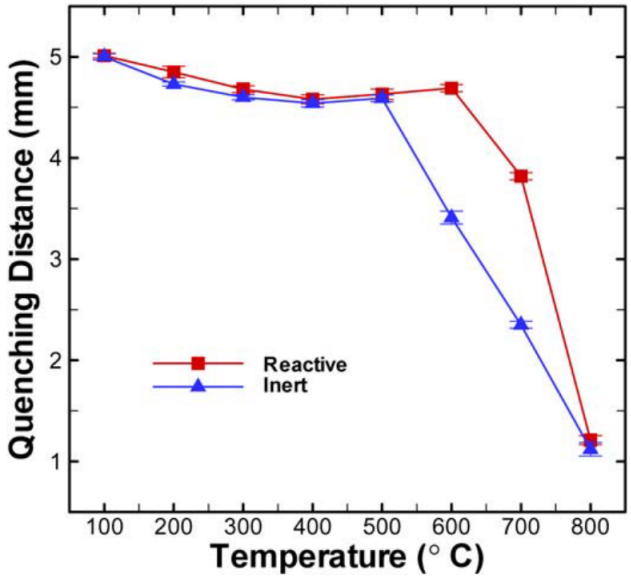

FIGURE 2.7 – *Quenching distances evolutions of both reactive and inert quartz plates with surface temperature (extracted from Kim et al. (2006)).*

from the surface the flame/wall interaction is weak (Aghalayam et al. (1998)). In conclusion, the wall temperature, the surface and the diameter have great influences on flame stability and flammability domains. In the presented work, and in view to the maximum temperature reached by the wall (T_w=850 K) at the highest equivalence ratio (ϕ=0.95) studied (2.3), the thermal quenching is dominant.

2.4 Diagnostics

To characterize the flame regimes and its thermal environment, several diagnostics are developed. In fact, to evaluate the flame regime, a position and shape tracking method is used. For the flame front/shape detection, CH* measurements are processed. Thus, to evaluate the heat exchanges, accurate temperature measurements are necessary.

2.4.1 Position and shape tracking methods

The mass flow rate is controlled so that the flame speed with respect to the tube (laboratory frame) is low. The position, shape and motion of the flame in the tube can be recorded by a standard reflex camera (Nikon 7000D - Lens micro Nikkor 60 mm f/2.8G). The bulk velocity is controlled so that no high speed camera is required to track the flame. The videos captured are decomposed into 24 frames per second. On each frame, an edge/contour detection is applied.

Since the flame spontaneous emission is very low, the recording is processed in complete darkness. Thus, three main methods are considered and compared to obtain optimum accuracy on the flame position and shape.
The **first method** converts the flame images to binary images based on a threshold of intensity. Each unity isolated group represents an object. The objects are ordered by areas and therefore the object with the greatest area represents the flame. The *regionprops* Matlab function performs shape measurements on the selected object, giving the area, center of mass, extrema etc. The coordinates of the center of mass serve as the position tracker for this method. In the **second method**, the Matlab *edge* function is used after binarizing the flame image, to contour the flame. The *edge* function is linked to a Canny method, that finds the edge by looking for a local maxima of intensity gradient. The tracker chosen is then the maximum of the fresh gases edge, namely the flame front. The **third method** uses the maximum of intensity of the spontaneous emission of the flame as a tracker.
The three methods are compared on Fig. 2.8, drawing a steady flame displacement at an operating point of ϕ=0.8 as a function of time (top) and the standard deviation between the three tested methods (bottom).

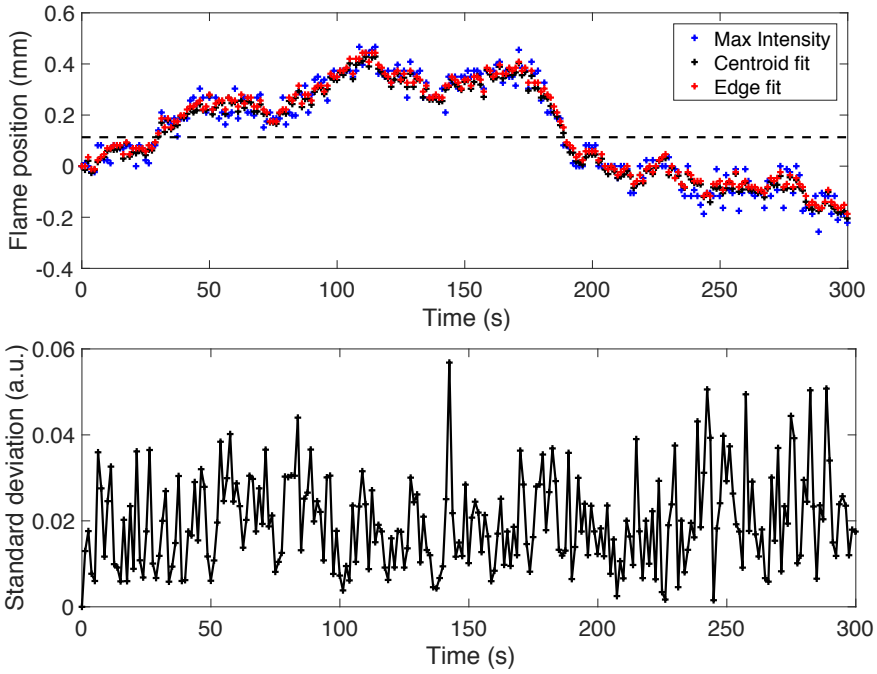

FIGURE 2.8 – *Three position trackers evolutions with time (top) for a steady regime (ϕ=0.8), comparing the previously exposed methods and the standard deviation between those methods (bottom).*

The standard deviation calculated between the three methods illustrates a low dispersion of the datas. However two methods are shown to have a better ac-

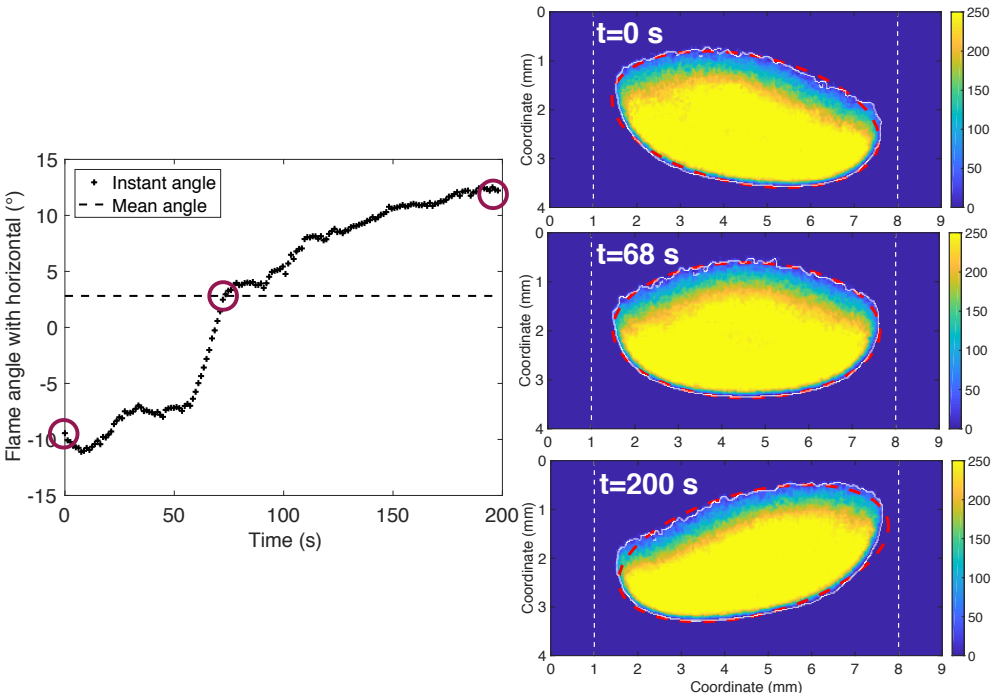

FIGURE 2.9 – *Limits in flame orientation detection, when the flame rotates around the tube axis (vertical tube configuration) : the flame angle is represented as a function of time. Three snapshots are extracted from the time evolution, the dashed red lines represent the fitted ellipse of the first method (centroid fit).*

curacy : the center of mass (centroid fit) and the flame front (edge fit). These two methods are used for the following flame displacement tracking.
The first method (centroid fit) is also used to get topological measurements of the flame. In fact, the *regionprops* function provides, among several parameters, a fit of the flame by an ellipse, thereby including the major and minor axis length, the eccentricity and the orientation of the ellipse. The aforementioned parameters allow to analyse the flame regime/stability, topology and orientation evolution in the various analyzed situations.
However, the flame spontaneous emission detection shows some limits on the flame orientation detection. In fact, when a flame is tilted and rotates around the tube axis, the detected orientation is not representative of the flame's actual angle. The Fig. 2.9 shows the flame orientation evolution during an axial rotation of a flame in a d_i=7 mm tube vertically positioned. The three snapshots are taken respectively at the minimum angle (left), at zero angle (center) and at the maximum angle (top). The first and last snapshots show the flame in a profile shot, while the center snapshots shows a zero angle since the flame faces the camera and the tilt is integrated to give a null angle.
Therefore the orientation detection must be monitored to capture the flame profile, especially in vertical tube positioning.

2.4.2 Flame front detection - CH* measurements

To observe accurately the flame front, and especially the CH* chemiluminescence, a band-pass interference filter centered at 430.0 nm with a fwhm of 10 nm (±2 nm) and 40% minimum peak transmission is positioned in front of the objective. The flame motion in steady regime being of the order of tenth of millimeters per minute, and the flame emission being very weak, the exposure time is set between 2 and 30 s. The CH* image of a stabilized flame at an equivalence ratio of ϕ=0.8 is represented in Fig.2.10.

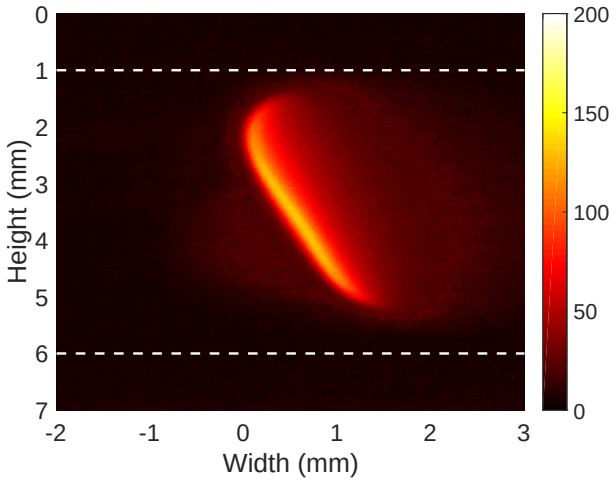

FIGURE 2.10 – *Flame front detection using CH* chemiluminescence on a stabilized flame at an equivalence ratio ϕ=0.8.*

Abel transformation is not performed in this study because of the asymmetry of the flame. The CH species being mostly present in the flame front, the chemiluminescence allows to highlight the flame front shape and orientation.

2.4.3 Temperature measurements

Temperature measurements on the external wall of the quartz tube are carried out using two main techniques. The first technique, easy and fast to implement, is to enforce a thermocouple against the external wall of the tube. The thermocouple measurements are an invasive method, since the thermocouple weld must be put in contact with the measured surface or gas. However, by choosing a very small weld diameter, the measurements do not alter much the surface temperature, giving a short temporal response.
The temperature profiles are measured by a 0.075 mm (Omega OPON-003) type N thermocouple enforced against the external wall and horizontally displaced with a 0.5 mm step by a horizontal displacement device (BSC 101 Thorlabs - 100mm travel stage), illustrated in fig. 2.11. At each spatial point, 500 temperature measurements are taken and averaged. Thus, the thermocouple has

a response time under the second and is of a high accuracy, which allows to follow the time evolution of the temperature at a given point along the tube.

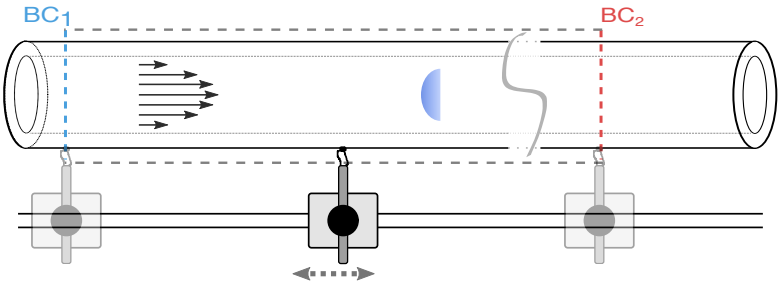

FIGURE 2.11 – *Scheme of the thermocouple temperature profiles measurements on the external quartz wall. A flame is stabilized inside the tube for different equivalence ratio.*

Upstream from the flame the tube temperature equals T_{W1}= 298 K. At a distance of 100 mm after the flame front, the tube temperature does not change anymore and came back to its original value. As expected, the maximum temperature is reached slightly downstream the flame front and has its value varies with the equivalence ratio of the mixtures. The temperature measurements on a stabilized flame for the different operating points studied, in a d_i=5 mm inner diameter tube, are represented in fig. 2.12.

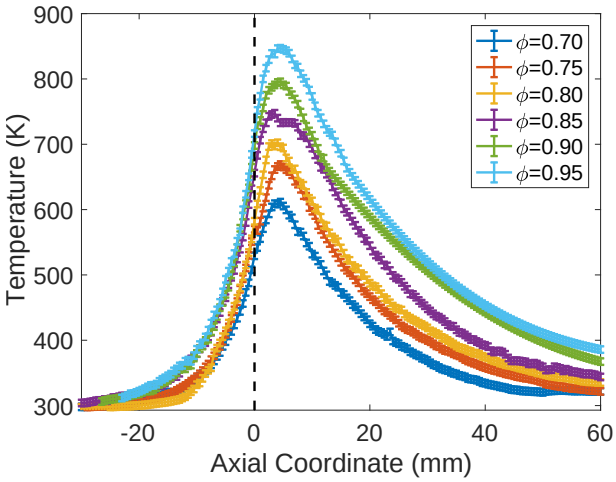

FIGURE 2.12 – *Thermocouple temperature profiles of the external quartz wall. A flame is stabilized inside the tube for different equivalence ratio. The flame position is marked by the zero coordinate and by the vertical dashed black line.*

This thermocouple method gives a good accuracy since the theoretical errors for the temperature and for the displacement position are all given by construc-

tors. Due to the very small diameter of the thermocouple, another imprecision can occur by the fact that the soldered joint is not directly in contact with the quartz tube's outer surface but with the surrounding air. The inaccuracies are estimated at ±10 K in temperature and at 0.2 mm in displacement. This method is cheap, easy to operate and accurate. However, the necessity of a higher accuracy method led to a second method, the Laser Induced Phosphorescence (LIP). This method is described in the following chapitre 3. Yet, the LIP technique is subject to optical misalignments and distortions, and a comparison method is necessary to estimate its accuracy when applied to the measurement on the outer surface of a narrow channel. As a result, the thermocouple measurements are used as a comparison method for the LIP technique on the outer surface of the quartz tube.

2.5 Conclusion

In this chapter, the experimental setup studied in the presented work is described. It is composed of a quartz tube inside which a lean methane/air premixture is injected. Three tube sizes are considered and investigated, with an inner diameter of d_i=4, 5 or 7 mm. Thus the tube is studied in horizontal and vertical position to observe the impact of the gravity direction on the flame. The aim is to study a flame in these conditions without any external assistance of the flame. Therefore, the dimensional limits of the systems are evaluated. First, the length of the tubes is justified by the characterization of the flame temperature domain, in order to reach constant gas and wall temperatures upstream and downstream from the flame. Thus, it also allows to size the temperature range reached by the external wall, from the lowest to the highest equivalence ratio studied. Then a literature review on the quenching distance allows to set the lower limit of the tube diameter, under which no flame can propagate without assistance. Finally the diagnostics carried out on the experimental setup are exposed. A first diagnostic used to establish the flame regime and its topology is the position and shape tracking of the flame. Then, the flame front is highlighted by CH^* chemiluminescence to better observe the shape and orientation variations. Lastly, a first temperature measurements method using thermocouple is described. The need of a more accurate temperature measurement method leads to the study of phosphors and Laser Induced Phosphorescence, described in the following chapter.

Chapitre 3

Phosphors and laser induced phosphorescence

Contents

3.1 Extended abstract

As previously shown, a lean premixed laminar flame can stand in a narrow quartz tube and heats up the surrounding medium through solid radiation and convection at the external walls. The flame, once stabilized, induces a temperature distribution along the wall. Inversely, a slight modification of the heat flux distribution between the wall and the external medium impacts the flame in the tube. The knowledge of the external wall temperature distribution and its evolution with respect to the time is crucial to understand this two-way coupling mechanism between the heat transfers and the flame. First measurements presented in the previous chapter were performed with a thermocouple in a stationary regime. It gives an idea of the maximum temperature and the diffusion within the wall upstream and downstream the flame. Two-dimensional temperature measurements based on the phosphorescence of temperature sensitive species have the potential to provide a more accurate value of the maximum temperature but also track temperature evolution with the time during transition phases. However this promising approach requires tests and validation to (i) choose the most appropriate phosphor, (ii) experiment different deposition methods on the curved quartz surface, (iii) capture the light emission induced by laser and (iv) process the raw data to obtain the temperature field. Three different phosphors are tested : the praseodymium doped yttrium aluminium garnet (YAG :Pr), the dysprosium doped yttrium aluminium garnet (YAG :Dy) and the magnesium fluorogermanate doped with manganese (Mg_4FGeO_5 :Mn). The former is manufactured at Keio University in the Prof. Yokomori laboratory. Its properties are validated with different tests among them Semi Electronic Microscopy (SEM), spectrofluometry and X-Ray diffraction. The deposition technique uses a high temperature binder (ZYP-HPC). After calibration, different ratios between binder and phosphors are tested to minimise the influence of the binder on the wall temperature measurement. The experimental setup allows to light up the painted tube with a mono-frequency laser source and the phosphor emission is then captured by an Intensified CCD camera (to get a two-dimensional temperature map) or a photometer (to gather a local intensity). Two processing strategies are used : the intensity ratio and the lifetime methods. With the appropriate combinaison of phosphor, deposition method, emission capture and processing strategy, the temperature distribution is obtained with accuracy and repeatability. It shows that the thermocouple underestimate the maximum temperature of about 100 K. It varies between 600 K for equivalence ratio equal to 0.70 and goes up to 850 K for equivalence ratio 0.95. Away from the high temperature region, all the temperature techniques describe the same decay rate and confirm the temperature diffusion observed initially.

3.2 Phosphor properties

Phosphor thermometry is a strategy for getting temperature from a distance. This method exploits the fact that phosphors are luminescent materials and that the emitted light is temperature dependent. In this section, the objectives are to explain what luminescence is and present the luminescent materials and their emission.

3.2.1 Luminescence

The definition of luminescence is the emission of light without incandescence, by a source submitted to an excitation whose origin can be light (photoluminescence), thermal (thermoluminescence), chemical (chemiluminescence) or electrical (electroluminescence). In other words it is the property of certain substances to restitute an energy not resulting from heat into photons.

3.2.2 Luminescent materials

Luminescent materials namely phosphors are materials that convert the received non-thermal energy into electromagnetic radiation. Concretely, they are rare-earth or transition metal doped ceramic materials. In more general terms, they are usually solid inorganic materials composed of a transparent host crystal lattice intentionally doped with a low concentration of impurity atoms. The concentration of impurity must remain low, because a high concentration of impurities would lead to a decrease in luminescence efficiency due to concentration quenching. The host is treated as a medium for the impurity, it is transparent and nonmagnetic. To thus avoid the phosphor absorbing visible light, it must have a white body color. When the phosphors are excited by an electron bombardment, X-ray or short-wavelength light, they emit visible light.
As a result the emission of light can emanate from the host excitation or from the processes that occur around and within the impurity atoms. The impurity atom or defect and its surrounding atoms form a luminescent or an emitting center. Two types of emitting centers can be introduced in the host ; one is activator ions ; chosen for their emission spectra, which usually have one or two emission peak(s) occurring at various wavelengths, and sensitivity to the system parameters (temperature, ..). When the activators show an absorption that is too weak, a sensitizer, the second kind of emitting center, is introduced, which absorb the energy and subsequently transfer the energy to the activators. Once excited, the relaxation of the phosphor back to the ground state process is obtained by radiative and non radiative energy transfers. The radiative transfers are linked to a spontaneous emission of at least one photon while non radiative transfers rely on internal energy transfer during molecule relaxation by collision. Phosphor thermometry uses the fact that non radiative transfers depend on the temperature of the phosphor. Indeed, thermal quenching occurs at high temperature where the internal energy transfers are enhanced.

The phosphor can be chosen according to its emission spectra peaks in order to avoid interactions with other phenomenon, and be adapted to the experimental setup. Thus, for the same host lattice, a choice of several doped ions are available, giving way to many possibilities.

3.2.3 Luminescent emission

When $t = 0$ s represents the end of the phosphor excitation, the intensity of the emitted light follows a mono-exponential decay described by :

$$I(t) = I_0 \exp(\frac{-t}{\tau}) \tag{3.1}$$

where I_0 the light intensity at $t = 0$ and τ the decay time, namely the lifetime defined by $I(\tau) = I_0/e$. The population of the excited state $N^*(t)$, depends on the rate of radiative and non radiative transfer processes, respectively R_R and R_{NR}, is described by the differential equation :

$$\frac{dN^*(t)}{dt} = -(R_R + R_{NR})N^*(t) \tag{3.2}$$

A solution of this equation depending on the lifetime and the population N^*_0 at $t = 0$ s can be written as :

$$N^*(t) = N^*_0 \exp\left(\frac{R_R + R_{NR}}{\tau}\right) \tag{3.3}$$

An evaluation of the lifetime can be subtracted considering Eq. 3.1 and Eq. 3.3 :

$$\tau = \frac{1}{R_R + R_{NR}} \tag{3.4}$$

Consequently, the lifetime depends on the rate of non radiative transfer processes, which is temperature dependent. The evaluation of the lifetime gives then information on the temperature of the phosphor.

3.3 Phosphor acquisition

As seen in the previous section, phosphors are composed of a host crystal lattice doped with impurity atoms, usually rare-earth or transition metals. Depending on the atom and on the host chosen, the phosphors can easily be created by a chemical process. Numerous phosphors can be bought from specialized companies. In this section, the creation of YAG :Pr is described as well as the steps to verify the identity of the created component.

3.3.1 Phosphor creation

There are several conceivable options for obtaining phosphors are conceivable. The first solution is to buy a batch from a manufacturer, like Phosphor Technology (2018). This solution guarantees an adapted particle size distribution, the excitation and emission graphs, and also the material density.
The second solution is to create a batch of phosphor. The following experimental protocol describes the making of yttrium aluminium garnet (YAG host) doped with the rare earth metal ions of praseodymium (activator) ($Y_3Al_5O_{12}$:Pr or YAG :Pr). This phosphor will be used in the following sections for temperature measurements.
In order to do so, the host is created by mixing yttrium nitrate ($Y(NO_3)_3$) with aluminium nitrate nonahydrate at 99,9 % ($Al(NO_3)_3$) both highly water soluble. Praseodymium ions (Pr^{3+}) are added with water to the previous mixture. The solution obtained is then magnetically shaken and heated at 60° C for 60 minutes. Ammonia(NH_2) is then added drop by drop into the mixture. Next, the solution is left to heat for another 30 minutes. The obtained solution is filtered using a pump filter system. The filtered solution is dried in an oven at 100° C for 24 hours. A white powder of supposedly YAG :Pr is finally obtained and ground to get a smaller particle size.
The proportions of components to make 20 g of YAG :Pr dry powder, are 0.3 g of yttrium nitrate ($Y(NO_3)_3$), 40 g of aluminium nitrate nonahydrate at 99,9 % ($Al(NO_3)_3$), 70 g of Praseodymium ions (Pr^{3+}) and 1 L of water.

3.3.2 Phosphor validation

Once created, the component needs to be validated to be sure of the obtained composition and particle size distribution. For this, three validation steps are followed.

X-Ray Diffraction pattern (XRD)

In the first step of validation, a X-ray diffraction device is used to determine the atomic and molecular structure of a crystal. X-rays can be considered waves of electromagnetic radiation.
The structure of crystals is composed of regular arrays of atoms. As a result, when a beam of incident X-rays encounters crystalline atoms, it diffracts into many specific directions. Using a crystallographer, a three-dimensional picture of the density of electrons within the crystal can be produced, by measuring the angles and intensities of these diffracted beams. The information that can be extracted from this electron density are especially the mean positions of the atoms in the crystal and their chemical bonds. As the wavelength of X-rays is of the same order of magnitude as the spacing between planes in the crystal, they are used to generate Bragg diffraction patterns.

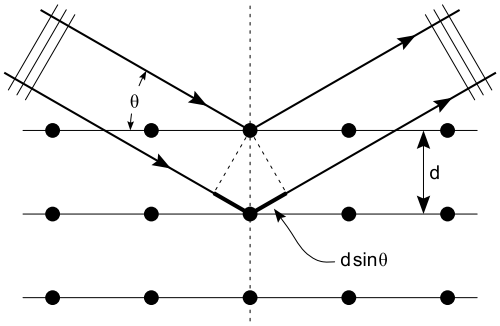

FIGURE 3.1 – *The scheme shows the Bragg diffraction from a cubic crystal lattice. θ is the angle between the incident beam and atom planes and d is the distance between two atom planes. The parallel incident waves reflect on the atom plan. The reflects interfere constructively if the Bragg condition is satisfied.*

In fact, as shown in Fig. 3.1, if two incident X-rays beams, parallel to one another, make an angle θ with respect to the atom planes, then their reflected beams will interfere constructively only if their path-length difference $2dsin(\theta)$ with d the spacing between diffracting planes, equals an integer multiple of the wavelength λ. Thereby, when the two incident X-rays are in phase they obey Bragg's law, that can be written as $2dsin\theta = n\lambda$ with λ wavelength of the beam and n and integer. As a result, when the incidence angle θ and the wavelength λ of the beam are known, the distance between the atom planes d can be found. The created component is processed through a crystallographer and its diffraction pattern is compared to data of the International center for diffraction data (ICCD (2018)). Thereby, Fig. 3.2 represents in red the X-ray diffraction pattern of Yttrium Aluminium oxide from the ICCD database and in black the X-ray diffraction from the created phosphor. The intensity counts are plotted against the angle 2θ in order to compare the pic intensities of the created component to the data base pattern.
By comparing Bragg positions from the standard pattern, the chemical component is then classified as well-crystallized as a body cubic centered and clearly identified as a YAG lattice.

Semi Electronic Microscope (SEM)

The second step is to determine the particle size distribution and the structural morphology of the prepared sample. In order to do so, a semi electronic microscope (Hitachi TM3030 plus) is used to get high resolution height maps and 3D images to illustrate the surface topography. The particle size distribution is then evaluated for several samples of the batch. It can be seen on Fig. 3.3 that the particles diameters remain under 100 μm but the distribution is quite spread. The particles are separated in two categories, the large particles with a diameter of over 80 μm leading to a thicker layer of phosphor and to the

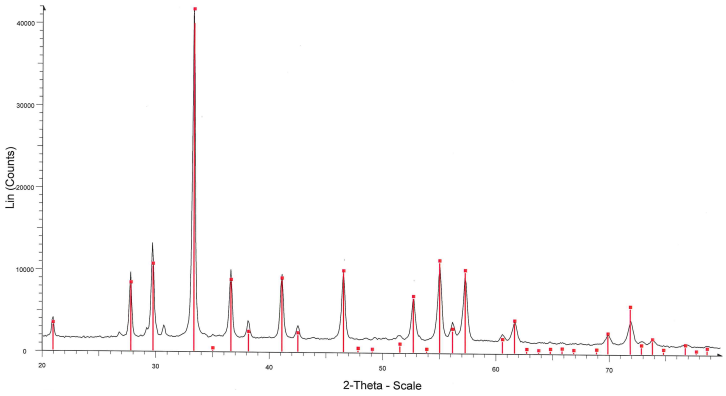

FIGURE 3.2 – *X-Ray Diffraction (XRD) pattern identification for Yttrium garnet, in red the graph from the database of Yttrium Aluminium oxide, cubic centered lattice, in black line the sample tested in the XRD.*

production of more light scattering and the small particles with a diameter under 0.2 μm which do not have high luminous efficiency due to grain boundary effect.

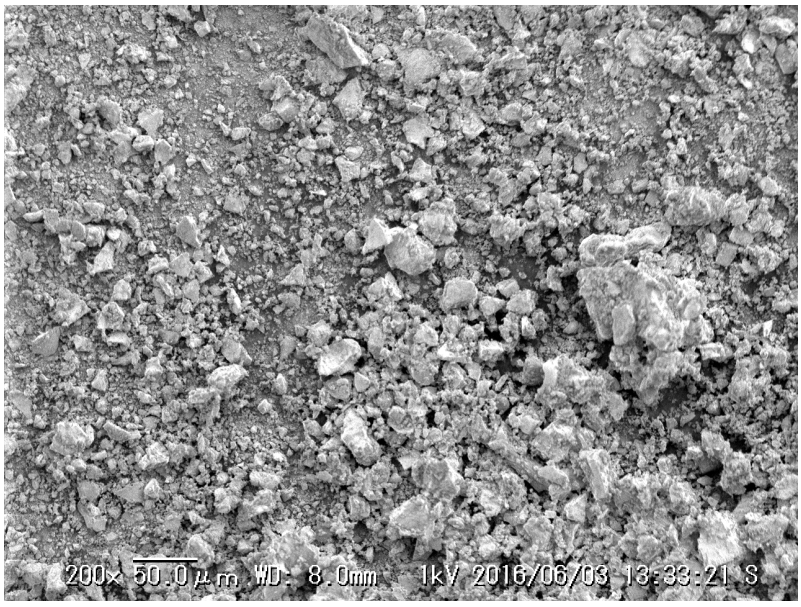

FIGURE 3.3 – *Semi Electronic Microscope (SEM) visualization of the created YAG in order to determine the particle size distribution. The magnification is by 200.*

To improve the particle distribution and thus the luminous efficiency of the phosphor, two acting strategies are available. One strategy is to adopt a more complex making process in order to obtain well shaped crystal forms with uniform size distribution, for instance by adding flux in the synthesis (Song et al. (2013)). The other strategy is to remove the particles that are either too small

or too big with post-production treatments like sedimentation, elutriation or sieving. The sedimentation allows removing the fine particles and consists in agitating the particles in water. Once the solution left to still, the larger particles sediment and the finer particles are then removed by decantation. The elutriation allows to remove coarse particles and consists in putting the particles in suspension in a fluid column. By adjusting the speed of the fluid, the larger particles would be detached of the other particles and then removed. The sieving process is used to remove very large particles whose dimensions are above the sieve lattice dimensions. Since the particle size of the created batch, evaluated by the SEM imagery, is under 100 μm, none of these processes where used. This threshold is a size imposed by the phosphor deposition method used and exposed in the following sections.

Spectrofluorometer

The purpose of this third step is to determine the excitation and emission spectra of the created component at room temperature. In order to do so a spectrofluorometer (Shimadzu RF5300PC) is used. A sample of the phosphor batch is deposited on a filter, and placed inside the spectrofluorometer. The phosphor is then excited by a Xenon lamp at 266 nm and the intensity of the emitted light is recorded by a photomultiplier. The emission and excitation spectra obtained are shown on Fig. 3.4. The two temperature dependent peaks are identified on the emission spectrum at the wavelengths 487 nm and 608 nm.

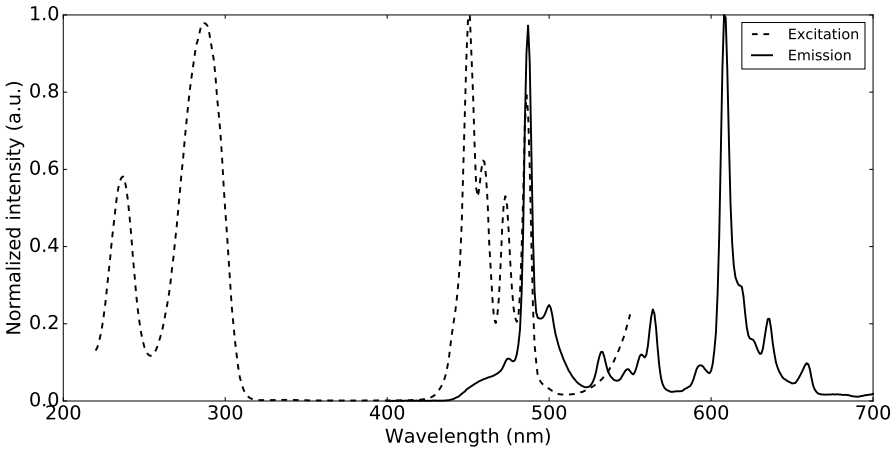

FIGURE 3.4 – *Excitation (dashed line) and emission (plain line) spectra of the batch at room temperature.*

The emission spectra drawn in Fig. 3.4 confirms that the component created is YAG :Pr by comparing its emission spectra with the literature (Jordan and Rothamer (2013)).
To sum up, first the atomic and molecular structure of the crystal was clearly

identified as YAG by comparing Bragg positions with international diffraction database patterns. Then, the particle size distribution and the structural morphology of the created component was observed using semi electronic microscopy. It is shown that particles diameters remain under 100 μm even if the distribution is extended. Finally, the emission and excitation spectra are compared to the literature. Through those three steps, the created component is stated as YAG :Pr.

3.4 Phosphor deposition methods and influence on the measurements

In order to measure surface temperatures using phosphor thermometry, the phosphor needs to be in contact with the measured surface. Thereby, several deposition methods and their influence on the measurement are investigated.

3.4.1 Description of phosphor deposition methods

The deposition method are numerous, and vary in difficulty and thickness precision. A compromise must be done between a complex method and a thin layer of deposition. As a result, the phosphor deposition can be separated in two types of deposition, the thin film deposition methods, which are complex, and the thick film deposition which is less complex.

Thin film deposition :

- The sol-gel method is a wet technique which consists in producing a solid material from small molecules by associating a liquid with a solid creating a solution that evolves from a diphasic system of both liquid and solid phases to a continuous molecule network. This gel is fixed on a substrate (surface to deposit the film) during the process. This method allows to use co-doping, namely the insertion of two activators ions in the host lattice to have a wider range of temperature. However no study on the adherence of phosphor coating on a substrate has been carried out.
- Physical vapor deposition (PVD) is a method of thin film deposition from gas phase. Indeed, the components of the film are first transformed to vapor phase, through physical processes like evaporation, sputtering or arc, and then condensed on the substrate.
- Chemical vapor deposition (CVD) is another method of thin film deposition from gas phase. The precursors are put to vapor phase and absorb on the substrate to produce the film deposition. The film is then activated thermally or by plasma, laser light or other processes. The film stability has been proven on the long term, its thickness usually between 0.5 and 3 μm, and the method can be applied to complex geometry and

porous materials. Hence the substrate needs to resist to the activation process.

A study presented in Ranson et al. (1998) states that the thin films have major advantages in comparison to thick films in terms of survivability, namely the robustness in harsh conditions of temperatures, and reducing the measurements errors since no layer temperature gradient are established in thin films. The thin film deposition methods are very useful to control the thickness of the deposition, but they require expensive materials and are complex to perform.

Thick film deposition :
A simpler possibility to deposit a film on a surface is to use adhesive bonding. Adhesive bonding is a very simple method, using a coating binder and mixing it with the phosphor powder and applying it to a surface. Several application methods are possible like airbrush paint or dip. The issues encountered with this method is that the deposit on the substrate is a thick film, thereby a temperature gradient might be established in the phosphor layer. It is also limited in durability.

The method chosen in a matter of celerity is the adhesive bonding. The binder used is a high temperature binder (ZYP-HPC), it is the most commonly used in the literature. It is a water-based binder, with a pH of 7 generally not reactive to materials and with a maximum use temperature of 1500 °C. Once mixed with the phosphor powder, the solution is painted with an airbrush on the measurement surface, in our case the quartz tube. Two issues remain to be to discussed. First the adherence of the phosphor coating on a substrate has not been studied. In order to avoid paint from peeling off the quartz, the paint is applied layer by layer respecting a drying time in between each layer application. Then the coating effect on the surface properties. The coating alters weakly the conductive resistance of the surface. Thus, the radiative transfers may also be slightly modified due to a decrease in the wall transmittance. These effects are considered negligible.

3.4.2 Thick film deposition : influence of the ratio binder phosphor on emitted light

The influence of the ratio binder/phosphor has not been clearly studied in the bibliography. In order to choose the better ratio, a setup was put in place to study its influence on the intensity and viscosity of the solution. The setup, shown in Fig. 3.5, is composed of a phosphor/binder sample placed in a tube furnace within a quartz chamber and excited by a xenon lamp coupled with a monochromater to select the appropriate excitation wavelength of the phosphor. The emitted luminescence is collected by a spectrometer. Behind the phosphor sample a thermocouple is placed in order to control its temperature and link it to the phosphor emission spectra. The tube furnace is stabilized at ten tempe-

ratures from 373 K to 1173 K by steps of 100 K. Once the furnace temperature stabilized, the emission spectra of the excited phosphor is registered. This setup is also used to calibrate the powder used for temperature measurements which will be tackled in the next section.

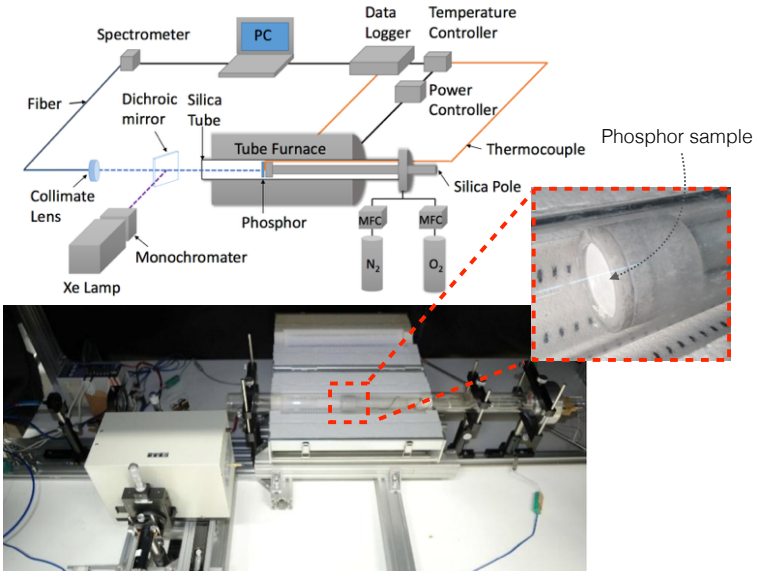

FIGURE 3.5 – *Experimental setup used to compare binder to phosphor ratio*

Four binder/phosphor ratio were tested, using the created YAG :Pr phosphor : 4 g of binder for 1 g of phosphor (4 :1), 4 g of binder for 3 g of phosphor (4 :3), 2 g of binder for 1 g of phosphor (2 :1), 1 g of binder for 1 g of phosphor (1 :1). The spectra are compared in Fig. 3.6 for temperatures 293 K, 473 K, 673 K and 873 K for the four ratios.
From this comparison, it can be said that the difference of intensity is not significative. Finally the choice of ratio phosphor/binder is a compromise between viscosity of the mixture and emission intensity. In fact the more phosphor is applied the higher is the emission intensity, but the more viscous is the solution. Since the phosphor will be airbrushed, it cannot be too viscous. A possibility is to add some water to the mixture to obtain a less viscous solution, since the binder is water based and that the water will evaporate when the substrate will be heated. The ratio chosen for the following study is 4 g of binder for 1 g of phosphor, since it gives a good emission intensity and the less viscous mixture.

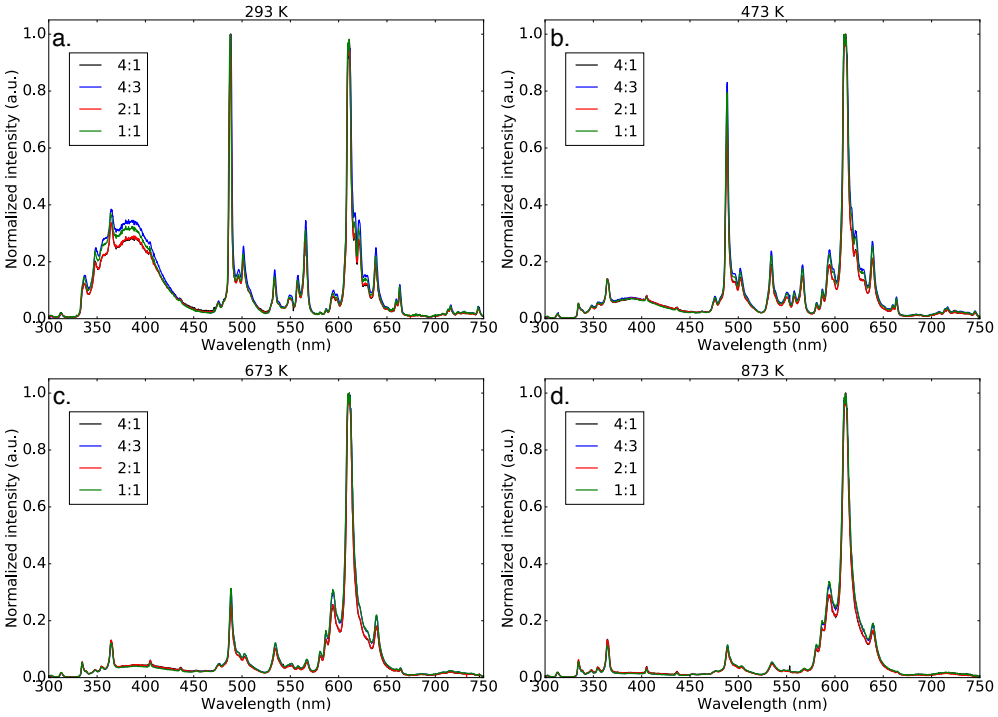

FIGURE 3.6 – *Intensity counts plotted against wavelength for binder/phosphor ratio 4 :1, 4 :3, 2 :1 and 1 :1 for four temperatures a.293 K, b.473 K, c.673 K and d.873 K*

3.5 Laser induced phosphorescence : Temperature measurements

Several objectives are tackled in this section. First objective is to evaluate the capacity of the Laser Induced Phosphorescence to measure temperature when applied to small and curved volumes subject to high temperature gradients. Then, two measurement strategies are exposed to get the temperature of the mesoscale quartz tube outer surface with a lean premixture flame stabilized inside at different equivalence ratio. Finally the goal is to compare the accuracy and sensitivity of phosphors as well as the two exposed measurement strategies.

3.5.1 Introduction to phosphor thermometry

Temperature is one of the fundamental thermodynamic state variables, and is necessary to quantify heat exchanges in thermal systems. Several temperature measurement methods exist that can be differentiated in three groups : the invasives, semi-invasives and non invasives methods (Childs et al. (2000)). First, the invasives methods imply placing a physical sensor on or within the object or surface. One straightforward example is to use thermocouples. Thermocouples

are easy, inexpensive and have good accuracy. However, it is an invasive method, since it must be put in contact with the measured surface and by that can alter the thermal environment. Thus, the placement of thermocouple must be planned during the design of the experimental setup, and their positioning is restricted. By that, the spatial (two-dimensional temperature imaging, or volume probing) and temporal resolution is strongly limited. Thus, another limitation of the thermocouple measurements is when using plasma. In fact, the plasma generation usually causes errors in instruments, leading to a impossibility to use thermocouple in plasma setups. Other techniques for temperature measurements, called semi-invasives are sensitive paints (Liu (2011)) or organic temperature-sensitive coatings such as thermochromic liquid crystals (Ekkad and Han (2000)). These methods confer the advantage of a 2D map temperature measurement, however they give no temporal resolution, and their use is not possible for high temperatures. Finally, another temperature measurements type is the non invasives methods. The measurements can be done from a distance using infrared pyrometry. Pyrometers get to temperature from the detection of radiative flux a body emits. Two-dimensional temperature maps can be visualized with very high temporal and spatial resolution. However, the precision of this method relies on the emissivity of the measured surface, which is difficult to determine with precision if not mentioned by the manufacturer of the surface material. Thus, the emissivity evolves with the variation of the surface properties like temperature and in time with oxidation, particle deposition, etc... Furthermore, if using semi-transparent or transparent materials like quartz, interference radiations might stem from burned gases or other heated materials in the measurement field.
Among the semi-invasive type of measurements, phosphor thermometry is a method that gives high spatial and temporal resolution over a broad temperature range of up to 1970 K, depending on the phosphors used. This method is generally insensitive to the surface properties and robust against interferences from scattered light, chemiluminescence or soot radiation.
This method is thereby chosen to measure, in the studied configuration, the external surface temperature of the quartz tube. One objective of this section is then to evaluate the capacity of the Laser Induced Phosphorescence to measure temperature when applied to small and curved volumes subject to high temperature gradients. From these measurements, the heat exchanges between the gas, the quartz walls and the ambient air can be evaluated, as they are key to control the stability of the flame inside the quartz tube.

3.5.2 Luminescence mechanisms

As exposed in detail in section 3.2, if a film of phosphor is deposited on a surface, and then excited by a light source, the subsequently emitted luminescence allows us to determine the temperature of the surface. The Laser induced phosphorescence is then a technique to measure temperature using the

temperature-dependency of the phosphor luminescence emitted after being excited by an ultraviolet light source. The application of thermographic phosphors includes choosing a phosphor, fixing it to a surface after its preparation or after buying it, selecting a measurement strategy and calibrating it.

Phosphor choice As above mentioned, phosphors are composed of the host lattice and of activators, the combination giving various properties like temperature range and sensitivity, lifetime range or oxygen sensitivity. Plenty of phosphors are available or doable and their properties are described extensively in the literature. The authors Shionoya et al. (2012) and Brübach et al. (2012) gave detailed information on an exhaustive list of phosphors. In order to choose a phosphor, one must estimate the range of temperature of the measurement. The choice also depends on the measurement strategy used. Thus, the phosphors can be oxygen dependent, as a result the environment properties must also be known (in contact with fresh or burned gas, ambient air, etc).

Film deposition The way to fix the phosphor to the surface is, as previously explained, by mixing the phosphor powder to a high temperature binder, and spray it using an airbrush on the surface. It is proven in Knappe et al. (2011) that a thick layer of phosphor deposited on a surface, about several tens of microns can lead to a response delay in the characterization of unsteady phenomena. However, the phenomena observed in this study using phosphor thermometry are measured under an established steady regime.

Excitation and measurement strategies The phosphor paint is excited by a Nd :YAG Laser quadrupled at 266 nm or tripled at 355nm, depending on the excitation wavelength of the phosphor, with a 10 Hz repetition rate. Two measurements strategies are available to get back to temperature from the phosphor emitted luminescence using two different characteristics of the emitted light : the time-resolved and the time-integrated luminescence characteristics. The time-integrated or intensity ratio technique is particularly advantageous in the study of surface temperatures and heat transfer in gas turbines, since it gives access to two-dimensional measurements where the temperature is too high for other techniques to be applied, but also for rotating objects (Heyes et al. (2006)). The time-resolved or lifetime technique is well suited for single-point measurements, and thereby for steady configurations. The two methods are compared in Fuhrmann et al. (2013), concluding that at low temperatures (under 500 K) both precision are of the same order of magnitude while when getting to higher temperatures, the lifetime proves to be 1 even 2 orders of magnitude more accurate.
In the present work, the measurements are carried out on a mesoscale quartz tube outer surface with a lean premixture flame stabilized inside at different equivalence ratio. The measurements are performed on a steady configuration.

The temperature range is expected to be between 300 K and 1000 K. The two methods are introduced and the results with both methods are exposed.

3.5.3 Intensity ratio, time integrated measurement strategy

The time-integrated or intensity ratio method uses the fact that the intensity maximum of the main emission peaks of the emission spectra of a phosphor are temperature dependent, as shown in Fig. 3.7 for two phosphors (YAG :Pr and YAG :Dy). The measurements and calibrations are performed by recording the phosphor emission at a wavelength where the emission spectrum of the phosphor has a temperature dependent peak. In order to remove the possible noises and interactions of the setup (optics, scatter lights..), it is preferable to select two temperature dependent peaks at two different wavelengths and perform the intensity ratio of these peaks. A calibration is then necessary to link the intensity ratio to the temperature. Since two wavelengths are selected, the method is also called the two-color method.

3.5.3.1 Phosphor choice

Two thermographic phosphors are of interest in our case for their large temperature range and presenting no oxygen dependence : the dysprosium and the praseodymium doped yttrium aluminium garnet ($Y_3Al_5O_{12}$:Dy and $Y_3Al_5O_{12}$:Pr). The YAG :Dy ($Y_3Al_5O_{12}$:Dy) (Technology (2018)) is excited at the 355 nm wavelength. Several peaks can be chosen for the ratio of intensities since this phosphor presents numerous temperature dependent peaks. However, the analysis of the influence of the peak choice on the intensity ratio is performed in Ishiwada et al. (2018) and Jovicic et al. (2015). By comparing the intensity ratios as a function of temperatures, they determine the more accurate peaks choices by looking at the curve's slope, the highest slope giving the greatest accuracy on the temperature determination. The two peaks selected are at the wavelengths 456 nm and 497 nm (emission spectra shown in Fig. 3.7 (right)). This phosphor is broadly used in the literature (Brübach et al. (2012)). The YAG :Pr ($Y_3Al_5O_{12}$:Pr) (see section 3.3.1), less common, is excited at the wavelength 266 nm and has also two main temperature dependent peaks at the wavelengths 487 nm and 611 nm (emission spectra shown in Fig. 3.7 (left)).
The spectra represented in Fig. 3.7 are normalized by the maximum intensity. The methodology to measure these emission spectra is described in the following sections.

3.5.3.2 Experimental setup

The phosphor painted tube is positioned as shown in Fig. 3.8. A flame is stabilized inside the tube. The phosphor paint is excited by a Nd :YAG Laser quadrupled at 266 nm (YAG :Pr) or tripled at 355 nm (YAG :Dy). The emitted luminescence response of the phosphor paint is recorded by an ICCD camera

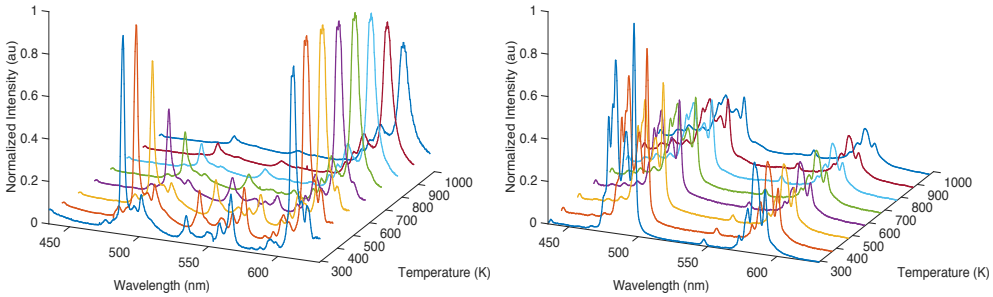

FIGURE 3.7 – *Emission spectra evolution with temperature measured for the two phosphors used : YAG :Pr (left) and YAG :DY (right).*

(Hamamatsu C12550) with image intensifier (C9016-21). The emission light pathway is split in two. The two different pathways go through two band pass filters, whose central wavelengths correspond to the two temperature dependent peaks of the emission spectrum of the chosen phosphor. The two tube images for the two wavelengths are recorded on two areas of the same camera chip.

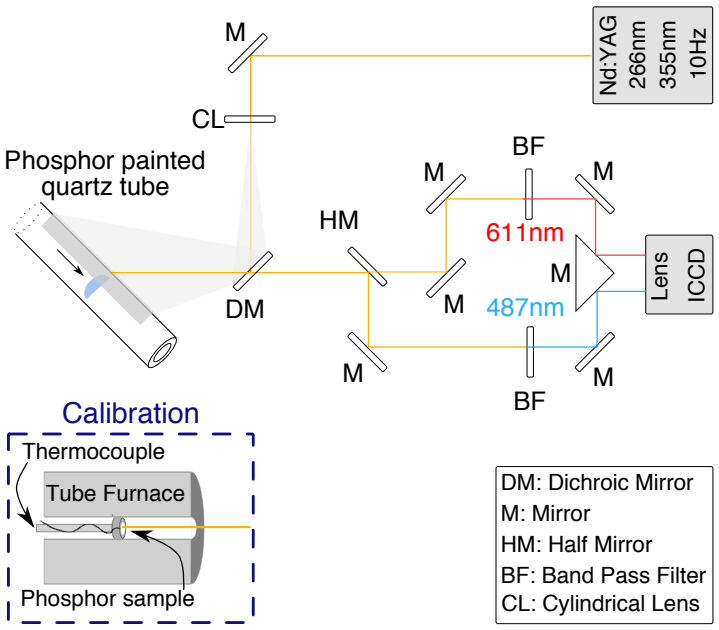

FIGURE 3.8 – *Experimental scheme of the intensity ratio measurements and calibration used for temperature acquisition on a quartz tube inside which a methane/air flame is stabilized. The two wavelengths displayed after each band-pass filter (611 and 487 nm) are given as an example as they represent the wavelength corresponding to the temperature dependent peaks of the YAG :Pr phosphor.*

An example of a camera chip image is shown on Fig. 3.9, with the two images at different wavelength (487 nm and 611 nm) without (top) and with (bottom)

a flame stabilized inside the tube, for a tube painted with YAG :Pr phosphor.

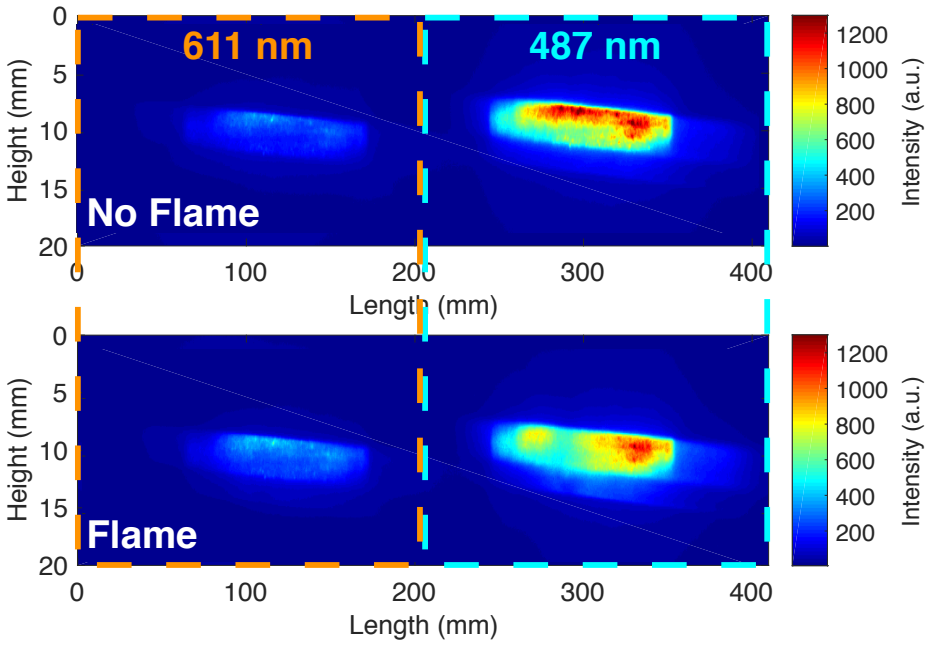

FIGURE 3.9 – *Camera chip image of intensity distribution (false colors) of the tube painted with YAG :Pr phosphor, top at room temperature and bottom with the flame, and for the two wavelength 611 nm (left) and 487 nm (right).*

As established in Fig. 3.7, the intensity of the emission is higher at room temperature for the 487 nm wavelength and on the contrary the emission gets higher with the increase of temperature at the 611 nm wavelength.

3.5.3.3 Post-processing

For each configuration, 500 images are taken successively and then averaged in order to obtain a mean image. The standard deviation from the images is calculated. The mean image obtained is then cut in two, differentiating the two object images as seen in Fig. 3.9. The two images, corresponding to the two wavelengths imposed by the bandpass filter upstream from the camera, are aligned through a Matlab process and by matching several points of reference. The intensities from one image are then divided by the intensities of the second image, yielding a matrix of intensity ratios. The intensity ratio matrix obtained with a flame inside the tube is then normalized by the standard matrix at ambient temperature. Finally, using the calibration curve, these intensity ratios are linked to temperatures, and a map of temperature is finally obtained.

3.5.3.4 Calibration

Three types of calibration are considered and compared. To reach a better accuracy the same phosphor paint batch created is used both on calibration samples and tube painting. The first calibration method is made by replacing the tube in Fig. 3.8 by a phosphor painted thermocouple placed in a heated flow (air blower). The phosphor paint is excited by the laser and the emitted luminescence is recorded by the ICCD camera, and simultaneously the thermocouple temperatures are also recorded. In the second calibration method the quartz tube is substitute by an electrical tube furnace within which a quartz pipe chamber is placed and inside which a sample of the phosphor paint is placed. As for the tube and the previous calibration method, the phosphor paint is excited by a laser and the ICCD camera records the subsequent emission of the phosphor and simultaneously the temperature is recorded by a thermocouple placed in contact with the sample. Temperature variation during the emission recording is controlled and maintained under 1 K oscillations. In the same configuration, a third calibration curve is created by replacing the ICCD camera with a spectrometer (Ocean Optics USB2000+), the subsequent emission spectra is then recorded for each temperature, and the ratio is calculated between the two peaks intensities. This last technique is used to record the emission spectra evolution with temperature of YAG :Dy and YAG :Pr represented in Fig. 3.7. The range of temperature for the calibration goes from 300 K to 1000 K.
The three calibration curves obtained for the YAG :Pr (a) and YAG :Dy (b) phosphors are drawn in Fig. 3.10.
It can be seen for both phosphors calibrations that all curves agree well in temperatures lower than 700 K. Above that, the dispersion is more important. Thus the technique of painted thermocouple shows a greater dispersion in repetition. In fact, this technique is less costly, but it raises more issues for intensity ratio : since the thermocouple is very small in surface, all the pixels are not individually calibrated and the temperature oscillations are not controlled, contrary to the furnace method. As a result even though the measurements are taken simultaneously, the calibration dispersion is important. Moreover, the YAG :Pr calibration curve from spectrometer shows a double valuation, the same ratio corresponding to two possible temperature. However, this double valuation happens only if the measured temperatures are greater than 1000 K. The maximum wall temperature reached was determined by thermocouple measurements in the previous chapitre 2, and reaches 850 K for the highest equivalence ratio operating point studied (ϕ=0.95). Therefore the range of temperature studied remains out of the double valuation area, and is for the most part in the good reproductibility area of the calibration curves.

3.5.3.5 Results

Two types of results can be extracted from the measurements processed on the quartz tube. First a 2D temperature map illustrated in Fig. 3.11 (bottom),

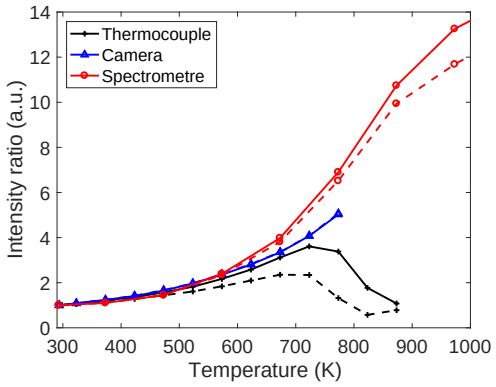

(a) YAG :Pr calibration curve

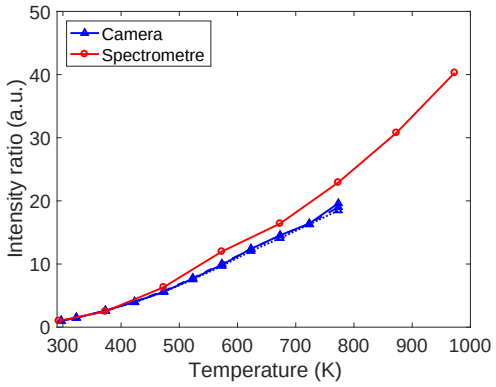

(b) YAG :Dy calibration curve

FIGURE 3.10 – *Calibration curve : graph linking the intensity ratio to temperature for YAG :Pr (a) and YAG :Dy (b) phosphor, for the three calibration methods exposed above, in black two repetition of the calibration using a painted thermocouple, the emission being recorded by a ICCD camera, in blue the calibration using the tube furnace, the emission being recorded by a ICCD camera and finally in red the calibration also using the furnace but the emission being recorded by a spectrometer.*

which is directly extracted from the intensity ratio matrix through the calibration curve. Then the centerline profile represented in Fig. 3.11(top) composed of the averaged ten lines of the map surrounding the maximum of temperature of the map. Those results were obtained using YAG :Pr phosphor and with a stabilized flame inside the quartz tube at the operating point (ϕ=0.8, U=21.1 cm·s^{-1}).
The temperature map allows to have a two dimensional estimation of the temperature, while the extracted centerline profile allows a better comparison to other types of measurements (thermocouples,...) or to other flame configurations.

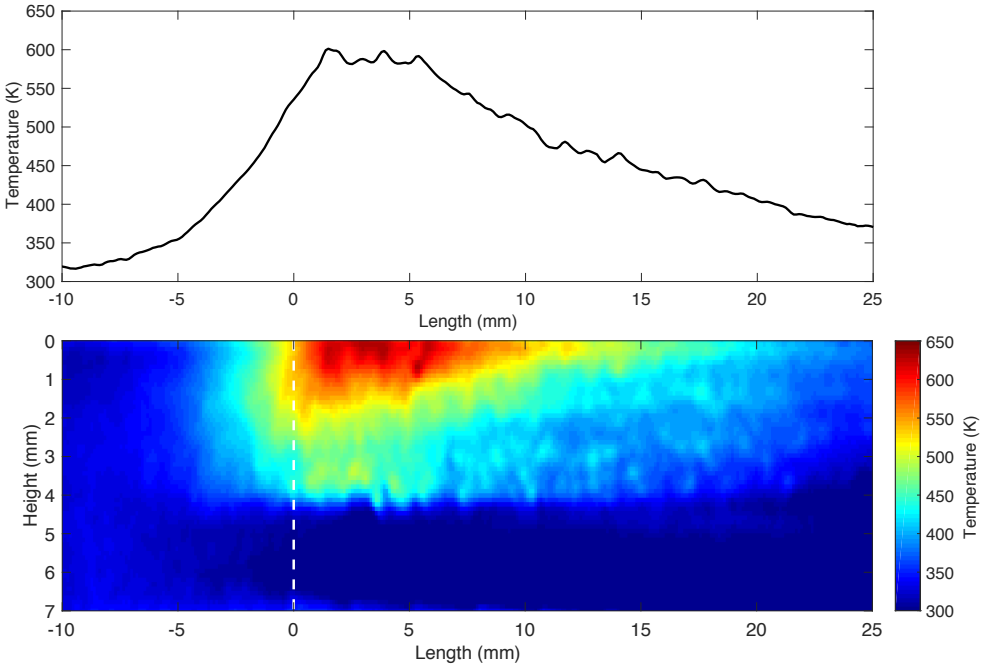

FIGURE 3.11 – *Results obtained from the intensity ratio measurements on a quartz tube painted with YAG :Pr phosphor paint and with a stabilized flame inside at the operating point (ϕ=0.8, U=21.1 cm·s^{-1}). The center line profile is obtained by averaging ten lines of the temperature map surrounding the maximum of temperature reached.*

Influence of the Calibration Three types of calibrations were previously described. In order to compare the impact on the temperature measurements, the same measurements data of the painted quartz tube, using YAG :Pr phosphor and with a stabilized flame inside at ϕ=0.8 are post-treated using the three calibration curves. The three centerline profiles extracted from the resulting temperature maps are compared in Fig. 3.12.
A discrepancy between the temperature profiles is observed. Two error sources are exposed. The first source of error comes from the use of a spectrometer, whose calibration is not considered as "in-situ" since the optical captor used differs from the calibration to the measurement. As a result the biggest discrepancy is observed between the resulting temperature profile using the spectrometer calibration. This first remark highlights the importance of an in-situ calibration in such sensitive measurement setups. Then, comparing the thermocouple and the camera profiles, which both are in-situ calibrations, it can be noted that the greatest variance is observed at high temperature. In fact, since the thermocouple diameter is 1 mm, it calibrates only few pixels of the camera chip. The optical captors such as camera chips suffer from well known inhomogeneities between pixels and non linearities. With increasing temperature, the imprecision increases, which explains the increase in the discrepancy between

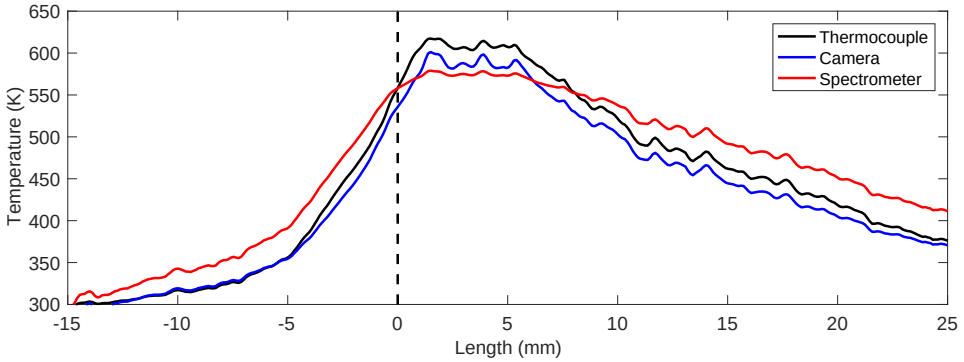

FIGURE 3.12 – *The same measurement data of the painted quartz tube, using YAG :Pr phosphor and with a stabilized flame inside (ϕ=0.8), are treated with the three different calibration curves equations.*

the two calibrations. Finally the most accurate solution is to use the camera calibration with a tube furnace, which would lead to pixel by pixel calibration.

Influence of the ICCD gain A source of noise in the images can be the amplification process of the intensified camera. In fact, when the signal is amplified, the input noise is also amplified. Thus, a noise can be created during the amplification process. For a camera, the noise is represented by a noise factor described by the relationship between the output and input noise and the amplification gain (G). For an ideal amplifier, the noise factor is equal to one. The effect of the ICCD gain on the measurements is exposed in Fig. 3.13 for the previously presented camera calibration and with a stabilized flame at ϕ=0.8.

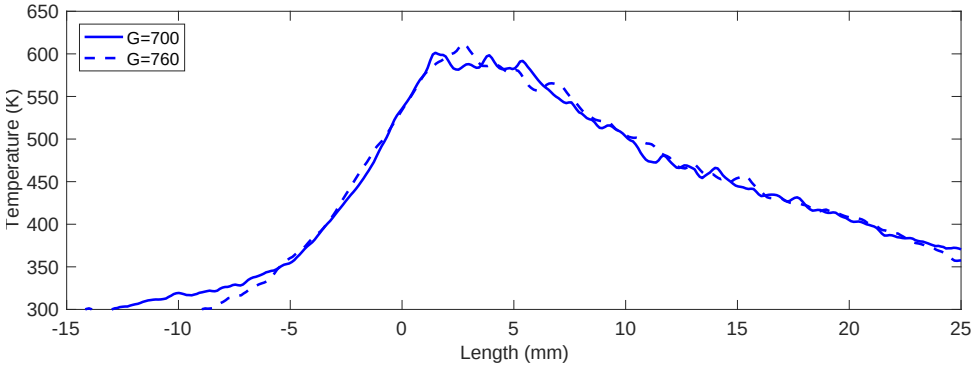

FIGURE 3.13 – *The same measurement data of the painted quartz tube, using YAG :Pr phosphor and with a stabilized flame inside (ϕ=0.8), is treated with the camera calibration curve equation for two amplification gain of 700 (plain line) and 760 (dashed line).*

The plain and dashed lines draw the extracted temperature profiles for an am-

plification gain of respectively 700 and 760. The variation between the curves is taken into consideration in the calculation of the incertitudes of the measurements.

Influence of the laser alignment Since radius of curvature of the quartz tube is low, the misalignment of the optical system causes deformation of the temperature map. The Fig. 3.14 shows the temperature maps obtained for the same conditions, with a flame stabilized at ϕ=0.75 and for different laser alignments. It can be seen that the flame area is shifted to the top of the tube in the bottom figure and that the temperature profile is not symmetrical according to the center line.

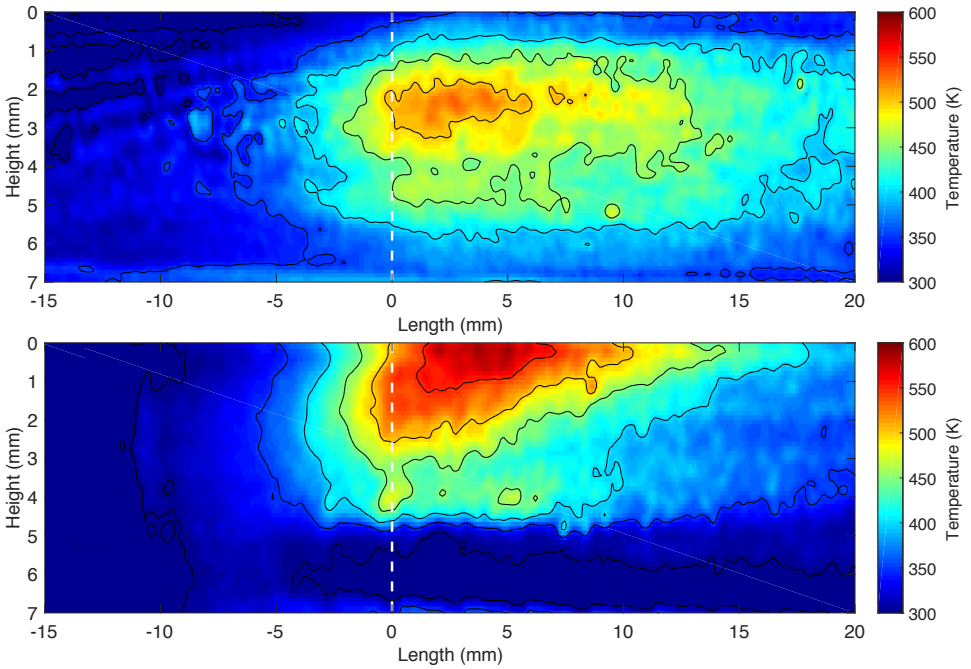

FIGURE 3.14 – *Temperature maps at ϕ=0.75 to show the consequences of laser misalignment*

Because of the small radius of curvature, the information is mainly obtained in the lines orthogonal to the laser line. Thereby if this line is shifted from the center of the tube, the resulting maps are also shifted.
To conclude, this method of intensity ratio has the advantages of resulting in instantaneous two-dimensional temperature maps, and therefore can be applied to moving systems and transitory phenomenon. However the accuracy of this method is discussed in the literature, and it is shown in the present study that several parameters influence greatly the measurements such as the camera chip calibration, the ICCD amplifier gain or the laser alignment. Another method of Laser induced phosphorescence is therefore considered.

3.5.4 Lifetime, time-resolved strategy

The lifetime method uses the fact that the luminescence intensity following a laser pulse can be approximated by a mono-exponential decay (see section 3.2.3), and this decay is temperature dependent. As illustrated in the Fig. 3.15, the decay time gets shorter as the temperature increases. Thereby, the phosphor choice in this method is a crucial parameter in order to get high accuracy on the measurements. Thus, in the detection of the phosphor emission, all electrical components must be studied to detect low and high frequencies, especially the optical captor, the signal amplifier, and the analogic numeric conversion.

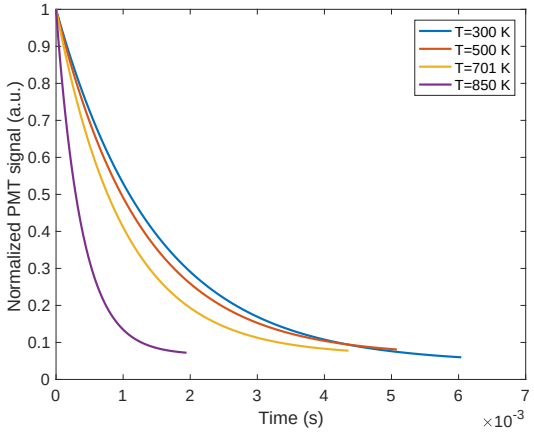

FIGURE 3.15 – *Emission intensity mono-exponential decay of Mg phosphor at several temperatures.*

Capturing high frequencies signals also limits the choice in optical captor. In fact, even if a lot of progress has been made in term of high speed camera, it is still unachievable to capture the decay of phosphors at high temperatures. In order to bypass this limitation, Omrane et al. (2002) used eight consecutively gated ccd detectors, each capturing a fragment of the luminescence decay on every pixel. The exposure and time delay between each detector is controlled to cover the whole decay signal. The lifetime, and then the temperature through calibration, is obtained on every pixel by fitting the exponential decay with the eight points from each ccd captors. However this technique suffers from poor accuracy at low temperatures and is limited depending on the phosphor. Another existing technique exposed in Khalid and Kontis (2009) uses the temperature dependent rise-time of the phosphors emission after a laser shot. With a 1 MHz high speed camera and a single chip, they measured the rise time on each pixel. However this technique is limited in number of frames, leading to poor accuracy in low temperatures (uncertainty of 20% at 673 K). Finally, Kissel et al. (2009) used a CMOS high speed camera at 675 kHz to perform two-dimensional lifetime measurements, correcting the non linearities and pixel-to-pixel inhomogeneities of the CMOS chip. The limited frame rate causes

the measurements to stop at 900 K. In fact, as the temperature increases, the number of samples decreases, and thus so is the accuracy. Finally, the mostly adopted captors are photomultiplier tubes allowing point measurements at high frequency, which limits the application of this temperature measurements method to steady configurations.

3.5.4.1 Phosphor choice

In the specific case of lifetime measurements, literature studies show the impact of several factors on the decay time. In fact Feist (2001) showed that the decay time of Y_2O_3 :Eu phosphor is decreasing when increasing the excitation energy. Another factor, presented in Ranson et al. (1998), is the decay time decrease with increasing concentrations of dopant in the host. Then in Brübach et al. (2007), the influence of gas composition and pressure over the decay time are studied and shown to have an impact. Thus, irreversible decay time modifications are observed after heat treatments. All those factors must be taken into account while choosing a phosphor for lifetime measurements. In the present study, the phosphor chosen for this method is the magnesium fluorogermanate doped with manganese Mg_4FGeO_5 :Mn (phosphor technology, EQD25/N-U1 Technology (2018)). This phosphor's decay time decreases from 5.10^{-3} s to 2.10^{-7} s for temperatures from 4 K to 1150 K. It is broadly used in the literature for its wide temperature range. Its emission spectrum is centered in 660 nm and extends from 620 nm to 680 nm. The study of the four previously exposed factors is carried out in Brübach et al. (2008) for the chosen phosphor. It can be extracted that no significant impact of the gas composition and the absolute pressure of the surrounding gas phase is observed. However, the phosphor's decay time decreases with the increase of dopant concentration in the host, with the increase of excitation energy and also with the increase in maximum temperature and extend of the heat treatments. Nonetheless, all combined, these errors order of magnitude is 1-2 K over the entire range of temperature. Thereby, the accuracy of the measurements is not limited by the phosphor properties variations.

3.5.4.2 Experimental setup

The experimental setup of lifetime temperature measurements is represented in Fig. 3.16. The phosphor painted tube is excited by a laser (Continuum, Minilite ML II) at the wavelength 266 nm and at 10 Hz. The emission light pass through two spherical lenses (f=500 mm), then through a long pass filter that suppresses wavelength under 550 nm in order to avoid all interferences from the laser, and finally through a band pass filter centered in 660 nm with a 10 nm band.
As previously exposed, the two-dimensional lifetime measurement is still complex at high temperature. Therefore, the temporal response of the phosphor paint is recorded by a photomultiplier tube (PMT) with a short response

time (5 ns) (Hamamatsu, R9880U-20). The electrical signal from the PMT is very weak and needs to be amplified, through a resistor with an non-inductive charge (Arcol, AP-821) and an operational amplifier which rise time is 10 ns (HCA-40M-100K-C). The signal is then recorded and filtered by an oscilloscope 350 MHz (Lecroy WaveSurfer 434), especially used to sample high frequencies signals. The emission is integrated on the vision field of the captor.
Following the work of Guiberti et al. (2014) and Degenève et al. (2018), a Labview routine computes in real time the decay time of the signals, using a predefined fitting window. The fitting window initially starts at 90% and stops at 10% of the maximum intensity. Thus, since the photomultiplier measurement is point wise, the phosphor painted quartz tube is positioned on a one-axis motorized translation stage. Thereby, a line of measurement is achieved along the tube's axis.

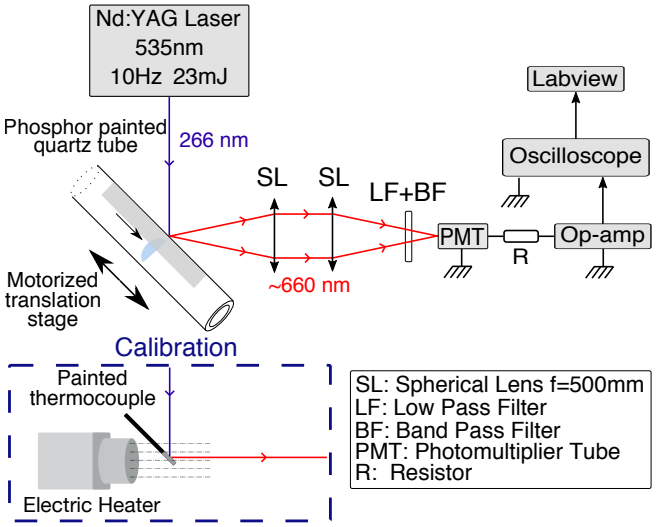

FIGURE 3.16 – *Experimental scheme of the Lifetime measurements and calibration used for temperature acquisition on a quartz tube inside which a methane/air flame is stabilized.*

3.5.4.3 Post-processing

For each point of measurement, a certain number of repetition (varying between 30 and 100) of measures is taken, and the average as well as the standard deviation is processed. A first approach of post-treatment is applied, following the literature Guiberti et al. (2014) on the treatment of the mono-exponential signal, an interrogation window is selected in percentage of the maximum intensity. The percentages chosen for the calibration and the measurements are p_{start}=90% and p_{stop}=10% of the maximum intensity.
The second approach, developed by Brübach et al. (2009) and depicted in

Fig. 3.17, is an iteratively adapted fitting window algorithm. The fitting window starts at t_1=t_0+$c_1\tau$ and stops at t_2=t_0+$c_2\tau$, with t_0 is the laser trigger point, c_1 and c_2 predetermined constants which depends on the configuration. The initial value of τ is given by τ_0=$c_0\Delta t$, with Δt is the observation time window and c_0 a constant. The parameters used for the calibration and measurements are c_1=0.1 and c_2=8. A sensibility study of those parameters is given in the following subsection 3.5.5.2.
The convergence criteria used is the one exposed in Brübach et al. (2009), given as :

$$max(\tau_i, \tau_{i-1}, \tau_{i-2}) - min(\tau_i, \tau_{i-1}, \tau_{i-2}) < 10^{-3}\frac{\tau_i + \tau_{i-1} + \tau_{i-2}}{3}$$

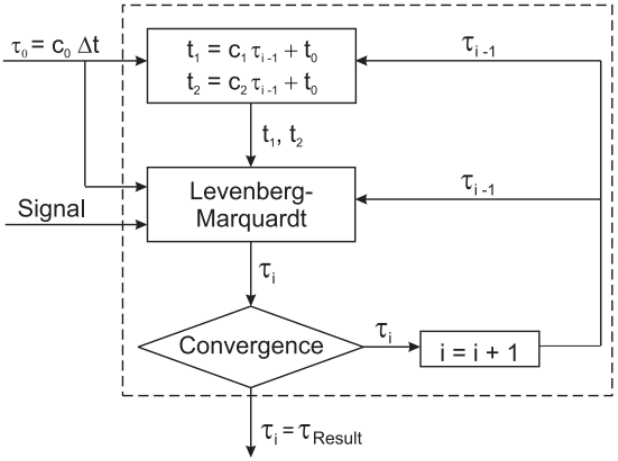

FIGURE 3.17 – *Chart describing the iteratively adapted fitting window algorithm (extracted from Brübach et al. (2009)).*

In both windowing strategies, the resulting curve fragment is fitted by a mono exponential model $I(t) = I_o\exp(-t/\tau)$ using least square method, thereby giving access to the lifetime τ. To be free from I_o, the signal is normalized by the signal at ambient temperature. The lifetime is then linked to the temperature through the calibration curve.

3.5.4.4 Calibration

The calibration used for this temperature measurement strategy is similar to one used for intensity ratio. In fact, a phosphor painted thermocouple (type K, diameter 1 mm) is put in a heated air flow (air blower LEISTER, CH-6056, 2850 W) for a temperature range from 300 K to 900 K. Since the measurements are one point measurements, the thermocouple solution is the easiest and the less costly.

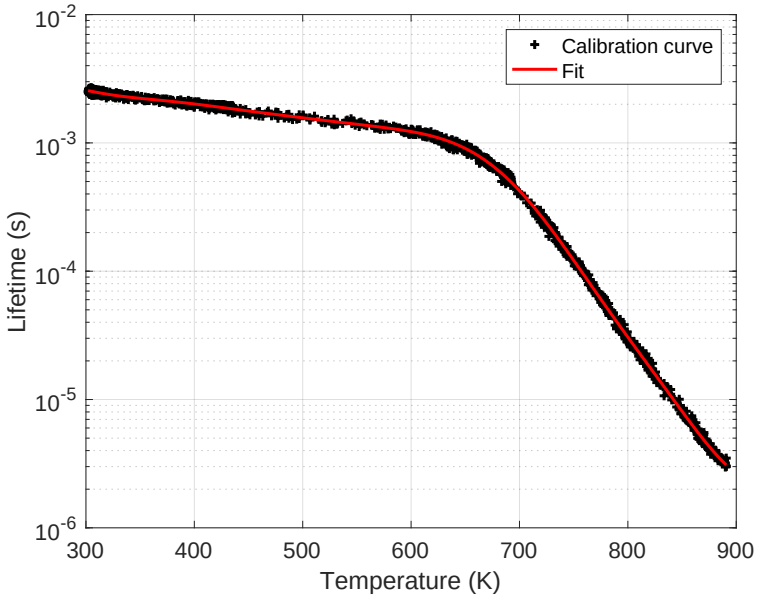

FIGURE 3.18 – *Calibration curve obtained by replacing the painted tube in the experimental scheme Fig. 3.16 by a painted thermocouple of 1 mm diameter, placed in a heated air flow. The resistor used in the amplification chain is $R = 13600\Omega$. The data are fitted using the adapted fitting window algorithm, the fit equation is used to convert decay time in temperature during the measurements.*

The lifetime in logscale is plotted against the temperature in Fig. 3.18. The black curve represents the raw calibration data and the red curve is the fit used to get back to temperature from the measurements data. This calibration curve is similar to the ones found in the literature for the magnesium phosphor (Brübach et al. (2012); Brübach et al. (2008)). The calibration is processed in-situ and therefore is adapted to the experimental configuration and peculiar to each configuration. The important matter is to keep the same configuration between the calibration and the measurements.

3.5.4.5 Results

The temperature profile resulting in lifetime measurements over a quartz tube painted with a phosphor (Mg_4FGeO_5 :Mn) binder inside which a flame is stabilized at ϕ=0.8, U=21.1 cm·s^{-1} is represented in Fig. 3.19. In all results the flame front is marked by $x = 0$ and by a vertical dashed line. The standard deviation between the consecutive measurements is represented as error bars on the graphs. Three phases can be clearly identified, the preheating zone, the flame area and the burned gases. In the first area, the fresh gas are preheated by the walls, meaning that the axial conduction retrocedes the heat from the flame area to the fresh gases. The temperature gradient is important since the the wall

temperature increases from ambient temperature to 600 K in 10 mm. In the flame area, the maximum temperature is reached 3 mm after the flame front. In this area the radiation, conduction and convection are linked to high temperature gradients. In this configuration (ϕ=0.8), the quartz tube reaches ambient temperature around 40 mm after the flame front. In the burned gases area, the quartz is being cooled by external natural convection, through conduction in the quartz.

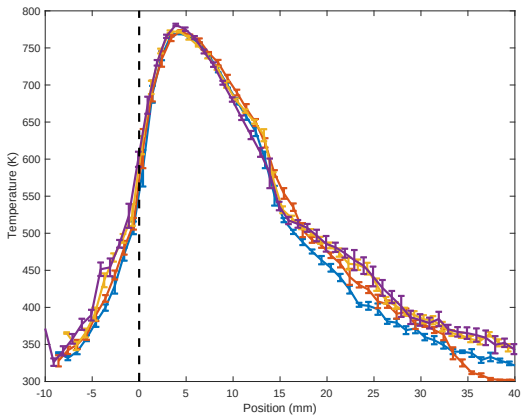

FIGURE 3.19 – *Repeatability on Lifetime measurements over a quartz tube painted with a phosphor (Mg_4FGeO_5 :Mn) binder, inside which a methane/air premixed flame is stabilized at the equivalence ratio of ϕ=0.8 and V=21.1 cm/s speed.*

Above 500 K the measurements have a very good repeatability. More dispersion is observed at low temperatures and especially in burned gases. Regarding the spatial repeatability, the three phases of the temperature profile namely the preheating, flame and cooling areas are accurately reproduced. The accuracy loss in low temperature can be explained by the calibration curve of the chosen phosphor, represented in Fig. 3.18, which shows a lower slope at low temperature giving less accuracy on the conversion from lifetime to temperature. Thus, a sensitivity analysis is processed to evaluated the impact of several factors on the accuracy of this method.

3.5.5 Sensitivity analysis

In order to assess the accuracy of the results, a sensitivity analysis of the experiment parameters is achieved.

3.5.5.1 Effects of the amplification chain

The amplification chain is composed of the resistor R, represented in Fig. 3.16 and of the operational amplifier. The variable in this chain is the value of the electrical resistance. Increasing the resistance notably improves the ratio signal to noise and reduces effectively the signal scattering. However, the resistor

behaves as a lowpass filter if the value of the resistance is too high. Since in this study the temperatures measured are under 800 K, the value of the resistance chosen is R=13200 Ω.

3.5.5.2 Effects of the interrogation window

The interrogation window is crucial to obtain accurate decay times, and thereby temperature measurements. On the same signal at room temperature the two previously introduced approaches are tested, and the resulting decay times computed and presented in Fig. 3.20.

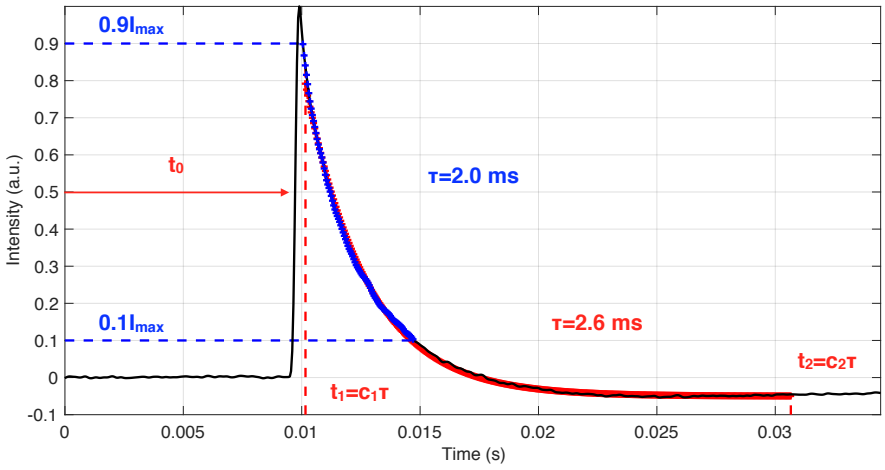

FIGURE 3.20 – *The intensity signal data is represented in black, the fitted curve through the percentages approach is in blue and the fitted curve through the iterative window is in red.*

The blue curve represents a 10% to 90% maximum intensity selection window, whereas the red curve represents the converged solution of the iterative windowing. The resulting lifetime is respectively of τ=2.0 ms and τ=2.6 ms. This discrepancy can lead in high temperatures to a great temperature difference. It highlights the crucial role of the adapted windowing on the accuracy of the measurements.

Concerning the second approach, a sensitivity study on the c_1 and c_2 parameters is carried out. In Brübach et al. (2009), the values given to those parameters are respectively 1 and 4. At a fixed temperature (T=300 K), N_s=200 emission samples are successively recorded. The algorithm is applied to samples for c_1 range from 0.1 to 1 with a 0.1 step and c_2 from 4 to 8 with a 0.5 step. The standard deviation between the 200 resulting time decay for each (c_1,c_2) couples is computed and normalized by the average time decay of the couple. This normalized standard deviation is mapped on Fig. 3.21.

As a result, the parameters values that minimize the standard deviation are

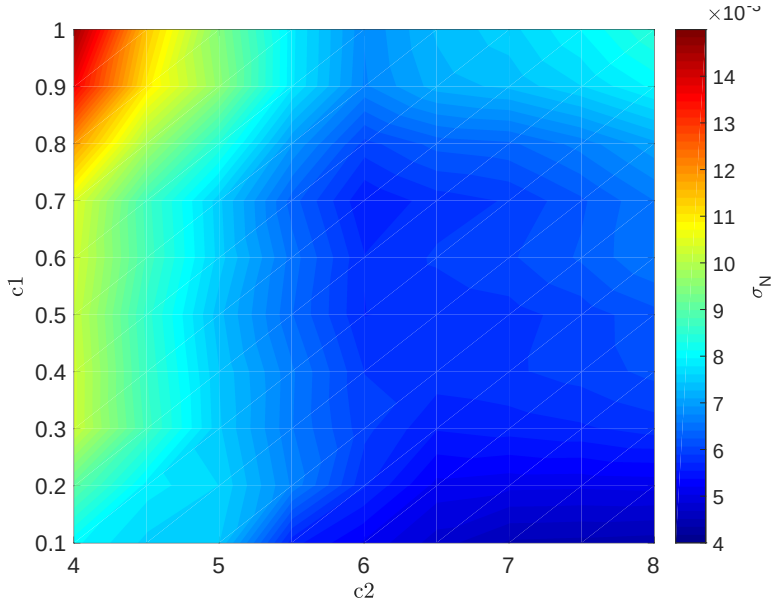

FIGURE 3.21 – *Standard deviation normalized by the time decay average of the N_s samples taken at T=300 K, mapped according to c_1 and c_2.*

c_1=0.1 and c_2=8. Those values differ from the ones used in Brübach, Janicka, and Dreizler (2009), however they depend on the experimental setup and the equipment used, and allow the adaptation of the method to all kinds of experiment. Thus, it shows the importance of caring out this sensitivity analysis and an in-situ calibrations.

3.5.6 Comparison between all methods, Lifetime and Intensity ratio applied on a narrow quartz tube

In the same configuration of (ϕ=0.75, U=16.6 cm·s^{-1}) and (ϕ=0.8,U=21.1 cm·s^{-1}), all the previously exposed methods with the different phosphors are exposed and put against thermocouple measurements (described in chapitre 2) and represented in Fig. 3.22.
First, the intensity ratio using YAG :Pr shows a good reproduction of the temperature profile but a low accuracy in temperature maximum. Indeed, a saturation is observable on the plots with a plateau shape at the temperature maximum for both operating points. The intensity ratio using YAG :Dy shows a better accuracy. Since the accuracy of the phosphors techniques increase with the temperature (due to a high slope of calibration curves), the intensity ratio (YAG :Dy) and Lifetime date are more accurate in reproducing the maximum of temperature. Thereby, the graphs show that the thermocouple underestimates the maximum of temperature, for both operating points.
At lower temperatures, the phosphors techniques loose in accuracy (due to a low

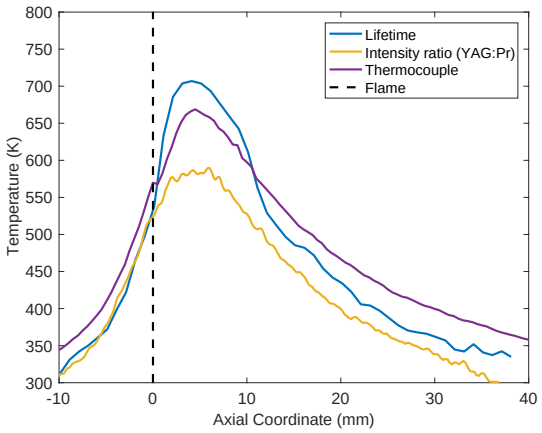

(a) (ϕ=0.75, U=16.6 cm·s^{-1})

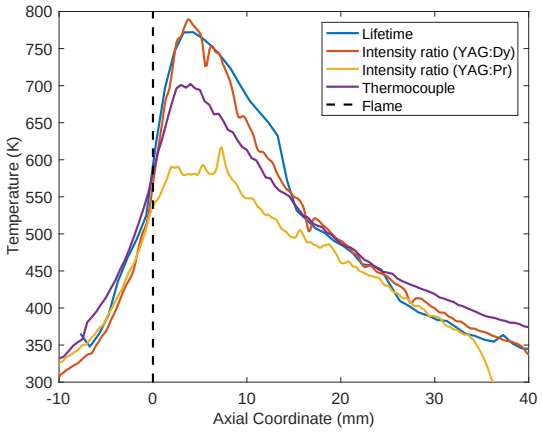

(b) (ϕ=0.8,U=21.1 cm·s^{-1})

FIGURE 3.22 – *Comparison between temperature measurements using lifetime and intensity ratio measurements and thermocouple at two operating points of equivalence ratio ϕ=0.75 (a) and ϕ=0.8 (b).*

slope of calibration curves), and the thermocouple suffering less from radiation and temperature effects becomes more accurate than the phosphor techniques, who underestimate the temperatures in low temperatures areas.
Finally, both techniques phosphors and thermocouple are complementary since their best accuracy is within different temperature ranges.

3.6 Conclusion

This chapter relates the possibility to apply the two Laser Induced Phosphorescence (LIP) strategies on a narrow channel with a low radius of curvature. The

intensity ratio method allows to obtain instantaneous two-dimensional temperature maps and can be applied to transitory or moving systems. Measurements lines are realized in the lifetime strategy forcing the system to be in a steady regime. The accuracy of both methods is evaluated in sensitivity analysis to several parameters. Finally, the resulting measurements are compared to the thermocouple temperatures presented in the previous chapitre 2. It is found that the temperature measurement strategy are complementary. In fact, the thermocouple shows a better accuracy in low temperatures ranges inferiors to 600 K since it is less subjected to radiations, and thus according to the calibration curves of the phosphors which slope are low reaching a lower accuracy. For temperatures above 600 K the thermocouple is subjected to several disrupting phenomena leading to an underestimation of the maximum of temperature. On the contrary in this range of temperatures the LIP methods show a high accuracy since the calibration curve slope are high. Therefore the comparison between those two methods allows to establish an "ideal" temperature profile, with a high accuracy in the low temperature range using thermocouple measurements and in the high temperatures using LIP methods. These results are used to analyse the temperature profiles used in the following work.
This chapter concludes this introductive part which presented the stakes of the study as well as the state of the art and context, the experimental setup and the diagnostic used for flame characterization. A focus was made on temperature determination using Laser induced phosphorescence. The following part presents the steady regime through experimental and numerical characterization.

Deuxième partie

Steady flames regime and thermal characterization

Chapitre 4

Stability definition and characterization

Contents

4.1 Extended abstract

The experimental setup being designed and the diagnostics tested and validated, the extensive analysis of the steady state is proposed here. Three parameters impacting the flame stability can be varied : the internal diameter of the tube (three different tubes of four, five and seven millimeters are tested), the equivalence ratio of the mixture and the orientation of the tube (namely the horizontal or vertical position). When changing these parameters, the bulk velocity of the flow has to be adapted to stabilize the flame. Contrary to what is observed when the flame is propagating in the tube, only one duet velocity/equivalence ratio can be found. There is no weak flame regime, for a given

equivalence ratio a unique bulk velocity allows to sustain the flame. A slight modification of one of the three parameters modifies also the flame shape, its orientation and the wall temperature distribution. Some observation are noticeable : (i) the equivalence ratio ranges from 0.7 to 0.95 with the five-millimeter diameter tube. This range shifts to the low values as the diameter increases and to higher values as the diameter decreases. (ii) The orientation of the tube has no influence for the small diameter tube but drastically changes the operating points for the seven-millimeter diameter tube. In particular, the flame can be slanted for large diameter whereas the configuration is perfectly symmetrical. (iii) Gravity has an impact on the flame regime but also the flame orientation. In the horizontal position, a slanted flame is observed. The angle of the flame changes with the internal diameter and the equivalence ratio. (iv) The tulip cannot be observed in the tested operating point. The curvature of the flame remains towards the burnt gases. Finally, the five-millimeter tube configuration is systematically investigated in order to quantify the different parameters involved in this steady regime.

4.2 Flame steady regime : definition and characterization

4.2.1 Definition of the steady regime

In narrow conducts, the stabilization mechanisms are characterized by coupled heat exchanges, convective at the interfaces flame/wall and wall/ambient air, and conductive within the wall. The slowest thermal exchange occurring in this configuration is the heat conduction through the quartz wall. It is then used as a reference of thermal establishment. Two characteristical times are then defined to describe the flame thermal environment. First, the conduction time can be written as the ratio of the wall thickness over the thermal diffusivity of the quartz : $t_{cd} = e_{\mathrm{w}}^2/\alpha_{\mathrm{s}}$. Then, a flame residence time is defined as the ratio between the characteristic flame thickness δ_F and the propagation speed : $t_{res} = \delta_F/V_p$. The characteristic flame thickness is expressed as : $\delta_F = \alpha_{\mathrm{g}}/\mathrm{S_L^o} = 76.8$ μm with α_{g} the fresh gas thermal diffusivity and $S_L^o = 28$ cm·s^{-1} at $\phi = 0.8$. The fresh gas thermal diffusivity is defined as $k_{\mathrm{g}}/(\rho_g \mathrm{C}_{p_g})$ with $k_{\mathrm{g}} = 34.4$ mW·m^{-1}·K^{-1}, $\rho_g = 1.14$ kg·m^{-3} and $\mathrm{C}_{p_g} = 1.10$ kJ·kg^{-1}·K^{-1}. The propagation speed -$\mathrm{V_p}\vec{x}$ is defined as the absolute flame speed in the laboratory frame. The bulk velocity $\mathrm{V_b}\vec{x}$ is the mean speed resulting from the Poiseuille profile of the incoming fresh gases. The Fig. 4.1 schematically illustrates the different velocities directions of the system.

These defined characteristical times allow to assess if the flame reside long enough in the same section of the tube for the thermal environment to establish itself. As a result, for $t_{cd}/t_{res} < 1$, the global flame motion is slow enough for the conduction to be established and to reach a steady state. On the contrary,

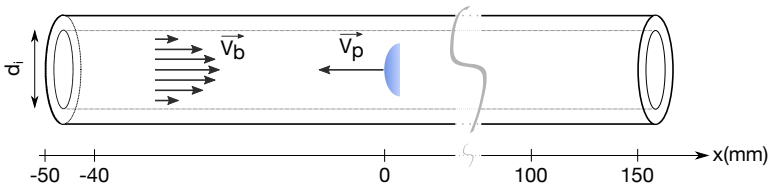

FIGURE 4.1 – *Schematic representation of the propagation velocity of the flame and the bulk velocity, in a narrow channel.*

for $t_{cd}/t_{res} \gg 1$, the wall temperature at the flame position remains in the order of 300 K and the flame propagates over an isothermal wall.
Experimentally, a steady regime is observed when $V_p \to 0$. In practice, the flame is first ignited in the output section of the tube. To drive the flame into the tube, the mass flow rate is progressively reduced, and by that the bulk velocity. Once the flame inside the tube, the mass flow rate is precisely adapted to the burning velocity (laminar flame speed) in these non-adiabatic conditions to stabilize the flame. Thereby the stability is reached when the temperature in the walls does not evolve anymore or evolves slightly at a large time scale (order of minute). The thermal environment exterior to the tube is not controlled so the heat losses are not quantified and the real flame speed can only be experimentally determined by trials and errors. Hence, the stabilization of a flame inside the aforementioned tube is challenging.
The edge tracking method is applied on recordings made at several bulk velocity to establish the propagation speed of the flame in the search of stability points. As a result the motion of the flame can be drawn according to time on Fig. 4.2 (d_i=5 mm, ϕ=0.8).

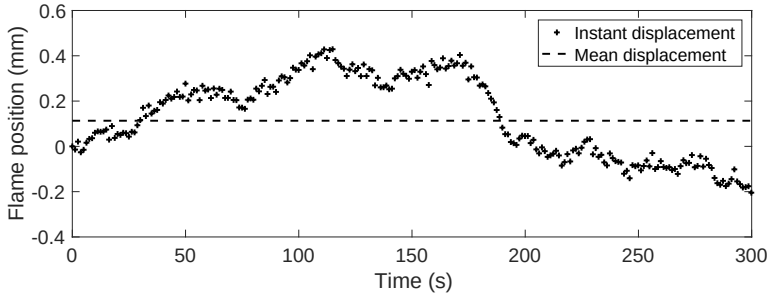

FIGURE 4.2 – *Flame position evolution with time at an operating point (steady regime) in the d_i=5 mm tube at ϕ=0.8. The dashed horizontal line represents the mean flame position over the time recorded.*

It can be seen that the flame is never perfectly steady and oscillates around a mean position represented by the horizontal dashed line on Fig. 4.2. Those oscillations are usually not visible at eyesight. However, as previously stated,

the steady regime is defined as a regime where the thermal exchanges are established, not as a regime where no flame motion is observed. Thus, the mean propagation speed calculated from the ratio of mean displacement on the recorded time is of order of 24 μm per minute.

4.2.2 Steady regime operating points dependance to channels diameter

The steady regimes of flames are observed in three tube configurations of inner tube diameter d_i=4 mm (Configuration A), d_i=5 mm (Configuration B) and d_i=7 mm (Configuration C), with a same e_w=1 mm wall thickness. For each configuration, horizontal and vertical tube positioning is considered. All inner tube diameters are greater than the quenching diameter of the methane air mixture injected.
The purposes of this first set of experiences are to identify the flow conditions that allow a stabilization of the flame at a constant position without assistance and to observe the changes of the flame's shape with respect to the equivalence ratio and to the tube diameter. Thus, the diameters are chosen as close as possible to the quenching diameter to observe stabilization mechanisms mastered by heat exchanges, but also to have a satisfying range of operating points and obtain a certain flame robustness.
In the literature, for the same equivalence ratio, several flow speeds are found to reach flame steadiness, using flame thermal assistance (Maruta et al. (2004); Maruta et al. (2005); Bai et al. (2013)). In the presented configurations, without flame assistance, steady operating points are characterized by a unique couple of equivalence ratio and bulk velocity. The equivalence ratio is varied from ϕ=0.7 to 0.95. Thus, the steady regime is characterized by $V_p \rightarrow 0$, and since $V_p = V_b - S_L$, the bulk velocity tends to burning velocity, $V_b \rightarrow S_L$. As a result, the operating points allow to determine the burning velocity of the flame at each equivalence ratio, by adjusting the bulk velocity.
The bulk velocity/mass flow rate varies greatly between the three cases. To keep a good accuracy in mass flow control, the range is chosen as a compromise between the three configurations, as a results the low equivalence ratio for the (A) case and the high equivalence ratio for the (C) case cannot be reached. Nonetheless, it is sufficient to make a selection.
The variation of inner tube diameter leads to a variation of the surface-to-volume ratio which has been presented as a critical factor in narrow channel combustion on the heat exchanges. To compare the ratio evolution with the increase of the inner diameter, a sum up is presented in Fig. 4.3.
As a result the surface-to-volume ratio increases of 74% between the 7 mm and 4 mm inner diameter tubes. The greater the surface-to-volume ratio is, the more heat losses to the wall occur, and therefore the flammability domain of the flame reduces. This comparison between the three configurations is then used to identify and understand better the effects of the phenomena which intensities

Configuration name	Inner diameter (mm)	Ratio S/V (m^{-1})
(A)	4	1010
(B)	5	810
(C)	7	581

(25%) (40%) (74%)

FIGURE 4.3 – *Sum up of the three tested configurations sections, and the order of magnitude in between the surface to volume ratio calculated on the diameter of the tube.*

vary with the section.
The first comparison is made on the steady operating points, and by that the power of each flame. The operating points are represented on Fig. 4.4 for the three configurations in horizontal (blue curves) and vertical (black curves) tube position. Thereby, Fig. 4.4 indicates the non-adiabatic laminar flame speed for several equivalence ratio and tube diameter.

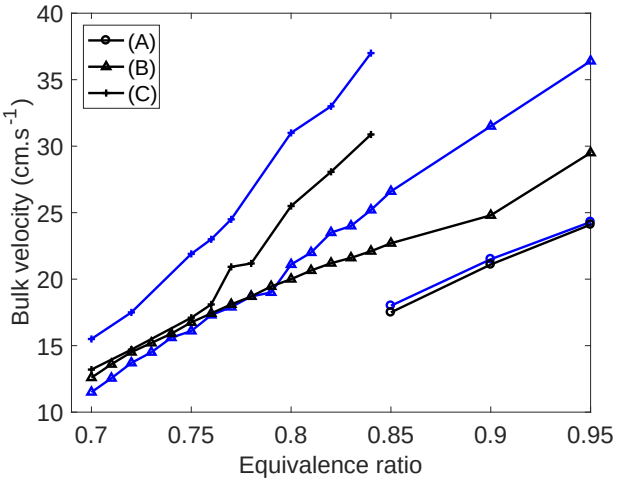

FIGURE 4.4 – *The flame steady operating points are represented by drawing the couples of flow speed and equivalence ratio for the three tested configuration, of inner diameter 4 mm (A), 5 mm (B) and 7 mm (C). For each configuration the horizontal (blue curves) and vertical (black curves) positioning of the tube is considered.*

Overall, the evolutions of the bulk velocities with the equivalence ratio can be linearly approximated, and the slopes increase with the inner section. For each equivalence ratio, the bulk velocities are of the same order. Thus, the bulk velocity for vertical positioning is found to be constantly lower than for horizontal. The velocity difference between both tube positions increases with

the section. Indeed, for the smaller section (A), the operating points are almost combined, whereas for the larger section (C), the speed gap is about 5 $cm.s^{-1}$ all along the equivalence ratios. Thereby as the section increases, the flame needs more power to stabilize at horizontal position than in vertical.
The limits of the configurations are also assed. For the (A) configuration, no flame could be ignited under the equivalence ratio 0.85. Thereby, the lower limit of the flammability domain was reached. Moreover, the flame is very sensitive to the environment, and can be extinguished by small perturbations. This configuration is the closest to the quenching diameter, but offers a reduced flammability domain and low robustness. The (B) configuration lower flammability limit is reached under the equivalence ratio 0.7. The flame is robust to the environment, meaning that the flame is well anchored in the tube and can withstand small perturbations without extinction. The (C) configuration lower flammability limit was not reached. The flame is well anchored in the steady regime, and thereby very robust. The more powerful the more robust a flame is and anchored to the walls.

4.2.3 Flame topology evolution with equivalence ratio and tube diameter

The CH^* chemiluminescence of the steady flames at each operating point is observed with a filtered digital camera (see chapitre 2). The residence time of a flame in steady regime is of the order of magnitude of several minutes. The flame luminosity being weak, a long exposure time (2 to 30 seconds) is needed. The flame topology evolves greatly with the equivalence ratio/power, but it evolves also with the section of the tube. Therefore the CH^* chemiluminescence images of the flame are compared for six operating points and represented in Fig. 4.5. The lower limit of the (A) configuration is marked by the flammability limit. The (C) configuration is limited at high equivalence ratio by the range of the mass flow meters used, in order to keep a certain accuracy in the mass flow control.
In order to compare the flame power for these equivalence ratio and link the flame power to the flame structure, the Fig. 4.6 draws the flame power for all configurations in horizontal (blue) and vertical (black) tube position.
In Fig. 4.5, the evolution of shape in the (B) configuration serves as a reference for the two other configurations. Indeed, the flame shape evolution from equivalence ratio ϕ=0.85 to 0.95 for the (A) configuration is very similar to the one of the (B) configuration from equivalence ratio ϕ=0.70 to 0.80. The flame moves from a symmetrical convex meniscus to a flat slant-shaped flame. This similarity can be explained by the similar flame power for these equivalence ratio in both configurations as highlighted by the blue rectangle in Fig. 4.6. A parallel can also be done between the flame shape evolution of the (C) configuration from equivalence ratio ϕ=0.70 to 0.80 and the one of the (B) configuration fromϕ=0.85 to 0.95. The flame is flat and tilted, and the angle to vertical in-

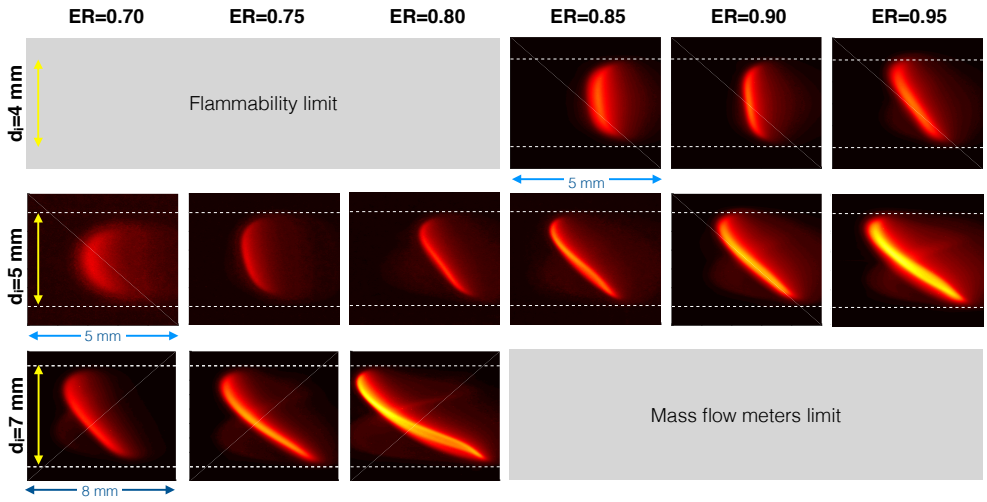

FIGURE 4.5 – *Flame topology evolution with equivalence ratio, put in relief by CH* chemiluminescence, for the three studied configurations, respectively from top to bottom (A),(B) and (C). In each picture, the white dashed lines delimit the inner wall, and the frame the outer wall limit. Thus the horizontal dimension is of 5 mm for configurations (A) and (B), and of 8 mm for the configuration (C).*

creases with the equivalence ratio. The last flame appears as a S shaped flame, anchored at the top of the tube, with a tail curved in the direction of the bottom wall. Again, when looking at the flame power (Fig. 4.6), the red rectangle highlights the three equivalence ratio for the (B) configuration and two of the (C) configuration. However this comparison shows that equivalence ϕ=0.95(B) and ϕ=0.75(C) (instead of ϕ=0.80(C)) are closer in power and thereby in same flame structure. In fact, the flame power at operating point ϕ=0.80(C) is 50% greater than at operating point ϕ=0.95(B). When looking back at the flame structure, the flame angle to vertical is indeed greater in the (C) configuration. These comparisons allow to make a link between flame power and flame structure, independently of the tube diameter. Another point of comparison is the temperature profile imposed by the flame to the wall in steady regime.

4.2.4 Wall temperature profiles : characterization of the flame domain

From the observation of the flame, the interest in temperature profile rises. The temperature measurements are operated on the external wall of the tube, on a stabilized flame (operating point). The experimental protocol to stabilize the flame does not determine the abscissa x where the flame will stand after entering the tube which depends on the reaction time of the flow rate control system. Once stabilized, the flame creates a temperature distribution within the wall that helps itself to stay anchored at this point.

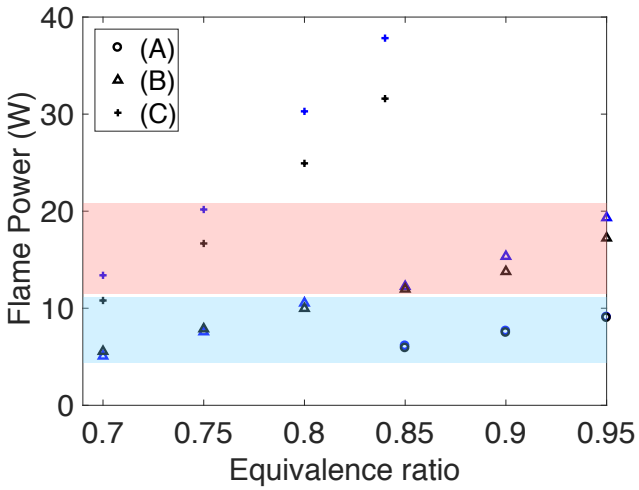

FIGURE 4.6 – *Flame power evolution with equivalence ratio, for configurations (A),(B) and (C). The blue rectangle highlights the flame power similarities between configurations (A) [ϕ=0.85,0.90 and 0.95] and (B) [ϕ=0.70,0.75 and 0.80]. In the same way, the red rectangle allows the comparison between flame power for configurations (B) [ϕ=0.85,0.90 and 0.95] and (C) [ϕ=0.70 and 0.75].*

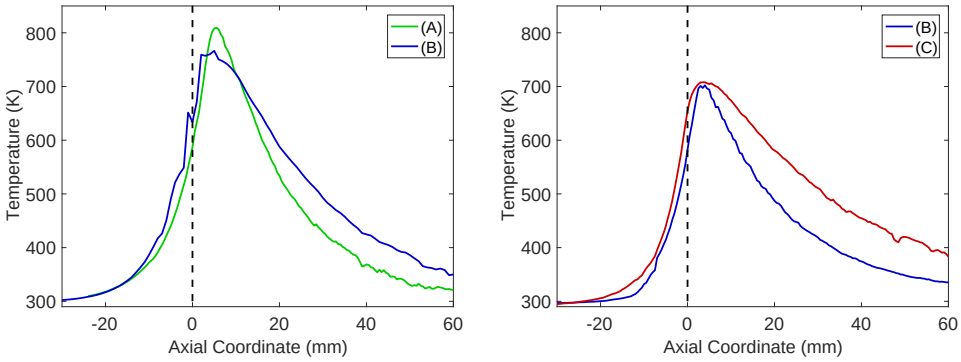

(a) Comparison (A) and (B) at ϕ=0.95 (b) Comparison (B) and (C) at ϕ=0.80

FIGURE 4.7 – *Horizontal configuration (A) and (B) external temperature profile at ϕ=0.95 (left) and (B) and (C) external temperature profile at ϕ=0.80 (right). The black dashed vertical line marks the flame front location.*

First, the external wall temperature of stabilized flame inside the tube are compared for the three configurations, at the same equivalence ratio. Since no common operating point is characterized between the three configurations, the (B) configuration serves as reference. Thereby, a first graph shows temperature profiles of stabilized flames at equivalence ratio 0.95 for the (A) (green curve) and (B) blue curve configurations Fig. 4.7(a). A second graph compares the temperature profile of stabilized flames at equivalence ratio 0.8 for the (B)

(blue curve) and (C) (red curve) configurations Fig. 4.7(b). In both graphs, the preheating zones are similar, and the maximum temperature reached is comparable. However, the higher diameter configuration cooling area is more extended, highlighting that the tube takes more time to cool down as inner diameter increases. This comparison states the flame domain dimension between two positions where the wall and gas temperature are equal to ambient temperature.
In a second approach, the external temperature profiles of flames in the three configurations with similar powers are plotted in Fig. 4.8.

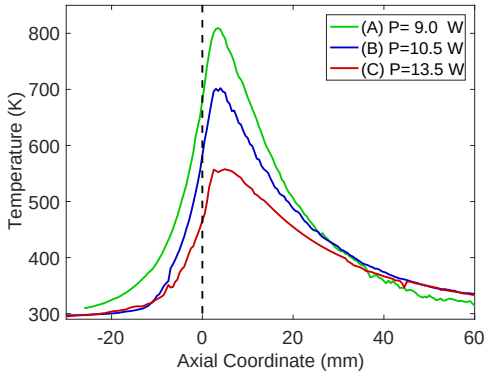

FIGURE 4.8 – *External wall temperature profile of flames in the three different configuration (A) (ϕ=0.95),(B) (ϕ=0.80) and (C) (ϕ=0.70) but with power comparable respectively P=9.0, 10.5 and 13.5 W.*

On this graph, the wall temperature of the (A) configuration, with the lowest flame power reaches the highest maximum. On the contrary, the (C) configuration with the highest flame power reaches the lowest temperature maximum. This analysis establishes that the (A) configuration presenting the highest surface-to-volume ratio, has a heat transfer rate to the wall higher than in the other configurations. Therefore to collect the energy created by the combustion, the compromise must be done between the poor stability of the flame in low diameter and the high heat transfer rate to the walls which leads to great temperatures.

4.3 Focus of the characterization on the d_i=5 mm tube

Considering the previous section comparison between the three configurations, the (B) configuration with an inner tube diameter of d_i=5 mm, is the configuration which gives the best compromise between the range of operating points, the flame robustness and the surface-to-volume ratio. Therefore, this configuration is the one mostly used along this work. The two other configurations (B)

and (C) are used as comparison when necessary and relevant.

4.3.1 Steady regime operating points

The steady operating points of the configuration (B) are represented in Fig. 4.9(a), for both vertical and horizontal tube positioning and put in parallel to the flame power evolution with equivalence ratio, represented in Fig. 4.9(b). The later graph allows to evaluate the flame power range over the studied operating points and by that, scaling the possible external assistance or on the contrary, collection of power.

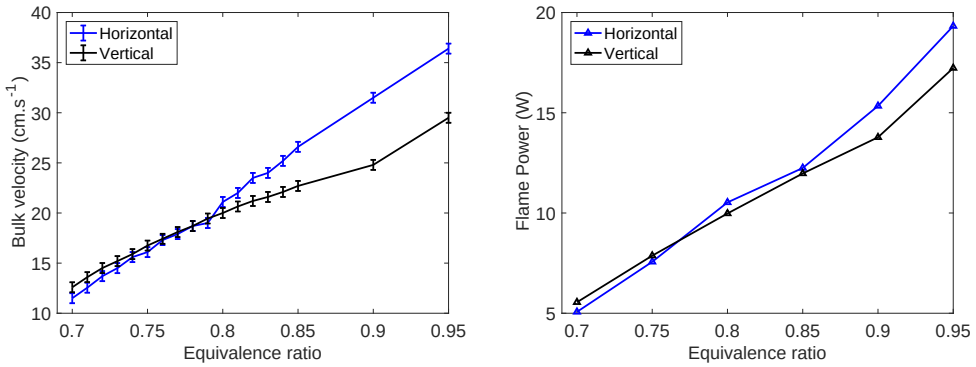

FIGURE 4.9 – ***Left :*** *The flame stability points are represented by drawing the couples of flow speed and equivalence ratio for the two studied configurations : the horizontal and the vertical tube. The error bars are determined by repetition of the experiment of stabilization.* ***Right :*** *The flame power is calculated for each operating point, by multiplying the methane mass flow rate and the LCV (chapitre 2).*

For the vertical configuration (black curve), flame speed increases smoothly with the equivalent ratio. The speed values are significantly lower than the adiabatic one meaning that the heat losses are large enough to impact the flame stabilization but not too large to allow the flame to reach a steady position. In the horizontal configuration (blue curve), the order of magnitude of the bulk velocity is identical to the vertical configuration, meaning that the heat losses are of the same order. For equivalence ratio under 0.76 the flame speed is lower in horizontal position than in vertical. Then, between 0.76 and 0.79 the operating points are nearly combined. Finally, for equivalence ratio above 0.8, the situation is inverted as the flame speed is lower in vertical position than in horizontal. The plot's slope is higher for horizontal tube than for vertical tube. This means that at higher equivalence ratio the flame needs less power to maintain its stability in vertical configuration. At lower equivalence ratio it is the opposite, the flame needs less power in horizontal configuration.
To stabilize the flame, an increase of the equivalence ratio requires an increase of the flow rate, so the stability map is drawn for flames with increasing power.

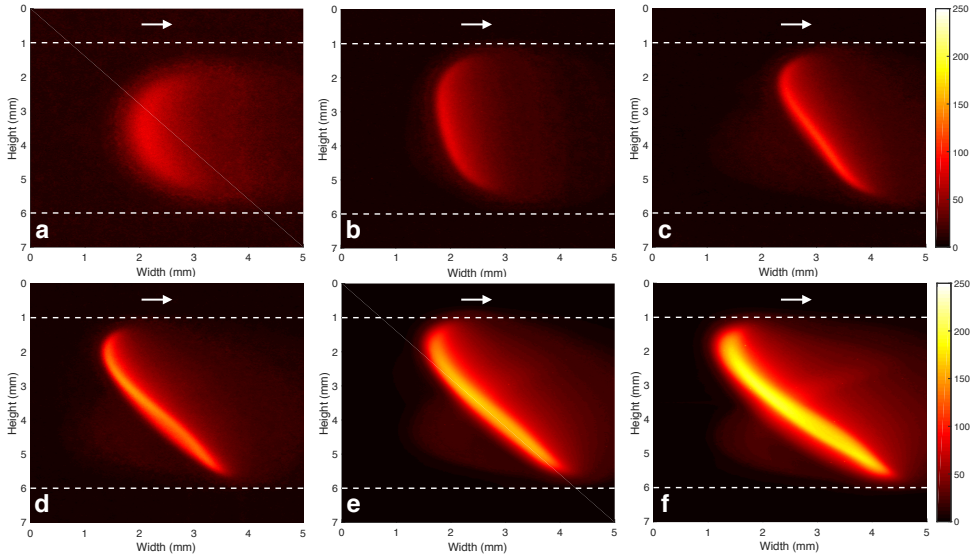

FIGURE 4.10 – *Mean chemiluminescence CH* flames (false color) corresponding to the six operating points of equivalence ratio 0.7(a), 0.75(b), 0.80(c), 0.85(d), 0.90(e), 0.95(f) for the horizontal (B) configuration. The white arrow represents the flow direction in the tube, and the white dashed line outlines the interior wall limits, and the frame of the picture delimits the outer wall.*

This power increase is represented in Fig. 4.9(b). As the equivalence ratio increase, the flame generates more and more heat that is dissipated to maintain the flame position. Consequently, the structure of the flame is different for each stable point.

4.3.2 Flame topology and orientation

The flame topology and orientation evolution with equivalence ratio are observed using CH* chemiluminescence. Figure 4.10 presents these mean flame emissions in the horizontal configuration for six operating points of equivalence ratio : 0.7, 0.75, 0.8, 0.85, 0.90 and 0.95.
It can be observed that the flames curvature decreases as the equivalence ratio increases. The curvature is convex with respect to the flow direction as computed by Daou and Matalon (2002) and Jackson, Buckmaster, Lu, Kyritsis, and Massa (2007). As expected the intensity of the flame increase with the power of the flame. The increase of the flow rate generates a loss in flame axial symmetry. At high equivalence ratio, the flame remains steady, meaning that both its position in the tube and its orientation toward the fresh gas do not change, but the flame is tilted. The flame flattens until a certain point where it partly inverts its direction, moving from an axisymmetric convex meniscus to an asymmetric S slant-shape flame, with a hump directed to the unburned mixture.

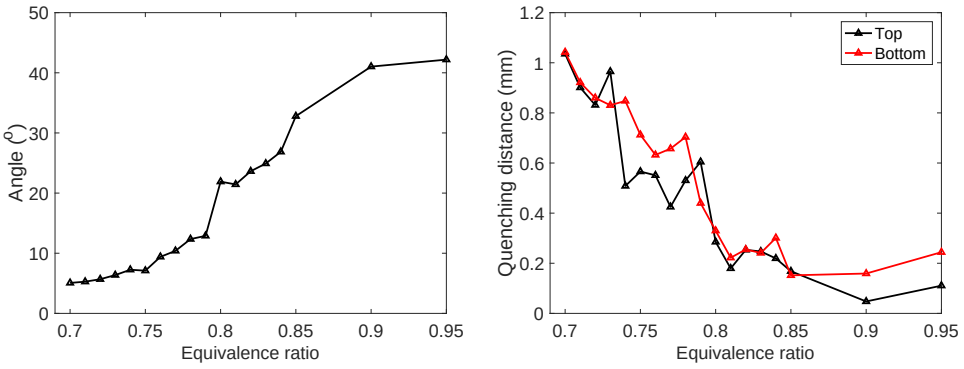

(a) Angle evolution

(b) Top and bottom quenching distance evolution

FIGURE 4.11 – *Angle (a) and quenching distance (b) evolution with equivalence ratio on horizontal basic configuration.*

Thus the flame's angle to vertical evolution is represented on Fig. 4.11(a). The greater the bulk velocity the more tilted is the flame. Thus the tilt is constantly oriented toward the fresh gases, meaning that the flame's speed is higher at the top of the tube. This loss of symmetry has already been observed experimentally and numerically in the literature but in different configurations where the walls are either adiabatic or isothermal, using different fuels, equivalence ratio or geometry.
While the flame flattens, its height increases, reducing the quenching distance between the flame and the wall. Indeed the edge/contour routine allows to determine the wall quenching distance. The top and bottom distances between the flame and the wall are represented on Fig. 4.11(b). It can be seen that the quenching distance is lower at the tube's top than at its bottom. The flame is preferentially anchored at the top, where the temperature is supposedly higher. Regarding the previous quenching distance analysis, it makes sense that the distance between the flame and the wall is lower where the temperature is higher, namely at the top of the tube. This phenomenon can be systematically repeated.

4.3.3 Thermal characterization of the flame domain

The Fig. 4.12 shows the external wall temperature along the longitudinal direction taken by thermocouple method for the same six operating points presented above, of equivalence ratio 0.7, 0.75, 0.8, 0.85, 0.90 and 0.95. The zero in abscissa corresponds to the flame front location.
Upstream from the flame, at 30 mm from the flame front, the wall temperature

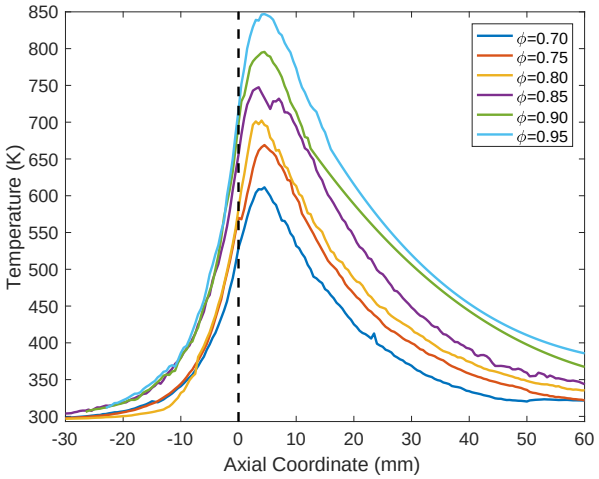

FIGURE 4.12 – *External wall temperature profile of a stabilized flame inside the channel measured by thermocouple. The flame is stabilized at operating point for an equivalence ratio of 0.7, 0.75, 0.8, 0.85, 0.90 and 0.95. The flow inside the tube goes from left to right. The flame coordinate is $x = 0$, marked by the vertical black dashed line.*

equals $T_{W_{UG}}$=298 K. For all equivalence ratios, at a distance of 100 mm after the flame front, the tube temperature reaches a constant value close to the ambient temperature. As expected, the temperature maximum increases with the equivalence ratio/power, and thereby the cooling area in the burned gas is extended.
The basic configuration of inner diameter d_i=5 mm has hereby been characterized at steady operating points, showing the evolution of flame topology and temperature profiles. These characterizations are used as reference in coming analysis and characterization of unsteady phenomenon observed. This configuration was chosen among the three tested diameters above the quenching diameter, for the dominant influence of the heat exchanges in the flame stabilization but also for the robustness of the flame without external assistance.

4.4 Conclusion

The definition and characterizations of flame stabilizations in several narrow channels are established in this chapter. The conduction is the heat exchange with the highest characteristic time and is therefore used as an indicator of the thermal establishment. The flame regimes are determined according to the ratio of this conduction characteristic time over the flame residence time calculated with the propagation speeds. Using this ratio as gage of steadiness, steady operating points are determined in three configurations with inner diameters d_i=4, 5 and 7 mm in vertical and horizontal tube position. At those operating

points the topologies of the flames as well as the external wall temperatures are characterized and compared. A compromise must be done between flame robustness, range in operating points and higher heat transfer rate in smaller diameters leading to greatest wall temperatures. Resulting from this compromise the d_i=5 mm is selected as basic configuration, but the two other configurations are used as comparison when relevant.

Chapitre 5

Stabilization mechanisms

Contents

5.1 Extended abstract

With appropriate conditions of flow rates, equivalence ratio and tube material, a lean premixed methane-air flame can sit in a five-millimeter tube. Direct observations of the flame and wall temperature measurements characterize the way flame stands depending on the operating conditions. However, heat transfer that control the flame position cannot be easily quantified experimentally. This chapter investigates the ability of a one-dimensional complex chemistry numerical code to simulate the experimental configuration, and so, highlight stabilisation mechanisms. REGATH code is used to compute 1-D flame with complex chemistry. Thermal coupling with walls is added to the existing code

to simulate convective heat transfer at the inner and outer walls, together with the axial solid conduction. First, a theoretical study is performed to validate appropriate models for the computation. The flow regimes are identified then different flames are computed for equivalence going from 0.75 to 0.95. Computation of radiative heat flux is implemented since it represents half of the total heat flux from the wall to the external medium. With temperature profiles within the walls and gas, heat fluxes are computed to draw heat exchanges through the system. As observed experimentally, a steady solution is computed for the range of equivalence ratio. The flame speed is over-estimated, mainly due to two-dimensional effects that are not taken into account. In the vicinity of the flame, gas heat up the walls. Heat is conducted axially in the walls and, a few millimeters prior to the flame, heat transfers from the wall to the gas contributing to the preheating of fresh gas : this is the so-called excess enthalpy assistance characterizing micro-combustion. Downstream the flame, burnt gases heat up the wall, its enthalpy decreases rapidly until the gas temperature equals ambient and wall temperature, vanishing heat transfers. These computations in a steady regime quantify the relative heat fluxes involved in the steady regime and validate the numerical strategy implemented.

5.2 Heat Transfer theoretical characterization

A theoretical characterization is necessary to quantify the heat exchanges between the flame, the walls, and the outside environment.

5.2.1 Dimensionless numbers characterizing the system

Dimensionless numbers allow to characterize the system. A first dimensionless number introduced is the **Reynolds number** characterizing the flow regime (laminar, transitory or turbulent) inside the tube :

$$Re = \frac{\rho_{\mathrm{g}} U d_i}{\mu_{\mathrm{g}}}$$

The range of Reynolds number in the studied configurations extends from 50 to 200. The flow is therefore clearly laminar.
The **Prandtl number** gives the importance of viscous diffusion compared to thermal diffusion, and therefore characterizes the speed and temperature profiles.

$$Pr = c_{p_{\mathrm{g}}} \mu_{\mathrm{g}} / k_{\mathrm{g}}$$

The Prandtl number remains close to the classical value of 0.7.
The **Nusselt number** characterizes the type of heat transfer : convection or conduction. Its characterization depends on the heat transfer and relies on correlations from experimental data. The determination of this dimensionless number will be described in the following sections.

The **Richardson number** characterizes the ratio between Archimedes forces and inertial forces : natural convection is negligible when $R_i < 0.1$, and forced convection is negligible when $R_i > 10$.

$$Ri = \frac{\beta g(T_w - T_0)d}{U_{ref}^2}$$

Thus, if $R_i >> 1$ the Archimedes force is greater than inertia and for $R_i = 1$ Archimedes force and inertia are equivalent.
The **Grashof number** characterizes the ratio between thermal effects and viscous effects in natural convection. It is similar to the Reynolds number by expressing the reference speed as $u_r = (\rho g \beta (T_w - T_0) d^2)/\mu$. The diameter-based Grashof number can be written as :

$$Gr_D = g\beta(T_w - T_0)d^3/\nu^2$$

.
The **Rayleigh number** is associated with buoyancy-driven flow, namely natural convection. When the Rayleigh number is below a critical value for a fluid, heat transfer occurs primarily in the form of conduction, and when it exceeds this critical value heat transfer occurs primarily in the form of convection. The Rayleigh number can be expressed relative to diameter, height or local-based, depending on the characteristical dimension of the system. The diameter-based Rayleigh number can be expressed as :

$$Ra_D = Gr_D Pr$$

These latter dimensionless number values will be defined in the following sections.

5.2.2 Forced convection : Heat transfer inside the tube

In long tubes (d/L→0) most of the transfer occurs in the thermally fully developed region. As a result, the Nusselt inside the tube with a forced convection can be approximated as a constant independent of other parameters. When the boundary at the wall is set as isothermal, Nusselt number tends to Nu_i=3.66. In case of constant heat flux to the wall, Nusselt number tends to Nu_i=4.36. In the studied configuration, the tube can be considered as long (d/L=0.025), thereby the heat transfer occurs in the fully developed region. When not in those cases of isothermal wall or constant heat flux to the wall, few correlations exist in the literature. It is then difficult to give a value to the Nusselt number. When the wall temperature is higher than the ambient temperature, the viscosity of the preheated gas near the wall is smaller than the viscosity of the center of the bulk and thereby the velocity gradient decreases as the heat transfer rate. Thereby, with great temperature gradient, the parameters must be temperature dependent, especially the heat transfer coefficients.

Sieder-Tate proposed a correlation (Sieder and Tate (1936)) of the Nusselt number for laminar flows, which is only applied in the thermal entrance region :

$$Nu_i = 1.86(RePr)^{1/3}\left(\frac{d}{L}\right)^{1/3}\left(\frac{\mu_g}{\mu_w}\right)^{1/3}$$

The thermal and hydrodynamic entrance regions are described as :

$$L_{th} \approx 0.05dRe \qquad L_{hy} \approx 0.033dRePr$$

These lengths decrease with the increase of temperature. At ambient temperature, in the studied configuration, their values are respectively 15 mm and 30 mm.
Another correlation exposed by Mills in laminar flows is independent of the tube's length and gives the average Nusselt number :

$$Nu_i = 3.66 + \frac{0.065RePr\frac{d}{L}}{1 + 0.04\left(RePr\frac{d}{L}\right)^{2/3}}$$

With the parameters evaluated at the film temperature $T^i_{film}=(T_w+T_g)/2$, the average Nusselt number evolution with temperature is represented in Fig. 5.1.

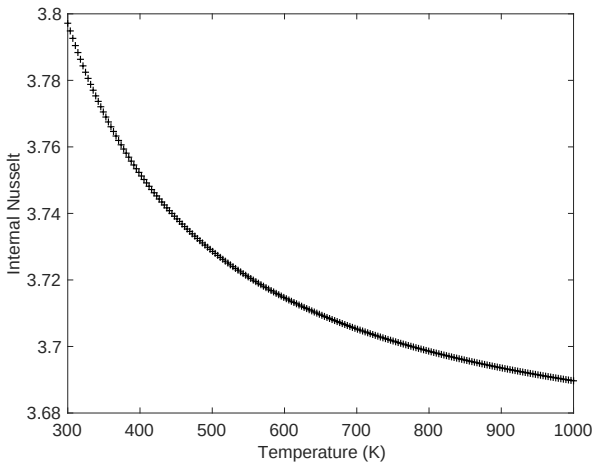

FIGURE 5.1 – *Forced convection Nusselt number evolution with temperature according to the Mills correlation for established temperature and mechanical regime.*

This figure shows that the internal Nusselt calculated from the Mills correlation varies slightly with the temperature, from 3.8 at ambient temperature to 3.7 at 1000 K. Therefore, the Nusselt is considered as constant. The value of the Nusselt number varies according to the chosen correlation, all values being around 4. In the following, the inside nusselt number is chosen according to the literature of narrow channels and set to 4.39.

5.2.3 Natural Convection on the outer tube surface

5.2.3.1 Literature review

Natural convection on horizontal and vertical cylinders is extensively treated in the literature. It can be separated in two categories, the analytical (usually early investigators) and the Nusselt correlations using computational fluid dynamics (more recent studies).

Horizontal tubes

Before 1970, early investigators (Saville and Churchill (1967); Tsubouchi and Masuda (1967)) studied experimentally and analytically the heat exchanges between a heated cylinder and ambient air by natural convection. An exhaustive list of these correlations is given in Sandra K. S. Boetcher (2014), and they mostly have the same form :

$$Nu = a(GrPr)^b$$

with a and b constants depending on the configuration. Later on, more accurate and complex Nusselt correlations were developed using several different methods. In this line, Churchill and Chu (1975) proposed a simple empirical expression of average Nusselt number over horizontal cylinder for all Rayleigh and Prandtl numbers based on Churchill, S.W. and Usagi (1972) comparing with the experimental results of Tsubouchi and Masuda (1967). Also, Kuehn and Goldstein (1976) numerically solved full Navier-Stokes and energy equations, giving the local and average Nusselt numbers for large ranges of Rayleigh and Prandtl numbers, for horizontal heated cylinder. They concluded that the boundary layer assumptions are not valid except for high Rayleigh numbers. A year later, using Blasius and Gortler series expansion method, with integral method and finite difference scheme, Merkin (1977) solved the full Navier-Stokes equations and the boundary layer flow for isothermal or constant heat flux, horizontal and vertical cylinders of elliptic cross sections. Farouk (1981) study was based on Kuehn and Goldstein (1976) model, extending it to uniform and non uniform temperatures and heat flux of the horizontal cylinder's surface. They concluded that the average Nusselt number evolves with the azimuth of the tube, as shown on Fig. 5.2, it decreases from bottom to top of the cylinder. Solving the same problem as Kuehn and Goldstein (1976), Wang et al. (1990) are the first (and only) to study the transient natural convection from a horizontal heated cylinder, using the spline fractional step method under diverse surface boundary conditions. Few years later, Saitoh et al. (1993), offered high-accuracy bench mark solutions for natural convection flow around a horizontal circular cylinder with uniform surface temperature, for Prandtl of Pr=0.7 and Rayleigh from Ra=10^3 to 10^5. They developed five methods of solution. Comparing their results to Kuehn and Goldstein (1976) and Wang et al. (1990) for azimuthal Nusselt, at different angles, they obtained similar values. Again

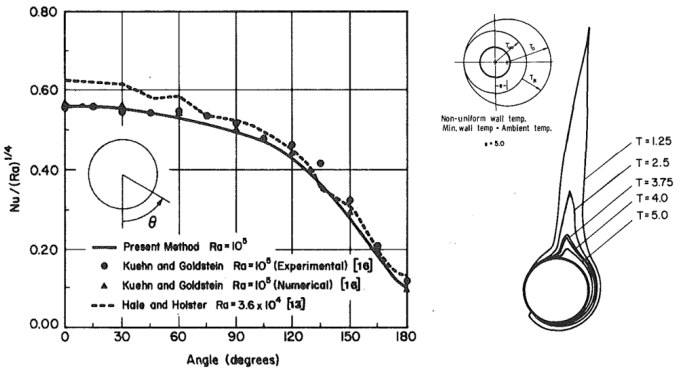

FIGURE 5.2 – *Average Nusselt number evolution with the azimuthal angle (left) and front representation of isotherms with a prescribed non uniform temperature distribution generated by an artificial temperature function* $T = \sqrt{T_o^2 - e^2 \cos^2\theta} - T_\infty + e \sin\theta$ *with* T_o*=23.85° C,* T_∞*=18.85° C and the eccentricity e=5.0.(Farouk (1981))*

the azimuthal Nusselt number was find to decrease from cylinder's bottom to top, as shown on the Fig. 5.3, with the computed streamlines and tangential velocity distribution (Left) and computed isotherms and vorticities (Right) for a Rayleigh number of Ra=10^5.

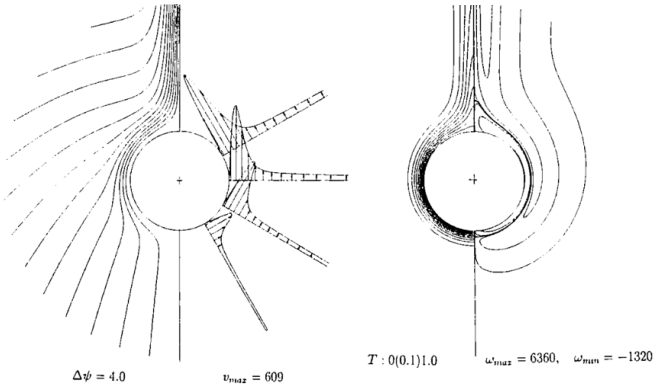

FIGURE 5.3 – *Computed streamlines and tangential velocity distribution (Left) and computed isotherms and vorticities (Right) for Ra=*10^5 *and Pr=0.7, on a horizontal heated plain tube with uniform surface temperature (Saitoh et al. (1993)).*

The tangential velocity and isotherms distribution show that the ambient air surrounding the cylinder is heated, and its density getting lower, it flows up around the cylinder. This effect is essentially a gravity-induced phenomenon. The same conclusion was drawn by Reymond et al. (2008), on a horizontal cylinder bounded with water. In fact, the average Nusselt number distribution is shown to reach a maximum at the bottom of the cylinder and, as the boundary layer developing, it decreases towards the top. At $\theta \approx 160°$ the surface heat transfer decreases sharply towards 180° (the top of the cylinder). This can be

attributed to the presence of a thermal plume which rises above the cylinder. The plume effectively insulates the cylinder from the bulk water and results in a lower heat transfer coefficient.
One of the most recent studies on the natural convection around an isothermal heated horizontal cylinders is given by Acharya and Dash (2017) using a three-dimensional numerical resolution of Navier-Stokes and energy equation. They compared the convection on solid and hollow cylinder, short and long, in air and on the ground, with and without external computation domain (thickness of the cylinder neglected). The equations are solved using multigrid CFD code Fluent. The cylinder is heated at a uniform temperature of 326 K. For solid cylinder, the Nusselt number can be considered as constant when the ratio of length over diameter (L/d) is higher than five. On the contrary for hollow cylinders, the Nusselt number does not reach constancy even at high (L/d) ratios. In the case of hollow cylinder, velocity vectors and temperature distributions are represented for different L/d values of the cylinder on Fig. 5.4.

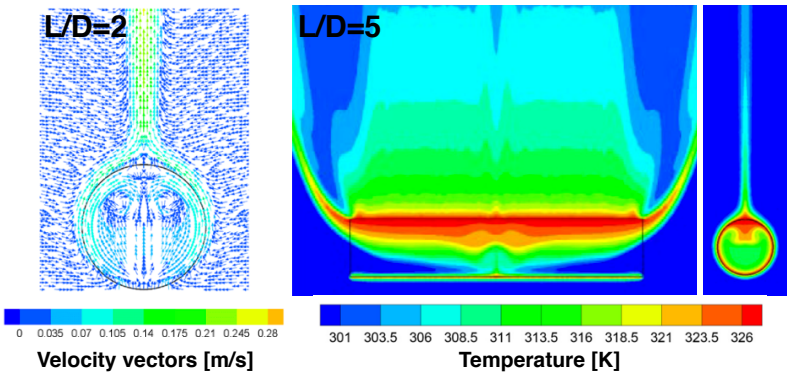

FIGURE 5.4 – *Velocity vectors (Left), and temperature distribution (Right) for* $Ra=10^6$ *and for L/d=2 and 5 respectively (Acharya and Dash (2017)).*

The temperature and velocity plume caused by natural convection is observed. The surrounding air is heated by the cylinder and flows up, creating a zone insulated from the ambient air, inside which the heat transfer coefficient is lower. Therefore, in this area, the azimuthal Nusselt decrease. Thus, the inner and outer heat losses are drawn for several Rayleigh number, as a function of the ratio (L/d) on Fig. 5.5. It clearly shows that the heat loss and therefore the Nusselt number increase with the Rayleigh number. Thus as the outer heat loss linearly increases with the ratio (L/d), the inner ratio reaches a constant value at a certain threshold point of the ratio (L/d). The value of this (L/D) threshold ratio increases with the Rayleigh number. It means that the inner heat exchange reaches a certain saturation with the air inside the cylinder for high (L/d), namely for long cylinders.

In conclusion, natural convection on a horizontal cylinder has an influence on

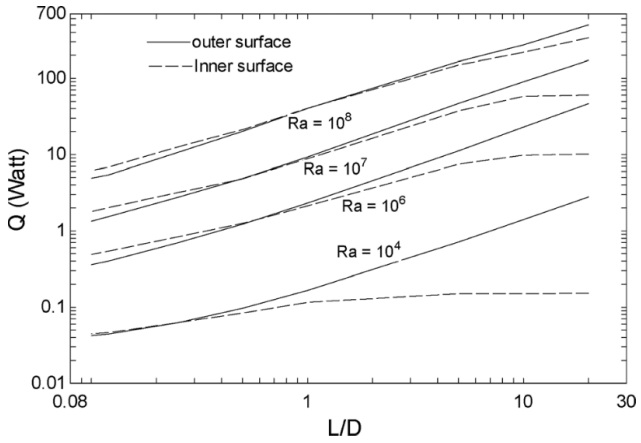

FIGURE 5.5 – *Evolution of the inner and outer heat losses Q with L/d (length/diameter) ratio for several Rayleigh numbers from* 10^4 *to* 10^8 *on a hollow horizontal heated cylinder (Acharya and Dash (2017)).*

the heat exchange coefficients and therefore on the Nusselt number. This influence depends on the experimental setup and on the temperatures used, and will be quantified in the following sections.

Vertical tubes

As previously exposed the natural convection on horizontal cylinder has been extensively studied. In parallel, several studies have been carried out for natural convection over vertical cylinders. Again an extensive list of the historical correlations on Nusselt number is exposed in Sandra K. S. Boetcher (2014). The problem is usually approximated as a vertical plate, which is only valid when the boundary layer thickness is small compared to the diameter of the cylinder. The wall being assumed as very thin, there is usually no accounting for conduction from the cylinder wall.
The first approximated solution for the laminar buoyant flow of air bathing a vertical cylinder heated with a prescribed surface temperature was developed by Sparrow EM (1956), by applying the similarity method and power series expansion. The studied problem is taken in conditions where the flat plate approximation is not suitable. In following work for the same problem and also using non-similarity method, Minkowycz and Sparrow (1974) obtained a solution for local and surface-integrated heat transfer. In Al-Arabi et al. (1991), the Nusselt correlation is carried out for cylinders with many inclination angles from horizontal to vertical. Na (1995) studied the natural convection over a thin hollow vertical cylinder with constant inner surface temperature and outer surface temperature was to be found out from the coupled conduction of the cylinder and the natural convection of the fluid over the cylinder. The overall effect of conduction of the cylinder is found to reduce the heat transfer. Chang

(2008) aimed their study at investigating the flow and heat transfer characteristics for the natural convection of a micropolar fluid flow along a vertical slender circular hollow cylinder with conduction effects, and the effect of wall conduction on local heat transfer coefficient and interfacial temperature was found. Billah et al. (2011) studied the convection in a lid driven cavity having a heated cylinder. A hollow cylinder was positioned at the center of a lid-driven cavity, and the governing equations were solved by residual finite-element method with Newton's Raphson technique. It was found that the flow field was strongly dependent on the cylinder diameter. Taking the same model as Chang (2008), Rani and Reddy (2012) investigated the conduction and natural convection over a vertical slender hollow cylinder with an isothermal heated inner surface. CFD has been used to solve the unsteady non-linear governing equations of a two dimensional laminar natural convection flow. The computations were carried out for different values of heat generation parameter $Q = Q_0 r_e^2/(c_p \mu)$ and conjugate-conduction parameter $P = (k_g/k_w)\ln(r_e/r_i)$. It is shown that for the velocity and temperature profiles, the time to reach the temporal maximum for velocity and temperature increases with the increasing values of Q and P. In the same way, the time to reach steady state increases with Q and P. Moreover, as heat generation parameter Q increases, an increase in velocity, temperature is observed. On the contrary these latter values decrease with the increase of conjugate-conduction parameter P. Finally, the average heat transfer rate decreases with the increase of P or Q.
In conclusion, natural convection on a vertical cylinder also has an influence on the heat exchange coefficients, and this impact depends on the temperature and velocity of the fluid.

5.2.4 Heat Transfer from cylinders

In natural convection the problem can be determined by seven variables : $\bar{h}$ (average heat transfer coefficient $[W \cdot m^{-2} \cdot K^{-1}]$), ρ_0 the density at ambient temperature, μ the dynamic viscosity, k the thermal conductivity $[W \cdot m^{-1} \cdot K^{-1}]$, c_p the specific heat capacity $[J \cdot kg^{-1} \cdot K^{-1}]$, L the length of the cylinder and the lead term $\rho_0 g \beta (T_w - T_0)$.
As previously presented, the natural convection on horizontal and vertical, solid or hollow cylinders has been extensively studied since it is used in many industrial engineering applications (such as, the cooling of electronic components, pipe lines, wires) but also to benchmark solutions to validate numerical simulations.

5.2.4.1 Horizontal cylinders

For horizontal cylinder configurations, most of the studies are carried out in steady state, and mainly two study cases are considered. The first case is at

small Rayleigh numbers, where the horizontal cylinder behaves like a line heat source. The second case is for larger Rayleigh numbers, where a boundary layer forms around the cylinder. However a wide dispersion in analytical, numerical, and experimental data exists among the numerous investigations. Indeed, in experimental data, this dispersion exists because of the difficulty to decouple other heat transfer mechanisms such as the conduction and the radiation, as well as the practical issues of measurement like axial heat conduction losses to the supporting structures, interference of the temperature and velocity fields by convective fluid movements, utilization of small containing chambers for the experiments, etc. In analytical and numerical methods, the dispersion is due to the hypothesis and parameters taken by the authors, like the use of the boundary layer assumption, boussinesq simplification, the domain size, the boundary conditions (solid or free) etc.
Solving methodology for natural convection problems requires the calculation of the Grashof and Prandtl numbers. According to the Grashof and the configuration, a correlation can be selected. The heat exchange coefficient and the natural convection flux can then be calculated.

Dimensionless number evaluation in the case of natural convection
In the case of a horizontal tube positioning, temperature profiles of external walls with a stabilized flame are used to quantify the dimensionless numbers linked to natural convection, especially Grashof, Prandtl and thereby Rayleigh numbers. It will allow to select a Nusselt correlation and then calculate the heat exchange coefficient h for natural convection. Using a temperature interval from T_0=300 (ambient temperature) to 1000 K (maximum temperature reached by the wall in the presented experiment), the Prandtl and Grashof corresponding intervals are calculated and give : $Pr(T) = [0.71, 0.77]$ and $Gr(T) = [2.0 \cdot 10^2, 9.3 \cdot 10^3]$ respectively at 300 K and 1000 K. Then the Rayleigh number is plotted against the temperature in fig 5.6, in order to observe its evolution.
Thereby the maximum interval of Rayleigh number in the case of this experiment is Ra=[$1.5{\cdot}10^2$,$7.0{\cdot}10^3$]. According to these results the Nusselt correlations were chosen, for a horizontal tube.

Nusselt correlations Three Nusselt correlations are selected to be the most accurate and with the widest ranges for Prandtl and Rayleigh numbers. Those correlations are then applied and compared. The correlation of Tsubouchi and Masuda (1967) is valid for all Prandtl numbers and Rayleigh in the range of $10^{-6} \leq Ra_D \leq 10^9$. The correlation can be expressed as :

$$Nu_D = 0.36 + 0.518 \left(\frac{Gr_D Pr}{[1 + (0.559/Pr)^{9/16}]^{16/9}} \right)^{1/4}$$

The correlation of Churchill and Chu (1975) is valid for all Prandtl numbers and Rayleigh in the range of $10^{-11} \leq Ra_D \leq 10^9$. The correlation can be expressed

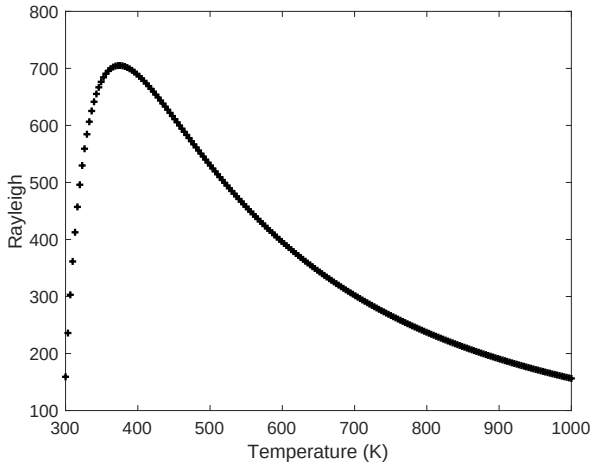

FIGURE 5.6 – *Calculated Rayleigh number evolution with temperature.*

as :

$$Nu_D^{1/2} = 0.60 + 0.387 \left(\frac{Gr_D Pr}{[1 + (0.559/Pr)^{9/16}]^{16/9}} \right)^{1/6}$$

The correlation of Kuehn and Goldstein (1976) is valid for all Prandtl and Rayleigh numbers. The correlation can be expressed as :

$$\frac{2}{Nu_D} = \ln \left[1 + \frac{2}{\left[\left(0.518 Ra_D^{1/4} \left[1 + \left(\frac{0.559}{Pr} \right)^{3/5} \right]^{-5/12} \right)^{15} + (0.1 Ra_D^{1/3})^{15} \right]^{1/15}} \right]$$

Applied to the temperature profile previously shown, with all properties being evaluated at the film temperature $T_{film}=(T_w+T_0)/2$, the Nusselt and heat exchanges are represented on Fig. 5.7.
The results show a dispersion between the three correlations results, especially between Kuehn and Goldstein (KG) and the two other correlations. In fact, the mean standard deviation is of 0.41 between the three correlations and of 0.04 between Tsubouchi Masuda (TM) and Churchill Chu (CC) correlations. The standard deviation for the heat exchange coefficient are of with 0.17 mean standard deviation between TM and CC and 1.74 between the three correlations. However, the variations of the Nusselt and thereby of the exchange coefficient, are not tremendous with a standard deviation of 0.6 along the temperature profile. Thus, even if the results show some dispersion, the tendencies between the correlations are similar.

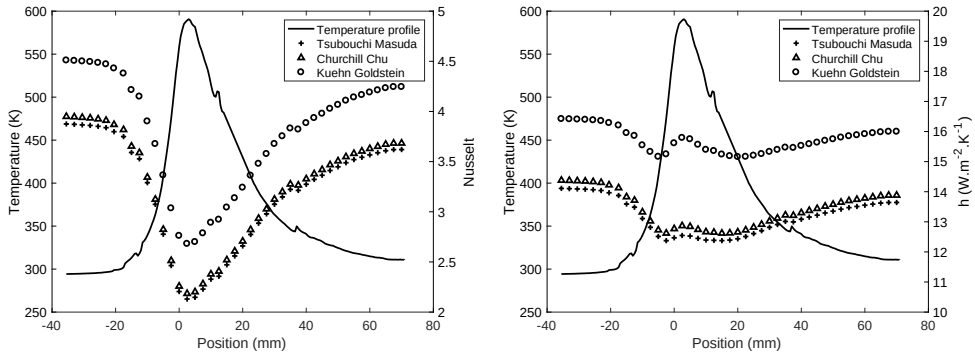

FIGURE 5.7 – *Nusselt (left) and Exchange coefficient h (right) evolution as a function of the axial coordinate of the tube, the temperature profile is represented (plain line). The Nusselt and Exchange coefficients are calculated for the three selected correlations (symbols)*

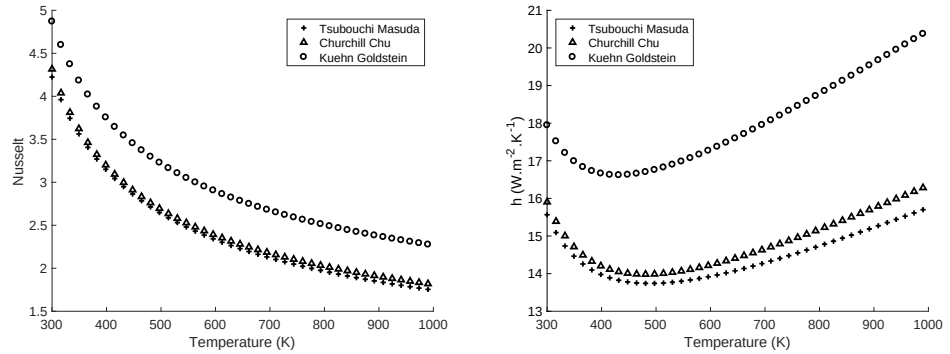

FIGURE 5.8 – *Nusselt (left) and Exchange coefficient h (right) evolution as a function of temperature, calculated for the three selected correlations (symbols)*

5.2.4.2 Vertical cylinders

For vertical cylinder configurations, the problem is usually approximated as a vertical plate, which is only valid when the boundary layer thickness is small compared to the diameter of the cylinder. When it is not the case, the literature is lacking. As for horizontal cylinders, a dispersion in analytical, numerical and experimental data exits.
The approximation as a vertical flat plate is valid if (Sandra K. S. Boetcher (2014)) :

$$\frac{D}{L} \geq \frac{35}{Gr_L^{0.25}}$$

In our configuration this criteria is not valid, the temperature of the cylinder is not constant neither is the heat flux, therefore as previously mentioned the correlation is lacking in the literature.

In conclusion to this theoretical study, the dimensionless numbers of the systems were characterized and the heat exchanges models were established to be used in the following computation.

5.3 Steady configuration of the 1-D computation

5.3.1 Resolution Methods

Several methods are used to solve the reactive flow governing equations. Two categories can be drawn out of these models.
A first category is reduced chemistry, where a limited number of reactions are used. The governing equations are formulated in finite difference form. The resulting coupled equations are solved implicitly in time using a block tridiagonal matrix inversion method, or integral method resolution using matrix inversion and a Runge-Kutta fourth order integration scheme (Huang et al. (1988)).
The second category is the complex chemistry resolution, based on codes like PREMIX, CHEMKIN or here used REGATH (Candel et al. (2011)). These codes use Newton method to solve the governing equations, with a time integration, and taking in account all elementary reactions from the principal chemical reaction.
For the resolution of the equations certain hypothesis are made. In fact, even though the flame propagation in a tube is usually two-dimensional, in the scales of this study, the diameter of the tube and the flame thickness are much smaller than the tube's length, thereby the problem can be simplified to one dimension. The resolution method adopted here is a complex chemistry computation using REGATH (Candel et al. (2011)).

5.3.2 Governing equations

The combustion governing equations are composed of reactive flow equations including the species and energy balance equations.
The resolution is one-dimensional, the equations are then projected on the x axis. The conservation equations of species, energies and mass are written as :

$$\frac{\partial \rho_{\mathrm{g}}}{\partial t} + \frac{\partial \rho_{\mathrm{g}} U}{\partial x} = 0 \tag{5.1}$$

$$\rho_{\mathrm{g}} \frac{\partial Y_k}{\partial t} + \rho_{\mathrm{g}} U \frac{\partial Y_k}{\partial x} = -\frac{\partial}{\partial x}\left[\rho_{\mathrm{g}} Y_k V_k\right] + \dot{\omega}_k W_k \tag{5.2}$$

$$\rho_{\mathrm{g}} \frac{\partial H_{\mathrm{g}}}{\partial t} + \rho_{\mathrm{g}} U \frac{\partial H_{\mathrm{g}}}{\partial x} = \frac{\partial}{\partial x}\left[k_{\mathrm{g}} \frac{\partial T_{\mathrm{g}}}{\partial x}\right] - \sum_{k=1}^{K} \rho_{\mathrm{g}} Y_k V_k H_k - \dot{Q}_{cvf_g} \tag{5.3}$$

$$\rho_{\mathrm{w}} C_{p_{\mathrm{w}}} \frac{\partial T_{\mathrm{w}}}{\partial t} + \frac{\partial}{\partial x}\left[k_{\mathrm{w}} \frac{\partial T_{\mathrm{w}}}{\partial x}\right] = \dot{Q}_{cvn} - \dot{Q}_{cvf_s} + \dot{Q}_{rad} \tag{5.4}$$

where :

$$\dot{Q}_{cvf_g} = \frac{2}{r_i} h_i(T)(T_{\mathrm{g}} - T_{\mathrm{w}})$$

the gas forced convection heat losses to the wall,

$$\dot{Q}_{cvn} = \frac{2r_e}{r_e^2 - r_i^2} h_e(T_{\mathrm{w}} - T_0)$$

the external natural convection heat losses from the wall to the ambient air,

$$\dot{Q}_{rad} = \frac{2r_e}{r_e^2 - r_i^2} \epsilon_S(T)\sigma(T_{\mathrm{w}}^4 - T_0^4)$$

the radiative heat losses from the wall to the ambient air, and

$$\dot{Q}_{cvf_s} = \frac{2r_i}{r_e^2 - r_i^2} h_i(T)(T_{\mathrm{g}} - T_{\mathrm{w}})$$

the forced convection heat losses from the wall to the inner gas.

with U the flow velocity, Y_k the species mass fractions, W_k the molecular mass of the k^{th} species, $\dot{\omega}_k$ the molar production rate by chemical reaction of the k^{th} species by volume unity, H the enthalpy and V_k the diffusion speed of the k^{th} species.

5.3.2.1 Chemical kinetics model

The source term $\dot{\omega}_k$ in species conservation described by Eq. 5.2 is calculated by considering detailed chemical reactions. In a chemical kinetics model, with a system composed by $\mathrm{N_{sp}}$ species, reacting in a specific mechanism of I elementary reactions, can be presented as :

$$\sum_{k=1}^{N_{\mathrm{sp}}} \nu'_{\mathrm{ki}} \chi_k \rightarrow \sum_{k=1}^{N_{\mathrm{sp}}} \nu''_{\mathrm{ki}} \chi_k \qquad \text{for i} = 1...\mathrm{I} \tag{5.5}$$

where χ_k is the chemical symbol of the k^{th} species, ν'_{ki} and ν''_{ki} the stoichiometric coefficients of the k^{th} species appearing in the i^{th} reaction. These coefficients verify the I mass conservation relations :

$$\sum_{k=1}^{N_{\mathrm{sp}}} \nu'_{\mathrm{ki}} \mathrm{W}_k = \sum_{k=1}^{N_{\mathrm{sp}}} \nu''_{\mathrm{ki}} \mathrm{W}_k \qquad \text{for i} = 1...\mathrm{I} \tag{5.6}$$

where W_k is the molar mass of the k^{th} species. Thus, the k^{th} species molar production rate is determined by the sum of the reaction rates of all i reactions :

$$\dot{\omega}^c = \sum_{i=1}^{I} (\nu''_{ki} - \nu'_{ki}) Q_i \tag{5.7}$$

with Q_i the rate of progress of the i^{th} reaction :

$$Q_i = K_{fi} \prod_{k=1}^{N_{sp}} [X_k]^{\nu'_{ki}} - K_{ri} \prod_{k=1}^{N_{sp}} [X_k]^{\nu''_{ki}}$$

where $[X_k]$ is the molar concentration of the k^{th} species. Q_i is the difference between the forward and reverse reaction rates, which i^{th} reaction speed constants K_{fi} and K_{ri} respectively, following the empirical Arrhenius law :

$$K_{fi} = A_{fi} T_g^{\beta_i} exp\left(-\frac{E_i}{RT_g}\right) \tag{5.8}$$

where A_{fi} is the pre-exponential factor, β_i the temperature exponent, E_i the activation energy, and R the universal gas constant.
The reverse speed reaction constant K_{ri} is given by the ratio of the forward reaction speed constant on the equilibrium constant.

5.3.2.2 Transport properties

The diffusion speeds of species V_k are solutions of a linear system exposed in Hirchfelder and al.(1954) and Kuo (1986). This system is very costly to invert, and thereby an approximation of the diffusion of the k^{th} species is given by :

$$V_k = -\frac{D_k W_k}{Y_k W} \frac{\partial X_k}{\partial x} + V^c \tag{5.9}$$

Where D_k is the k^{th} species diffusion coefficient in the mixture. Due to this approximation on the diffusion coefficient, a correction velocity V^c is added here in order to guarantee the mass conservation so that :

$$\sum_{k=1}^{Nsp} Y_k V_k = 0$$

with

$$V^c = \sum_{k=1}^{Nsp} D_k \frac{W_k}{W} \frac{\partial X_k}{\partial x} \tag{5.10}$$

5.3.2.3 Temperature dependent properties of quartz

The quartz thermodynamical properties, namely thermal conductivity, heat capacity and emissivity, are temperature dependent. Some evolutions of these parameters being notable, it is of importance to take them into account. The density is considered as constant with a value of 2100 kg/m^3. Experimental data of heat capacity and thermal conductivity evolutions with temperature are available. The quartz thermal conductivity evolutions data are given by Heraeus (). These data and a polynomial fit are represented in Fig. 5.9. The quartz conductivity dependance on temperature is given by Rodrigues et al. (2018) :

$$\frac{k_w(T)}{k_w^0} = a_0 - a_1(\frac{T}{T_0}) + a_2(\frac{T}{T_0})^2 - a_3(\frac{T}{T_0})^3 \tag{5.11}$$

with : a_0=0.97980, a_1=0.10063, a_2=0.13677, a_3=0.011744, T_0=293 K and k^0=k_w(293 K)=1.38 W/(m·K).

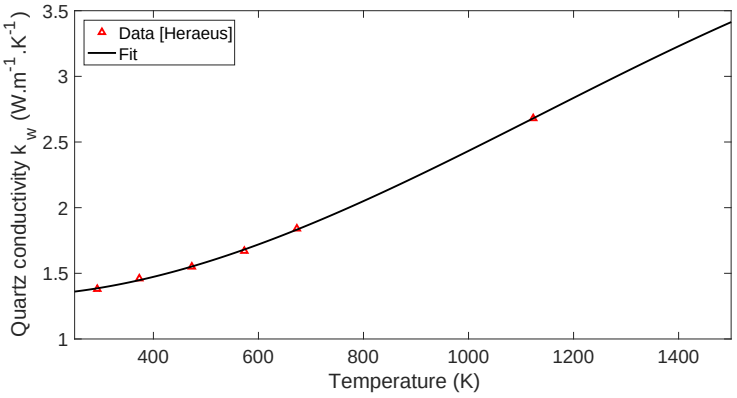

FIGURE 5.9 – *Quartz thermal conductivity fitted from the literature data taken from Heraeus ().*

Heat capacity measurements were performed by Sosman (1927), and represented in Fig. 5.10, with a polynomial fit. The evolution of heat capacity with temperature is given by Rodrigues (2018) :

$$\begin{aligned} c_{p_S}(T) = -b_0 + b_1\left(\frac{T}{T_0}\right) - b_2\left(\frac{T}{T_0}\right)^2 + b_3\left(\frac{T}{T_0}\right)^3 \\ -b_4\left(\frac{T}{T_0}\right)^4 + b_5\left(\frac{T}{T_0}\right)^5 - b_6\left(\frac{T}{T_0}\right)^6 \end{aligned} \tag{5.12}$$

with : b_0=62.8778, b_1=1148.41, b_2=468.192, b_3=119.116, b_4=21.6623, b_5=2.5091, b_6=0.131465 and T_0=293 K.

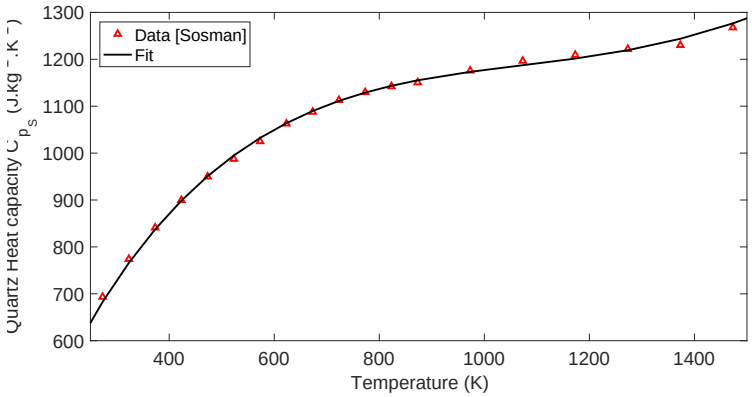

FIGURE 5.10 – *Quartz heat capacity fitted from the literature (Sosman (1927))*

The quartz emissivity is also temperature dependent and can be linearly approximated, with values of 0.95 at 293 K and 0.75 at 1800 K, giving :

$$\epsilon_S(T) = -7535 \cdot T + 2.21 \cdot 10^6 \tag{5.13}$$

5.3.2.4 Temperature dependent properties of air

The external air thermodynamic properties are computed from polynomial fits ($c_{p_{air}}$,k_{air}, μ_{air}). The air density ρ_{air}(T) is computed through the ideal gas law. The pressure is 1 bar.

5.3.2.5 Heat transfer analytic : Nusselt and heat exchange coefficients

The heat exchanges between the walls and the inner and outer gases are dependent on the convection heat exchanges coefficients h_e and h_i. They are used to calculate the heat flux between the wall and the fluid. Usually these coefficients are averaged over the heat transfer surface, however in cases of important temperature gradient, this approximation is not always relevant.
On the outer surface of the tube, the natural convection imposes a low value of the exchange coefficient, and as a result a constant value is fixed at :

$$h_e = 14 \text{ W} \cdot \text{m}^{-2} \cdot \ K^{-1} \tag{5.14}$$

Inside the tube the heat transfers with the wall are due to forced convection. The internal heat coefficient can be written as :

$$h_i(T) = \frac{Nu_i k_{\mathrm{g}}(T)}{2r_i} \tag{5.15}$$

The internal Nusselt is taken as constant, equal to 4.39 calculated at ambient temperature for forced convection. The thermal conductivity of the gas, $k_g(T)$ is calculated at each iteration, and thereby as is the internal coefficient, represented in Fig. 5.11 as a function of the axial tube coordinate, with a stabilized flame front inside the tube at the 0 mm coordinate.

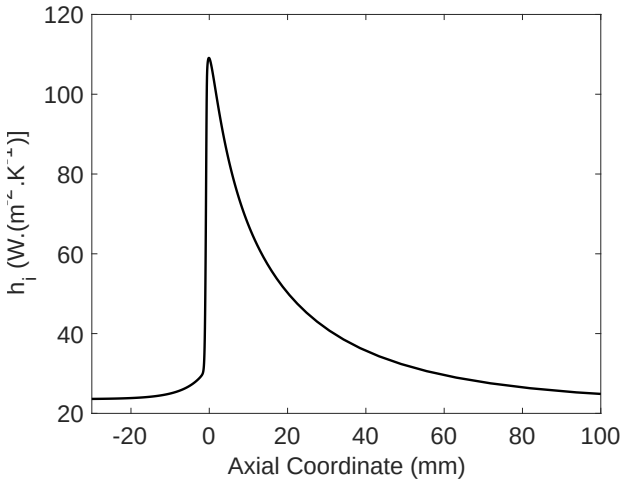

FIGURE 5.11 – *Internal heat exchange coefficient evolution with a flame front stabilized at the coordinate $x = 0$ mm.*

The range of evolution of the internal heat coefficient is in agree with the literature for forced internal convection. Its observed important variation with temperature makes it important to be taken it into consideration in the present simulation.

5.3.3 Time integration in steady computation

The steady state solution of the equations system is the result of a transitory physical phenomenon. Solving the transitory equations with the Newton method is very reliable but slow, with usually convergence problems. Another possibility of a premixed flame modelisation is to use transitory computation, avoiding convergence problems, but the computation is less efficient.
REGATH combines both methods : during the computation, first Newton steps are used, and if convergence issues occur, time steps are used instead. It is a mean to move from a trial solution that doesn't belong to the Newton convergence domain to a solution belonging to it. The time step and number of steps are determined by the user.

5.3.3.1 Newton method

Problem definition All steady ordinary differential equations system can be transformed into a first order ordinary differential equation system. First, a

solution S is defined depending on the equations variables (Temperature, mass fraction, mass etc...)

$$S(T_{\mathrm{g}}, Y_1, Y_2, ..., Y_{N_{SP}}, \dot{m}, T_{\mathrm{w}})$$

The equations system can be written as (Versaevel (1996)) :

$$\frac{\mathrm{d}S_j}{\mathrm{d}x} = g_j(S_1, ..., S_M, x) \quad for\ j = 1, M$$

with S_j and g_j real values functions. For each j equation, the value of S_j in $x = 0$ or in $x = 1$ is fixed at γ_j.

Discretisation A mesh is introduced on the tube's length : $M = (x_1 < ... < x_i < ... < x_N)$
With N the number of points in the mesh, fixed at 1020 in the simulation.
For the j equations where the value of S_j in $x = a$ is known, the functions associated to the equations are defined and the limit of these function toward zero is studied with the convergence of the solutions. The system established is :

$$\begin{cases} f_{1j} = S_j(x_1) - \gamma_j = 0 \\ f_{ij} = \frac{S_j(x_i) - S_j(x_{i-1})}{x_i - x_{i-1}} - g_j(S_1(x_i), ..., S_M(x_i), x_u) = 0 \ i = 2, N \end{cases} \tag{5.16}$$

The discrete problem can be written as :

$$F(S) = 0$$

with $F = (f_{ij})$ and $S = (S_j(x_i))$

Resolution The resolution is processed using Newton method :

$$S^{n+1} = S^n - \left(\frac{\partial F}{\partial S}\right)^{-1} F(S^n)$$

With S^n the solution at the n iteration.
The calculation of the Jacobian matrix $J = \left(\frac{\partial F}{\partial S}\right)$ and its inversion are costly in computation time. These operations can be fasten if the matrix F is a tridiagonal block matrix. This structure is obtained is the relations written at the i node only depend on the values of S_j at the row $i - 1$ and $i + 1$.

5.3.3.2 Boundary conditions

The boundary conditions of the equation system are defined as :
Left boundary conditions

$$x \to -\infty : T_{\mathrm{g}} = T_0, Y_k = Y_{k_0}, \dot{m} = \rho_0 U_0 \tag{5.17}$$

$$x \to -\infty : T_{\mathrm{w}} = T_0 \tag{5.18}$$

Right boundary conditions

$$x \to +\infty : \frac{\mathrm{d}T_{\mathrm{g}}}{\mathrm{d}x} = 0, \frac{\mathrm{d}Y_k}{\mathrm{d}x} = 0 \tag{5.19}$$

$$x \to +\infty : \frac{\mathrm{d}T_{\mathrm{w}}}{\mathrm{d}x} = 0 \tag{5.20}$$

5.3.4 Fuel and kinetic scheme choice

The kinetic scheme applied is the GRI 3.0 (Smith et al. (2011)) with methane fuel and 53 species.

5.3.5 Code validation with the added solid equation

In the presented work, the wall domain is implemented in REGATH, with the wall heat exchanges to/from the ambient air and from the combustion gas. By changing the conditions to the walls, especially the heat exchange coefficients and the initial conditions, several cases can be tested to validate the behavior of the code after the addition of the wall resolution. The gas and wall temperature profiles are plotted as a function of the axial distance of the tube in Fig. 5.12, with initial conditions of adiabatic wall. The obtained profiles are similar, except for the maximum temperature which is higher for gas than for the wall due to the heat losses to the external air. Thus the wall temperature starts to increase upstream from the flame front due to axial conduction in the walls.
Three test cases are considered to evaluate the code behavior : the case of adiabatic walls, the case of high external convection heat coefficient to reproduce a semi-infinite wall and finally the case of a constant initial wall temperature equal to the ambient temperature. In all those tested cases, the initial wall and gas temperature profiles are considered with adiabatic walls.

Case of adiabatic walls

In order to validate the behavior of the code with heat losses, the case of adiabatic wall is reproduced by imposing $h_e = 0\ W/(m^2 \cdot K^1)$. The initial and final temperature profiles are represented in Fig. 5.13. It can be seen that computed gas and wall temperatures are similar to the initial conditions. This is a first validation of the expected results.

Case of semi infinite wall

The external heat exchange coefficient is then increased to a value corresponding to forced convection equal to $h_e = 100\ W/(m^2 \cdot K^1)$, to reproduce a semi-infinite wall. The resulting temperature profiles are represented in Fig. 5.14.

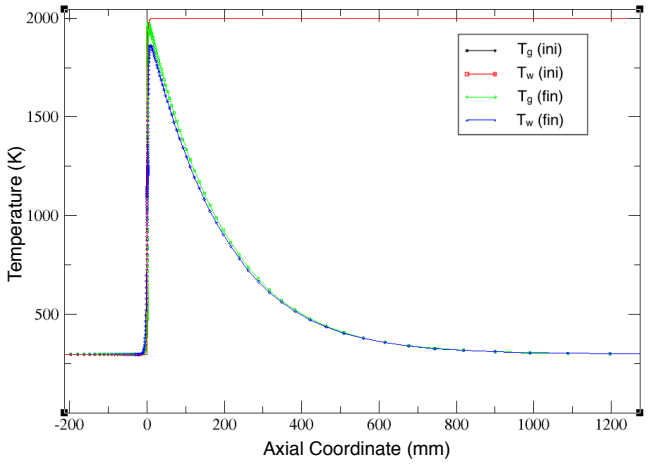

FIGURE 5.12 – *Wall and gas initial with adiabatic walls (resp. red and black curves) and finals with solved wall (resp. blue and green curves) according to the axial distance (mm) for external heat loss coefficient* $h_e = 7\ W/(m^2 \cdot K^1)$ *and internal* $h_i = 250\ W/(m^2 \cdot K^1)$.

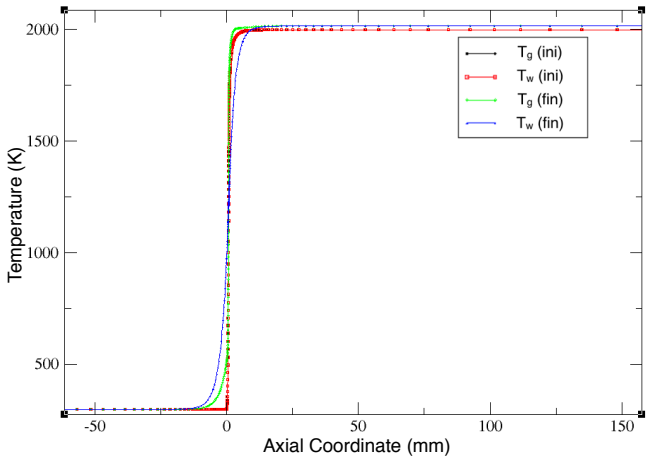

FIGURE 5.13 – *Solution with adiabatic walls : wall and gas initial (resp. red and black curves) and finals (resp. blue and green curves) according to the axial distance (mm) for external heat loss coefficient* $h_e = 0\ W/(m^2 \cdot K^1)$ *and internal* $h_i = W/(m^2 \cdot K^1)$.

The maximum of temperature reached by the wall is greatly reduced, close to the half of gas maximum temperature. Thus, the gas maximum temperature reached is slightly lower than in the basic case previously observed. Furthermore, the cooling slopes are higher leading to a reduced cooling area. These observations attest an expected evolution of the temperature profiles while moving to a semi-infinite solid and thereby represent another code validation.

Transitory regime with temperature dependent thermal losses

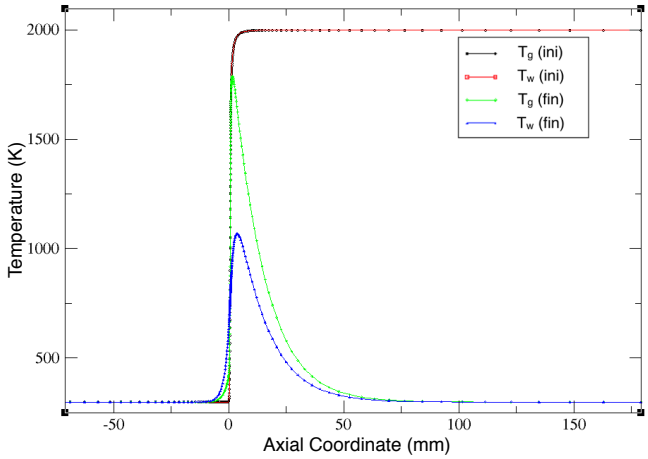

FIGURE 5.14 – *Solution with semi-infinite walls : wall and gas initial with adiabatic wall (resp. red and black curves) and finals with solved wall (resp. blue and green curves) according to the axial distance (mm) for external heat loss coefficient* $h_e = 100\ W/(m^2 \cdot K^1)$ *and internal* $h_i = 250\ W/(m^2 \cdot K^1)$

The code is tested in transitory regime with an initial wall temperature imposed at T_w=300 K. By computing several iterations until reaching convergence, the wall temperature profile evolves to reproduce the previously observed established profile, represented in Fig. 5.15.

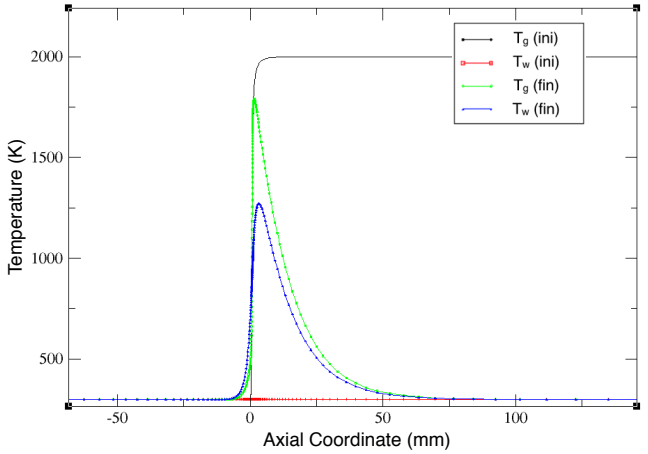

FIGURE 5.15 – *Wall and gas initial with adiabatic wall (resp. red and black curves) and finals with solved wall (resp. blue and green curves) according to the axial distance (mm) by imposing a constant initial temperature to the wall at* T_w*=300 K and then by reaching convergence for external heat loss coefficient* $h_{ext} = 50\ W/(m^2 \cdot K^1)$ *and internal* $h_{int} = 250\ W/(m^2 \cdot K^1)$*. The independence of the wall temperature to the initial conditions is hereby tested.*

The wall temperature is then independent from the initial conditions.
These three tests reproduce the expected evolutions of the temperature profiles according to the boundary conditions imposed, an therefore the code is validated. The results in steady regime are exposed in the following section.

5.3.6 Computation results in steady regime configuration

The resolution of the one-dimensional governing equations, taking into account the temperature evolutions of the quartz parameters, as well as the heat exchange coefficients gives gas and wall temperature profiles of the simulated flame. The gas (plain lines) and wall (dashed lines) temperature profiles in steady configuration are represented in Fig. 5.16, for equivalence ratios from ϕ=0.75 to 0.95. The flame front is located at $x = 0$.

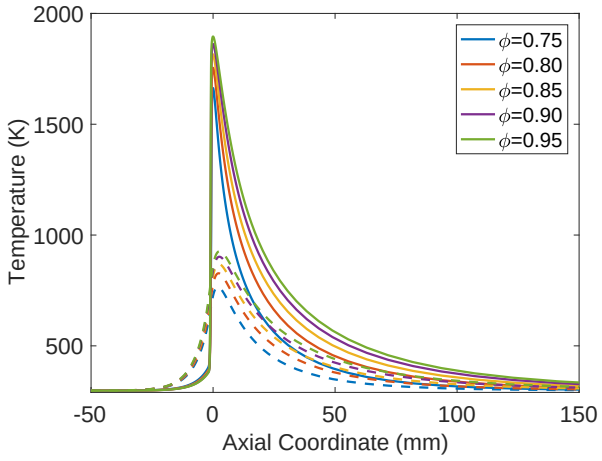

FIGURE 5.16 – *Gas (plain lines) and wall (dashed lines) temperature profiles for equivalence ratios from 0.75 to 0.95 with a steady flame front.*

It can be seen that for all equivalence ratios, the wall is preheated upstream from the flame front due to axial conduction in the wall. For both gas and wall temperature profiles, the maximum temperature reached increases with the equivalence ratio. The cooling area also increases with the equivalence ratio. In fact, the lower the maximum temperature is the faster the gas and wall cool down.
The evolution of the outer natural convection (Φ_{cvn}), inner forced convection (Φ_{cvf}) and radiation (Φ_{rad}) heat fluxes with a flame stabilized at $x = 0$ are depicted in Fig. 5.17 for equivalence ratios from ϕ=0.75 to 0.95.
Since the power of the flame increases with the equivalence ratio, the heat fluxes follow the same tendency. The natural and forced convection (respectively blue and black curves) follow a maximum increase of the same order respectively 35% and 30% between the operating points of equivalence ratio ϕ=0.75 and ϕ=0.95.

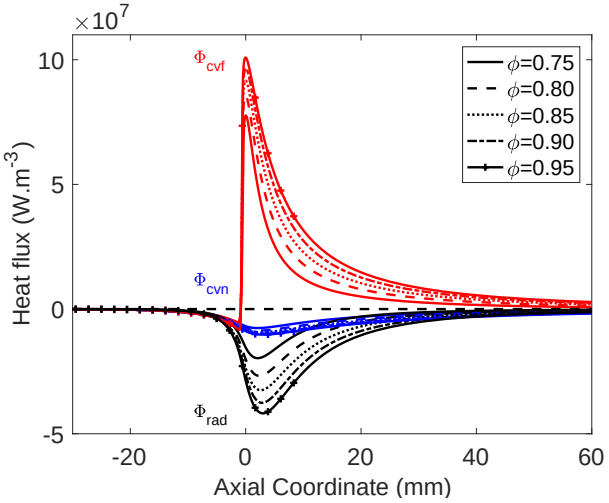

FIGURE 5.17 – *Evolution of the outer natural convection (blue curves Φ_{cvn}), inner forced convection (red curves Φ_{cvf}) and quartz radiation (black curves Φ_{rad}) heat fluxes with a stabilized flame at $x = 0$ for equivalence ratios from ϕ=0.75 to 0.95.*

The radiation increase is more important : 112% of increase between the two operating points. When computing the integral of the positive forced convection flux, the power of the flame is estimated. Then by comparing the integration of

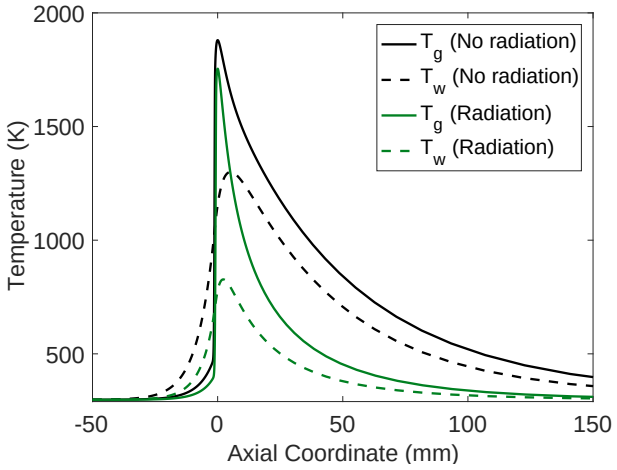

FIGURE 5.18 – *Gas and wall temperature profiles with (green) and without (black) quartz radiation in a steady regime at an equivalence ratio of ϕ=0.8.*

the radiation and natural convection, it is shown that 96% of the flame power is transmitted to the ambient air through natural convection and radiation for an equivalence ratio of ϕ=0.8. The preheating of the fresh gas represent 4% of the flame power. As the equivalence ratio increases, the percentage of flame power transmitted to the external air increases. These values clearly show an

overestimation of the external heat fluxes due to modelisation inaccuracies. Thus, it is to be noted that the quartz radiation has a non negligible impact on heat exchanges, and this influence increases with the equivalence ratio. In order to illustrate specifically this impact, Fig. 5.18 represents the gas and wall temperature profiles with and without accounting for the quartz radiation in the solved equations, for a flame at operating point ϕ=0.8. The results show a great drop in wall maximum temperature and on the cooling area of the gas temperature. Thereby, the quartz radiation must be taken into account as it has a great influence on the heat exchanges.

5.3.7 Wall temperature comparison between numerical computation and experimental measurements

A comparison between the thermocouple measured temperatures and the computed wall temperatures is represented in Fig. 5.19 for equivalence ratios from 0.75 to 0.95. The wall temperature profiles are centered at the zero axial coordinate.

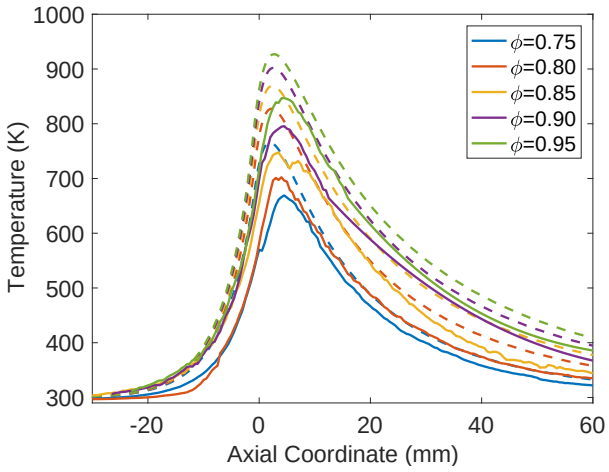

FIGURE 5.19 – *Experimental (plain lines) and Numerical (dashed lines) wall temperature profiles for equivalence ratios from ϕ=0.75 to 0.95 in steady regime.*

The temperature profiles shapes between numerical and experiment measurements show a good agreement. The temperatures are of the same order of magnitude, however the maximum of temperature reached by the simulation is higher than that of the experimental measurements. Indeed, first it was shown in the experimental section (chapitre 2) that the thermocouple measurements underestimate the maximum of temperature. Then, since the resolution is one dimensional, the computed temperature does not take into account the radial conduction, meaning that the temperature represented is not the external surface wall temperature but a radial wall temperature average.

The experimental (plain line) and numerical one dimensional (dashed line) operating points are represented in Fig. 5.20 by plotting the flow velocity as a function of the equivalence ratio of the obtained steady flames.

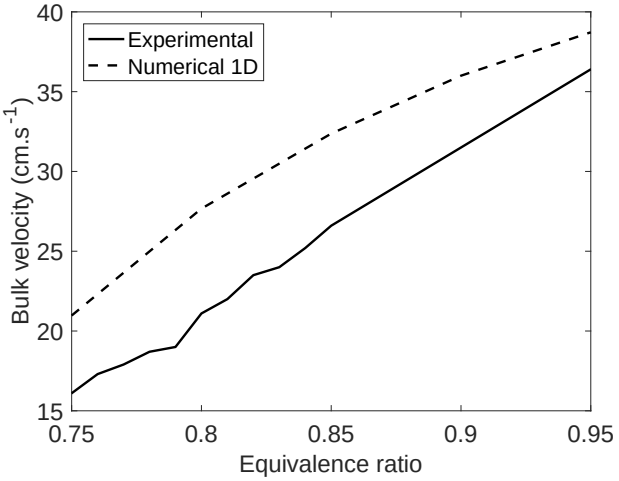

FIGURE 5.20 – *Experimental (plain lines) and Numerical (dashed lines) operating points for equivalence ratios from ϕ=0.75 to 0.95 in steady regime.*

It can be seen that the steady bulk velocity is higher for the one-dimensional numerical computation. However the order of magnitude of bulk velocity are similar. This discrepancy of approximately 5 cm·s^{-1} can be explained by the difference of the velocity profile which is an established Poiseuille in the experimental case while in the one-dimensional computation the speed is a uniform profile.

5.4 Conclusion

This chapter presents a theoretical analysis and literature review on forced and natural convection over heated cylinders, in vertical and horizontal position. A steady one-dimensional complex chemistry computation is exposed. The resolution methods as well as the solved governing equations are presented. The computation of a wall domain is added to the existing reactive mixture resolution, as well as the coupling terms of heat exchanges between the wall, the gas, and the external ambient air. The heat exchanges implemented between the external air and the wall are the natural convection and the quartz radiation fluxes. The conduction in the wall is not computed since the resolution is one-dimensional. Then, the heat exchanges between the reactive mixture and the wall is forced convection. The coefficients implemented in the computation are based on the theoretical analysis carried out in the first part of the chapter. A code validation is processed after these additions, resulting in a logical behavior

of the code to several critical cases studied such as adiabatic walls. The results of the code, reproducing a steady flame interactions with walls in ambient air are in good agreement with the experiments. Thus the flux analysis allows to better understand the thermal establishment of the flame, and to compare the involvement of the different heat exchanges in the stabilization. By that, the importance of quartz radiation on wall temperature is established. Finally, without giving quantitative data, the one-dimensional computation helps to understand the implications of the different phenomena in the flame stabilization or propagation.

Chapitre 6

Origin of the flame asymmetry

Contents

6.1 Extended abstract

The flame in steady regime is experimentally found to be asymmetric in both horizontal and vertical tube positioning for tubes inner diameters greater than 4 mm. Different mechanisms may generate this, that depends on the tube orientation. First a comparison of horizontal and vertical tube positioning is exposed to highlight the influence of gravity. On the horizontal position, two effects can influence the flame orientation : (1) the gravity affecting the external flow around the tube creating non-symmetric heat transfer between top and bottom walls, (2) the gravity affecting the internal flow in the vicinity of the curved flame where large density gradients are observed. For different equivalence ratios, flames are observed when propagating with isothermal or fully coupled

walls in order to discriminate thermal from gravity effects. By coupling experimental observation and processing of Direct Numerical Simulations performed at CORIA in the framework of the MAPEE ANR project, the mechanism leading to the slanted flame is identified in the horizontal configuration. Gravity creates vorticity in the internal flow that breaks the symmetry of the reaction zone. This is then amplified by external thermal effect that lead to the flame observed experimentally, oriented towards the lower wall of the tube. The case of the vertical orientation remains unclear. Presumably, we are facing a case of bifurcation where the steady position of the flame is slanted whereas all other parameters of the system feature axisymmetry.

6.2 Experimental description of the flame asymmetry

6.2.1 Effect of the positioning of the tube (horizontal or vertical) on a stable flame

In the steady regime characterization chapter, a difference in bulk velocities between vertical and horizontal operating points for the basic configuration is observed. Indeed, as the equivalence ratio increases, vertical stabilization is reached at lower bulk velocities than in horizontal. Thereby, at high equivalence ratio the flame needs more power to maintain itself in a horizontal tube. However, the heat losses remain of the same order in both tube positioning. The aim of this section is then to compare the impact of the tube position on the flame stabilization, by looking at the flame topology and at the wall temperature profiles.

6.2.1.1 Flame topology

First, a comparison is made on the flame topology for both tube positions and for the three different tube's dimensions (configurations A, B and C previously introduced). In chapitre 4, it was established that for the configuration (B) (d_i=5 mm), the bulk velocity of steady operating points differs from horizontal to vertical. However, in this configuration, between the equivalence ratio 0.76 and 0.78 the bulk velocities are very close. To remove possible hydrodynamic and power effects, the flame topologies between the two tube positioning are compared within this range of operating points. As a result, two flames at equivalence ratio of ϕ=0.78 are represented in Fig. 6.1 for vertical (left) and horizontal (right) tube positioning. Throughout this section, the images of vertical tube flames are rotated of 90° in the indirect direction when put in parallel to horizontal tube flames, for a better comparison of the images. Thus, the orientations of the flames are assessed between the flame's axis and the orthogonal to the tube axis : angles are considered as angle to vertical in the horizontal tube and angle to horizontal in the vertical tube.
The fitted ellipses highlighted in red dashed lines on the figure allow to ob-

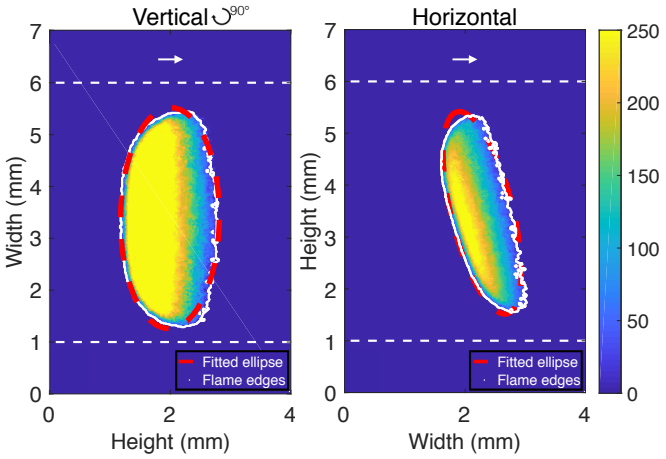

FIGURE 6.1 – *Flame images (false color) for vertical (left) and horizontal (right) tube position, at equivalence ratio ϕ=0.78. The vertical flame image is rotated of 90° in the indirect direction for the images to be comparable. The red dashed lines represent the fitted ellipse and the white dotted line is the flame edge. The flow direction is marked by a white arrow.*

tain the eccentricity and orientation of the flame. In Fig. 6.1, the comparison between both flames reveals that the horizontal tube flame is flat and tilted while the vertical tube flame is thicker and straight. Indeed, the eccentricity in the horizontal case is 30% greater than in the vertical case, meaning that the flame is more circular in vertical. Thus, in the vertical tube, the flame's angle to horizontal is 2.5°, whereas the flame makes a 12° angle to the vertical in the horizontal tube, which is almost five times higher. This comparison at same bulk velocity for two stable flames and between vertical and horizontal tube position highlights a great difference in thermal and gravitational effects on the flame stabilization.

Once this assessment made, to compare more thoroughly the influence of the positioning, the 4 mm inner diameter (A) configuration is chosen, for two reasons. First, it is the configuration where the heat exchanges have a maximum influence on the flame stability, thereby the observations would be transposable in the other tube dimensions. The second reason is that the horizontal and vertical tube operating points are very close in bulk velocity and this for a larger range (ϕ=0.85 to 0.99) than in the (B) configuration (ϕ=0.76 to 0.78). It frees us from the possible speed effects on flame deformation. Therefore, CH* chemiluminescence flame images for three equivalence ratio ϕ=0.85, 0.90 and 0.95 in horizontal (top) and vertical (bottom) tube position are represented in Fig. 6.5.

In horizontal tube position, the flame follows a previously described evolution from a low tilt angle convex meniscus to a flat slant-shaped flame. However, in vertical tube position, the flame's deformation with the increase of equivalence ratio is not that significant. Indeed, the flame slightly flattens and thereby its

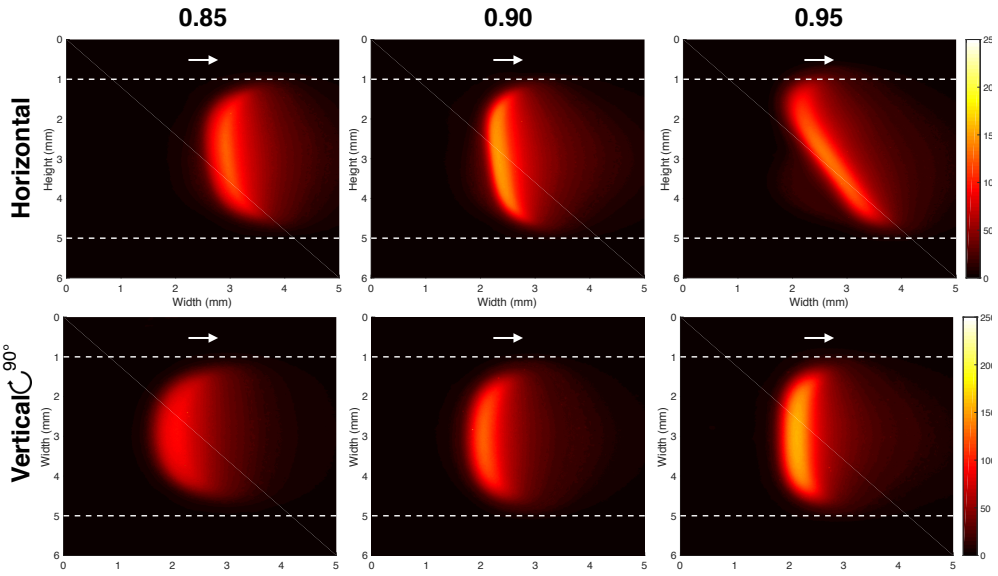

FIGURE 6.2 – *CH* chemiluminescence flame images (false color) of (A) configuration (d_i=4 mm) for horizontal (top) and vertical (bottom) tube positioning. The flow goes from left to right (white arrows). The white dashed line represents the inner walls limits.*

height increases, but no tilt evolution is remarkable.
Yet, for high equivalence ratio and for diameters equal or higher to the (B) configuration (d_i=5 mm), a tilt angle is also observed on vertical tube flame. The CH* chemiluminescence image of a flame at equivalence ratio ϕ=0.90, (C) configuration (d_i=7 mm), represented in Fig. 6.3, illustrates the profile of a tilted flame in vertical tube position. Contrary to the horizontal positioning where the tilt angle is constant and always oriented hump towards the fresh gases, in vertical, the tilted flame rotates inside the tube, and thereby the flame's orientation varies in time.

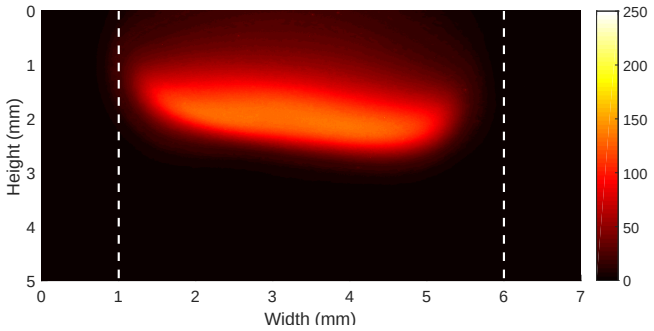

FIGURE 6.3 – *Tilted flame at equivalence ratio ϕ=0.90, in the vertical (B) configuration. The dashed white lines represent the inner wall limits.*

Using the orientation of flame's profile, the evolution of the tilt angle with the increase of equivalence ratio is drawn in Fig. 6.4(a) for three tube diameter (A), (B) and (C) configurations in vertical tube. Thus, the comparison between horizontal and vertical tube positioning for the (B) configuration is shown in Fig. 6.4(b).

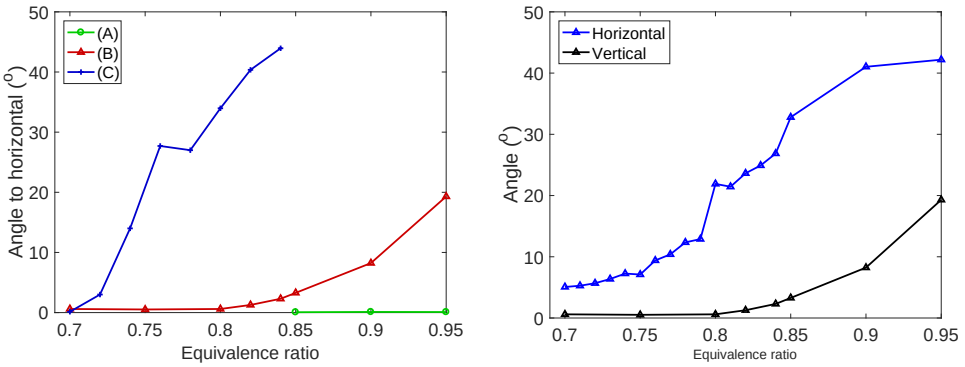

(a) (A),(B) and (C) in vertical tube

(b) (B) in horizontal and vertical tube

FIGURE 6.4 – *Evolution of the flame angle to horizontal with the increase of equivalence ratio for the three configurations (A), (B) and (C) in vertical tube positioning (left), and evolution of the angle in (B) configuration for horizontal and vertical tube positioning (right)*

In the dimensions of (A) configuration, the angle to horizontal is constant and close to zero for the tested equivalence ratios, meaning that the flame is nearly horizontal. In both (B) and (C) configurations the angle evolves with the increase of equivalence ratio. In (C) configuration, the angle increases drastically at equivalence ratio 0.7, starting from zero. In the (B) configuration the angle remains close to zero up to the equivalence ratio 0.8 where it starts increasing. The slope is greater in (C) than in (B) configuration, which is consistant with a higher slope in the power increase of the flame. The flame tilt angle is then linked to the amplitude of flame power increase.
However, when comparing the horizontal to vertical flames angle evolution with equivalence ratio in Fig. 6.4(b), the vertical flame angle remains lower than in horizontal, even though the flames have equivalent powers.
The question is, in what situation can a flame be asymmetrical in symmetric geometries. This issue was rarely investigated but three major articles of the literature Lee and Tsai (1994),Tsai (2008)and Fernández-Galisteo and Kurdyumov (2018) numerically studied the impact of gravity on flame in narrow channels. The results were presented in the introductive chapitre 1. In those study, it was established that for gravity parallel to burner axis (channel or tube) and opposite to flow direction, the buoyancy forces push the heated gas of the reaction area away from the fresh gas, in the opposite direction of the gravity, leading to an increase in the flame area with the increase of g, and re-

sulting in the increase of flame propagation speed. Thus, Tsai (2008) observed a break in flame symmetry when varying the Froude number and depending on the channel dimensions. In fact, mushroom shaped flames were found in small conducts and asymmetrical slant-shaped in larger ducts. In interim dimensions, both mushroom and slant-shaped flames were observed, and the transition occurs at a certain Froude number. This behavior is similar to the one previously observed when increasing equivalence ratio leads to a transition from mushroom to slant-shaped flames, which occurs at a certain value of equivalence ratio, and depends on the tube diameter. In fact, by increasing the equivalence ratio and/or the tube diameter, the power of the flame rises (higher temperature) and the effects of gravity on the flame are therefore more significant. When the burned gas are positioned above the unburned gas, the asymmetry of the flame is attributed to Darrieus-Landau instabilities. However Fernández-Galisteo and Kurdyumov (2018) demonstrated that a critical value of a gravity parameter exists above which the buoyancy forces can suppress the Darrieus-Landau and the diffusive-thermal instabilities. Finally, when gravity and the flow have the same direction, the break in flame symmetry seams attributed to Rayleigh-Taylor instabilities (Lord (1900); Taylor (1950)). Thus buoyant instability occurs at an interface between two fluids of different densities, when the lighter fluid is located below the denser one.

6.2.1.2 Flame temperature domain comparison

To scale the difference in thermal exchanges the external wall temperature profiles are measured by thermocouple in horizontal and vertical tube positioning for the (A) configuration at equivalence ratio ϕ=0.95, where the flames show an important tilt angle in horizontal but no tilt in vertical. This comparison of temperature profiles is drawn in Fig. 6.5. The comparison shows that in the preheating zone, the temperature in horizontal is higher than in vertical. Indeed, the flame being titled and closer to the wall, the preheating of the wall is more efficient in horizontal. Thus in vertical, when the fresh gas are preheated their density decreases and thereby they move downstream faster, leaving little time for the heat exchanges with the walls to establish. Thereby the preheating zone is shorter in vertical positioning. Both flames have similar power, but a gap in maximum temperature reached is observed by more than 50 K. Thus the reacting zone is more extended in horizontal, due to the flame tilt. In the cooling area, post reaction zone, the wall temperature in horizontal drops under the vertical one. Two possibly combined phenomena occur. First in vertical, the heated external close-wall air flows up along the walls and exchange heat with the walls far from the reaction zone. Secondly, inside the tube, the burned gases with a lower density flow downstream faster in vertical position and thereby heat the wall further away from the horizontal.
The comparison between stable flames in horizontal and vertical configurations highlights the importance of the thermal exchanges and thereby the flame power

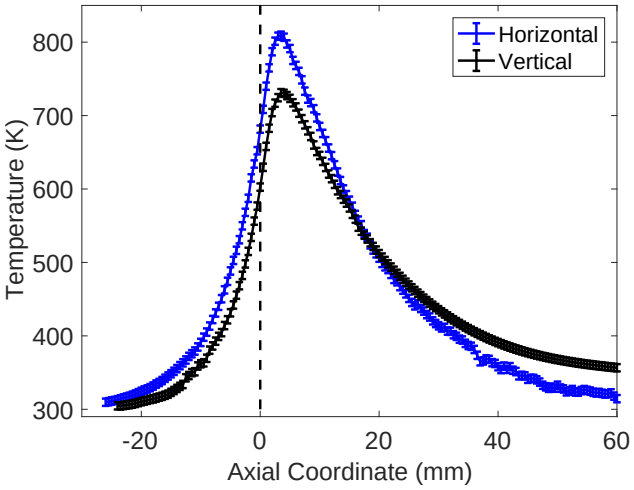

FIGURE 6.5 – *Comparison of temperature profiles of the external wall with a stabilized flame inside the tube at the same equivalence ratio ϕ=0.95, for horizontal (blue) and vertical (black) tube positioning. The flame front is marked by the zero coordinate and the black dashed vertical line.*

in the tilt of the flame. However, as the vertical tilt is caused by hydrodynamic instabilities, the asymmetry origin in horizontal is not identified. Thus, the main difference between the two configurations being the gravity direction, further analysis must be pursued. In order to remove the influence of thermal exchanges in the tilt origin analysis, the flame is studied in propagation regime over isothermal walls.

6.2.2 Propagation of the flame on isothermal walls

In the previous section, the tilt of the flame is shown to be linked to coupled phenomena, of heat exchanges and gravity. The aim of this section is to uncouple these effects on the flame angle in order to identify the origin of the tilt in horizontal configuration. To uncouple these phenomena, the propagation of a flame inside the tube is studied along isothermal walls. Experimentally, the flame is first stabilized at an operating point inside the tube, the mass flow rate is then decreased and an upstream propagation is observed. This section is centered only on the (B) configuration tube of inner diameter d_i= 5 mm. As exposed in chapitre 4, a ratio of conduction time t_{cd} over flame residence time t_{res} is calculated to assess if the thermal environment is established. As a reminder, for $t_{cd}/t_{res} < 1$, the heat exchanges are established and reach a steady state. On the contrary, for $t_{cd}/t_{res} \gg 1$, the flame propagates over an isothermal walls around 300 K.
Table 6.1 sums up all tested mass flow rates for an equivalence ratio ϕ=0.8 in a horizontal tube (B) configuration, starting from the steady operating point

case (1). The flame motion during the upstream propagation is recorded to extract propagation speed (V_p), tilt evolution and eccentricity through a contour fitting routine. Thus for each case, the time ratio is calculated to identify the regime of the flame.

Cases	Regime	U [cm·s^{-1}]	V_p [cm·s^{-1}]	t_{cd}/t_{res}	V_b [cm·s^{-1}]
(1)	Steady	23.10	≈ 0	≈ 0	23.10
(2)	Quasi-static states	22.10	0.003	0.33	22.10
(3)	Quasi-static states	21.10	0.005	0.51	21.10
(4)	Quasi-static states	20.80	0.008	0.91	20.81
(5)	Propagation	20.70	0.46	52.0	21.16
(6)	Propagation	20.60	0.85	93.0	21.45
(7)	Propagation	20.10	1.32	145	21.42

TABLE 6.1 – *Table characterizing the cases studied, giving for each the regime, the bulk velocity U, the flame propagation speed -$V_p\vec{x}$ in the laboratory frame, the time ratio previously introduced and the burning velocity $V_b\vec{x}$.*

For the cases (2) to (4), the flame propagation speed is slightly above zero, but the time ratio is under unity, meaning that the flame motion is a succession of quasi-static states, and that the propagation speed is low enough for the thermal exchanges to reach a steady state. The motion of the flame is hardly perceptible. On the contrary, in the cases (5) to (7), time ratios are much greater than unity, and thereby the flame propagates along isothermal walls around 300 K. The propagation speeds are of the order of few millimeters per seconds, the motion is then clearly noticeable.
When looking at the flow speed, the threshold between the two regimes is located between U=20.70 and 20.80 cm·s^{-1}, meaning that the flame is very sensitive to the flow rate. Experimentally, the flame motion recording is started ten seconds before the mass flow rate modification in order to observe the variables evolutions from the steady state (1) to the other cases. As a result, the angles to vertical are plotted according to time for all transitions from the case (1) to the other cases in Fig. 6.6.
To better visualize the gap between the two regimes, snapshots of the flame are shown in Fig. 6.10. In both propagation regimes, the snapshots are taken at three different times, first at $t = 0$ s in steady state (1), then at $t = 10$ s in the transition in between regimes, when the mass flow rate is lowered and finally at $t = 15$ s when the flame has reached a constant propagation speed. The top snapshots represent the transition from the steady state case (1) to the case (4) and the bottom snapshots corresponds to the transition to the case (5).
Several observations can be deduced from the snapshots in Fig. 6.10 and the angles evolutions Fig. 6.6.
First, the eccentricity of the fitted ellipse decreases while propagating, meaning that the flame gets more circular. Thus, the change in propagation speed and

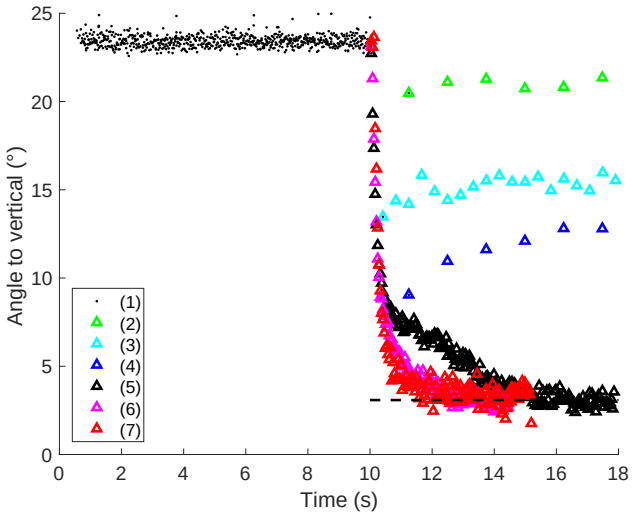

FIGURE 6.6 – *Angle to vertical evolution with time for transition from steady case (1) to quasi-static and propagation cases (2) to (7). The three quasi-static states reach different angles, decreasing with the increase of the flame propagation speed. The three isothermal propagations converge to the same final angle around 3° from vertical. The dotted line represents the mean value reached by those three cases.*

bulk velocity is clearly associated with a change in the tilt angle of the flame. The three quasi-static states, from case (2) to (4), reach different angles which value decrease with the increase of the flame propagation speed. Thus, in near zero propagation speeds the flame keeps an angle to vertical greater than 10°, and thereby remains visible (top snapshots in Fig. 6.10). Indeed, starting from a steady state with an angle of 23.5° the angles of the cases (2), (3) and (4) are respectively 20.9°, 16.3° and 11.9°, which represent a decrease of respectively of 11.3%, 30.8% and 49.5%. Thereby, a variation of the flame angle is perceptible from the steady state to quasi-static state, revealing the influence of the bulk velocity on the tilt of the flame. Indeed the angle to vertical decreases with the bulk velocity. For instance, between the cases (1) and (4) the bulk velocity decreases of 11% and the angle decreases of 49.5%. Hence, with established thermal exchanges, an increase in bulk velocity provokes an accentuation of the tilt.

The three isothermal propagations, case (5) to (7) converge toward the same final angle, around 3° from vertical, yielding a relative decrease in inclination of 87.5% and as a result the inclination gets less notable in the snapshots progression. In those three cases, no influence of the bulk velocity on the angle to vertical is remarkable. Yet, the inclination still exists which is an indicator of a symmetry breaking phenomenon other than the heat exchanges.

From these observations can be deduced that the thermal coupling and the bulk velocity have a dominant role in the tilt of the flame. However, the flame

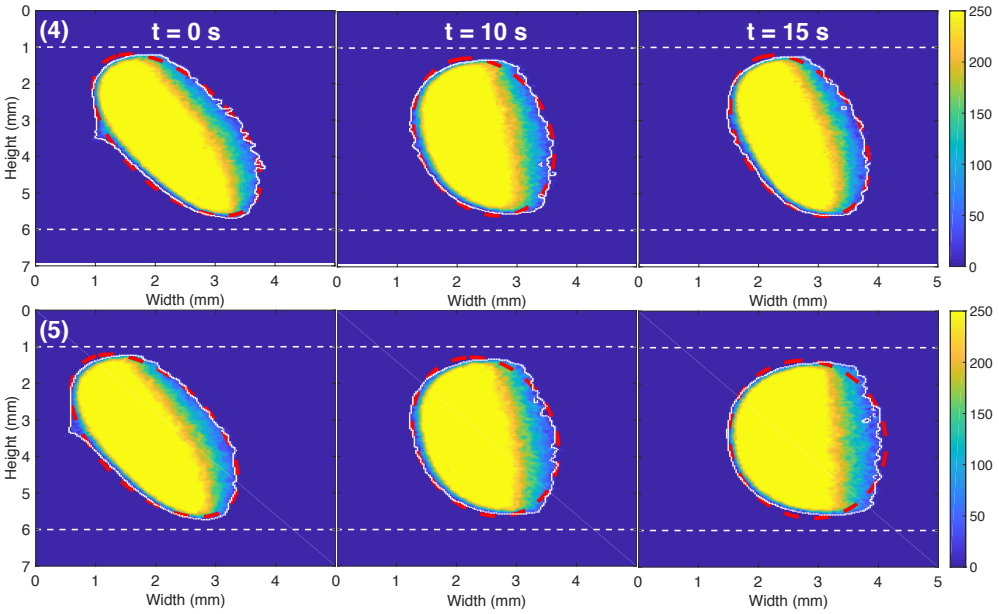

FIGURE 6.7 – *The first snapshot of each line is taken at time t=0 s, in the steady case (1). The top snapshots correspond to the transition from this steady case to the case (4) of quasi-static state. The bottom snapshots represent the transition to the case (5) of isothermal propagation. The white dotted lines represent the flame detected contour and the red dashed line represents the fitted ellipse used to track the position, tilt angle and area of the flame. The white dashed lines represent the inner wall limits.*

angle in cold wall propagation regime does not reach zero. As a result the flame tilting is not entirely due to heat exchanges. The action of a directional force seems to point out gravity effects as source of this additional tilt. To make sure of this, a comparison between the experiment and a numerical computation is performed.

6.3 Existing work on the asymmetrical flames and phenomena at the origin of symmetry breaking

In chapitre 1, the literature review indicates that a great majority of the studies consider domain symmetry when investigating narrow channel combustion. Under this condition two symmetrical flames were observed : the mushroom and tulip shaped flames. It is only recently that asymmetrical flames were studied in numerical and experimental studies, without the domain symmetry hypothesis. According to the configuration, multiple physical phenomena justify the appearance of an asymmetric flame. These possible phenomena and their fields of application are presented.

- The Darrieus-Landau (D - L) hydrodynamic instabilities (Darrieus (1938);

Landau (1944)) cause an amplification of the flame surface due to gas expansion. These instabilities require a minimal characteristic length to develop, and therefore cannot exist in small-dimension channels or tubes as the ones used in the presented work.

- The viscosity induced Saffman-Taylor (S - T) instabilities (Saffman and Taylor (1988)), resulting of viscous-induced pressure gradients are characteristic of combustion in narrow channels.
- The diffusive-thermal (D - T) instability is directly linked to the Lewis number. For Le < 1, the existence of non-symmetrical flames is discussed in various studies (Zamashchikov (2004); Pizza et al. (2010); Kurdyumov (2011); Jiménez et al. (2015)), which demonstrate that under certain conditions, the asymmetric flame is a stable manifestation of an unstable symmetric flame. For Le > 1, at low mass flow rate flames are found asymmetric (Kurdyumov (2011)) and vibratory instability of the planar flame in the tube can develop (Clavin et al. (1990)). Finally for unity Lewis number flames have been found symmetric when approaching the micro-combustion scale.

However all of these study do not consider gravity. Therefore, a possible instability considered in this work are body forces. In fact, in small-scale combustion numerical studies, gravity is often neglected based on the relatively high Froude number (Fr) associated, this last varying as $1/L_c$. E.g.

$$\mathrm{Fr} = \frac{U_o^2}{gL_c} \simeq 1.59\,, \tag{6.1}$$

for a characteristic velocity of 28 cm.s^{-1} and a characteristic length of 5 mm. Having a Fr higher than one yields that gravitational effects do not drive the flame dynamics but not necessarily that these can be completely neglected. Experiments treating the flame propagation in horizontal tubes show the appearance of slant shaped flames with a preferential direction (Ju and Xu (2006a); Zamashchikov (2004)), suggesting the role of a directional force.

Experiments on flame propagation in horizontal tubes show the appearance of slanted flames with a preferential direction. So far this observation was explained by a flame stabilisation mechanism influenced by the free convection in the air surrounding the tube.

Indeed, the natural convection on horizontal cylinders has been extensively studied, but a wide dispersion in analytical, numerical, and experimental data exists among the numerous investigations in the literature.

However, several studies (Saitoh et al. (1993); Acharya and Dash (2017); Wang et al. (1991)) show that a thermal and flow plume develops around a heated tube, consequently the Nusselt number decreases toward the top of the cylinder as the boundary layer thickens. In fact, the plume insulates the cylinder from the surrounding air and results in a lower heat transfer coefficient. A temperature difference between the top and bottom wall also results from the establishment of this plume around the tube. This phenomenon can be a possible symmetry

breaking source. Gravity is driving the flame shape indirectly by affecting the flow surrounding the tube.
Besides, a theoretical study Kazakov (2012), in the context of a model equation for flame propagation, points out that gravity might play a role not only through external free convection but also via buoyant effects inside the channel. Various parameters are known to influence the above mentioned instabilities such as, the channel dimensions, the nature of the fuel, the wall temperature as well as the application area (micro-gravity, on-earth). From the numerous symmetry breaking sources, stable tulip flames have rarely been observed experimentally. Nevertheless, observations of a stable tulip-shaped stoichiometric methane-air flame has been realized for a tube of 2.15 mm inner diameter (Di Stazio et al. (2015)). Such a configuration was obtained with a high temperature profile imposed, via an intense external heating of the quartz tube (temperature peak at 1600 K), and an inlet flow rate of 1 m.s^{-1}.

6.4 Comparison between experimental results and numerical computation

A numerical computation of a planar channel in two-dimension with the same dimensions as of the experiment was realized in the MAPEE ANR project framework by K.Bioche, G.Ribert and L.Vervisch. Due to the cost of simulation, only two of the cases presented above are selected to compare with the numerical computation. Thus the dimensions are the (B) configuration characteristic length d_i= 5 mm in experimental and $\ell_i = 5$ mm in numerical planar channel. This section was submitted for review to the Combustion and Flame journal in October 2018 and accepted for publication (Bioche, Pieyre, Ribert, Richecoeur, and Vervisch (2019)).

6.4.1 Experimental cases

The two cases chosen for the comparison are summed up in the table 6.2. The cases (i) and (ii) correspond respectively to the cases (1) and (5) of the previous section, namely a steady heat conductive interaction with the wall and a propagation regime over isothermal wall around 300 K. Thereby, the flame is examined, (i) stabilized by an adjusted incoming flow matching the overall burning rate and (ii) during an upstream propagation after decreasing the mass flow rate. Because the heat diffusivity is much larger in the gas than in the solid, in case (ii) the flame propagates along an almost isothermal wall. In case (i), as established in the previous chapters, the stabilization mechanism of the steady flame depends on complex heat exchanges with the wall, including heat transfer between the gas and the wall, conduction of heat in the solid wall and convective heat transfer between the outside wall and the environment (Jiménez et al. (2015); Bioche et al. (2018)). Thus, the section 6.2.2 demonstrate that

with a time ratio $t_{cd}/t_{res} \gg 1$, in case (ii) the flame propagates over isothermal walls.
The burning velocity, $V_\mathrm{b} = U + V_\mathrm{p}$ increases by 9.17% between the flame moving upstream and the stabilized one. This enhancement of the burning velocity results from heat retrocession by the wall to the flow slightly upstream of the stabilized flame front. The increase in amplitude of the flame speed depends on the amount of heat release and therefore on the equivalence ratio of the mixture.

Case	Wall	V_bulk [cm·s^{-1}]	V_p [cm·s^{-1}]	$\mathrm{t_{cd}/t_{res}}$	V_b [cm·s^{-1}]
(i)	Heat-conductive	23.10	≈ 0	≈ 0	23.10
(ii)	Iso-thermal	20.70	0.46	52	21.16

TABLE 6.2 – *Experimental conditions. Lean premixed methane/air flame ($\phi = 0.8$). $V_{bulk}\vec{x}$ is the bulk flow velocity. $-V_p\vec{x}$ is the flame front velocity in the laboratory frame. t_{cd} is a characteristic heat conduction time in the solid. t_{res} is a flame residence time. V_b is the burning velocity.*

6.4.2 Numerical setup

To verify that the studied gravity mechanisms do not depend significantly on the details of the flow configuration, and also because experiments in the flame tube show no sign of azimuthal effects, the most simple case of a planar channel is numerically studied in two-dimensions, with a channel height $\ell_i = 5$ mm and quartz walls of thickness $e_\mathrm{w} = 1$ mm, thereby with characteristic lengths similar to the experimental ones.
The fully compressible form of the unsteady conservation equations of mass, momentum and total sensible energy are integrated with a finite volume method on a Cartesian grid with the SiTCom-B flow solver (Domingo et al. (2008); Domingo and Vervisch (2017); Bouheraoua et al. (2017); Duboc et al. (2018)). Fourth-order skew-symmetric-like scheme for the convective fluxes (Ducros et al. (1999)) and fourth-order centered scheme for the viscous and diffusive fluxes, are used for spatial integration. Time advancement is performed with a Runge-Kutta scheme of order four. Due to CFL stability restrictions and spatial resolution, the time step is limited to 16 ns approaching the steady state. One-dimensional NSCBC (Poinsot and Lele (1992)) are employed for inlet and outlet boundary conditions. The molecular transport properties of the gaseous mixture are computed following the Curtiss and Hirschfelder approximations (Curtiss and Hirschfelder (1949)). A two-way flow/solid coupling is organized to solve heat transfers between the gas and the wall. The coupling procedure proposed in Duchaine et al. (2009) is employed for parallel computation in the two solvers. The alternate direction implicit Douglas-Gunn method (Douglas (1955)) is adopted to solve for the temperature in the solid. The exterior wall surface exchanges energy with the surrounding air at 300 K,

with a heat transfer convective coefficient 30 $W{\cdot}m^{-2}{\cdot}K^{-1}$ and by radiation, through a gray body hypothesis with an emission coefficient decaying linearly from 0.95 at 290 K to 0.75 at 1800 K. The wall thermal conductivity and capacity are the ones of fused quartz tabulated versus temperature from Momentive (2017). The density of the solid wall is fixed at 2200 $kg{\cdot}m^{-3}$. Due to the large difference in the characteristic time scales of internal energy evolution in the solid and the flow, a de-synchronization method is employed when converging toward the steady state solutions (Koren (2016)). More details concerning the set of equations solved along with the boundary conditions of the present case studied may be found in Bioche et al. (2018).

The origin of the axial coordinate ($x = 0$) is set at the flame position taken as the peak heat release rate on the axis of symmetry. The mesh extends from -51 mm to the left in the fresh gases to 15 mm to the right in the burnt gases. This domain is long enough to capture the upstream heat diffusion through the wall while ensuring a zero-velocity gradient in the streamwise direction at the inlet. Great care is thus taken to generate conditions free from inlet effects, in other words the distance between the tube inlet and the flame is large enough so that the exact stabilisation position is not relevant for the analysis. The mesh is composed of regular squares of resolution $\delta_x = 25$ µm from the inlet down to $x = 9$ mm. It is then progressively coarsened in the longitudinal direction down to the outlet, with a geometric coefficient of 1.0025. The spanwise mesh resolution does not vary in this Cartesian grid and is fixed to $\delta_y = \delta_x$, resulting in a mesh composed of 512k cells.

A specific procedure is applied to rapidly determine the inlet bulk velocity, so that the incoming flow balances the two-dimensional flame burning velocity. As in previous works (Ruetsch et al. (1995); Bioche et al. (2018)), this is achieved by measuring the progression velocity of the methane iso-surface relative to the flow, at the location of its peak burning rate, to adjust the incoming velocity accordingly. Then, this flow velocity is kept fixed at the inlet.

A reduced chemical mechanism composed of 17 species and 53 reactions has been specifically developed based on the GRI-1.2 mechanism Frenklach et al. (1995) using the ORCh (Optimised and Reduced Chemistry) approach Jaouen et al. (2017), targeting the flame speeds and species profiles of freely propagating premixed flames for various levels of heat loss up to quenching and auto-ignition in homogeneous reactors at various initial temperatures. The reference adiabatic flame speed with the detailed scheme for the equivalence ratio $\phi = 0.8$ is $S_L^o = 28.40$ $cm{\cdot}s^{-1}$ and the reduced scheme leads to $S_L^o = 28.56$ $cm{\cdot}s^{-1}$. Representative species and temperature profiles compared in the one-dimensional flames at equivalence ratio $\phi = 0.8$, between the detailed and reduced schemes are given in the supplemental material. The actual thermal laminar-flame thickness based on the temperature gradient is of the order of 500 µm and the intermediate radical layers considered in the reduced mechanism are fully resolved for this lean flame.

Wall boundary conditions similar to the two experimental cases of Table 6.2

are considered, *i.e.* (i) heat-conductive with all heat transfers active and (ii) iso-thermal (T = 300 K). In the two-dimensional iso-thermal channel with gravity, the flame burning velocity is $S_L = 24.95$ cm·s^{-1}, to become 27.09 cm·s^{-1} with wall heat-transfer. As it should, the absolute values of these flame burning velocities differ between the axisymmetric tube in the experiment (Table 6.2) and the two-dimensional channel in the simulation. However, the relative increase in burning velocity between iso-thermal and non-isothermal wall cases are quite close, 9.17% in the experiment and 8.57% in the simulation, which brings some confidence in the retained strategy.

6.4.3 Analysis of gravity effects

Case (i) : Flame stabilized with heat-conductive wall

The flame stabilized by an incoming flow exactly balancing its burning rate is considered at first (case (i) of Table 6.2). The CH* chemiluminescence is collected in the experiment over an exposure time of 2 s and the mean flame emission is represented in Fig. 6.8 left. The reaction zone makes an angle with the vertical of 24°, whereas the numerical simulation without gravity reports a fully symmetric flame shape (Fig. 6.8 top-right). Adding the gravity force in the Navier-Stokes equation, the flame takes a tilt as in the experiment (Fig. 6.8 bottom-right), even though the simulation is planar and the experiments axisymmetric. The angle of the reaction zone with the vertical is 30° in the simulation.

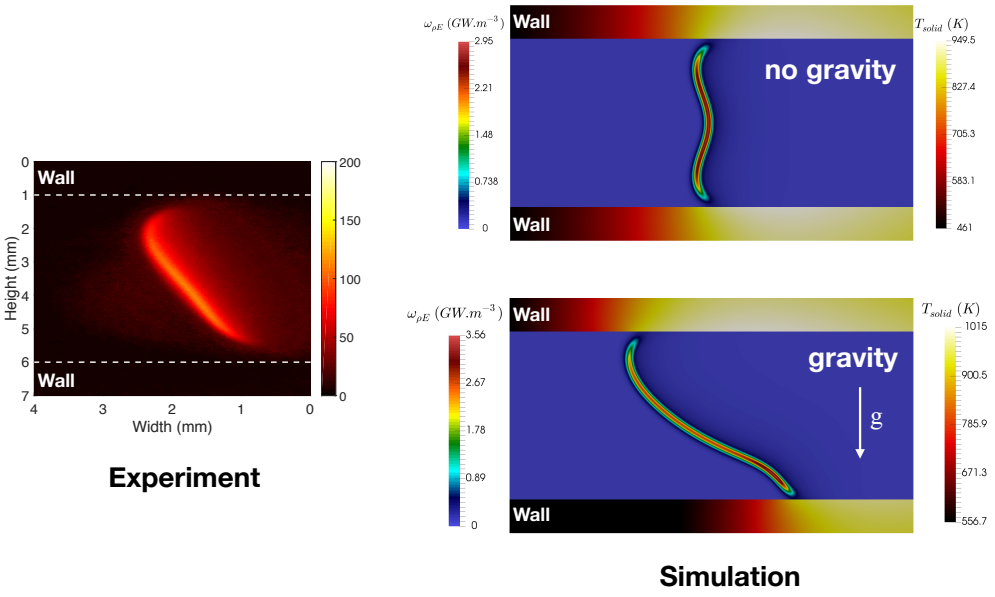

FIGURE 6.8 – *Case (ii) of Table 6.2. Experiment (flame in tube) : Mean chemiluminescence CH*. Simulation (flame in channel) : Wall temperature and heat release rate.*

In the case with gravity, the top and bottom close-to-wall edge-flame shapes differ (Fig. 6.8). The topology and the relative progression velocity of these edge-flames benefit from the preheating of the gases upstream of the flame after diffusion of heat inside the wall. Streamwise profiles of velocity and temperature taken at a distance of 0.7 mm from the top and bottom channel walls are now analyzed. The streamwise component of the velocity is larger at the bottom due to the confinement of the flow by the concave flame shape (Fig. 6.9(a)). This higher velocity goes with smaller residence times and thus a less efficient preheating by the wall thermal boundary layer, leading to smaller temperature ahead of the bottom edge-flame (Fig. 6.9(b)).

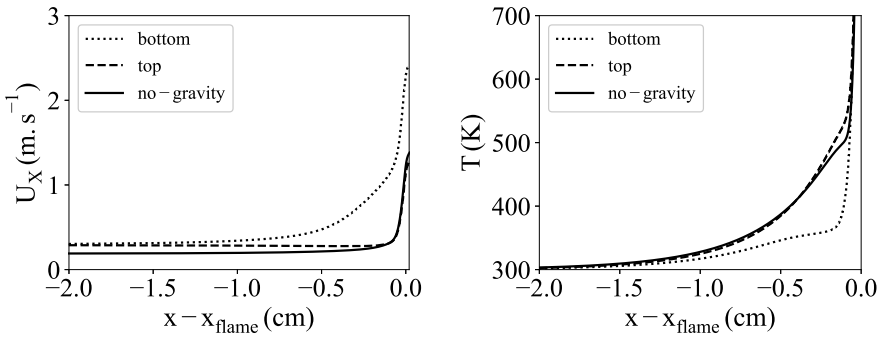

(a) Streamwise velocity (b) Temperature

FIGURE 6.9 – *Streamwise velocity and temperature distribution at a distance of 0.7 mm from the top and bottom walls. x_{flame} : maximum of heat release on the probed line (top or bottom). No-gravity : symmetric flame.*

Because an eventual modification by gravity of the free convection surrounding the channel is not included in the simulation, another mechanism driven by gravity is at play inside the channel. To isolate this mechanism from heat transfer inside and outside the wall, the flame propagating over an iso-thermal wall is further examined (case (ii) of Table 6.2).

Case (ii) : Flame propagating over a quasi-isothermal wall

In the experiment, starting from a stabilized flame (case (i)), the mass flow rate is lowered to reach the operating point of case (ii), in which the flame propagates inside the tube over quasi-isothermal walls. The diagnostics reported above are applied, the recording starts ten seconds before the mass flow rate modification and is pursued up to a steadily propagating flame. Figure 6.10 shows flame images taken initially and then subsequently at 10 and 15 seconds. The flame inclination is significantly reduced.
The time evolution of the flame angle with the vertical determined from the fitted ellipse is given in Fig. 6.11. Starting at a steady state with an angle of

24°, the propagation state is reached at which the angle is 3°, yielding a relative decrease in inclination of 87.5%. This decrease of angle to the vertical (reduction of inclination) is also observed in the simulation, where the experimental processing routine is applied to compute the flame angle from O species concentration. Snapshots of the iso-thermal wall simulations with and without gravity are shown in Fig. 6.12. The angle taken by the flame with gravity and iso-thermal wall is 6°, also much less pronounced than in case (i) (30°). The relative decrease in inclination of flame simulated is of 80%. The breaking of the symmetry is thus reported in both experiments and simulations with iso-thermal and cold wall (T =300 K).

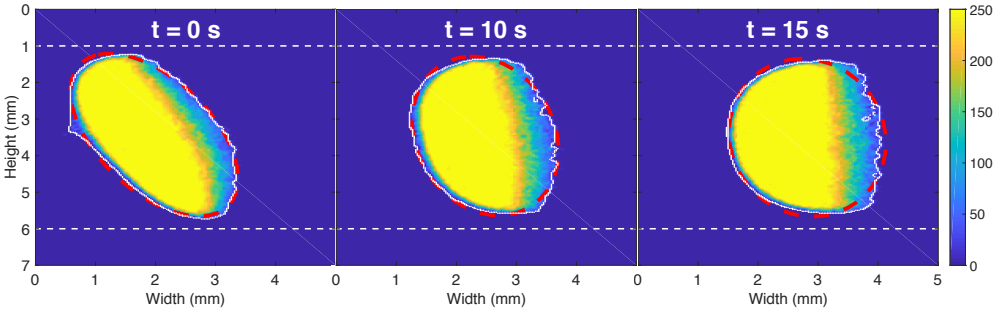

FIGURE 6.10 – *Experimental snapshots at $t = 0$ s, $t = 10$ s and $t = 15$ s. White dotted line : flame detected contour. Red dashed line : fitted ellipse.*

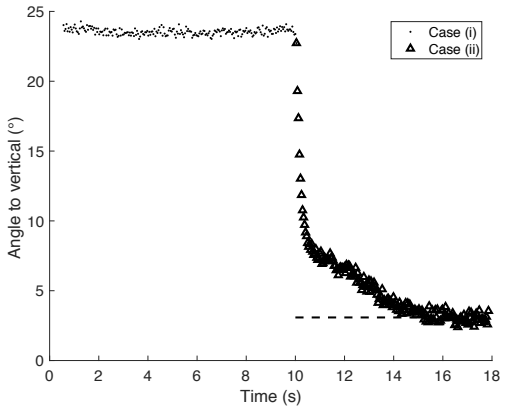

FIGURE 6.11 – *Time evolution of the flame angle to the vertical. $t = 0$ denotes the decrease in mass flow rate. Dotted : Stabilized flame with heat-conductive wall (case (i)). Triangle : Propagating flame with iso-thermal wall (case (ii)).*

6.4.4 Analysis of baroclinic-torque response to gravity in 2D narrow channel

Kazakov (2012) discussed in a detailed theoretical analysis the effect of gravity on confined flames. Body forces generate pressure and density gradients and

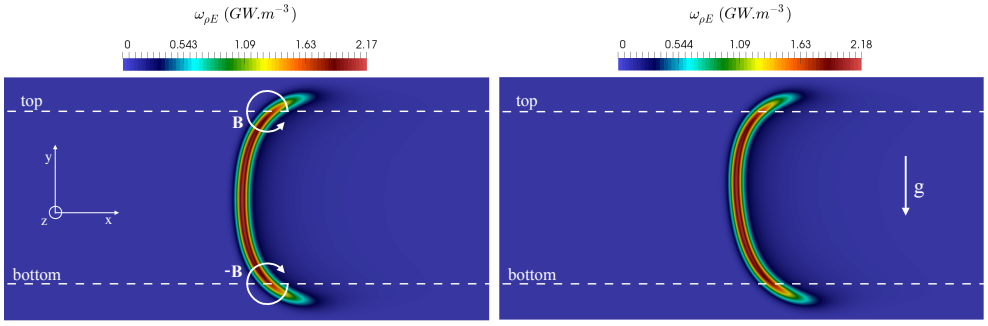

(a) Without gravity (b) With gravity

FIGURE 6.12 – *Simulation of iso-thermal wall (case (ii)) of Table 6.2), with and without gravity. Dashed-line : lines used for probing the vorticity budget.*

among the numerous coupling between density and pressure gradient present in flames, the baroclinic torque is a well-established source of vorticity in curved reaction zones Clavin and Searby (2016)

$$\mathbf{B} = \frac{1}{\rho^2}\nabla\rho \times \nabla P = \frac{1}{\rho^2}\left(\frac{\partial\rho}{\partial x}\frac{\partial P}{\partial y} - \frac{\partial\rho}{\partial y}\frac{\partial P}{dx}\right)\mathbf{z}\,, \tag{6.2}$$

where ρ is the density and P is the pressure. $\mathbf{x}$ is the streamwise coordinate (flow direction), $\mathbf{y}$ is the transverse coordinate (gravitational acceleration is $-g\mathbf{y}$) and $\mathbf{z}$ the coordinate normal to the channel plane. The balance equation for the vorticity $\boldsymbol{\omega} = \nabla \times \mathbf{u}$ reads

$$\frac{\partial\boldsymbol{\omega}}{\partial t} = \underbrace{-\left(\mathbf{u}\cdot\boldsymbol{\nabla}\right)\boldsymbol{\omega}}_{i} + \underbrace{\left(\boldsymbol{\omega}\cdot\boldsymbol{\nabla}\right)\mathbf{u}}_{ii} - \underbrace{\boldsymbol{\omega}\left(\boldsymbol{\nabla}\cdot\mathbf{u}\right)}_{iii} + \underbrace{\boldsymbol{B}}_{iv} + \underbrace{\boldsymbol{\nabla}\times\left(\frac{1}{\rho}\boldsymbol{\nabla}\cdot\boldsymbol{\tau}\right)}_{v}\,, \tag{6.3}$$

where $\boldsymbol{u}$ is the velocity vector and $\boldsymbol{\tau}$ is the viscous tensor. In this two-dimensional case, there is no change in vorticity due to vortex stretching and the term (ii) in Eq. (6.3) is zero. (i) is the transport of vorticity by convection, (iii) is vorticity stretching by density change and (v) is the transport of vorticity by viscous effects.

In the isothermal case without gravity, approaching the edge-flame close to the wall, the pressure and density gradients in the y-direction feature opposite sign on both sides of the channel centerline, whereas the density and pressure gradients in the x-direction stay the same. The baroclinic torque given by relation (6.2) therefore changes its sign on both sides of the channel centerline, as do all the terms of Eq. (6.3). This is verified in Fig. 6.13 displaying the magnitude of the baroclinic torque along the dashed-lines seen in Fig. 6.12. These plots are versus a reaction progress variable defined from the CO_2 mass fraction normalized by its value in the fully burnt gases ($Y^{\mathrm{b}}_{\mathrm{CO}_2} = 0.122576$), also collected along the dashed lines of Fig. 6.12. The baroclinic torque in Fig. 6.13

(squares) is positive on upper part of the channel (Fig. 6.13(a)) and negative on the bottom part (Fig. 6.13(b)), confirming the symmetric effects pictured by the white arrows in Fig. 6.12(a). All the terms contributing to the vorticity budget in Eq. (6.3) are shown in Fig. 6.13, along with the total budget, which sums up to zero as expected for both gravity (lines) and no-gravity (symbols) steady cases. Because the density difference between fresh and burnt gases and flow acceleration are very close with or without body forces, the magnitudes of the various terms of Eq. (6.3) are only slightly affected by gravity (difference of the order of $10^4 s^{-2}$ in Fig. 6.13). To elucidate the mechanism that makes the flame to rotate, it is then necessary to examine the transient when the gravity is added.

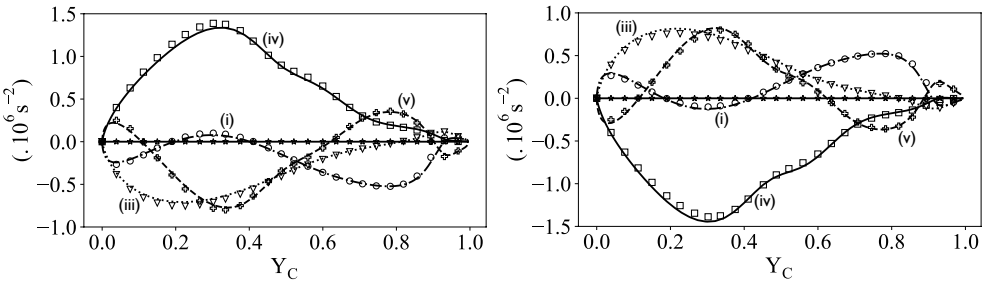

(a) Top line of Fig. 6.12 (b) Bottom line of Fig. 6.12

FIGURE 6.13 – *Vorticity budget versus $Y_{CO_2}/Y^b_{CO_2}$ along the dashed-lines of Fig. 6.12. Lines : With gravity. Symbols : Without gravity. Circles : (i) of Eq. 6.3 . Triangles : (iii). Squares : (iv) Baroclinic torque. Crosses : (v). Stars : budget.*

Starting from the converged simulation without gravity, the body force is added and the upper edge-flame rotation is completed in 16 ms, to reach the slanted flame steady state of Fig. 6.12(b). The introduction of gravity leads to an additional contribution to the baroclinic torque (6.2), which may be approximated as

$$\frac{1}{\rho^2}\left[\frac{\partial\rho}{\partial x}\left(\frac{\partial P}{\partial y}\right)_g - \left(\frac{\partial\rho}{\partial y}\right)_g \frac{\partial P}{\partial x}\right] . \tag{6.4}$$

Isolating the effect of gravity, its premier impact is to promote flow stratification with negative density and pressure gradients in the vertical direction, $(\partial P/\partial y)_g < 0$ and $(\partial\rho/\partial y)_g < 0$. Considering an isentropic flow at rest subjected to gravity, the relative variation of pressure and density defines the speed of sound $c^2 = (\partial P/\partial\rho) > 1$. Therefore, the magnitudes of the density and pressure gradients in the vertical direction and due to gravity may be ranked as $(\partial P/\partial y)_g < (\partial\rho/\partial y)_g < 0$. Across the premixed reaction zone, $(\partial P/\partial x) < 0$, $(\partial\rho/\partial x) < 0$ and $(\partial T/\partial x) > 0$. The ranking in pressure and density gradient evolves across the flame front (Fig. 6.14, without gravity). In the upstream part of the flame front $(\partial\rho/\partial x) < (\partial P/\partial x) < 0$, while further downstream

$(\partial P/\partial x) < (\partial \rho/\partial x) < 0$. These gradients in the streamwise direction are orders of magnitudes larger than those in the vertical direction, therefore they may be assumed weakly affected by the addition of gravity. Combining these observations, the baroclinic torque induced by gravity (Eq. (6.4)) should be largely positive in the upstream part of the flame front and decrease after, yielding globally a positive enhancement of the baroclinic torque across the reaction zone.

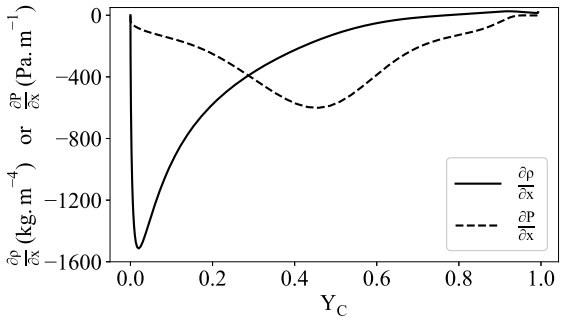

FIGURE 6.14 – *Pressure and density streamwise gradients versus $Y_{CO_2}/Y^b_{CO_2}$ along the dashed-lines of Fig. 6.12(a).*

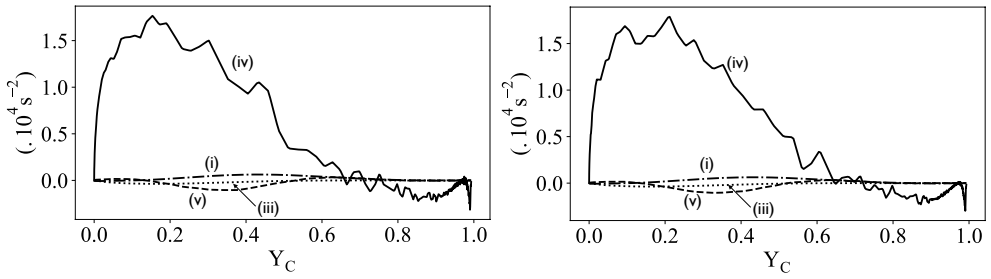

(a) Top line of Fig. 6.12 (b) Bottom line of Fig. 6.12

FIGURE 6.15 – *Deviation of vorticity balance versus $Y_{CO_2}/Y^b_{CO_2}$ along the dashed-lines of Fig. 6.12. Dashed-dot : (i) of Eq. 6.3. Dotted : (iii). Solid : (iv) Baroclinic torque. Dashed : (v).*

To verify this simple scaling, at the time $t = 18$ µs after adding gravity, the source of vorticity is analyzed by computing the variation of all the terms of Eq. (6.3). This variation is measured in the simulation between their steady state value without gravity (Fig. 6.13) and their value at $t = 18$ µs after gravity addition. In both the upper and the bottom edge-flame close to wall, a positive source of baroclinic torque is indeed observed, corresponding to a positive source of vorticity (Fig. 6.15). This addition of vorticity represents a few percent of the overall baroclinic torque and is located across the reaction zones, where the longitudinal pressure and density gradients occur. In the top part of the channel,

the streamlines deviate less toward the centerline with gravity when crossing the flame (Fig. 6.16), leading to their spreading upstream of the flame with a local flow deceleration, followed by an upstream flame movement (see Fig. 6.17, dashed line). In the bottom part of the channel, the opposite mechanism is found, with a highest concentration of the streamlines by the added vorticity (Fig. 6.16(b)), leading to a local flow acceleration and a downstream flame movement (see Fig. 6.17, dotted line). The net result is a reaction zone that is pushed downstream at the bottom and pulled upstream at the top to evolve towards a slanted shape.
In summary, the baroclinic torques that are of opposite signs in a stable flame, benefit from about the same positive increase on both sides of the axis of symmetry when gravity is turned on, leading to the flame rotation and modification of the streamlines, up to a new equilibrium condition, but featuring a non-symmetric deviation of the streamlines. The difference in term (iv) of Eq. (6.3) during the transient (*i.e.* when gravity is added in Fig. 6.15) therefore explains the flame rotation. Once the flame stable again, the difference between terms (iv) with or without gravity in Fig. 6.13 informs on the change in flow topology (change in streamlines deviation).

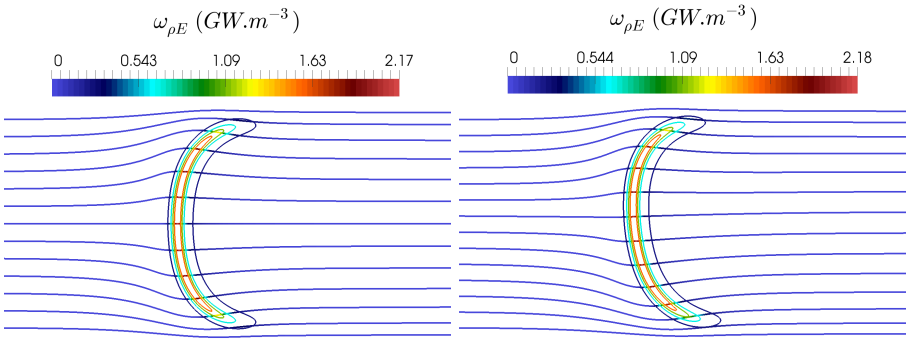

(a) Without gravity (b) With gravity

FIGURE 6.16 – *Case (ii). Streamlines and flame contours of 10, 30, 50 and 70% of max heat release rate. The dashed line denotes the vertical axis.*

6.5 Conclusion

Experimentally, a flame in steady regime is found to be asymmetric in both horizontal and vertical tube positioning for tubes inner diameters greater than 4 mm. First a comparison of horizontal and vertical tube positioning is exposed to highlight the influence of gravity. To validate the hypothesis made in this first section, the flame propagation over isothermal walls at 300 K is examined in a second section. It allows to uncouple the heat exchanges from the body forces effects.

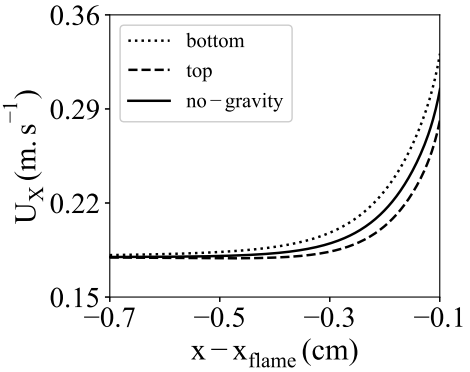

FIGURE 6.17 – *Velocity distribution at a distance of 0.7 mm to the top and bottom wall. x_{flame} : maximum of heat release on the probed line. No-gravity : symmetric flame.*

The effect of introducing gravity in flames propagating in a narrow-channel is studied from numerical simulations with comparison against experiments conducted in a narrow-tube (channel of internal width or tube diameter of $\ell_i =$ 5 mm). Experimental measurements and simulation reports similar trends for flames freely propagating above iso-thermal walls or stabilized by the incoming flow with strongly coupled heat exchanged with and within the wall. Both flames are asymmetrical, with an inclination that is less pronounced in the iso-thermal wall case. In the absence of modification by gravity of the convection on the outside channel wall, the flame is still tilted, with an anchoring at the upper wall. The heat-retrocession via conduction in the wall and the thermal boundary layer in the fresh gases upstream of the flame, increase the inclination of the slanted flames. Following previous works Kazakov (2012), the response of the baroclinic torque to gravity is explored and results confirm its driving role in such narrow combustion-systems. These findings differ from previous works devoted to flame instabilities in vertical tubes, as in the present horizontal tubes, the inclined flame is the single solution observed in presence of gravity. Both stable (wall thermally coupled) and flame moving with a finite velocity with respect to the wall (isothermal wall) configurations are affected by gravity effects.

This chapter concludes the second part of this thesis work. This part was focused on the steady regime characterization experimentally and numerically. Thus the origin of the experimentally observed flame asymmetry is established as an effect of gravity. The following part focuses on transitory regimes and possible assistance of the flame.

Troisième partie

Transitory flames and perspectives

Chapitre 7

Thermal induced flashback

Contents

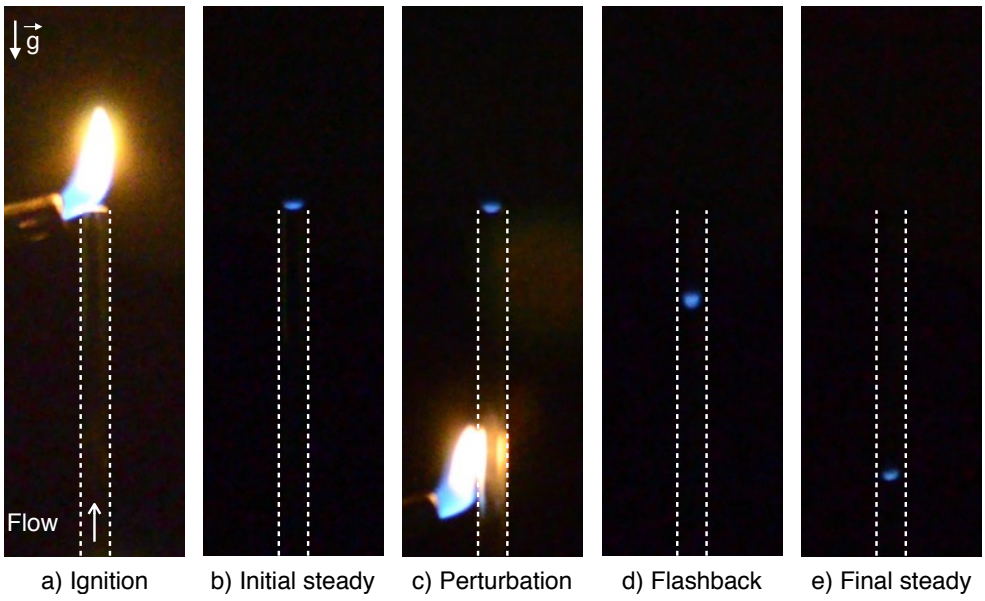

FIGURE 7.1 – *Flashback step details on a vertical tube, using a lighter as a perturbation heat source.*

7.1 Extended abstract

Once stabilized at a steady position in the tube, a premixed methane/air flame induces a temperature distribution within the quartz walls. Walls are the medium used to extract or recycle heat from the flame and burnt gases : a percentage of the heat generated by the flame is conducted within the walls towards the fresh gases preheating them, the remaining part is transferred to the external medium through radiative and convective heat transfers. These heat fluxes in the walls make the steady state possible. Thus, modifying the heat distribution in the walls impacts the flame steady state. This hypothesis is tested here by heating the tube walls at different distances upstream from the flame. The response of a stabilized flame inside the narrow channel to a thermal perturbation is studied. The experimental perturbation steps are described on Fig. 7.1. First a flame is ignited (a) and stabilized (b) on the extremity of the vertical tube. Then, a heat source (here a lighter on Fig. 7.1) is placed at a fixed distance upstream from the stabilized flame surrounding the external part of the tube. The purpose is to locally heat up the wall, modify the temperature distribution within the wall and observe the flame's motion induced by this heat addition. Between the start of the heating and the beginning of the flame motion exists a delay time of Δt=13.1 s. Therefore, the phenomena responsible for the flashback have a large characteristic time. Thus, the flame retrieves its initial regime after the thermally induced propagation.
The example of flashback shown on Fig. 7.1 is the first configuration in which the

flashback has been experimentally observed. Further work on the heat source, the tube positioning (Horizontal/Vertical) and the flow characteristics is presented in this chapter.
The objectives of this chapter are then to :

- Choose an optimum experimental heat source
- Characterize the influence of the heating on gas and wall temperature : spatial and temporal temperature characterization of the heating, for several intensities and distance between the heat source and the flame front.
- Characterize the flashback : track during the flashback the displacement, speed, shape and orientation of the flame
- Compare flashback in horizontal and vertical positioning of the tube
- Numerically reproduce the experimental flashback in one dimensional complex chemistry computation
- Identify the physical phenomena involved in the flame motion

7.2 Characterization of the heating system

7.2.1 Choice of an experimental heat source

Several heat sources were tested to find an optimal configuration, the heat source should reach high temperatures, while giving a good accuracy on the application point for both horizontal and vertical configurations of the tube. Those sources are a lighter, an electric resistance and two different materials (Constantan and Kanthal) of resistive wires.

- Initially, a small diffusion burner (gas lighter) is used as heat source as described in the Fig. 7.1. The lighter allows a short response time of the flame since the maximum temperature imposed to the wall is high ($\approx$ 600 K), the temperature profile is spread (Fig. 7.2) and the lighter flame emitted radiation is important. However the precision and repeatability given by this heat source is not satisfactory since a good accuracy on the application point could not be reached. Thus, the difference between temperature profile of the horizontal and vertical configurations is substantial. Furthermore the lighter flame radiation effects can not be controlled. For this, the lighter is not kept as a solution.
- Another considered heat source is a PTC heater (Ω ref : DBK HPG 2/22 75x35 100-240 V Q38V) powered by a DC current, which temperature can reach 470 K. A circular notch is created on the PTC heater frame, with a diameter slightly above the tube's diameter in order to circle half of the tube. In this solution, the application point can be controlled with a spread of 5 mm, however, as depicted on Fig. 7.2, the maximum temperature reached is too low, and leads to very high characteristic time of flashback.
- The last tested solution is a heating resistance wire rolled around the

quartz tube and powered by a DC current power supply. Two materials of heating wire were considered. The first material tried is a 0.2 mm diameter Constantan wire. Constantan material consists of 55% copper and 45% nickel and its most interesting feature is to have a constant resistivity over a wide range of temperatures. The results obtained using this configuration were satisfactory, but several drawbacks were encountered as the wire would break when subject to high power. In fact, once heated, the wire becomes easily breakable, and therefore causes repeatability and durability issues. The second material used and adopted for the experiments is Kanthal (FeCrAl), a family of iron chromium (20 to 30%) aluminium (4 to 7.5%) alloys used in a wide range of resistance and high temperature applications. Kanthal resists well to power supply (up to 50 W), keeps its flexibility properties after being heated, and doesn't break easily. As a result a Kanthal wire of 0.25 mm diameter is chosen as heat source, with a resistance of R=4.5 Ω.

As for the steady flame temperature measurements, a displacement device allows to move a Type N thermocouple and measure the outer wall temperature along the tube's axis. The temperature profiles imposed by the different sources on the outer tube wall, using the same power for the electrical components, are measured and represented on Fig. 7.2.

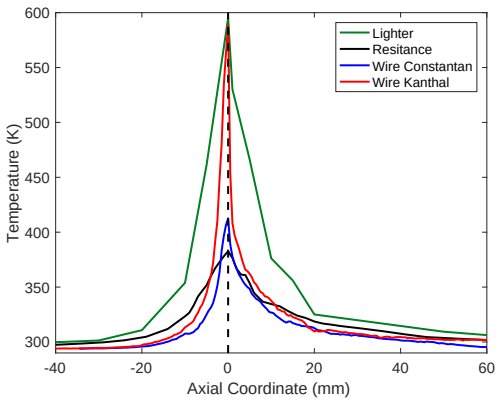

FIGURE 7.2 – *Wall temperature profiles using different heat sources : lighter, resistance, Constantin and Kanthal resistive wire. The same power is used for the electrical components.*

The thermocouple has a response time less than one second and is of a high accuracy in low temperature (T<1000 K), which allows to follow the time evolution of the temperature at a given point and its spatial evolution by gradually moving the thermocouple along the tube. The temperature profiles are obtained by averaging 500 temperature measurements at each spatial point, with a displacement step of 0.5 mm over 100 mm of total length in the horizontal configuration of the tube.

The temperature profiles represented in Fig. 7.2 confirm the choice of Kanthal

wire since it presents a temperature maximum close to the lighter, with a low profile width providing a high accuracy on the application point, its intensity can be easily controlled through the DC power supply, and it can be used in both horizontal and vertical configurations.

7.2.2 Kanthal resistive wire : Spatial characterization

A Kanthal wire is rolled around the quartz tube, inside which a flow speed corresponding to operating points is injected. The wall inner and outer temperature profiles are taken along the tube axis in horizontal position using a Type-N thermocouple. A scheme of the experiment is represented in Fig. 7.3.

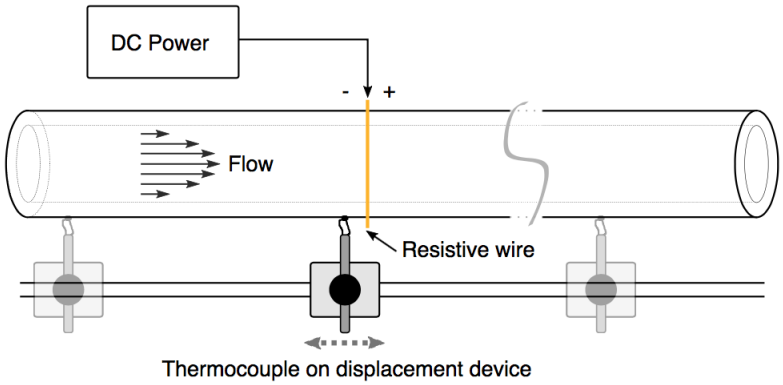

FIGURE 7.3 – *Scheme of the spatial characterization of the heating wire. The wire power is P=13 W, the mean flow speed is varied U=15 cm·s^{-1} and U=25 cm·s^{-1}. The displacement device course is 100 mm.*

The electrical power imposed to the wire is set to P=13 W. The resulting inner (red curve) and outer (black curves) temperature profiles are represented on Fig. 7.5(a) for two flow speeds U=15 cm·s^{-1} (plain lines) and U=25 cm·s^{-1} (dashed lines). It can be seen that the temperature maximum reached by the wall and gas are higher for U=15 cm·s^{-1}, namely for the lower flow speed. Thus the cooling area is shorter in low flow speed.
Considering the heat exchanges at the wall, three heat fluxes are relevant.
First, the conduction through the wall can be expressed as :

$$\Phi_{cd} = \frac{T_{\mathrm{w_i}} - T_{\mathrm{w_e}}}{R_{cd}} \tag{7.1}$$

where : $R_{cd} = ln(r_e/r_i)/\left(2\pi k_{\mathrm{w}} L\right)$ is the conduction resistance of the wall, and $T_{\mathrm{w_i}}$ and $T_{\mathrm{w_e}}$ are respectively the inner and outer wall surface temperatures.
Then, two heat exchanges occur from the outer surface wall to the ambient air, the natural convection and the radiation of the quartz, leading to a total flux

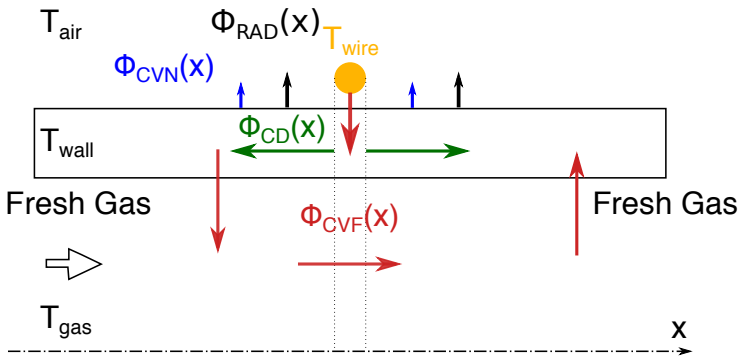

FIGURE 7.4 – *Scheme of the heat fluxes in half a tube, with the external wire, representing the axial conduction flux (Φ_{CD}), the inner gas forced convection flux (Φ_{CVF}) and the external fluxes of natural convection (Φ_{CVN}) and quartz radiation (Φ_{RAD}). The vertical links are handled through the cross exchanges terms in the energy equations.*

expressed as :

$$\Phi_{cvn+rad} = \frac{T_{\mathrm{w_e}} - T_0}{R_{cvn} + R_{rad}} \tag{7.2}$$

where : $R_{cvn} = 1/\left(h_{cvn} S_e\right)$ is the natural convection resistance, with h_{cvn}=14 $W \cdot m^{-2} \cdot K^{-1}$ the natural convection coefficient and S_e the external tube surface. $R_{rad} = 1/4/\left(\epsilon_q S_e T_0^3\right)$ is the radiation resistance with ϵ_q the quartz emissivity.
These fluxes are represented on Fig. 7.5(b) for both flow speeds U=15 cm·s^{-1} (plain lines) and U=25 cm·s^{-1} (dashed lines) using the temperature profiles represented on Fig. 7.5(a), centered on the wire position at $x = 0$.
Since the fluxes are defined from the inner to the outer wall surface, the resulting conduction flux of an external heating is mainly negative at the wire position. The positive areas of the conduction flux upstream and downstream from the wire position highlight the preheating of the wall and of the inner gas. Thus, an asymmetry of the temperature profiles and thereby of the fluxes reveals the influence of the inner gas forced convection.
In the positive area upstream from the wire (for $x < -2$ mm), the wall is heated by axial conduction and through convection preheats the incoming fresh gas and thereby the wall temperature drops in few tenth of millimeters to ambient temperature. In the positive area downstream from the wire (for $x > 2$ mm), the wall is also heated through longitudinal conduction in the quartz, however the gas heat retrocession to the wall allows to maintain an elevated temperature up to 40-50 millimeters from the wire.
At the temperatures imposed by the wire the quartz radiation is not very important.
The flux are greater at lower flow speed, due to longer residence time and higher

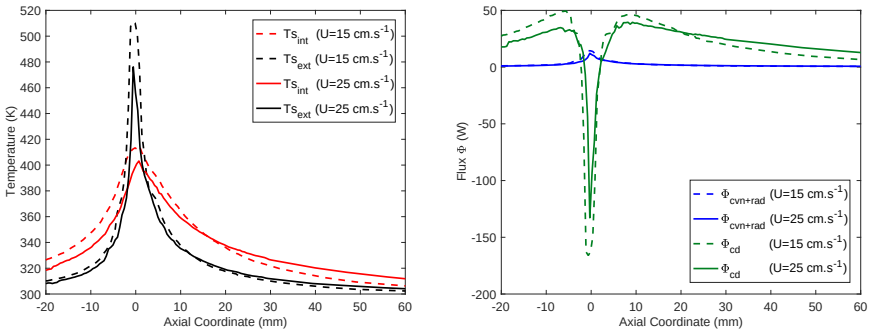

(a) Temperature profiles P=13 W (b) Heat fluxes profiles

FIGURE 7.5 – *(a) Inner (red curves) and outer (black curves) wall temperature ; (b) conduction (green curve) and natural convection added radiation of the solid (blue curve) fluxes ; for flow speeds of U=15 cm·s^{-1} (dashed lines) and U=25 cm·s^{-1} (plain lines). The resistive wire position is positioned at $x = 0$.*

temperatures. At lower speed the gas retrocedes its heat faster than at higher speeds, therefore the cooling area of the gas is shorter at low flow speeds. Thus, those profiles allow to analyse again the distances of influence of the heating system. Indeed, fifty millimeters downstream from the wire position, the inner and outer temperatures are almost back to ambient temperature, and thereby would have a limited impact if a flame is positioned at this distance.
In conclusion three phenomena occur. First, the efficiency of the convection is better at low flow speed since the maximum of temperature reached is higher. Thus, the temperature decreases faster, at low flow speed leading to a shorter cooling area. On the contrary at high flow speeds, the heated gas are transported further away from the flame front and exchange less with the wall leading to a longer cooling area. As a result, when studying the flashback at an operating point of high flow velocity the convection would be less efficient leading to higher a characteristical time of the unsteady phenomena. However, the heated gas would be transported further away, extending the action distance of the heat source.

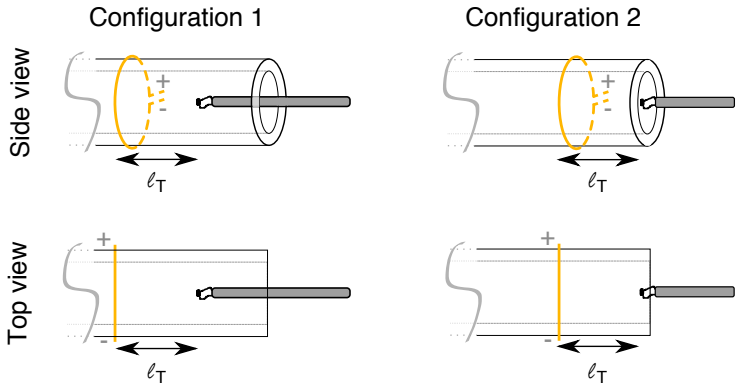

FIGURE 7.6 – *Schema presenting the two tested configurations of the thermocouple position inside the tube, in order to see the intrusive influence of the thermocouple support (represented in grey) and possible recirculation created by it. In the first configuration the thermocouple is inserted several centimeters inside the quartz tube. In the second configuration, only the weld of the thermocouple is placed inside the quartz tube, the support remains outside.*

7.2.3 Choice of a thermocouple configuration through temporal characterization of temperature measurements

In order to evaluate the effect of the intrusion of the thermocouple inside the quartz tube, two configurations schematically represented in Fig. 7.6 are compared. In the first configuration (Fig. 7.6 left) the thermocouple is inserted several centimeters inside the quartz tube conter-flow, with its support. In the second configuration (Fig. 7.6 right), only the weld of the thermocouple is placed inside the quartz tube, the support remaining outside.
The distance between the thermocouple weld and the heating wire is varied and the temperature is temporally characterized inside the tube at these different distances, represented in Fig. 7.7.
Figure 7.7(a) represents the temporal temperature comparison between the two configurations, made at a constant flow speed U=21.1 cm·s^{-1} and electrical power of the resistive wire P=17 W, for several distances between the heating wire and the thermocouple weld. The temperature profiles are fitted to an exponential function in order to extract the heating time constant τ_T. It can be observed that the maximum of temperature reached for distances ℓ_T from 5 to 50 mm is lower in the second configuration than in the first. This might be explained by the ambient air interaction with the internal gas at the end of the quartz tube, causing a drop in temperature. Thus, the maximum of temperature reached according to the distance between the wire and the thermocouple, represented in Fig. 7.7(b), depicts a decrease of maximum temperature reached with the increase of the distance for both configurations. Furthermore, at ℓ_T=5 mm, the

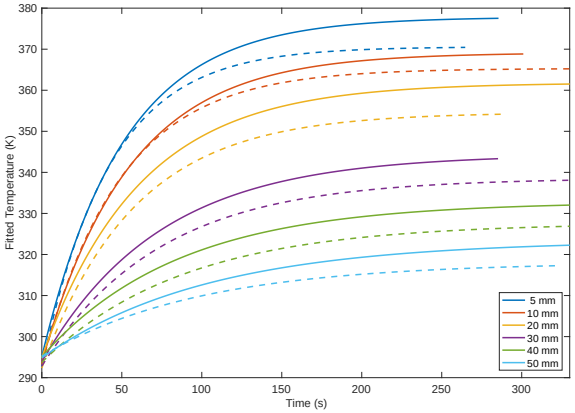

(a) Fitted Temperature evolution with time and distance from the wire for both configurations 1 (plain lines) and 2 (dashed lines)

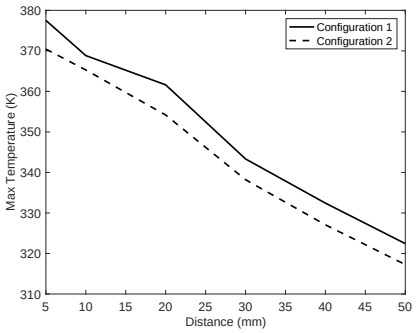

(b) Maximum temperature reached evolution with distance from the wire

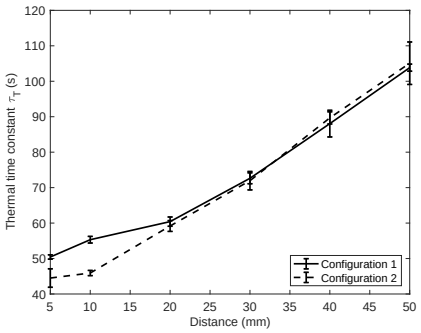

(c) Thermal time constant evolution with distance from the wire

FIGURE 7.7 – *Choice of thermocouple positioning by comparing the temporal thermal characterization of the resistive wire (a). The evolution of the maximum of temperature reached as well as the thermal time constant with the distance between the wire and the thermocouple are also represented in (b) and (c). The plain lines represent the results of configuration 1 and the dashed lines those of the configuration 2.*

maximum of temperature reached by the gas represents approximatively 6% of the adiabatic flame temperature. As a result if a motion of the flame is observed at 50 mm, the gas temperature increase represents 1% of the adiabatic flame temperature. Thereby the sensibility of the flame motion trigger can be assessed. The thermal characteristic time constant increase τ_T evolution with distance ℓ_T is represented in Fig. 7.7(c). The characteristic time increases with the distance, meaning that the gas takes more time to reach the maximum temperature as the distance between the wire and the thermocouple increase. The offset time is the only variable which evolution does not make sense. It can be explained by convertor non constant latences, and file registration, thereby it is not taken into account in this analysis.

Fixing the distance between the resistive wire and the thermocouple weld at ℓ_T=10 mm, the repeatability of the temporal temperature profiles is tested for both previously exposed configurations. The profiles are represented on Fig. 7.8. The plot lines represent an average of ten measurements in the same configuration, and the error bars show the standard deviation. The results of the first configuration are represented in plain line, and those of the second configuration are plotted in dashed line.

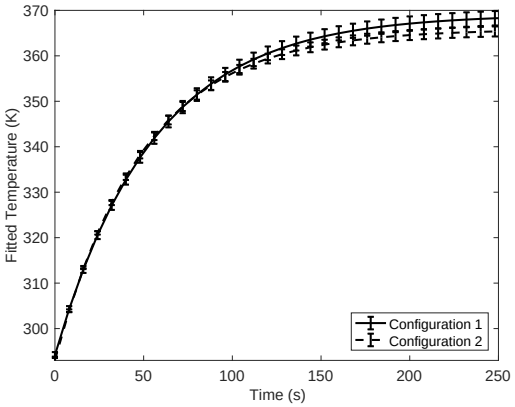

FIGURE 7.8 – *Repeatability on the temporal temperature characterization of the wire by varying the configuration of the thermocouple, at fixed distance ℓ_T=10 mm.*

It can be seen that the error bars show a good repeatability of the measurements, and a good reproduction of the temperature profiles for both configurations.
Finally, both configurations are similar in tendencies and in repeatability. It can be concluded that the thermocouple position does not have a great influence on the thermal characterization of the resistive wire. For the following measurements, the first configuration is used, in order to avoid all tampering of the inner gas temperature by ambient air.

7.2.4 Temporal characterization of the resistive wire for several distances ℓ_T, varying the flow speed

Using the first configuration of thermocouple positioning, the temporal thermal profiles of resistive wire at same electrical power (P=17 W) are characterized for two different mean flow speeds and for several distances ℓ_T between the heating wire and the thermocouple weld. The resulting profiles are represented in Fig. 7.9, where the plain lines correspond to a flow speed of U=21.1 cm·s^{-1} and the dashed lines represent U=16.6 cm·s^{-1}. The flow speed used are operating points flow speeds respectively of ϕ=0.8 and ϕ=0.75. The maximum of temperature reached as well as the thermal time constant evolutions with the distance ℓ_T are also represented in Fig. 7.9.

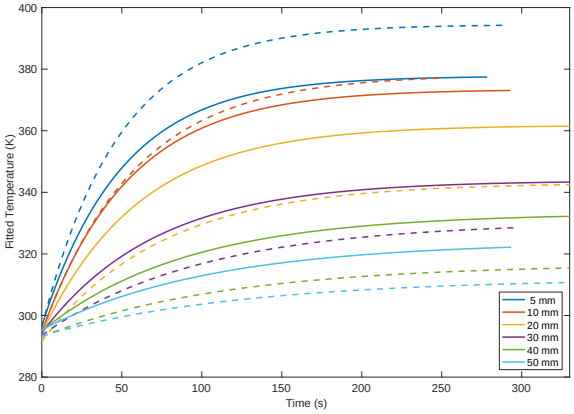

(a) Fitted Temperature evolution with time and distance from the wire

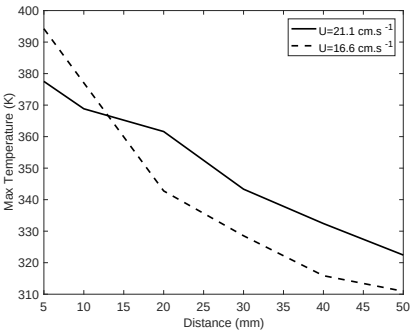

(b) Maximum temperature reached evolution with distance from the wire two flow speed

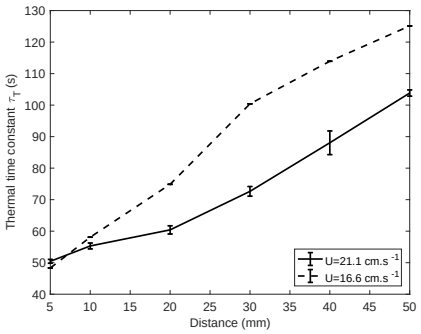

(c) Thermal time constant evolution with distance from the wire two flow speed

FIGURE 7.9 – *Temporal characterization of the wire by varying the configuration of the thermocouple for two flow speeds : U=21.1 cm·s^{-1} (plain lines) and U=16.6 cm·s^{-1} (dashed lines).*

For distances ℓ_T equal or under to 10 mm, the maximum temperature reached

is higher for the lower flow speed value (U=16.6 cm·s^{-1}), however, as shown in Fig. 7.9(b), few millimeters after ℓ_T=10 mm, this tendency is inverted, and the maximum of temperature reached is greater for higher flow speed. In fact due to lower flow speed, the gas residence time in the heating area is greater than for higher flow speed. Thereby for small distances between this heating area and the thermocouple the temperature is greater for lower flow speed. However as the distance increases, again with a greater residence time at lower flow speed, the heated gas exchanges more heat to the cold walls of the quartz tube and thereby the maximum of temperature reached drops under the temperature for higher flow speed, where the gas faster convected exchanges less with the walls, and thereby "stores" the temperature more efficiently. Moreover, as depicted in Fig. 7.9(c) the time constant of temperature increase is greater in the low flow speed case, meaning that the gas takes more time to reach its maximum. The flow speed has a great influence on the convection of the heated gas, thereby the temperature reached, and on the heating characteristic time. It must be taken into account in the comparison of flame displacement for different flow speeds.

7.2.5 Wire heating temporal characterization at fixed distance ℓ_T=10 mm, variation of several parameters

Several heating and flow parameters are varied to assess their influence on the thermal environment created by the resistance wire. The variation of the following parameters is processed at a fixed distance ℓ_T=10 mm between the thermocouple and the heating wire. The varied parameters are summed up in table 7.1.

Case	Parameter studied	Constant parameters
(a)	ϕ (0.7,0.8,0.9)	U=21.1 cm·s^{-1}
(b)	U [cm·s^{-1}]	ϕ=0.8
(c)	P [W]	ϕ=0.8 and U=21.1 cm·s^{-1}
(d)	R [Ω]	P=17 W and d=0.025 mm

TABLE 7.1 – *Sum up of the parameters varied to observe their influence*

The effect of the equivalence ratio on the temperature temporal evolution is represented on Fig. 7.10(a) for a fixed flow speed of U=21.1 cm·s^{-1}. The profiles are similar, meaning that the equivalence ratio has no impact on the temperature reached by the gas.
In Fig. 7.10(b), the influence of the flow speed on the temperature temporal evolution is tested at fixed equivalence ratio. As previously observed, the maximum temperature reached decreases with the increase of flow speed. Thus as shown on Fig. 7.10(e), the heating time constant τ_T also decreases with the increase of flow speed, meaning that the maximum of temperature is reached faster as the flow speed increase, which corresponds with gas convection.

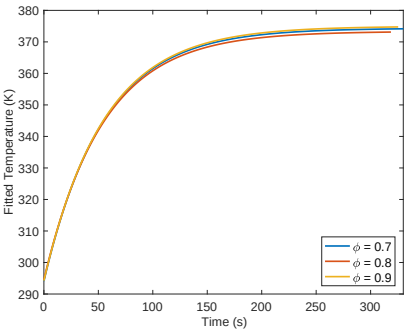

(a) Equivalence ratio variation U=21.1 cm.s^{-1}

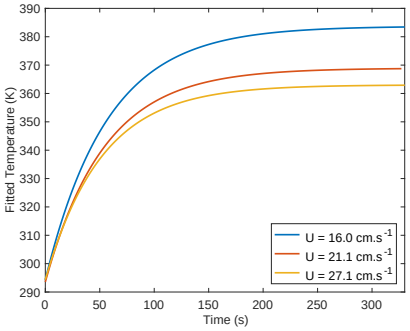

(b) Flow speed variation ϕ=0.8

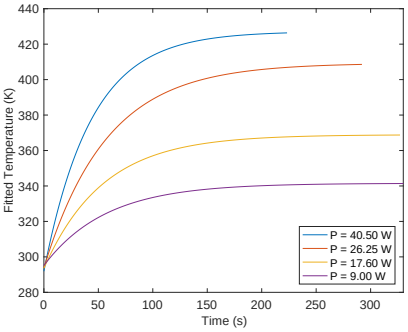

(c) Power variation (ϕ,U)=(0.8, 21.1)

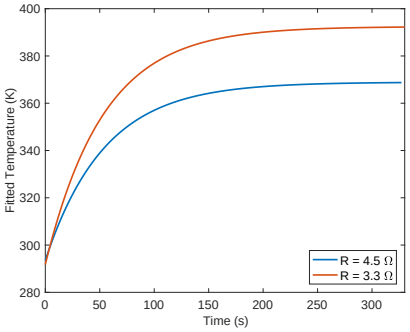

(d) Resistance variation (P,⌀)=(17,0.025)

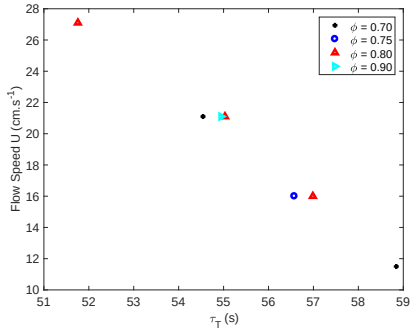

(e) Flow speed with thermal time constant

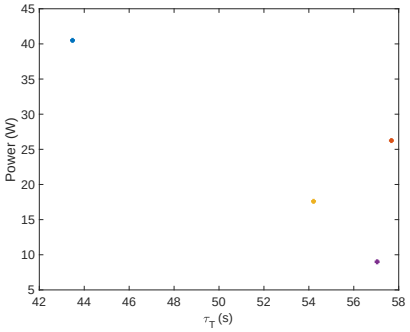

(f) Power with thermal time constant

FIGURE 7.10 – *Temporal characterization of the wire by varying the equivalence ratio (a), the flow speed (b), the wire power (c), the wire electrical resistance (d). Flame speed (e) and power (f) are plotted against the thermal time constant.*

The temperature profiles with electrical power variation represented in Fig. 7.10(c) show that the temperature maximum reached by the gas increases with the increase of power. Thus, Fig. 7.10(f) shows that the thermal time constant globally decreases with the increase of electrical power.
Finally, Fig. 7.10(d) depicts the variation of resistance of the wire at same

power (P=17 W), showing that the increase of resistance induces a decrease of maximum temperature reached. The DC power supply being limited in intensity and voltage, the wire resistance is chosen to have a better adaptability to the power supply.
In conclusion, the previous subsections allowed to assess the influence of heating and flow parameters of the establishment of the thermal profile by the resistive wire. Indeed, the sensitivity of the motion trigger to temperature increase can be analyzed through the profiles at several distances between the wire and the flame front. Thus, the flow speed and electrical power are shown to have an influence on the heating time constant and on the maximum temperature reached. The heating wire used for the following experiments is also characterized with an electrical power of P=17 W, the inner gas reaches a maximum temperature of T_{g_i}=400 K and with a heating time constant around 50 s. These data can be of use to understand the flame motion phases and to reproduce numerically the heating provided by the wire.

7.3 Flame characterization during flashback

The flashback studied in this section is slightly different from the one presented in the introduction of this chapter using a lighter as heat source. In fact, the goal was to provide a heat source more localised, with a high maximum temperature. Two pictures of the studied horizontal configuration are depicted in Fig. 7.11(b). The top picture shows the flame downstream from the wire, which is not powered on, while the bottom picture shows the flame upstream from the flame after the flashback, with the resistive wire powered on.
The influence of several variables is studied. Those parameters are the operating points (speed and equivalence ratio), the distance ℓ_T between the resistance wire and the flame front represented in Fig. 7.11(a) and finally the electrical power imposed to the wire. In the previous section the influence of those parameters on the thermal characterization of the wire was carried out. The results are then analyzed in the light of the effects of these parameters of the wire.
The flame characterization during flashback is carried out by position and shape tracking. The position and the motion of the flame in the tube can be recorded by a standard reflex camera shooting series of individual pictures. The recording and the wire are powered on simultaneously to observe the evolution from the stable position. The video is decomposed frame by frame and the flame position and shape are tracked using an edge/contour selecting routine. Knowing the time between two frames and the position of the flame, a mean displacement velocity can be calculated.

7.3.1 Flashback characterization at a fixed distance ℓ_T=10 mm

The first results on the flame flashback are given at a fixed distance flame front-wire ℓ_T=10 mm and for flames at a fixed operating point of ϕ=0.8 and

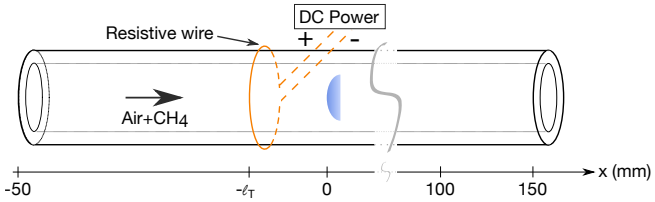

(a) Flashback general schematic presentation

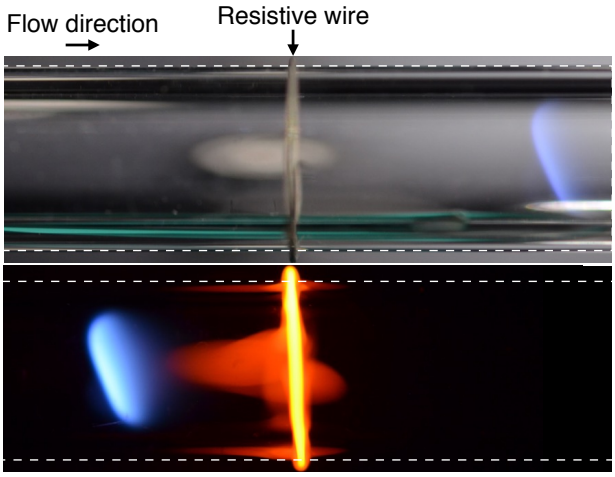

(b) Spontaneous flame emission before and after flashback

FIGURE 7.11 – *General scheme and images of flashback configuration with a resistive wire. The flow direction is from left to right.*

U=21.1 cm·s^{-1}. The flame propagation speed with respect to the tube and the flame position in the tube are plotted in Fig. 7.12. The error bars are the standard deviations determined by repetition of the experiments with the same initial conditions. The green circles on the displacement curve highlight the time when the flame has traveled respectively 5,10 and 15 mm, namely ℓ_T=5 mm, ℓ_T=0 mm and ℓ_T=-5 mm.

The flame motion can be decomposed in two phases. The first phase is characterized by a fast continuous displacement, from t=0 s to t≈100 s when the flame reaches the resistance wire position at 10 mm. During this phase, the flame accelerates drastically then decelerates. The flame reaches a peak of propagation speed during a short lapse of time, and then decreases to reach the wire with a speed lower then 50 μm·s^{-1} (0.005 cm·s^{-1}). This phase lasts about 100 s. The second phase starts at the vicinity of the resistive wire position (located at 10 mm). It is characterized by a slow displacement speed. The flame propagation speed slowly decreases toward zero and the flame tends asymptotically to a new steady position. The heating power can then be switched off, the flame will stay at its new position, it is anchored in the vicinity of the new maximum

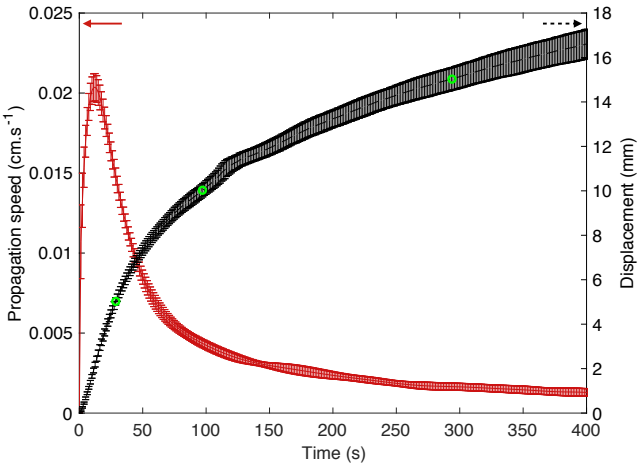

FIGURE 7.12 – *The flame displacement (black curve) is tracked in time by video recording and the flame mean propagation speed (red curve), is calculated with the distance traveled between two frames. The green circles on the displacement curve show the time when the flame has traveled respectively 5,10 and 15 mm, namely ℓ_T=5 mm, ℓ_T=0 mm and ℓ_T=-5 mm. An average of several repetitions of the experiment is made and the error bars represent the standard deviation.*

temperature location in the tube.
As the flame travels in the tube at different velocities, its shape and orientation also evolve. From the frames recorded during the motion, the flame emission is fitted to an ellipse by an auto correlation method and the eccentricity and area of the fit are recorded for each frame. The eccentricity and the flame angle with respect to the horizontal axis are plotted as a function of time in Fig. 7.13. The time scale stops when the flame reaches the heating wire, meaning that only the first phase of the displacement is represented. As for the displacement and propagation speed, the plot is the average over several repetitions of the experiment, and the error bars represent the standard deviation between those repetitions. This tracking shows that the flame changes its shape to compensate the sudden increase in heat and flow velocity when quickly moving toward the heat source. Indeed, in a first stage, the flame's eccentricity drops when the flame starts moving meaning that the flame bends, leading to a shape closer to a circle and an increase of the flame area as shown in the left snapshot of the flame edges. During this stage, the flame angle with the horizontal axis increases, which means that the flame straightens up. When the flame loses speed, a second stage starts where the eccentricity grows back to its initial value and the flame area decreases to its original value. In addition, the flame tilts back to its initial orientation as shown in the right snapshot of the flame edges. Once the flame has overcome the wire and is in the slow phase of displacement, the flame takes back its original shape and orientation as it moves asymptotically to a new stable position.

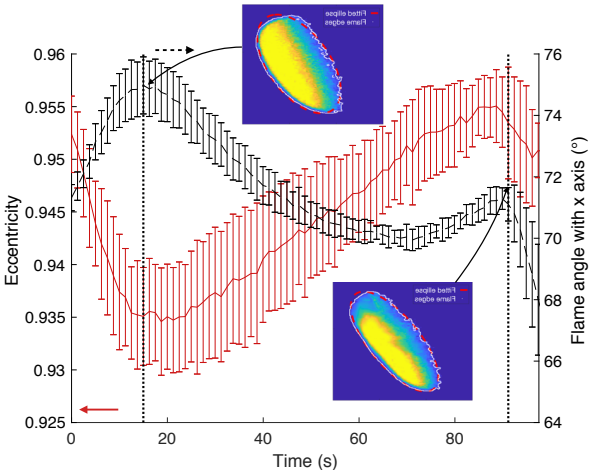

FIGURE 7.13 – *Evolution of the eccentricity (red plain line) and flame's angle with the horizontal axis (black dashed line), during the flashback. The graph only represents this evolution from the moment where the heating wire is powered on to the moment where the flame reaches the wire. The plots are an average of several repetitions and the error bars are the standard deviation. Two snapshots of the flame edges are represented in an equal frame to highlight the change in flame shape and orientation. The vertical frame is limited by the inner wall frontier.*

The response of the flame to the temperature perturbation induced by the heating wire is a displacement toward the heating source then a stabilization to a new position. By changing the temperature distribution surrounding the flame, its propagation speed was modified to induce the displacement. The speed variation is small but sufficient to be observed and to lead the flame to a new stable position.

7.3.2 Influence of the wire-flame front distance ℓ_T on the flame flashback

The influence of the distances ℓ_T=5, 10, 20, 30, 40 and 50 mm between wire and flame on the flashback is assessed. The flame motion and speed are represented in Fig. 7.14.

Two motion modes can be distinguished in Fig. 7.14(a). For wire-flame distances under ℓ_T=10 mm, the motion can be described as a root square function, with two phases. First a sharp displacement from the start followed by a slow stabilisation. The tangent slope at the origin increases with the distance.

For wire-flame distances over ℓ_T=20 mm, a three-phase motion is observed. The first phase can be described as an exponential increase of the distance. The tangent slope at the origin decreases with the increase of distance. The second phase is characterized by a peak in the flame speed and therefore a sharp increase in the flame motion, until reaching the vicinity of the heated

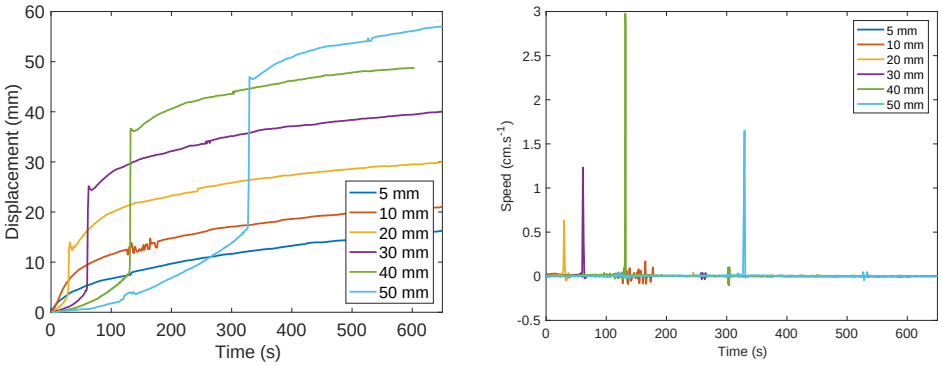

(a) Flame displacement (b) Flame propagation speed

FIGURE 7.14 – *Flame displacement (a) and propagation speed (b) at equivalence ratio ϕ=0.8 for distances between the heat source and the flame front from 5 to 50 mm.*

area. The second phase ends upstream from the wire position. Near this region, the flame moves on to the third motion phase, with a low speed displacement towards stabilization, equivalent to the second phase of the first motion mode. Figure. 7.14(b) represents the flame propagation speed along the recording time. A peak in flame propagation is observed corresponding to the second phase of the second motion mode. It can be noted that the maximum propagation speed increases until 40 mm and then decreases. The maximum propagation speed is of the order of cm·s^{-1} which is two orders of magnitude above the propagation speed for wire-flame front distances of 5 or 10 mm.

These two modes and different phases can be linked to thermal phenomenon. The temperature profile of external tube wall inside which a flame is stabilized at an operating point of ϕ=0.8, U=21.1 cm·s^{-1} is plotted in Fig. 7.15. The zero coordinate marks the flame front. On this, graph, the inner wall temperature imposed by the resistive wire at different distances ℓ_T=5, 10, 20 and 40 mm are superimposed on Fig.7.15. This graph allows to understand the thermal exchanges implications on the phases of flame motion.

For distances ℓ_T under 20 mm, the wire is located in the gas and wall preheating area of the flame. This area was referred before as indirect excess enthalpy, since the fresh gases are preheated trough axial heat conduction in the wall. Therefore both thermal environment of the flame and the wire are overlapping and the flame is already in the thermal environment of the wire through conduction in the wall. The movement is therefore slow since the gas and wall are preheated few millimeters upstream from the flame front.

For distances ℓ_T above 20 mm, the profiles appear more separated. Therefore first the flame receives heated gas through inner gas convection, which increases its speed and it starts moving slowly towards the wire : it is the first phase of the motion mode. When the flame has moved away from its thermal environment (wall temperature profile), but reaches the heated walls from the wire,

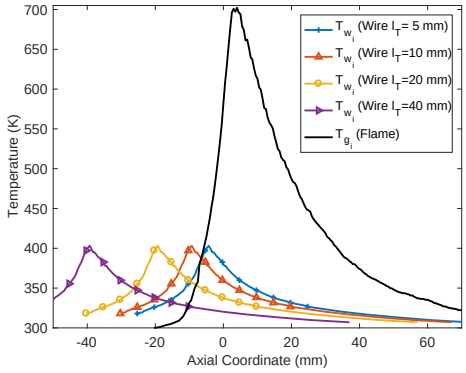

FIGURE 7.15 – *Flame temperature profile at an operating point of ϕ=0.8, U=21.1 cm·s^{-1} where the zero coordinate marks the flame front, with superimposed temperature profiles of resistive wire placed at different distances ℓ_T.*

it accelerates since the flame propagates upstream over heated walls, it is the second phase of the motion mode. This isothermal propagation stops around the wire position where the temperature in the wall is maximum, which marks the beginning of the third phase.

7.3.3 Influence of the operating point variation on the flame flashback

The variation in operating points modifies the methane mass flow and thereby flame power as well as the flow speed, both having an impact on the flame shape and behavior, but also on the establishment of the wire temperature profile. The flame displacement is represented in Fig. 7.16 for two operating points, at ϕ=0.75 U=16.6 cm·s^{-1} (dashed lines) and at ϕ=0.8 U=21.1 cm·s^{-1} (plain line).
For all distances the end positions are similar. For ℓ_T=5 and 10 mm, the flame motion and speed are very similar for the two operating points. However in the close-up represented in Fig. 7.16(b), at ℓ_T=10 mm (red curve) a discrepancy starts to appear in the flame motion, with a sharper displacement in the first phase of the motion for the lower flow speed. A focus is made on flame propagation speeds during the second phase of the second motion mode. Therefore the speeds represented in Fig. 7.14(b) are centered on the maximum and plotted for both equivalence ratio on Fig.7.16(c), as a function of the recording time. For greater distances between the heat source and the flame front, it can be seen that propagation speeds are comparable.
The difference lays in the characteristic time to reach the end position, namely the time of the first phase of the motion mode. This characteristical time, summed up in table 7.2, is clearly reduced for the lower equivalence ratio/flow speed operating point.

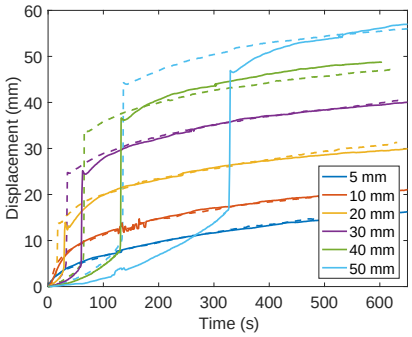

(a) Flame displacement

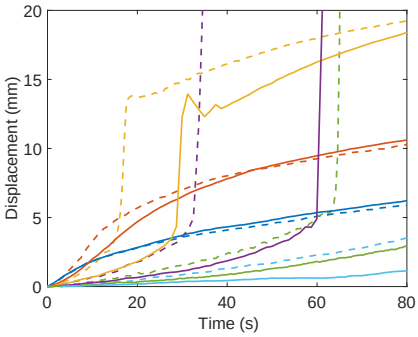

(b) Flame displacement close-up

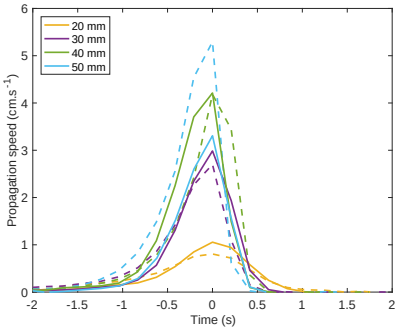

(c) Flame propagation speed V_p

FIGURE 7.16 – *Flame displacement (a) and (b) and flame propagation speed during the second phase of the motion mode (c) at operating points ϕ=0.75 U=16.6 cm·s^{-1} (dashed lines) and ϕ=0.8 ϕ=0.8 U=21.1 cm·s^{-1} (plain lines) for distances between the heat source and the flame front from ℓ_T=5 to 50 mm.*

Distance (mm)	Time (s) for ϕ=0.75	Time (s) for ϕ=0.80
20	18.7	31.2
30	35.0	62.4
40	65.8	132.5
50	136.2	329.6

TABLE 7.2 – *Sum up of the time when the flame reaches the end of the second phase*

7.3.4 Comparison between horizontal and vertical configuration motion of the flame

The comparison of the flashback of a flame at a same wire-flame distance of ℓ_T=10 mm between horizontal (left) and vertical (right) configurations is depicted in Fig. 7.17, decomposed in three times t=5, 100 and 600 s of the motion. The same operating point is chosen for both configuration, with an equivalence ratio ϕ=0.8 and a mean flow speed U=21.1 cm·s^{-1}. The vertical images are represented with a clockwise rotation of 90°.

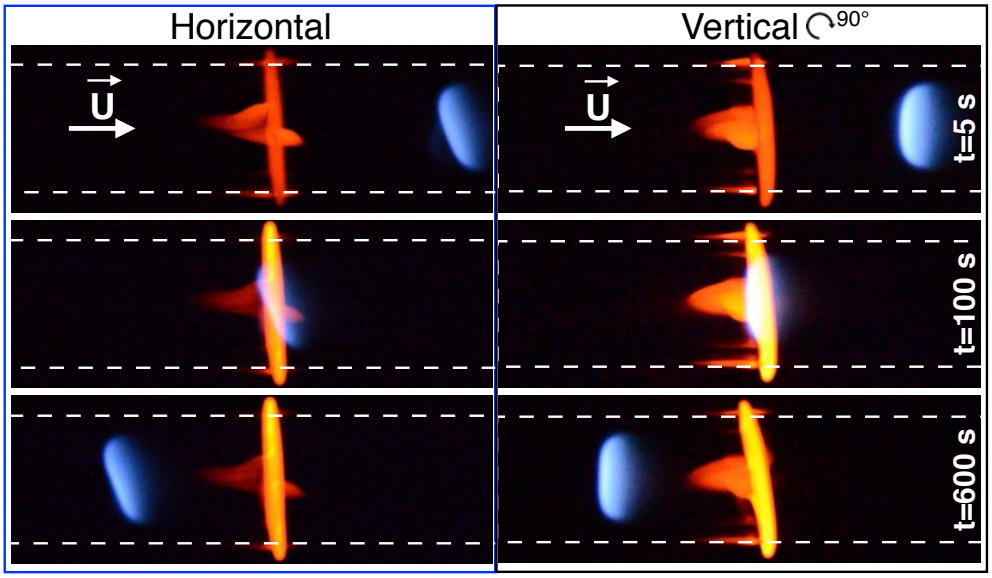

FIGURE 7.17 – *Flame image evolution in the case of a heating wire placed at ℓ_T=10 mm and (ϕ,U)=(0.8, 21.1 cm·s^{-1}) for horizontal (left) and vertical (right) configurations, at three times, t=5, 100 and 600 s.*

It can be seen that the flame shapes and orientations are notably different in the two configurations. The displacement and speed of the flame during flashback are represented in Fig. 7.18.

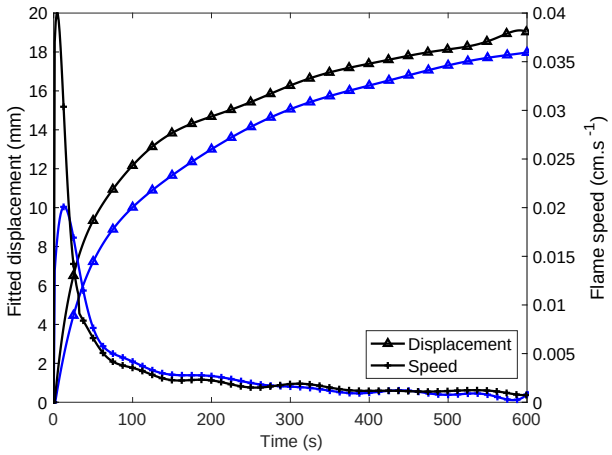

FIGURE 7.18 – *Flame displacement and speed in the case of a heating wire placed at ℓ_T=10 mm and (ϕ,U)=(0.8, 21.1 cm·s^{-1}) for horizontal (blue curve) and vertical (black curve) configurations.*

In the first phase of the motion, the flame displacement and speed are greater in the vertical tube positioning. The maximum propagation speed is doubled

in vertical. Thus, in horizontal configuration, the time to reach the maximum speed is greater than in vertical, the flame reaction to the heat input is then slower. In the second phase, the gap between the displacement is reduced, however the overshoot for the vertical configuration remains greater than for the horizontal.
The flame shape and orientation is also tracked during its flashback in both tube positioning. As a result, the shape and angle of the flames in both configurations are represented in Fig. 7.19 by the eccentricity (left) and the angle of the fitted ellipse with the tube's axis (right).

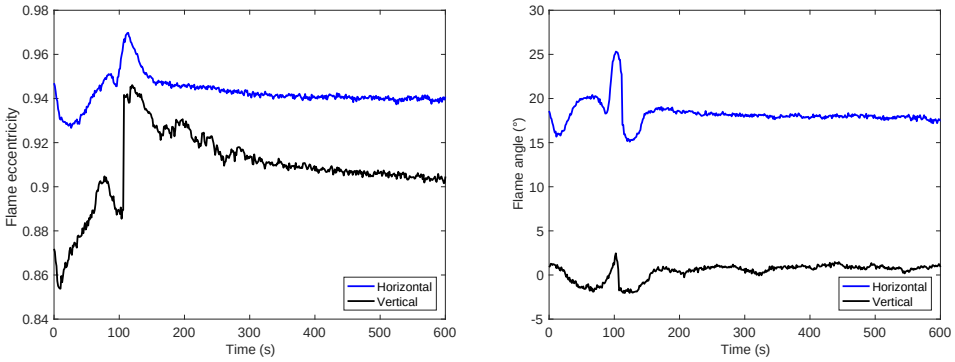

(a) Flame eccentricity evolution

(b) Flame angle evolution

FIGURE 7.19 – *Flame eccentricity and angle to vertical and horizontal evolution for respectively the horizontal (blue curve) and vertical (black curve) configurations.*

One can see that the flame in vertical configuration is more circular with a lower eccentricity than in horizontal. Thus, the flame's angle to the tube's axis shows a slight variation of ±5 degrees during the motion in both configurations, with a stabilization at the initial value in the second phase of the motion. As previously stated, at this operating point, the mean angle of the flame to the tube axis is around 20° in horizontal while it is close to 0° in vertical.
This comparison between horizontal and vertical configuration shows the impact of gravity on the configuration. In fact the motion in vertical configuration is promoted by gravity since the gas density lowers when heated, and thereby is convected downstream faster than in the horizontal configuration. This phenomenon explains the slower reaction of the flame in the horizontal configuration, but also the lower speed and displacement. The literature review on the effect of gravity on vertical tube was carried out in chapitre 1.
In this section the characterization of a flame during flashback induced by a heating wire placed upstream from the flame front was carried out. According to the distance between the wire and the flame front ℓ_T, two motion modes were observed : a continuous mode in two phases for ℓ_T under 20 mm and a disrupted three phases motion mode for ℓ_T above 20 mm. These two modes

were linked to thermal exchanges phenomena of gas convection and conduction through the wall. Thus the variation of the operating point, has an impact on the flashback since the mean flow speed to reach flame stabilization differs from one operating point to another. It is observed that the displacement are very similar in tendency and final position reached. Thus the speeds reached during fast motion are similar. The difference lays for ℓ_T above 20 mm, where the distance travelled by the flame during the first phase of the motion is greater for higher mean flow speeds. Therefore the characteristical time of this phase is likewise greater for higher mean flow speeds. Furthermore, a comparison between flame flashback in horizontal and vertical tube position is carried out at fixed distance ℓ_T. It is shown that the propagation speed reached during flashback in vertical is twice as great as in horizontal. It is linked to the gravity effects parallel to the tube's axis promoting the flame motion upstream in vertical configuration.
In the following section, the flashback will be reproduced using a one-dimension complex chemistry code by imposing a temperature profile in the surrounding air upstream from the flame.

7.4 Computation of the thermal flashback solved with 1-D complex chemistry code (REGATH)

Numerically, the objective is to reproduce the flashback phenomenon experimentally observed by imposing in the complex chemistry code REGATH previously described in chapitre 5, a temperature profile in the external ambient air upstream from a stabilized flame front. After several iterations the temperature profile is transmitted to the wall and then to the fresh gas by conducto-convection heat transfers. The gravity is not taken into account in the present work computation. Indeed, it was shown in chapitre 6 that the buoyancy effects have an impact on the flame shape, however since in one-dimensional the flame shape is not reproduced, the gravity effects are de-coupled from the thermal ones. The aim is then to understand the thermal phenomena involved in the flame flashback in response to an upstream heat source.
The mass flow is progressively adapted to obtain a stabilized flame, but the flame has no anchor point contrary to steady computation. Using this "moving front" one-dimension modelization, the flashback is reproduced.

7.4.1 Characterization of the numerically imposed heating source

The temperature profile imposed in the surrounding air is a gaussian type, with three input parameters, σ_g the gaussian width characteristic, T_{max} the maximum of the imposed temperature at the coordinate x_p. The equation of

the gaussian is given by :

$$T_a(x) = T_0 + (T_{max} - T_0) \exp\left(-\frac{(x - x_p)^2}{2\sigma_g^2}\right) \tag{7.3}$$

The profile centered coordinate is defined as : $x_p = x$(Flame Front)-ℓ_T. Two gaussians, with different width, are compared in Fig. 7.20 to the experimental temperature external wall profile imposed by the wire.

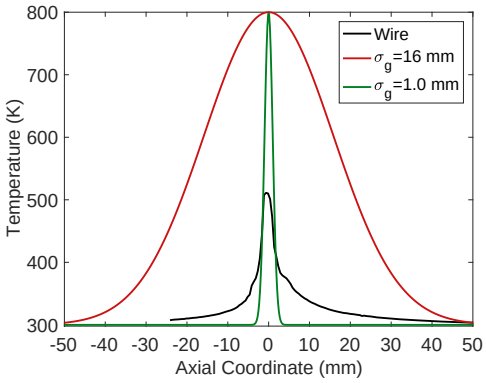

FIGURE 7.20 – *Gaussian temperature profile for two values of σ_g=16 mm and 1 mm, with x_p=0, compared to the experimental temperature profile of the external wall imposed by the heating wire.*

According to the input of temperature and the distance between the flame front and the temperature profile, the computation time differs greatly. A cartography of distances and temperatures is carried out to characterize the flame motion during flashback.

7.4.2 Spatial characterization of the heat source imposed to the surrounding air

The first step is to describe the temperature profile imposed from the ambient air to the inner gas, depending on the the temperature maximum chosen and the gaussian width characteristic σ_g.
The temperature profiles of external air (dotted line), wall (dashed line) and inner gas (plain line) at t = 150 s are represented on Fig. 7.21, for a profile defined by T_{max} = 800 K, σ_g=16 mm and ℓ_T=106 mm. At this selected time, t = 150 s, the temperature profiles are established in the wall and in the gas.
At t=150 s, the temperatures in the wall and in the gas have reached their maximum, and the flame front starts to move toward the heat source. The maximum temperatures reached by the wall and gas are lower than the imposed temperature in the ambient air due to external heat losses and axial heat transfers. The conduction in the wall leads to a local increase of the temperature at the heat source position (Fig. 7.21(b)), the wall temperature then

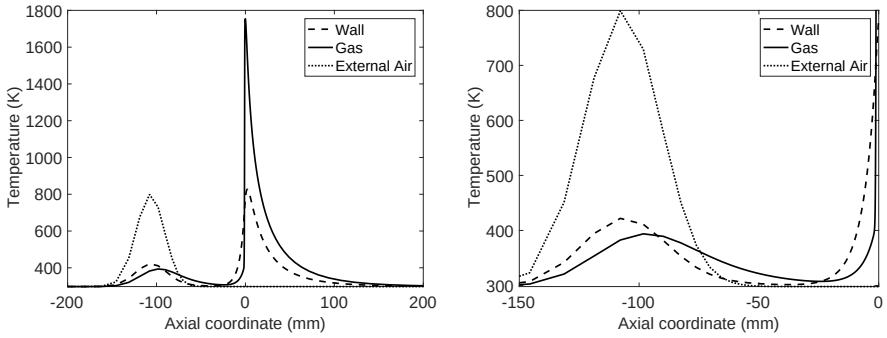

FIGURE 7.21 – *Temperature profiles of the external air (dotted line), wall (dashed line) and gas (plain line), for T_{max} = 800 K, σ_g=16 mm and ℓ_T=106 mm in global view (left) and close-up on the heating source (right). The zero coordinate marks the initial position of the flame front.*

drops close to the fresh gas temperature, and starts increasing again tenth of millimeters upstream from the flame front. The inner gas convection leads to an increase of temperature slightly downstream from the heat source, followed by a gas cooling with a decreasing slope lower than in the wall. The hypothesis is that the gas preheated by the wall at the heat source flows to the flame front area, and increases the mixture enthalpy and therefore the flame speed, which will start to move upstream since the mass flow rate is constant. The flashback would then be triggered by the convection of preheated gas to the flame front. The width of the gaussian profile is crucial to the flashback characterization in terms of characteristical time, and motion modes since the energy deposited varies. Its variation impact on the flashback is studied in the following sections.

7.4.3 Temporal characterization of the heating source

The second step is to describe the temporal evolution of temperature from the ambient air to the inner gas. The temperature profile is progressively imposed in order to reproduce the heating wire behavior with a temperature increase time constant similar to the one of the experiment ($\tau_T \approx 50\ s$). The wall and gas temperature increases as a function of time are represented on Fig. 7.22 taken at the maximum temperature coordinate x_P of the heat source profile.
The wall and gas temperatures follow an exponential increase which heating time constants, respectively τ_w=38 s and τ_g=42 s are printed on the graph. The heating constant and the maximum of temperature reached are of the same order as in the experiment.
The temperature profiles on the computed domain with the heating source placed at a distance ℓ_T=106 mm of a stabilized flame is represented in Fig. 7.23. The gaussian temperature profiles imposed by the heat source in the wall (dashed lines) and in the gas (plain lines) are depicted for several times from 0 to 240 s. As the wall temperature profile is centered at ℓ_T=106 mm, the gas tempe-

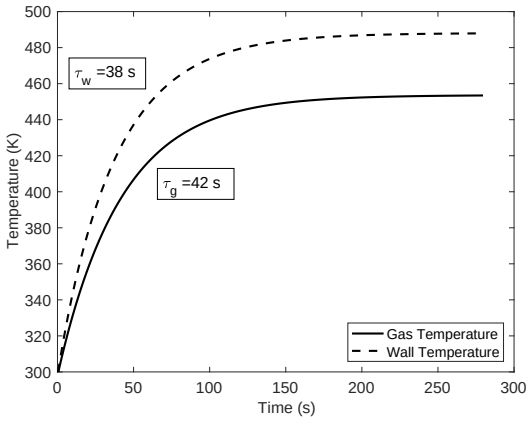

FIGURE 7.22 – *Evolution of the wall and gas temperature with time at the local maxima of heating.*

rature maximum is positioned slightly downstream due to inner gas convection. The gas temperature increases progressively due to the quartz wall inertia. The coupling between the wall and the gas is clearly observed, since the increase in wall temperature induces an increase in gas temperature and an increase in gas speed. Therefore, locally an increase of the mass flow rate is observed upstream from the flame front.

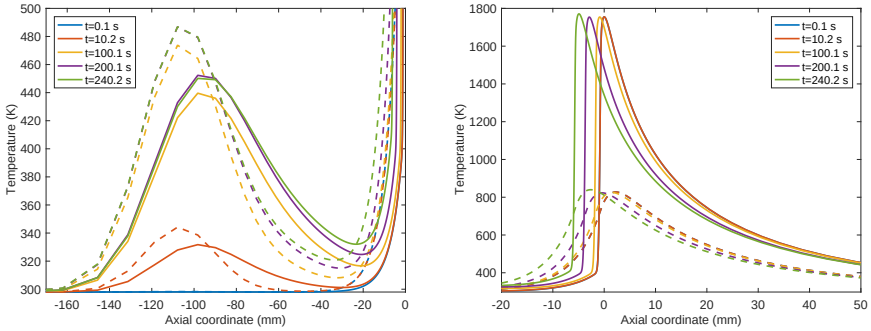

(a) Close-up on the external heat position : wall preheating steps at ℓ_T=106 mm

(b) Close-up on flame front front

FIGURE 7.23 – *Evolution of the gas (plain lines) and wall (dashed lines) temperature profiles as a function of the axial coordinate for several times from t =0 to 240 s, with an external temperature profile characteristics : T_{max} = 800 K, σ_g=16 mm and ℓ_T=106 mm. The stabilized flame front is located at the zero coordinate.*

The upstream displacement of the flame front, represented by the peak of the gas temperature initially at $x = 0$ mm, is notable on Fig. 7.23. As observed in the experiments, the propagation speed of the flame front depends on the heating temperature profile and the distance between the flame and the heating source. Therefore, the influence of both parameters is tested in the following.

Calculated from the temperature profiles of the gas and the wall, the inner forced convection Φ_{cvf}, outer natural convection Φ_{cvn} and radiation Φ_{rad} fluxes are represented on Fig. 7.24 for the same case. The conduction flux could not be calculated since the temperature is not solved radially but only axially, due to the choice of a one-dimensional computation.

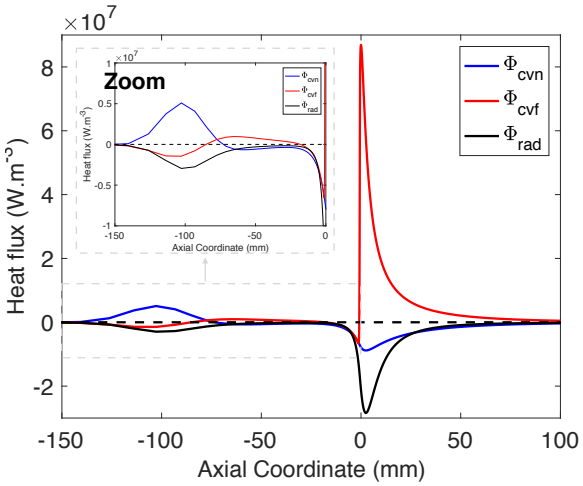

FIGURE 7.24 – *Evolution of the outer natural convection (Φ_{cvn}), inner forced convection (Φ_{cvf}) and radiation (Φ_{rad}) heat flux with a stabilized flame at the zero axial coordinate and an external heating with T_{max} = 800 K, σ_g=16 mm and ℓ_T=106 mm*

The forced convection flux observes a negative peak at the heating source coordinate revealing the energy input, followed by a positive plateau reaching the flame preheating area which characterizes the heated gas convection. On the contrary, the natural convection shows a positive peak at the heat source coordinate since the local ambient temperature is superior to the wall temperature in this area. Thus, in the two areas where the quartz is heated, namely the heat source and the flame, the radiation flux shows a negative peak, greater than the natural convection in the flame front, again revealing the importance of the radiation. Different parameters of the temperature profile show impacts on the flame flashback. Their variation is studied in the following section.

7.4.4 Parameter variation impact on the flashback

The impact of the variation of different parameters on the flashback is studied. The parameters varied are : the distance between the heat source and the flame front ℓ_T, the maximum of temperature imposed T_{max}, the gaussian width σ_g and the operating point characterized by the couple (ϕ,U). A sum up of the variable and fixed parameters is given in table 7.3.
In the following, the displacement profiles are extended by dashed lines of the same color starting from the converged point to reduce the computing time and in order to have a better visualization of the profiles. Thus, the displacements

Variable	Fixed	Subsection
σ_g	ϕ=0.8 ;T_{max}=800 K ; ℓ_T=10 mm	7.4.4.1
ℓ_T	ϕ=0.8 ; σ_g=16 mm ; T_{max}=800 K	7.4.4.2
ℓ_T	ϕ=0.8 ; σ_g=1 mm ; T_{max}=800 K	7.4.4.2
T_{max}	ϕ=0.8 ; σ_g=16 mm ;ℓ_T=10 mm	7.4.4.3
T_{max}	ϕ=0.8 ; σ_g=1 mm ;ℓ_T=10 mm	7.4.4.3
(ϕ,U)	ℓ_T=10 mm ; σ_g=16 mm ;T_{max}=800 K	7.4.4.4
(ϕ,U)	ℓ_T=30 mm ;σ_g=16 mm ;T_{max}=800 K	7.4.4.4
(ϕ,U)	ℓ_T=10 mm ;σ_g=1 mm ;T_{max}=800 K	7.4.4.4

TABLE 7.3 – *Sum up of the varied parameters to study their impacts on flame flashback*

of the flame are negative since the flame propagates in the opposite direction of the flow. The displacements are however represented in absolute value to a better comparison.

7.4.4.1 Variation of the width σ_g of the gaussian profile

The width of the gaussian profile is a crucial parameter since it determines the energy input to the system and the distance between the flame front and the downstream end of the temperature profile imposed by the heat source. The width is varied between σ_g=0.85 mm to σ_g=22 mm, for fixed parameters of equivalence ratio ϕ=0.8, a maximum temperature of T_{max}=800 K and a distance between the heat source and the flame front of ℓ_T=10 mm. The resulting displacement curves are represented in Fig. 7.25(a). Two cases are selected to further comparison of the effect of the width on the flashback : σ_g=16 mm and 1 mm. Thus, the flame displacements of these two cases are isolated in Fig. 7.25(b). For the two widths, the extremum coordinates at which the external temperature starts to be greater than 300 K are registered to demarcate the imposed profile. These limits of the temperature profiles, upstream and downstream from x_p are represented in red and green dotted lines in Fig. 7.25(a), respectively for σ_g=16 mm and 1 mm. In the case of σ_g=16 mm, only one extremity of the external profile is represented since the other one is negative. As the gaussian width increases, the energy deposited also increases and therefore as is the tangent slope at the origin, leading to sharper propagation speed and a convergence at different final distances. Indeed the profile being wider, the flame moves further away from the maximum of temperature (set at ℓ_T=10 mm) since it continues to receive preheated gases, which increase the mixture enthalpy and therefore the flame speed. The flame stops it motion when the imposed external temperature profile has no more impact on the wall nor the inner gas temperatures. However, as depicted in Fig. 7.25(b), the flame steady position is located downstream from the extremity of the imposed temperature profile.

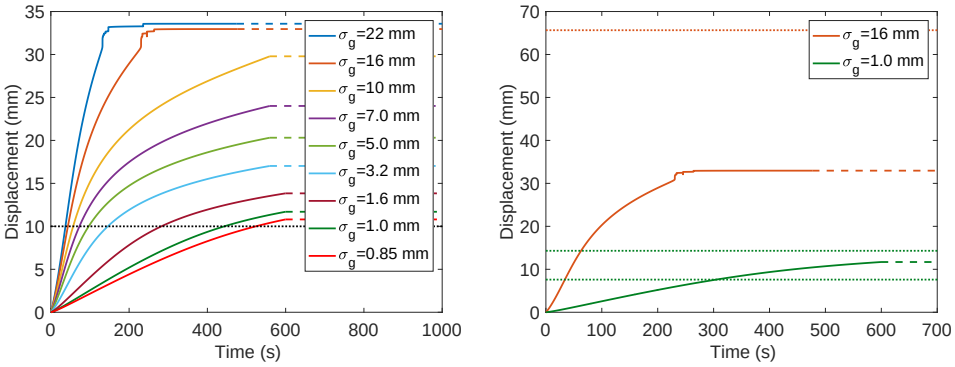

FIGURE 7.25 – *Evolution of the absolute value of the displacement as a function of time with a variation of the gaussian width for : T_{max}=800 K, ℓ_T=10 mm, ϕ=0.8. The dotted lines demarcate the limits of the imposed external profile in green for σ_g=1 mm and red for σ_g=16 mm. Only one limit of the σ_g=16 mm profile is represented, since the other limit is negative.*

To better visualize the evolution of the temperature profiles according to the external heat source profile, the initial and final wall and gas temperature profiles are represented in Fig. 7.26 for the two selected cases of gaussian width σ_g=16 mm (a,c) and σ_g=1 mm (b,d). The initial and final profiles correspond to steady flames. Thus, in figures 7.26(c) and 7.26(d), both profiles are superposed to better observe the temperature modifications between both states.
The temperature profiles allow to understand the increase in origin tangent slopes with the gaussian width, represented in Fig. 7.25. Indeed, the external temperature at the coordinate of the flame front is higher when the external temperature profile is wider, leading to a higher initial propagation speed.
When comparing initial and final steady states of the flame, one can see that in the case of σ_g=1 mm, the profiles are perfectly superposed, while in the case of σ_g=16 mm, a slight difference is notable in the preheating area upstream from the flame, with a final temperature higher than the initial. In the latter case, a great difference is observed in the burned gas zone, where the gas and wall are still under the heat source influence. However, these modifications have no impact on the stability of the flame since they are located in the burned gases.

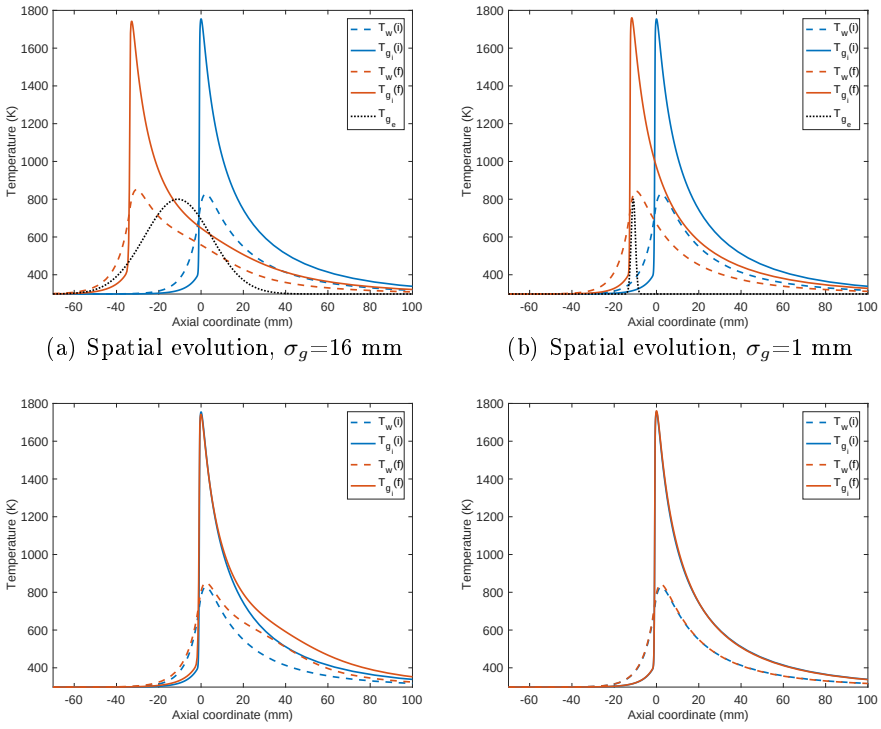

(a) Spatial evolution, σ_g=16 mm (b) Spatial evolution, σ_g=1 mm

(c) Profile superposition, σ_g=16 mm (d) Profile superposition, σ_g=1 mm

FIGURE 7.26 – *Evolution of the wall (dashed lines) and gas (plain lines) temperature profiles as a function of the axial coordinate, from initial (blue) to final (red) profile of the flashback. Both are steady flames. The flashback is represented for a fixed distance ℓ_T=10 mm, for two cases of gaussian width σ_g=16 mm (a,c) and σ_g=1 mm (b,d), with T_{max}=800 K, ϕ=0.8. The first two plots (a,b) depict the spatial evolution of the profiles according to the external air profile (dotted line). In the last two plots (c,d) the initial and final profiles are superposed to better compare the temperature modifications.*

7.4.4.2 Variation of ℓ_T the distance heat source - flame front

First, the influence of distance between the flame front and the heat source is evaluated for two cases of gaussian width value, σ_g=16 mm and 1 mm and at fixed parameters of ϕ=0.8 and T_{max}=800 K. Both cases are represented in Fig. 7.27 for ℓ_T from 5 to 100 mm.
In the narrow gaussian width case, σ_g=1 mm, and for distances equal or under to ℓ_T=20 mm, the root square function increase of the displacement profile observed in the experimental flashback is retrieved. For distances equal or above to ℓ_T=30 mm, the displacement profile evolves to the exponential increase with a decreasing slope of the tangent to the origin. However no peak movement of the flame is observed. At ℓ_T=100 mm the heating source has no effect on the flame which remains stable at its initial position. The convection of heated gas allows to increase the flame speed, but the flame does not receive enough

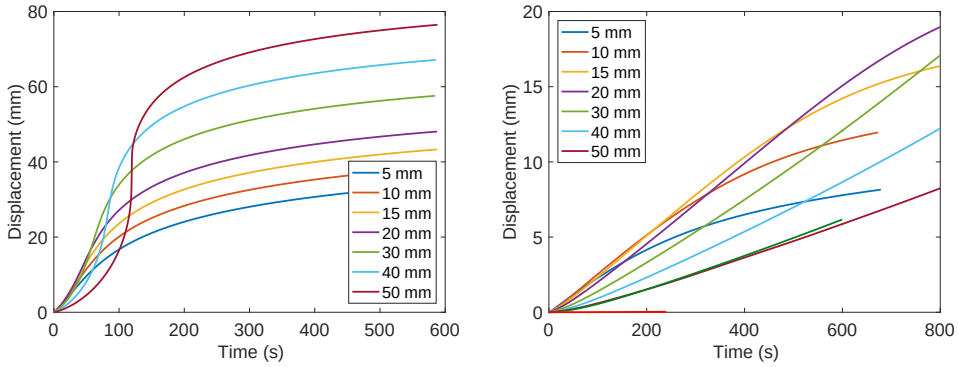

(a) Variation of ℓ_T, σ_g=16 mm (b) Variation of ℓ_T, σ_g=1 mm

FIGURE 7.27 – *Evolution of the absolute value of the displacement as a function of the distance heat source - flame front ℓ_T for two cases of gaussian width σ_g=16 mm (a) and σ_g=1 mm (b), with T_{max}=800 K, ϕ=0.8*

energy to propagate over cold walls, and therefore do not reach the established thermal environment of the wire.

In the wide gaussian width case, σ_g=16 mm, the two motion modes experimentally observed are retrieved. In fact, for distances under ℓ_T=30 mm, the displacement of the flame is continuous and follows a root function increase. For distances over ℓ_T=30 mm, and especially for ℓ_T=40 and 50 mm, a first phase of slow displacement is observed, followed by a second phase of sharp increase in the flame propagation speed and then a third phase of flame stabilization.

The case of ℓ_T=30 mm is more specifically analyzed. The wall and gas temperature profiles are extracted for times right before (t = 39.96 s) and right after (t = 40.0 s) the bifurcation, to identify the phenomenon causing this abrupt change in flame position.

It is seen that the bifurcation occurs when the gas temperature reaches the wall temperature. The difference between both temperatures is reduced leading to a convection heat flux close to zero. The forced convection heat fluxes are plotted in Fig. 7.28(c) to evaluate the impact of the heat source. The maximum flux in the flame front increases as the flame gets closer to the heat source. Thus the negative heat flux upstream from the flame, which represents the wall preheating through axial conduction, decreases highlighting the increase in wall and gas temperatures. The bifurcation occurs when both the flame front positive flux is maximum and the negative flux upstream from the flame is minimum. Thus, the flame propagates over nearly isothermal heated walls, which justifies the high flame propagation speed. After the bifurcation, the convection heat fluxes shift back to their initial states.

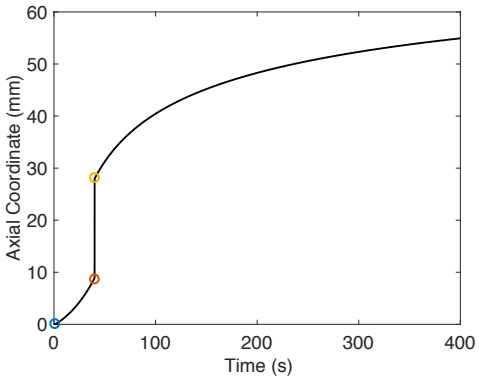

(a) Flame absolute displacement, ℓ_T=30 mm, σ_g=16 mm

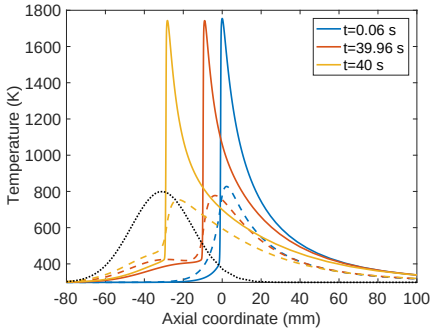

(b) Temperature profiles, ℓ_T=30 mm, σ_g=16 mm

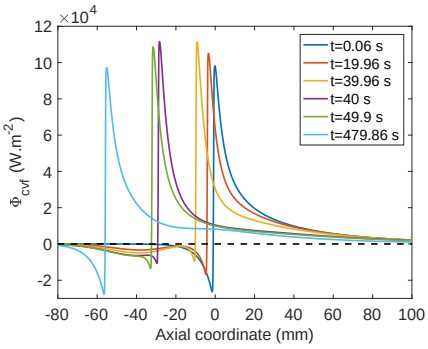

(c) Forced convection heat fluxes, ℓ_T=30 mm, σ_g=16 mm

FIGURE 7.28 – *Evolution of the temperature profiles before and after the bifurcation ℓ_T=30 mm, σ_g=16 mm, with T_{max}=800 K, ϕ=0.8*

7.4.4.3 Variation of the imposed maximum temperature T_{max} (integrated power variation)

Fixing the distance between the maximum temperature of the heating profile and the flame front at ℓ_T=10 mm, the maximum of temperature is varied from 600 K to 1000 K, for the two cases of gaussian profile width, σ_g=16 mm and

σ_g=1 mm. The resulting flame displacements are represented in Fig. 7.29.

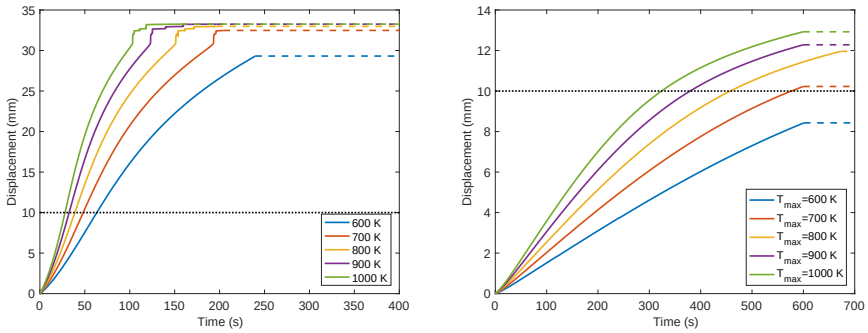

(a) Variation of T_{max}, σ_g=16 mm (b) Variation of T_{max}, σ_g=1 mm

FIGURE 7.29 – *Evolution of the displacement according to the maximum temperature of the heat source for ℓ_T=10 mm, ϕ=0.8, and for two cases of gaussian width σ_g=16 mm(a) and σ_g=1 mm(b).*

As the energy given to the steady system increases with the maximum of temperature, the displacement speed follows this tendency in both cases. Thereby the time constant to reach the final position gets lower as the temperature maximum increases. This time constant to reach final flame position is approximately 3 times higher in the case of the narrow gaussian profile (σ_g=1 mm) than in the wide gaussian profile (σ_g=16 mm).

7.4.4.4 Variation of the operating point

The change in operating point modifies the methane mass flow rate, as well as the mean flow rate. Indeed, higher is the equivalence ratio, greater is the mean flow speed at which the flame stabilizes, and thus greater is the flame power. Therefore the flashback of the flame is studied for operating points from ϕ=0.75 to 0.95, for the two gaussian profile widths σ_g=16 mm and 1 mm. Figure 7.30 represents the displacements for the two values of σ_g, with a heat source profile placed at ℓ_T=10 mm from the flame front.
The tendency in both graphs is similar : as the equivalence ratio increases, the final flame position decreases and gets closer to the ℓ_T=10 mm position, and therefore the overshoot reduces.
Then, for the case of σ_g=16 mm, the impact of the equivalence ratio is studied at ℓ_T=30 mm and represented in Fig. 7.31, since at this distance another motion mode was observed.
The first noticeable result is that, by decreasing the equivalence ratio from ϕ=0.8 to 0.75, the displacement moves from the three-phase motion mode to the two-phase mode. Then, from ϕ=0.8 to 0.95, in the first phase the origin tangent slope gets higher as the equivalence ratio increases, and in the third phase it is the contrary as lowest final displacement corresponds the highest

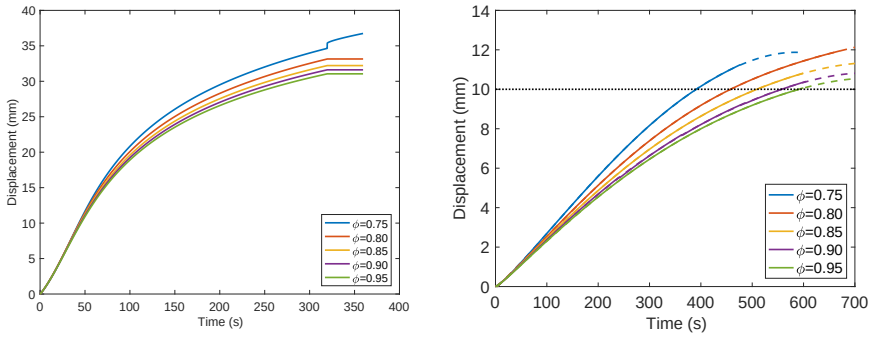

(a) Variation of (ϕ,U), σ_g=16 mm (b) Variation of (ϕ,U), σ_g=1 mm

FIGURE 7.30 – *Evolution of the displacement according to the operating point for ℓ_T=10 mm, T_{max}=800 K, and for two cases of gaussian width σ_g=16 mm (a) and σ_g=1 mm (b).*

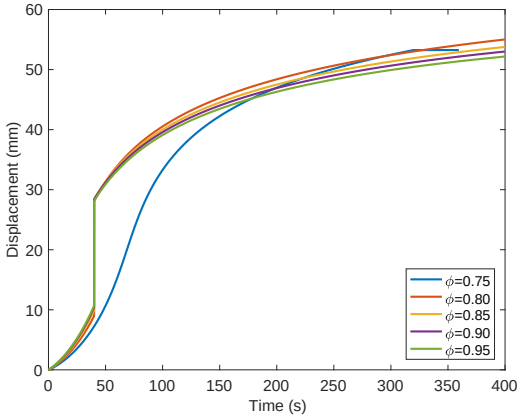

FIGURE 7.31 – *Flame motion according to the stable operating points from ϕ=0.75 to 0.95 σ_g=16 mm at ℓ_T=30 mm.*

equivalence ratio (as in the ℓ_T=10 mm).

7.5 Conclusion

The response of a stabilized flame to a thermal perturbation is studied experimentally and numerically using one-dimensional complex chemistry computation, by imposing a gaussian temperature profile upstream from the flame. Experimentally, the localized heat source is chosen and characterized spatially and temporally. According to the distance between the heat source and the flame front two modes of propagation were observed. The flame flashback is numerically reproduced, retrieving the two propagation modes at the different flame front-heat source distances. The first mode is a slow two phased flame propagation, for distances under 20 mm, which is justified by the positioning

of the heat source in the preheating zone of the flame. In the second mode, for distances above 20 mm, a fast propagation is observed when the flame propagates over isothermal heated walls. In fact, the axial conduction at the heat source combined with the gas heat retrocession to the walls and with the flame preheating allow to reach an almost constant temperature in the walls between the flame front and the heat source. Thus a numerical parametrical study is carried out on the impact of the gaussian width, the maximum of temperature and on the operating point.

Chapitre 8

Perspectives : Plasma assisted combustion

Contents

8.1 Introduction

8.1.1 Plasma definition and types

The plasma is a state of the matter composed of charged particules, ions and electrons. Therefore, plasmas are controlled by electromagnetic forces. Seve-

ral types of plasma exist according to their generation. An example of plasma generation is by using an electric field. In this case, the electric field accelerates the electrons composing a gas. The collision of these accelerated electrons with neutral molecules or atoms, produce a pair of electron-ion, following the reactional scheme :

$$e^- + n \rightarrow i + 2e^-$$

with e^- an electron, n a neutral molecule or atom and i an ion. The additional electron can also be accelerated by the electric field and again collide with neutral molecules, producing a plasma through this electronic avalanche.
The energy of atoms ionisation is of the order of magnitude from few to tenth of electronvolts. Once created, the charged species can be lost either by interacting with reactors surfaces, by diffusion (collision or buoyancy) or by recombination to other species according to the type of plasma. To maintain a plasma energy needs to be added continuously.
A plasma can be at equilibrium or non-equilibrium state. The Local Thermodynamic Equilibrium (LTE) is defined by a state where the temperature of the electrons and heavy (ions, neutral) species are the same. It is reached when the discharge energy is sufficient and long enough. Arc plasma or fusion plasma are examples of equilibrium plasmas. The role of chemical and ionisation processes depend strongly on the gas temperature, the electron temperature and the plasma. Non equilibrium or non-thermal plasmas are plasmas where the temperature of the electrons is different from the heavy particules temperature. Most of laboratory discharges are non-thermal plasmas.

8.1.2 Plasma diversity

To illustrate the plasma diversity, it is common to plot the electron temperature according to the average electron number density as represented in Fig. 8.1.
The classical plasma cover plasma from astrophysics, industrial fields or laboratory plasma. Three main communities come out of this : cold, hot and spatial plasmas.

Cold or non-thermal plasmas are weakly ionized, created in neutral gas (usually argon or xenon) by an external electromagnetic energy source. The choices of gas, pressure, reactor geometry as well as the characteristics of the energy source (frequency, absorbed power etc..) determine the type of discharge. Figure 8.1 represents the main types of discharge. Usually the density of charged particles (electrons or ions) is very weak compared to the neutral species density, thereby the ionisation rates are very low (10^{-5} to 10^{-1}).
In view to mass ratios, the momentum transfers are very weak from electrons to neutrals and very efficient from ions to neutrals (similar mass). Therefore,

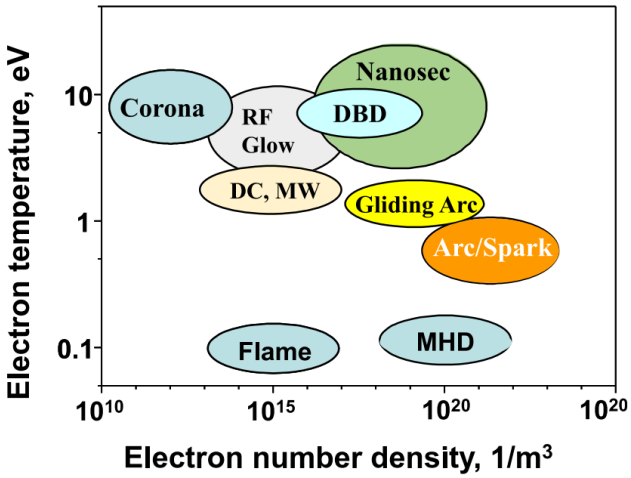

FIGURE 8.1 – *Schematic of electron temperature and number density for different discharges, Corona, direct current (DC) discharge, microwave (MW) discharge ; dielectric barrier discharge (DBD), radio-frequency discharge (RF), glow discharge, gliding arc, nanosecond pulsed discharge (NSD), arc, magneto-hydrodynamic discharge (MHD), and flame (extracted from Ju and Sun (2015a))*

the temperatures of the electrons and heavy species (ions, neutral) are very different in a cold plasma at low pressure : cold plasmas are not at thermodynamic equilibrium. Closer to atmospheric pressure, as the collision rate increases the electrons and heavy species tend to have similar temperatures, and the plasma tends to reach thermal equilibrium (LTE).

Hot plasmas are created at high electronic density and high electronic temperature. These plasmas are completely ionized. Examples of these industrial plasmas are magnetic confinement Tokamaks, laser confinement (inertial fusion) or magnetic compression (Z-pinch).

Spatial plasmas are for instance composing stellar interior. Several plasmas are also observable in earth environment, like lightning, aurora borealis or ionosphere.
All these types of plasmas have different possible applications, according to the demand : energy production, charged species, photon emissions, etc...

8.1.3 Plasma applications

In the industry, plasma have lots of possible applications. Hot plasmas are mainly developed in a way to produce energy. Non equilibrium plasma are

usually used as a convertor of electromagnetic energy into other forms of energy. Some examples of conversion of electromagnetic energy are :

- Conversion into photons emission (plasma screen, lasers, lighting...)
- Conversion into kinetic energy, source of charged particles (electrons beam, ionic propulsion, ion source...)
- Conversion into chemical energy, source of chemically active species : surface decontamination (Brandenburg et al. (2018); Dasan et al. (2018); Moisan et al. (2001)), sterilization, medical applications such as cancer treatments, remediation, surface treatment, etc...

Several types of plasma are also broadly used as a way to assist combustion.

8.1.4 Plasma-assisted combustion (PAC)

The plasma coupling to combustion has been extensively studied in the recent decades. In fact, it was proven to enhance the flame's ignition, stability and extend flammability limits, but also reduce polluant emissions and increase fuel efficiency.

Several types of plasmas can be used in the assistance of combustion. First, **equilibrium plasma** can be used like plasma torch (Barbi et al. (1989); Takita et al. (2005); Jacobsen et al. (2008)) or spark plug. Then, **non equilibrium plasma** can also be used like nanosecond repetitively pulsed discharges (Pancheshnyi et al. (2006); Starikovskii et al. (2006); Bao et al. (2007); Kosarev et al. (2008)), microwave discharge (Esakov et al. (2004); Stockman et al. (2007)), corona discharge(Wang et al. (2005)), dielectric barrier discharge (Kim et al. (2005); Ombrello et al. (2010)) or gliding arc discharge (Ombrello et al. (2006); Ombrello and Ju (2008); Ombrello et al. (2008)), etc.

Indeed, using nanosecond pulsed plasma discharges (NPPD), Kim et al. (2010) showed an extension of the flammability limit by 10% in the stabilization of ultra lean premixed methane/air. It is demonstrated that small amount of H_2 and CO, generated in a stream of discharge-activated species, plays a role in enhancing the stability of the premixed flame. Thus, in Pilla et al. (2006), nanosecond repetitively pulsed plasmas (NRPP) is shown to improve combustion efficiency and increase the lean flammability limit of a 12.5 kW lean turbulent premixed propane/air flame. The plasma power represents less than 1% of the flame power. The flames with and without plasma discharges are represented in Fig. 8.2.

On this figure, one can see that the reactive zone is larger with plasma and a new emission region exists. Using spectroscopic measurements, an increase of free radicals concentration in the flame has been observed, possibly explaining the flame enhancement. In a same way in Barbosa et al. (2015), the stability domain of a premixed propane/air flame in a swirled burner is shown to be greatly extended by the addition of NRP discharges in the flame. The plasma power represents around 1% of the flame power. The lean extinction limit is found to be four times lower with plasma. As in Pilla et al. (2006), the importance of the

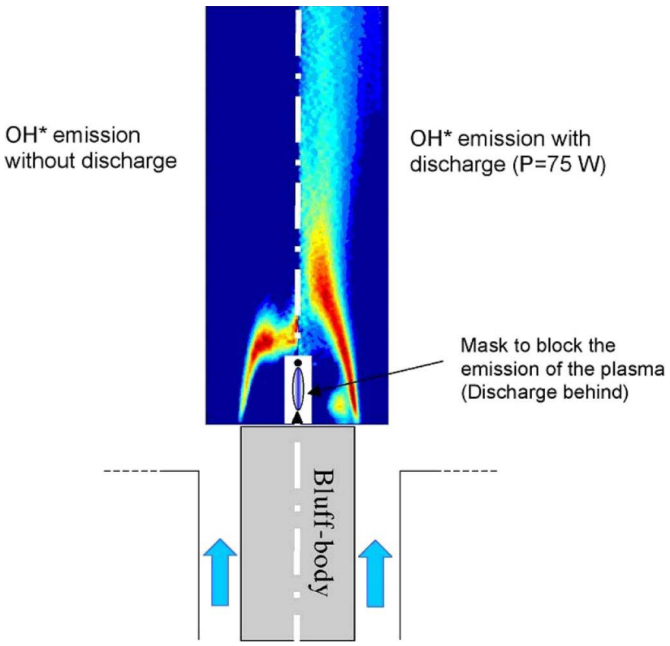

FIGURE 8.2 – *Comparison of OH emission with and without NRPP discharges (P_{plasma}=75 W) in a premixed propane/air flame (P_{flame}=12.5 kW) (extracted from Pilla et al. (2006)).*

discharges repetition frequency on the combustion effectiveness is observed.
Changing type of plasma, Ombrello et al. (2008) studied the kinetic ignition enhancement in methane/air and hydrogen/air counterflow diffusion flame burners, using magnetic gliding arc (MGA), a non equilibrium plasma. The explanation of the mechanisms of enhancement through experimental and numerical analysis is exposed. Indeed, the significant kinetic ignition enhancement by the MGA plasma is shown to be due to NO_x, the ignition regime depending on the concentration of NO addition.
Again introducing another type of plasma, Ombrello et al. (2010) studied experimentally and numerically the thermal and kinetics effects of ozone on flame propagation, using Dielectric Barrier Discharge (DBD) to produce ozone. The flame is a propane/oxygen/nitrogen laminar lifted flame. Experimentally, with a 1260 ppm of ozone addition to the oxygen/nitrogen oxidizer, the flame propagation is enhanced by 8%. Numerically, in the preheating area, the ozone decomposition produces atomic oxygen which will react with the fuel and produce hydroxide (OH). In parallel, the ozone reaction with atomic hydrogen (H) produces more hydroxide, which will react with fuel and fuel fragments providing a chemical heat release leading to an increase in flame propagation. One conclusion of this study is that the kinetics effects are greater than the thermal effects in this combustion assistance by ozone production.
Finally, in Wolk et al. (2013), microwave-assisted spark ignition were used to

enhance the development of a laminar methane/air flame. The assistance results in an increase of the flame kernel size leading to an increase in the flame speed, and an extension of lean and rich ignition limits. In fact, Chen and Ju (2007) and Chen et al. (2009) showed that the minimum ignition energy is linked to a critical flame initiation radius which is a strong function of the mixture Lewis number. By breaking large fuel molecules, the lewis number is reduced and thereby the ignition kernel size gets greater than the critical flame initiation radius, which explains the enhancement effects of the plasma in Wolk et al. (2013).

In the literature, several types of flame enhancements are exposed and demonstrated, using different kinds of non-thermal plasma. To sum up, those enhancements are represented in Fig. 8.3.

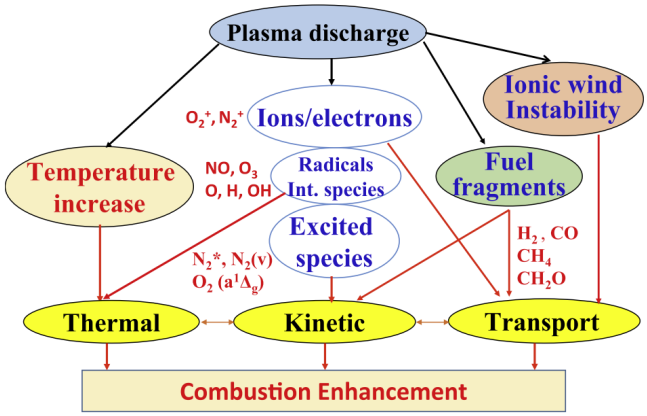

FIGURE 8.3 – *Four combustion enhancement pathways of plasma-assisted combustion (extracted from Ju and Sun (2015b))*

Indeed, in assisting combustion, a plasma can have four main effects (Ju and Sun (2015b)) :

- **Thermal enhancement** : by increasing the gas temperature through energy transfer from electrons to neutral molecules, chemical reactions are accelerated.
- **Kinetics enhancement** : by providing high energy electrons and ions and electronically and vibrationally excited molecules leading to the production of active radicals and reactive species involved in new chain-initiating and branching reactions.
- **Fuel decomposition enhancement** : by electron impact dissociation of heavy particles modifying the fuel reactivity and diffusivity in the mixture.
- **Transport enhancement** : changing local flow velocity and increasing the flow mixing through hydrodynamic instability, ionic wind and flow motion via Coulomb and Lorentz forces.

8.1.4.1 Combustion assisted by microwave plasmas

Microwave discharges are usually non equilibrium plasmas. They are generated in particular, using the propagation of a surface wave at ultra high frequencies, usually in quartz capillary. A very efficient launching device for such waves is called a surfatron, powered by a microwave plasma source. The obtained plasma is highly reproducible (Moisan et al. (1974); Moisan et al. (1979)). The main advantage of using microwave plasmas to assist combustion is that there is no electrodes. In fact, the excitation being at high frequency (2.45 GHz), the ions cannot follow the electromagnetic field variations. The discharge is thereby almost continuous. Not being under an electromagnetic field in the combustion chamber is indeed an advantage since it has been extensively observed that electromagnetic fields have an impact on flame behavior and thereby it is another effect to decorrelate from the chemical and thermal assistance when using plasma assisted combustion. Thus, electrodes are intrusive and difficult to insert into already existing configurations and can constitute flame holders. Therefore both are considerable advantages to the microwave configurations. Moreover microwave plasmas have a high coupling efficiency, a long life time and can operate under high or low pressures (Rao et al. (2011)). Thus, plasma assisted combustion studies using microwave plasma demonstrate an influence on the flame structure, volume, speed and temperature and extend the fuel lean flammability limits. Indeed, Hong and Uhm (2006) and Bang et al. (2006) showed a significant temperature increase using plasma torches burners, by injecting hydrocarbons into the plasma torch generated by air and air-oxygen mixture. In Hemawan et al. (2006), the study of a coupled plasma to a premixed methane/oxygen flame in a torch burner demonstrates that a 10 W addition of microwave power to the combustion allows to extend the lean flammability limits (equivalence ratio) by 5% to 12% (9% in average). In the work of Hemawan et al. (2009), using a different applicator, the effects of the plasma on the flammability domain can be observable with even less microwave power addition. Figure 8.4 depicts the flame extinction limits curves with several microwave power addition. The effect of the plasma power input is clearly visible as the lean flammability limit is extended.
Stockman et al. (2009) studied the enhancement of a laminar premixed methane/air flat flame by microwave assistance. An increase up to 20% of the laminar flame speed is observed as well as a temperature increase from 100 to 200 K, and an increase in the peak hydroxide (OH) number density. Later on, Hammack et al. (2011) and Hammack et al. (2012) used atmospheric microwave plasma discharge as direct coupling to a stoichiometric premixed methane/air resulting in a better stabilization of the flame at high flow rates, the elimination of soot particles and the reduction in flame front discontinuities for rich premixed flow. It is established that microwave plasma helps to initiate combustion through methane decomposition by facilitating additional chemical pathways. Figure 8.5 illustrates the evolution of the methane/air flame

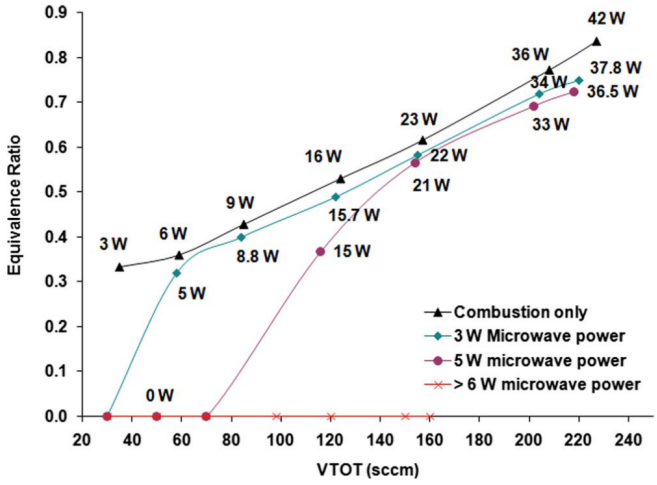

FIGURE 8.4 – *Flame extinction curves adding 0, 3, 5 and 6 W of microwave power. Combustion power is displayed for each point (extracted from Hemawan et al. (2009)).*

(bottom), its averaged temperature (middle) and OH number density (top) at several plasma power. They proved that the OH number density can be increased up to 50% and the combustion temperature up to 40% with the plasma assistance.

More recently, Wu et al. (2015) presented an up-tunning and down-tunning of premixed and non-premixed methane/air flames. The up-tuning represents an increase of the plasma power until seeing effects on the injected fuel premixed (ignition-stabilisation). For the down-tuning, the plasma is started at high power with an ignited flame, and lowered until flame extinction. The coupling of the combustion gas and the plasma is performed using a cross of three quartz tubes of 4 mm inner diameter. The combustion gas are injected in the vertical tubes and the microwave plasma is generated in argon in the horizontal tube. The flame is stabilized in the ambient air. Figure 8.6(b) illustrates the up and down-tunning of a premixed flame. It can be observed that the initial ignition requires more power since the flame ignites at 50 W in the up-tunning while it remains stable down to 20 W in the down-tunning. At a same power of 30 W the spectral emission differs between the up and down-tunning, highlighting different chemical reaction pathways involved.

Thus, the effects of plasma power on the flame ignition and stabilization limits are represented in Fig. 8.6(a), where the lowest plasma power at which argon plasma-assisted combustion flames are observed is plotted according to the fuel equivalence ratio.

The premixed curve plotted in Fig. 8.6 (left) displays a minimum of power at an equivalence ratio close to 0.6. The plasma power necessary to ignite a flame increases for equivalence ratios lower than 0.6. This is due to the fact that the heat losses to the surrounding gas are more important, and the ignition

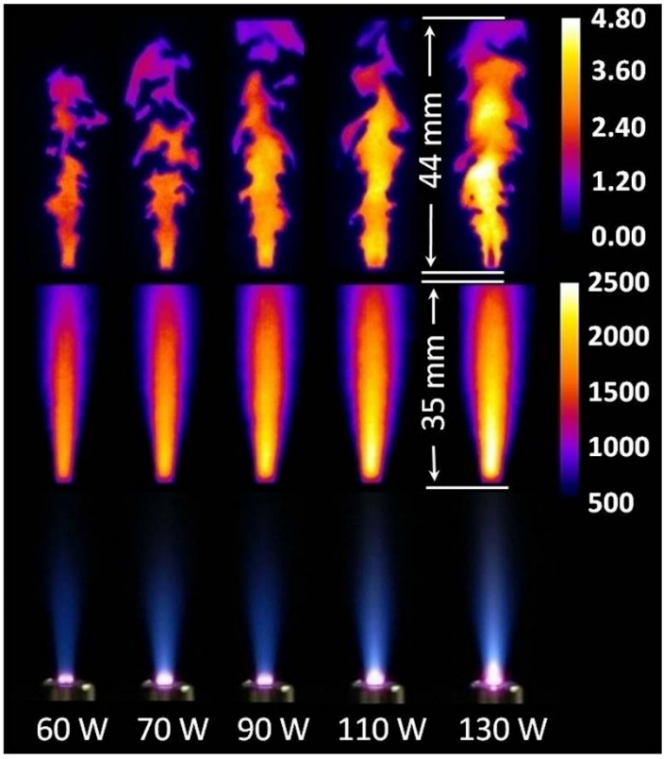

FIGURE 8.5 – *Top : OH number density (10^{16} cm^{-3}) ; Middle : averaged temperature (K) ; Bottom : spontaneous emission of a direct coupling of microwave plasma with a stoichiometric methane/air flame. Total flow rate : 15 $L \cdot min^{-1}$. Plasma power is varied from 60 W to 130 W (left to right) (extracted from Hammack et al. (2011)).*

delay is higher for lower equivalence ratios, consequently more power assistance is needed. Then, for equivalence ratios higher than 0.6, the power needed to ignite and stabilize a flame also increases. This phenomenon is explained by the quenching of the plasma by the fuel which increases with the equivalence ratio. This minimum establishes an optimum equivalence ratio for the assistance.
To conclude this literature review, the ability of the microwave plasma to interact with combusting hydrocarbon systems in order to provide enhancement at different levels is demonstrated. Thus, with two major advantages, being no electrodes and no electromagnetic field in the combustion chamber, the microwave plasma is a good candidate in the choice of a plasma to assist the previously introduced mesoscale flame. The experimental investigation on this coupling is exposed in the following section.

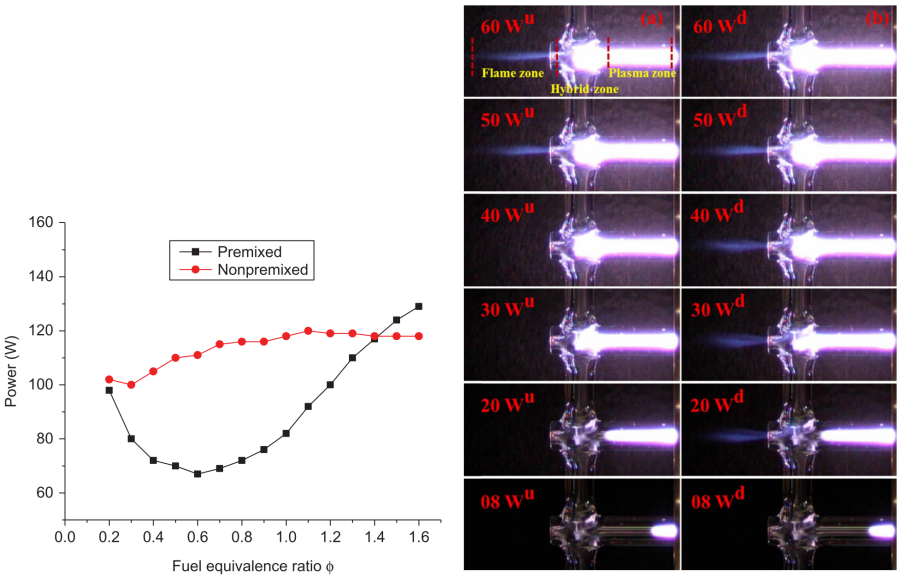

FIGURE 8.6 – *Left : Lowest plasma power at which argon plasma-assisted flames are observed ; Argon flow rate is 0.84 slm ; Methane/air flow rate is 2.0 slm. Right : Up-tunning (W^u) and down-tunning (W^d) of a premixed methane/air flame. Argon flow rate : 0.49 slm ; Combustion gas equivalence ratio : 0.7 ; Camera exposure time : 1/15 s (extracted from Wu et al. (2015)).*

8.2 Present experimental investigations on the coupling of premixed mesoscale flame to a microwave plasma

This section is to be taken as first steps of testing several experimental configurations to find a way to assist the previously exposed mesoscale flame with microwave plasma. The objective is to deposit the charged species and radicals created by the plasma into the fresh gas slightly upstream from the flame.

8.2.1 Coupled configuration : combustion and microwave setup

The main challenge in plasma-assisted combustion configuration is the coupling between the combustion and the microwave plasma setup, both being constrained in several points. The combustion setup used is the previously introduced mesoscale burner with an injection of methane/air mixture inside a 5 mm inner diameter, 1 mm thick quartz tube. The microwave configuration adopted is exposed in Coche et al. (2016) and Stancu et al. (2016) and represented in Fig. 8.7 at atmospheric pressure. It is composed of a quartz capillary of 1 mm inner diameter, 1 mm thick, inside which argon gas is injected. A mass flow meter (Bronkhorst F-201CV-1K0-AAD-33-V ; range [20,1000] Nml/min) is used to

control the argon flow input in the capillary. The quartz capillary is inserted into a microwave plasma cavity referred as surfatron.

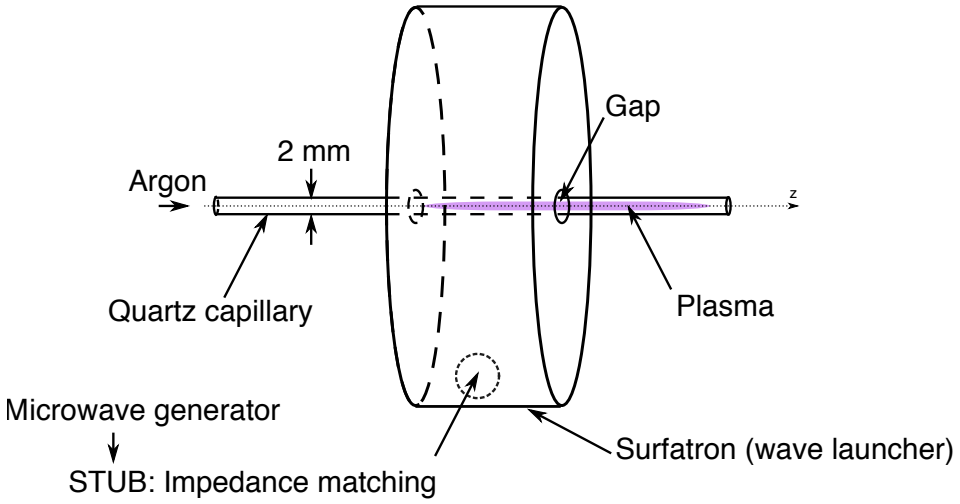

FIGURE 8.7 – *Microwave experimental setup. The surfatron gap is located at z=0 cm.*

The surfatron is a coaxial cavity with an end gap. At this gap, the electric field reaches its maximum of intensity and gas breakdown occurs. The electron density is maximum at the gap location. The surfatron is called a surface wave launcher since it generates surface waves propagating along the capillary surface (dielectric) and the plasma. The wave only propagates at high enough plasma density. It is absorbed by the plasma, and as its power decreases with the distance from the surfatron gap, the plasma electron density drops. The microwave plasma cavity is powered by a 2.45-GHz continuous wave (CW) microwave plasma source (AJA International) via a 0.6-m low-loss coaxial cable (LMR-400, Times Microwave Systems). An impedance matching stub is placed between the microwave generator and the surfatron to reduce the reflected power, and therefore maximize the power transmitted to the plasma. The typical fraction of transmitted power to plasma is on the order of 20%.

The power input to the system is varied from 5 to 50 W. Increasing the microwave plasma power leads to a greater plasma length. Thus, since the surface wave generated by the surfatron propagates in both directions, the plasma extends upstream and downstream from the surfatron gap. Due to the argon flow, the plasma is asymmetrical, with a greater length downstream from the gap. Hence, at a same microwave power, increasing the flow speed leads to a longer extend of plasma downstream.

The commonly adopted law of assisted combustion by plasma is that the plasma power represents one percent of the flame power. In the present case, this law is not respected since the average flame power is 10 W (depending on the methane mass flow rate). Thereby the plasma power is of the same order or greater than the flame power.

Several coupling configurations are considered, according to combustion and plasma setup contraints.

8.2.2 Considered coflow coupling configurations

Chronologically the three first configurations considered are represented in Fig. 8.8 as a top view of the system. In all configurations the microwave plasma is generated in the quartz capillary, inside which argon gas is injected.

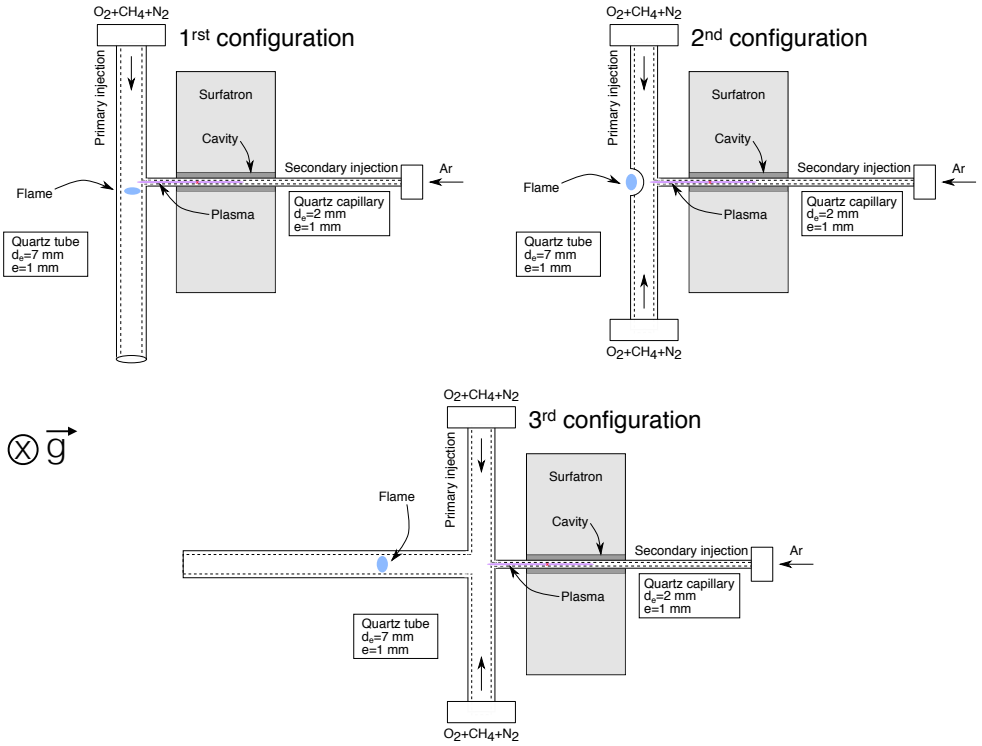

FIGURE 8.8 – *Schematic top view of three tested configurations to couple microwave plasma to a premixed lean methane/air flame. The combustion gas flow through the primary injection(s), and argon through the secondary injection. The first configuration is referred as orthogonal and the two latter as parallel, depending on the flame propagation direction and the plasma injection.*

The two first configurations are T shaped, and the third one is cross shaped. All the configurations are composed of a main injection of combustion gas (oxygen, methane and nitrogen) in the 7 mm external diameter tube(s) and a secondary injection of argon in the quartz capillary. In order to compensate for the input of argon and maintain a constant equivalence ratio, the argon mass flow rate is subtracted from the rate of nitrogen in the main injection. Thereby the total mass flow rate and equivalence ratio are conserved comparing with a configuration without plasma.
In the **first configuration** (top left), the main injection is unique and the

secondary flow meets the first one at the center of the main tube. This configuration allows a good control of the flame position according to the capillary entrance. In the **second configuration** (top right), the main injection was doubled and a hole was drilled in the main tube straight in front of the secondary injection. The mass flow rate of the main injection was divided between the two injections. The flame stabilization is better controlled since the flame gets anchored at the hole's edges. In the **third configuration** (bottom), the main injection is also doubled and a tube of the same dimensions as the combustion tube is merged straight in front of the secondary injection, creating a cross. The first configuration is referred as orthogonal since the axis of the capillary ($\vec{z}$ on Fig. 8.7) is orthogonal to the $\vec{x}$ axis of the combustion tube. Thereby, the flame propagates orthogonally to the plasma/argon flow input. The second and third configurations are referred as parallel, since the capillary and combustion tube axis (or hole in the case of the second configuration) are parallel, and thereby the flame propagates/stabilizes alongside the plasma/argon flow input.
Two main issues are highlighted in these configurations. The first issue is the thermal input of the argon gas, heated at the plasma generation. In fact, the argon temperature at the exit of the capillary is around 520 K. Hence, the thermal effect on a flame has been studied in the previous sections, and the sensitivity of the flame to heat input is very high. Thereby the heat input cannot be decorrelated from the chemical addition, and if a stabilization is observed, it cannot be assigned only to the chemical effect.
The second issue lays on the secondary injection inside which the mass flow must be important to extend the plasma downstream and by that, convect the charged species to the fresh gases. However the dimensions of the capillary (1 mm inner diameter) lead to an argon flow speed seven times higher than the combustion tube flow speed, for the maximum mass flow rate used. This jet flow causes flame instabilities which prevents flame stabilization close to the capillary exit. Thus in such conditions, the argon is not mixed to the combustion gas leading to a local equivalence ratio higher than expected.
Figure 8.9 illustrates the distortion of the flame due to the incoming argon flow, in the first configuration. The flow creates a hole in the flame since argon is neutral in combustion reactions.

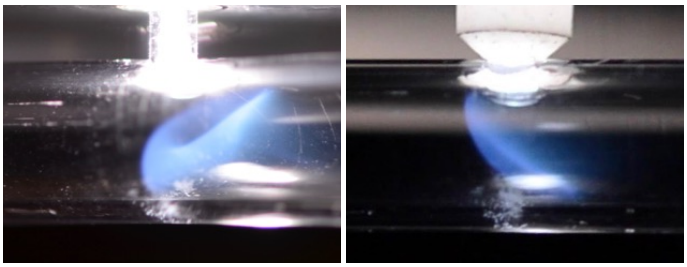

FIGURE 8.9 – *First configuration orthogonal : effects of argon flow on the premixed flame for ϕ=0.80, Q_1=353 ml·min^{-1} (U_1=30 cm·s^{-1}) and an argon mass flow rate of Q_2=60 ml·min^{-1}(U_2=127 cm·s^{-1}). The combustion flow is from left to right.*

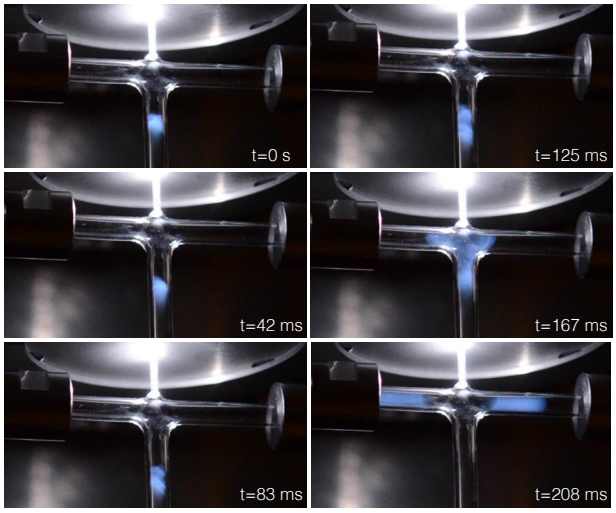

FIGURE 8.10 – *Third configuration : effects of argon flow on the premixed flame for ϕ=0.95, primary injection Q_1=648 ml·min^{-1} (U_1=55 cm·s^{-1}) and secondary injection Q_2=150 ml·min^{-1} (U_2=318 cm·s^{-1}).*

In parallel configurations (2 and 3), the closer the flame is from the capillary output the more instable it gets, but the more chemical and heat assistance it receives from the plasma. Figure 8.10 depicts top view snapshots of the time evolution of a flame and plasma in the third configuration. The flame oscillates until it flows upstream to the injection tubes and extinguishes. No stability was reached in configurations 2 and 3, meaning that the plasma heat and chemical assistance do not compensate for the hydrodynamic instabilities created by the capillary output.
The conclusion drawn from these observations is that the plasma must be generated in a larger quartz tube to reach a flow speed in the same order of magnitude to the one used in the combustion tubes, and thereby not disrupt the flame stability. The flame could then be approached from the argon plasma and an assistance could possibly be observed, as established in the literature (Wu et al. (2015)).

8.2.3 Configuration showing an influence of the plasma on the flame stabilization

A last configuration was considered in order to observe an influence of microwave plasma on the studied methane/air flame. This configuration represented in Fig. 8.11 is a parallel counterflow configuration. Indeed, the argon capillary is inserted at the free end of the combustion tube. The combustion gas injection is made from left to right, and the argon is injected from right to left.
A flame is ignited in the combustion tube at ϕ=0.95 and Q_1=471 ml·min^{-1} (U_1=40 cm·s^{-1}), and a plasma is generated at P_{plasma}=50 W, Q_2=60 ml·min^{-1}

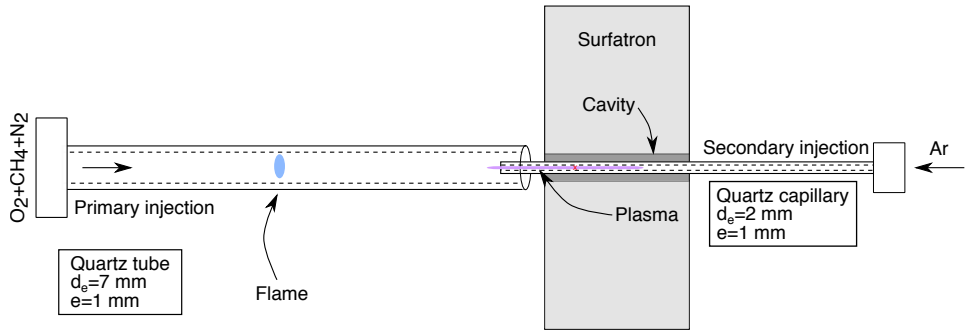

FIGURE 8.11 – *Schematic top view of a counterflow tested configuration to couple microwave plasma to a premixed lean methane/air flame. The primary injection of combustion gas is from left to right while the argon is injected through the secondary injection from right to left.*

(U_2=127 cm·s^{-1}). The flame is placed upstream from the plasma, at few millimeters from the capillary output. The secondary mass flow rate is then increased from Q_2=60 ml·min^{-1} to 150 ml·min^{-1} (U_2=318 cm·s^{-1}). The flame reaction to this secondary injection mass flow rate increase is represented on time evolution side view snapshots in Fig. 8.12.

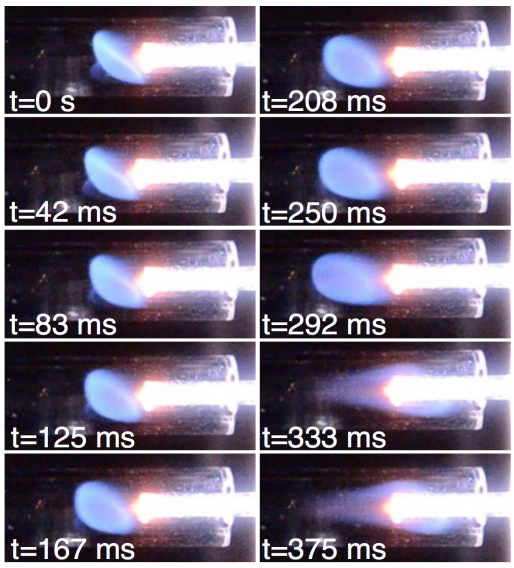

FIGURE 8.12 – *Counterflow experimental setup side view snapshots of the flame time evolution after a change of secondary injection mass flow rate from Q_2=60 to 150 ml.min^{-1}. The main injection characteristics are ϕ=0.95 and Q_1=471 ml.min^{-1} (U_1=40 cm·s^{-1}). The plasma power is set to P_{plasma}=50 W.*

The time evolution illustrated in Fig. 8.12 shows that the flame firstly flows

upstream with a slight rotation (t=83 ms and 292 ms), as if pushed by the increase in argon mass flow rate, and then stabilizes on one side of the capillary (t=333 ms and 375 ms). In this configuration, the argon mass flow rate is not subtracted from the nitrogen input in the primary injection, thereby after the capillary injection, the equivalence ratio decreases and total mass flow rate increases. In the case described in Fig. 8.12, with a secondary mass flow rate of Q_2=60 ml.min^{-1}, the local equivalence ratio dips to ϕ=0.77 and the total mass flow rate increases to Q_{tot}=531 ml.min^{-1} leading to a mean flow speed around the capillary of U_{tot}=47 cm·s^{-1}. As the secondary injection is increased to Q_2=150 ml.min^{-1}, the local equivalence ratio drops to ϕ=0.66 and the total mass flow rate increases to Q_{tot}=621 ml·min^{-1} leading to a mean flow speed around the capillary of U_{tot}=55 cm·s^{-1}. At this mean flow speed and equivalence ratio, a new flame stabilization is obtained, illustrated on Fig. 8.12 at t=333 ms and 375 ms. The side and top views of this observed flame are represented on Fig.8.13 for spontaneous and CH* flame emissions. The flame is laterally stabilized, starting in the combustion tube upstream from the capillary end, and expanding to the sides of the capillary. The stabilization of this flame occurs at a low equivalence ratio ϕ=0.66 and high flow rate Q_{tot}=621 ml.min^{-1}, a stabilization that could not have been reached in a standard configuration.

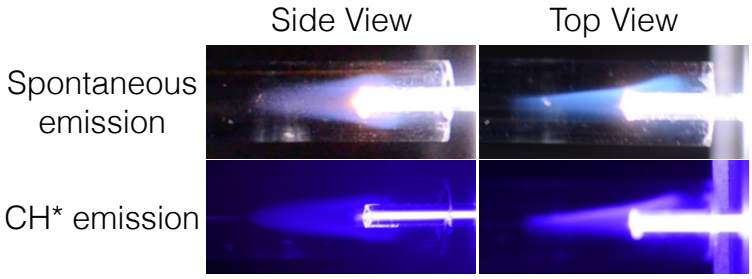

FIGURE 8.13 – *Side and top views of the flame stabilization observed with plasma addition, in spontaneous (first line) and CH* emissions (second line).*

As previously mentioned, this stabilization can be due to two phenomena : the thermal assistance of the plasma with an argon flow preheated by the plasma generation, and the production of charged and excited species enhancing the combustion.
In order to investigate the effects of a thermal assistance, two cases are studied. In both cases, the same protocol is used concerning the previously described increase in secondary mass flow rate. In the first case, the flame is ignited and positioned close to the capillary output. The capillary is thereby heated by the flame burned gases. In the second case, the argon flow is preheated by placing a torch 1 cm upstream from the capillary output. Thus, as in first case, the capillary is heated by the flame burned gases. For both cases, the argon mass flow rate is then increased from Q_2=60 to 150 ml·min^{-1}. The flame reaction

to this argon mass flow increase is represented in Fig. 8.14(a) for the first case, and in Fig. 8.14(b) for the second case.

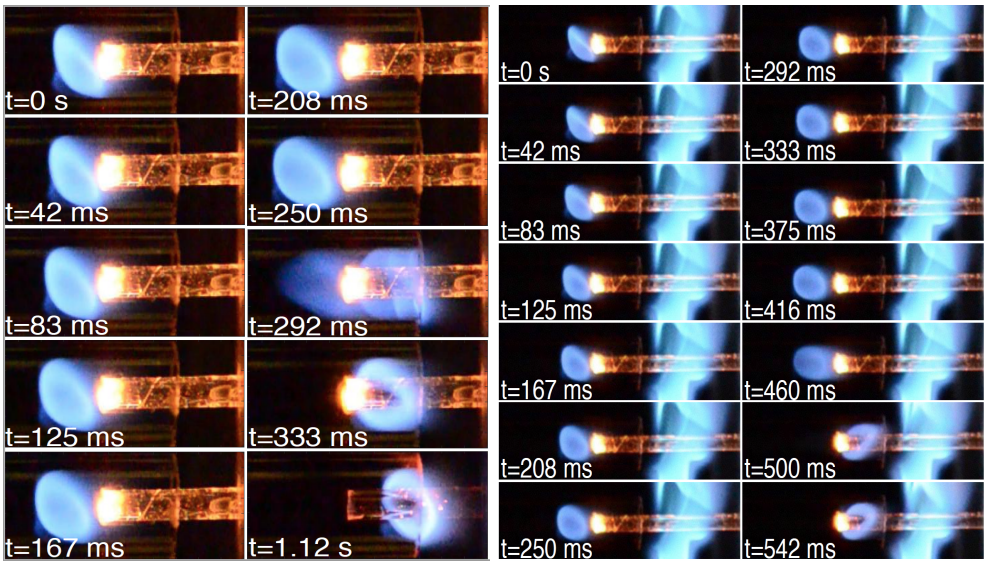

FIGURE 8.14 – *Two possible thermal effects are tested, in the first case (left) the capillary is heated in contact to the flame burned gases and in the second case (right) the argon gas is preheated by a torch 1 cm upstream from the capillary output, and the capillary is preheated by the flame burned gases. The secondary mass flow rate is increased from Q_2=60 to 150 ml·min^{-1}, and the flame reaction to this mass flow increase is captured by snapshots of the flame.*

In both cases, the flame is pushed upstream as the argon mass flow rate increases, rotates and then flows downstream around the capillary until reaching the end of the combustion tube. Therefore no flame stabilization could be observed. Without any quantitative measurements, these results show a first approach to a flame assistance by the microwave plasma.
To conclude, the goal in this section was to suggest a configuration were a chemical effect of the plasma on the studied flame, by decoupling the thermal effects from the chemical ones. The stabilization of a flame was observed at lower equivalence ratio and higher flow rate. However, no quantitative measurements were carried out, and further work should be done to characterize the system : quantify the thermal effect (wall temperature), estimate the charged and radical species proportions in the fresh gases, etc... The counterflow configuration was the product of a long quest in merging the two existing configurations of combustion and plasma. This section enters into the perspectives of the presented work.

8.3 Implementation of a plasma modelisation into the previously introduced 1-D complex chemistry code (REGATH)

The aim of this section is to numerically investigate a possible chemical assistance to a steady one dimension methane/air flame. To do so, a high level of NRP discharges modeling developed by Castela (2016) is used. This model was implemented in the complex chemistry code REGATH and adapted to the previously exposed modelisation of combustion (Castela et al. (2016)).

8.3.1 Model description and addition of the plasma to the previously established equations in steady configuration

Nanosecond Repetitively Pulsed (NRP) discharges are a non-equilibrium plasmas, of high-voltage (tens of kiloVolts) pulses lasting tens of nanoseconds, and repeated at a Pulse Repetition Frequency (PRF) of the order of tens of kiloHertz. Three NRP regimes exist, the corona, glow and spark discharges according to the discharge parameters (PRF, reduced electric field E/N,...).
Two main energy transfers occur during a discharge in air, having a direct impact on the flow. First the excitation and relaxation of electronic states of nitrogen molecules following two steps :

$$N_2(X) + e^- \rightarrow N_2(A, B, C, a', ...) + e^- \tag{8.1}$$

$$N_2(A, B, C, a', ...) + O_2 \rightarrow 2O + N_2(X) + heat \tag{8.2}$$

with $N_2(X)$ and $N_2(A, B, C, a', ...)$ respectively ground state and electronically excited nitrogen molecules.
This last step leads to an ultrafast heating of the gas and oxygen molecules dissociation. Oxygen molecules dissociation can also result from direct electron-impact following :

$$O_2 + e^- \rightarrow 2O + e^- \tag{8.3}$$

The second energy transfer occurs through the excitation and relaxation of vibrational states of nitrogen following :

$$N_2(X) + e^- \rightarrow N_2(v) + e^- \tag{8.4}$$

$$N_2(v) \rightarrow N_2(X) + heat \tag{8.5}$$

with $N_2(v)$ the vibrational excited nitrogen molecules. The heat release resulting from the vibrational translation relaxation leads to a slow gas heating. Based on temperature measurements and absolute density of oxygen and electronically excited nitrogen molecules, it is assumed in the plasma modelisation and zero dimensional approach, Castela et al. (2016) that 90% of the NRP discharges energy is consumed by the electronic and vibrational excitation of N_2 molecules and dissociation of O_2 molecules through direct electron impact. This result is applicable in air and in hydrocarbon mixture since the mass percentage of fuel is usually very low. The model developed by Castela et al. (2016) is schematically summed up in Fig. 8.15. Three major assumptions are made in the model. First, two times define the energy transfer from the pulse to the gas, characterizing the relaxation time of N_2 molecules electronically excited (τ_{pulse}) and vibrationally excited (τ_{VT}). Then, the discharge energy deposition rate $\dot{E}^p$ is decomposed in three resulting deposition rates : a change in chemical energy at a rate of $\dot{E}^p_{chem}$ due to species ultrafast dissociation, an ultrafast gas heating at a rate of $\dot{E}^p_{heat}$, and an ultrafast vibrational energy increase at a rate of $\dot{E}^p_{vib}$. Thereby, the deposited energy can be written as :

$$\dot{E}^p = \dot{E}^p_{chem} + \dot{E}^p_{heat} + \dot{E}^p_{vib} \tag{8.6}$$

Finally, the rate $\dot{R}^p_{VT}$ represents the increase of the total energy by the relaxation of vibrational energy into the translational mode.

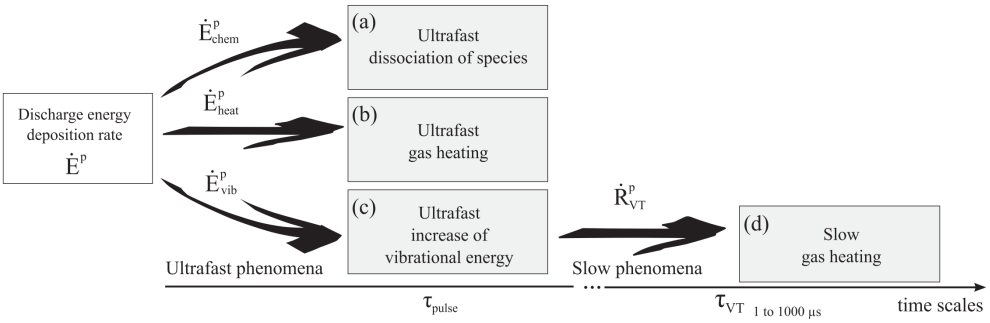

FIGURE 8.15 – *Schematic representation of the NRP discharges model assumptions. The discharge energy is assumed to be deposited into (a) chemical, (b) sensible and (c) vibrational energies within the pulse characteristic time τ_{pulse}. The vibrational energy relaxes after the pulse, leading to an increase of the (d) sensible energy within a characteristic time τ_{VT}. (extracted from Castela et al. (2016))*

The governing equations considering the discharge contribution can be written as :

$$\frac{\partial \rho_g}{\partial t} + \frac{\partial \rho_g U}{\partial x} = 0 \tag{8.7}$$

$$\rho_{\mathrm{g}}\frac{\partial Y_k}{\partial t}+\rho_{\mathrm{g}}U\frac{\partial Y_k}{\partial x}=-\frac{\partial}{\partial x}\left[\rho_{\mathrm{g}}Y_kV_k\right]+W_k\dot{\omega}_k^c+W_k\dot{\omega}_k^p \tag{8.8}$$

$$\frac{\partial \rho_{\mathrm{g}}e_{vib}}{\partial t}+\frac{\partial \rho_{\mathrm{g}}Ue_{vib}}{\partial x}=\frac{\partial}{\partial x}\left(\rho_{\mathrm{g}}\alpha_{N_2}\frac{\partial e_{vib}}{\partial x}\right)+\dot{E}_{vib}^p-\dot{R}_{VT}^p \tag{8.9}$$

$$\rho_{\mathrm{g}}\frac{\partial H_{\mathrm{g}}}{\partial t}+\rho_{\mathrm{g}}U\frac{\partial H_{\mathrm{g}}}{\partial x}=\frac{\partial}{\partial x}\left[k_{\mathrm{g}}\frac{\partial T_{\mathrm{g}}}{\partial x}\right]+\dot{E}_{chem}^p+\dot{E}_{heat}^p+\dot{R}_{VT}^p-\sum_{k=1}^{K}\rho_{\mathrm{g}}Y_kV_kH_k-\dot{Q}_{cvf_g} \tag{8.10}$$

$$\rho_{\mathrm{w}}C_{p_{\mathrm{w}}}\frac{\partial T_{\mathrm{w}}}{\partial t}+\frac{\partial}{\partial x}\left[k_{\mathrm{w}}\frac{\partial T_{\mathrm{w}}}{\partial x}\right]=\dot{Q}_{cvn}-\dot{Q}_{cvf_s}+\dot{Q}_{rad} \tag{8.11}$$

with e_{vib} the vibrational energy and $\dot{\omega}_k^p$ the molar production rate associated with species dissociation due to plasma.
where :

$$\dot{Q}_{cvf_g}=\frac{2}{r_i}h_i(T_{\mathrm{g}}-T_{\mathrm{w}})$$

the gas forced convection heat losses to the wall,

$$\dot{Q}_{cvn}=\frac{2r_e}{r_e^2-r_i^2}h_e(T_{\mathrm{w}}-T_0)$$

the external natural convection heat losses from the wall to the ambient air,

$$\dot{Q}_{rad}=\frac{2r_e}{r_e^2-r_i^2}\epsilon_S\sigma(T_{\mathrm{w}}^4-T_0^4)$$

the radiative heat losses from the wall to the ambient air, and

$$\dot{Q}_{cvf_s}=\frac{2r_i}{r_e^2-r_i^2}h_i(T_{\mathrm{g}}-T_{\mathrm{w}})$$

the forced convection heat losses from the wall to the inner gas.

Two crucial parameters, determined in Castela et al. (2016) through experimental and numerical literature, are the ratio of discharge energy going into ultrafast oxygen dissociation set to η=0.35 and the ratio of energy transferred into ultrafast heat set to 0.20. The terms τ_{pulse}, τ_{VT}, $\dot{E}_{chem}^p$, $\dot{E}_{chem}^p$, $\dot{E}_{heat}^p$, $\dot{E}_{vib}^p$ and $\dot{R}_{VT}^p$ are modeled in Castela et al. (2016). The global model is adapted and used to the narrow size combustion modelisation previously established.

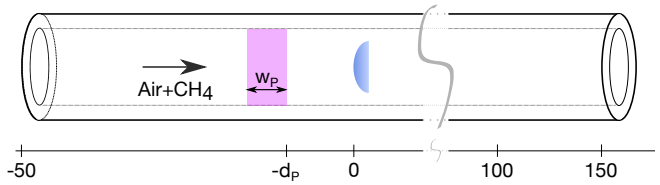

FIGURE 8.16 – *Schematic representing the plasma deposition upstream from the flame, with d_P the end deposition coordinate and w_P the width of the deposition.*

8.3.2 Adaptation of the existing model to the studied combustion model

The deposition is characterized by the discharge energy, its end position d_P, its width w_P, the frequency of the nanosecond repetitive pulse, the pulse characteristical time τ_{pulse} and the pulse number. A scheme of the studied configuration is represented in Fig. 8.16. A space filter is used on the discharge to smooth discharge energy input. This space filter can be expressed as :

$$F(x) = \text{erfc}\left(\frac{(x - x_{cd})^2}{(w_P/2)^2}\right)^{2.5} \tag{8.12}$$

with $x_{cd} = d_P - w_P/2$ the discharge center coordinate. The parameters are computed to ensure that the area defined by the space filter is equal to $\pi(x - x_{cd})^2$.
The characteristic time of the flame motion in flashback is of the order of hundreds of seconds, and thereby, millions of discharges of τ_{pulse}=50 ns would be necessary to observe a complete flashback. Here, the choice is made to impose a continuous discharge, the number of discharges is set to one and the discharge time is set very high (τ_{pulse}=100 s). By doing so, the relaxation from the vibrational states of nitrogen is not represented, thereby the discharge gas heating linked to this phenomenon is not taken into account. These hypothesis are made as a first step to test the code coupling with the plasma modeling and to see if effects of the discharge on the flame are observable, and to try to distinguish the thermal effects from the chemical effects.
An energy and distance cartography of the discharge is carried out, keeping a constant width of w_P=5 mm.

8.3.2.1 Discharge characterization at d_p=-6 mm

According to the parameters entered in the model, the energy deposition is divided into 35% of O_2 dissociation and 20% of heat input. Therefore the effects of the deposition on the O_2 specie dissociation and on temperature are observed. The mass fraction evolution of O_2 and O species as a function of the axial coordinate are represented on Fig. 8.17, with a discharge end position of d_P=-

6 mm and a deposition width of w_P=5 mm. The energy deposited is varied from 0 to E_p=10^9 J·m^{-3}. The global graphs are represented on the left of the Fig. 8.17 and a zoom from 1 mm before the discharge to the flame front is represented on the right of the figure.

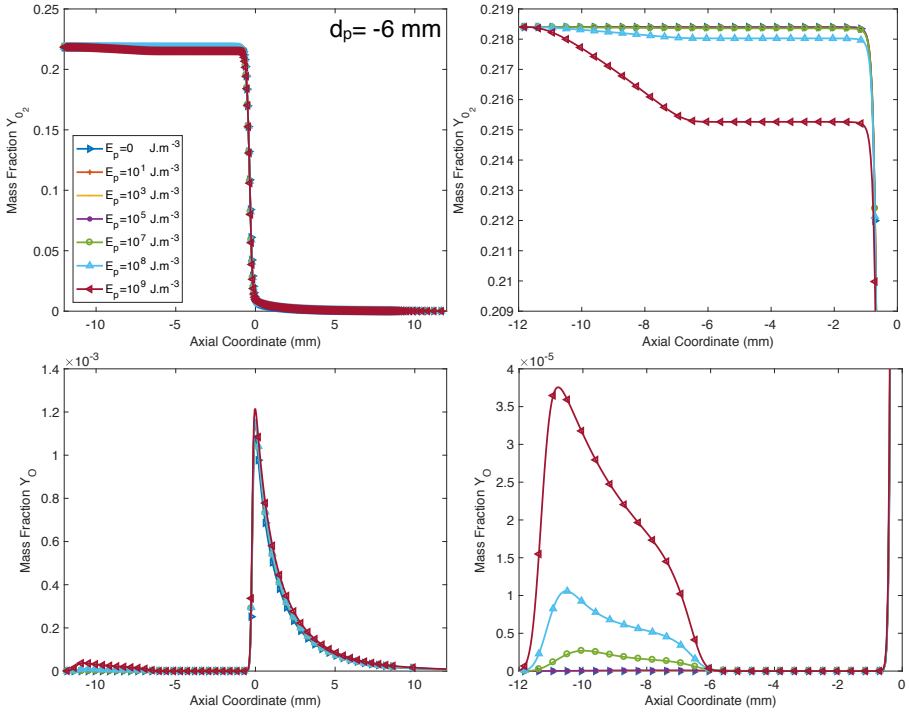

FIGURE 8.17 – *Mass fraction of O_2 (top) and O (bottom) species according to the axial coordinate, with a stabilized flame at the zero coordinate. The zoom on the discharge area is represented on the right. The deposition energy is varied.The end deposition coordinate is d_P=-6 mm and the deposition width is w_P=5 mm.*

The discharge is characterized by a drop in O_2 species, which is dissociated in O species, and therefore a peak in O species. The more energy is given to the discharge the more dioxygen molecules are dissociated and thus atomic oxygen species created. However, the increase in O species only occurs within the discharge width. Thus, a minimum energy is required for the dissociation to occur, and therefore, under E_p=10^5 J·m^{-3}, no dissociation is observed.
In experimental studies, it was established that a NRP discharges have an impact on O, OH and H species, which are species crucial for combustion. In order to measure the influence of the presented deposition upstream from the flame front on O, OH and H species, their mass fractions are represented in Fig. 8.18, for several deposition energies.
On the discharge zoom (right), an increase of OH species can be observed in the discharge, for the highest input energy. Thus, in the global profile representation

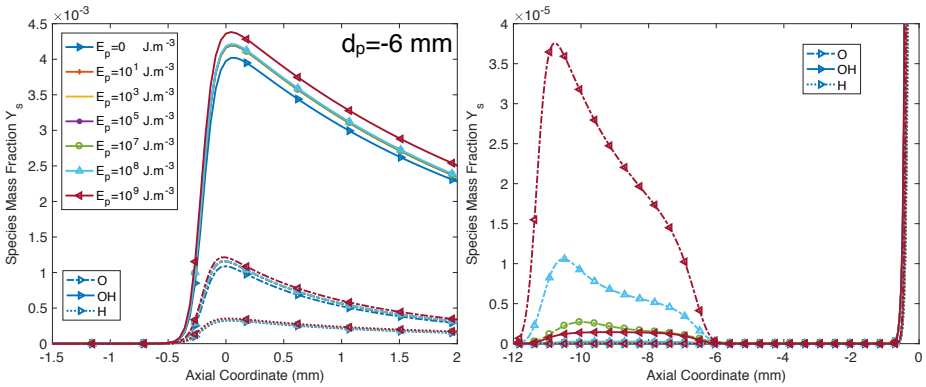

FIGURE 8.18 – *O, OH and H mass fraction profiles according to energy of the deposition, with d_P=-6 mm and w_P=5 mm. The zero coordinate represents the flame front position. The graph on the left represents a global view and the one on the right is a close-up on the discharge.*

(left), the species mass fraction of OH and H increase in the flame front. The deposition has therefore an impact on the production of these three species, that play a crucial role in the combustion chemical reactions.
The species increase in the deposition area follow the spatial filter represented in Fig. 8.19.

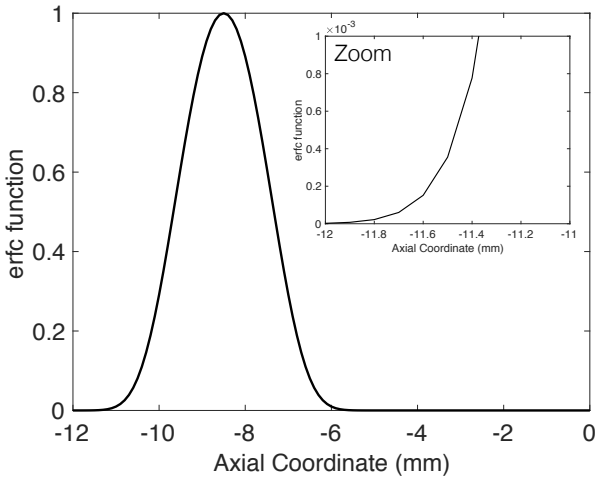

FIGURE 8.19 – *Space filter plot with d_P=-6 mm and w_P=5 mm. A zoom is displayed for values up to the coordinate $x = -12$ mm to show the non zero values.*

As depicted in the zoom, the smoothing of the function up to the coordinate $x = -12\ mm$ leads to the peak of species near this coordinate. The more energy is given to the discharge, the larger smoothing of the discharge is extended. This

first peak is followed by a decrease of the species mass fraction, highlighting a non linear recombinaisons.
The temperature profiles of wall and gas are represented in Fig. 8.20. It can be noted that in the area of the deposition, an increase of gas temperature is observed for the highest deposited energy. Therefore, under the deposition energy of E_p=10^7 J·m^{-3}, no effect on gas temperature is noticeable.

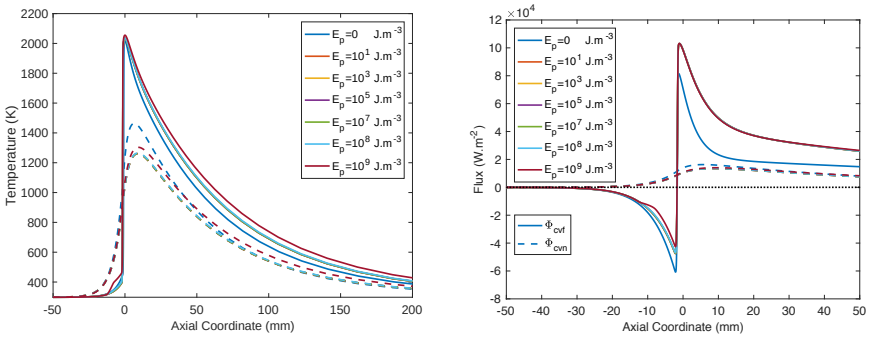

FIGURE 8.20 – *Gas (plain lines) and wall (dashed lines) temperature profiles of a steady flame positioned at zero coordinate, as a function of the energy of the deposition. The end deposition coordinate is d_P=-6 mm with a width of w_P=5 mm.*

An impact of the discharge is observed on the O, O_2, OH and H species within the discharge width but also in the flame front, and on the temperature profile of the wall and gas. The study is therefore carried out for several end deposition d_p in a steady flame configuration.

8.3.2.2 Discharge effects according to the end deposition d_p, in steady configuration

The effect of the discharge is evaluated according to the end deposition coordinate d_p. The maximum energy is chosen to see the maximal possible impact. The temperature profiles of the wall and gas for three end deposition cases are represented in Fig. 8.21. The end deposition cases are d_p=-6 mm, which is the case presented in the previous subsection, d_p=0 mm meaning that the end deposition is in contact with the flame front, and d_p=2 mm, which represents a discharge ending in the burned gas, astride the flame front.
The temperature profile is weakly modified for end depositions coordinate d_P=0 and 2 mm, but as previously established, an increase of the temperature profile is noticeable for d_P=-6 mm.
The mean flow speed modification for a steady flame according to the end deposition coordinate, and for several energy deposited is represented in Fig. 8.22. As the deposition energy increases, the steady bulk velocity rises at a constant deposition end coordinate. The deposition must then be close to the flame front, to decorellate as much as possible the heat effect from the chemical one, and

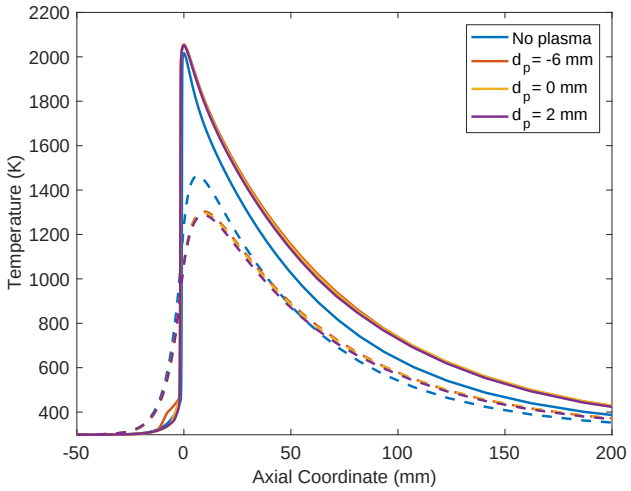

FIGURE 8.21 – *Gas (plain line) and wall (dashed lines) temperature profiles of a steady flame for three end deposition coordinate d_P with w_P=5 mm at a maximum imposed deposition energy of $E_p = 10^9$ $J{\cdot}m^{-3}$.*

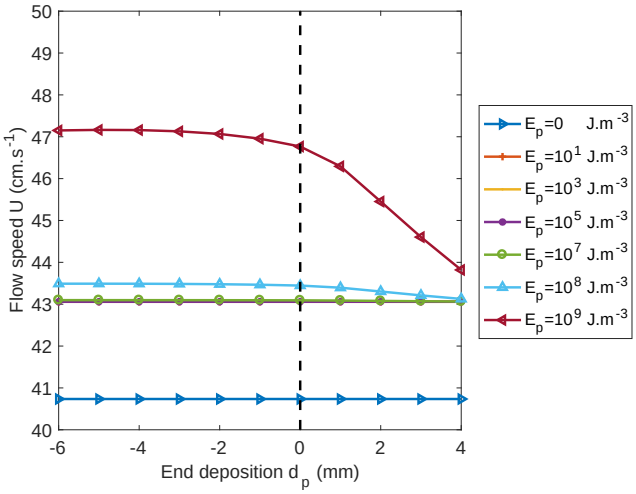

FIGURE 8.22 – *Flow speed of a steady flame according to te energy of the deposition and to the end deposition coordinate d_P with w_P=5 mm.*

so that the dissociation of the species are in contact with the reaction zone.

8.4 Conclusion

This chapter is presented as perspectives of further work to assist a flame using a plasma. Experimentally a configuration was found to observe an assistance on a stabilized flame. In this counterflow configuration a new flame stabilization was observed. However no quantitative measurements were performed. Numerically,

an existing NRP plasma modelisation is used, adding the wall to the reactive mixture computation. The effects on the flame are observed at several plasma deposition distances from the flame with an increase of the O, OH and H species in the flame front, and with a higher stabilization flow rate. These effects are only observed for deposited energy higher than a threshold value. However the discharge also creates a thermal assistance as the deposited energy is 20% transformed into a heat source term. Further work on the decoupling of these effects and on the assistance must be carried out.

Conclusion

Thesis achievements

In a context of reducing devices scale and increase their portability, the narrow channel combustion shows a great potential for power supply, considering the high energy density of hydrocarbon fuels. However, a major issue of combustion at this scale is the massive heat losses due to a high surface-to-volume ratio. In the literature, micro and mesoscale combustions are mostly studied compensating these heat losses by assisting the flame and thereby extending the flammability limits. Yet, few studies were carried out on flames in "natural environment", without external assistance, and therefore evaluating the possibility to use this combustion as power supply. The objective of the present work was to provide a better understanding on the stabilization mechanisms of flames in narrow channels, considering all heat exchanges from the inner gas to the ambient air : forced convection, wall conduction, natural convection and solid radiation. No assistance was given to the compensate the heat losses or extend the flammability limits, therefore in a first part the limits of the system were established. Then the different flame regimes and shapes were characterized experimentally and compared to a one-dimensional numerical computation. The first part of this work was focused on delimiting the system, on justifying the configurations studied and on validating the diagnostics used. Experimentally, the configuration studied was selected so that no external assistance of the flame was needed. Therefore, the limits of the system are determined by this condition, fixing the tube length to obtain a constant and equal wall and gas temperature upstream and downstream from the flame. The lower limit in burner diameters is fixed by the quenching distance, under which no flame can propagate without assistance and which depends on equivalence ratio, temperatures and fuel. Thus, temperature measurements are a crucial parameter of the heat exchanges characterization and therefore of this work. Hence, Laser Induced Phosphorescence (LIP) was implemented and validated as a diagnostic over small dimensions tubes. The comparison to thermocouple measurements allows to assess the accuracy of the two techniques over different ranges of temperatures. It is established that both measurements are complementary, since the thermocouple measurements have a greater accuracy in low temperatures while the LIP measurements are more reliable in reproducing the maximum of

temperature reached. To establish an "ideal" temperature profile, both temperature measurements are necessary.
The heat exchanges characterization of a steady system was carried out in the second part of this work. Looking at the characteristic times, the wall conduction was established as the slowest thermal exchange. Therefore a ratio of this conduction time over the flame residency characteristic time was calculated as an indicator of the flame regime. When this ratio is under unity, the thermal establishment is reached. On the contrary when the ratio is greater than unity the flame is propagating over isothermal walls.
The steady regime of a flame was firstly characterized experimentally. As exposed in Fig. 8.23, a unique steady flame is obtained for three input parameters : the tube diameter, the equivalence ratio and the tube position (horizontal/vertical). These steady flames are characterized by their temperature domain, but also by their shapes and orientations. These parameters reveal the strong impact of the thermal interactions on the flame regimes.

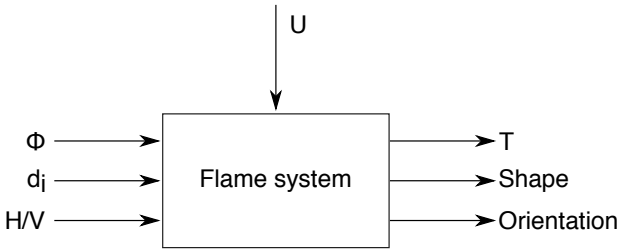

FIGURE 8.23 – *Scheme representing the flame system, with three input entries of equivalence ratio ϕ, inner tube diameter d_i and tube position H/V. According to those parameters, one flow velocity (U) corresponds and leads to a unique flame characterized by its temperature profile (T), its shape and orientation.*

In fact, by reducing the tube diameter, the surface-to-volume ratio increases leading to greater heat losses and therefore a higher transfer rate to the external air. However, the stability domain of the flame is reduced.
Then, after literature review and using theoretical analysis on forced and natural convection over heated cylinders in vertical and horizontal position, the heat exchanges are sized. Based on this characterization, and to enhance the description and knowledge on the heat exchanges, a one-dimensional complex chemistry code is used to compute flames in a simulation close to the experiment. The resulting flame speeds and temperatures are in good agreement with the experiments. Thus, an analysis of the heat fluxes allows to better understand the thermal establishment of the flame, and to compare the involvement of the different heat exchanges in the stabilization. By that, the importance of quartz radiation on wall temperature is demonstrated. Thus, it is computed that 96% of the flame power is transmitted to the ambient air through natural convection and radiation for an equivalence ratio of ϕ=0.8. The preheating of the fresh gas represents 4% of the flame power. As the equivalence ratio increases, the per-

centage of flame power transmitted to the external air increases. These values clearly show an overestimation of the external heat fluxes, however they put in relief the tendency of heat exchanges.
Moreover, in steady experimental observations the flame shape and orientation highlight the presence of a symmetry breaking phenomena. First by comparing horizontal and vertical flames and then using a two dimensional DNS simulation processed by CORIA lab research team (K.Bioche, G.Ribert and L.Vervisch), the origin of this tilt was attributed to gravity effects. Indeed, by decoupling the heat effects from the gravity the flames remain asymmetrical, with an inclinaison angle lower than in the coupled case. This slight inclinaison is demonstrated to be caused by the baroclinic torque response to gravity.
Finally, the third part of the presented work relates the response of a flame to an upstream temperature perturbation. This finding is an original way to modify the flame location. Through the characterization of this transitory regime toward the thermal perturbation, the heat exchanges mechanisms are analyzed. In fact, two modes of propagation are observed according to the distance between the flame front and the heat perturbation. The first mode is a slow propagation, where the flame is already in contact with the heat source temperature profile. In the second mode, the flame propagates over isothermal walls, with a high propagation speed, before reaching stabilization. The initial and final states of the flames are compared and shown equal, meaning that the flame moves from a steady regime to another through this transitory translation.

Perspectives

The improvements and perspectives of the presented work can be further discussed in several fields. A first axis of improvement would be to determine the origin of the flame asymmetry in vertical tubes. In the same way microgravity experiments could be pursed to further understanding on the effects of gravity on the flames in narrow channels. In a second axis, reaching a better comparison between experimental measurements and numerical computations could be achieved. In fact, because of the dimensions of the micro-burners, few diagnostics are feasible leading to difficulties to acquire quantitative data. On the other hand, the complex coupling of thermal exchanges makes the modeling a challenge. As a third axis, the optimisation of a micro-burner could be carried out, which could lead to small-scale power source devices. The aim is then to increase the heat available outside from the tube, and therefore enhance the flame power and the efficiency of the system. To optimise the heat transfer, the wall conductivity can be varied. However, it can lead to a break in flame stability. To avoid that, an assistance to flame stability is necessary. In the introduction chapter of this work, several possible assistance are exposed, especially thermal, chemical and mechanical assistance. As a chemical assistance, the use of plasma is considered in the last chapter of the presented work. It was shown experi-

mentally that with the use of the plasma in contact with the flame, the mass flow rate could be increased leading to an increase in flame power. Numerically, the plasma addition also leads to an increase in the steady mass flow rate. Further work on this coupling must be carried out for quantitative data and to distinguish the thermal effects of the plasma on the flame from the chemical ones. Another possible chemical assistance is the catalytic combustion presented in the introduction, which has a great potential in flame stabilization and in enhancing the thermal exchanges. Finally, several applications using thermal assistance are already submitted to patents, such as the swiss-roll burner or an integrated micro-combustion power generator that converts hydrocarbon fuel into electricity (Patent number : US8,686,278B2). Thus, very recent studies (Milcarek et al. (2019); Milcarek and Ahn (2019)) showed that with a two stages combustor using methane, high power density (>300 mW·cm^{-2}) and high electrical efficiency ($>1.2\%$) are achieved for equivalence ratios below 1.6. However, as these accomplishments are achieved, new challenges are unveiled and the dilemma of obtaining high power density, high electrical efficiency and no soot is discussed. It is evident, then, from all that was exposed that micro and mesoscale combustion are a promising field of research and that it has a bright future as a portable power source.

Références

Acharya, S. and S. K. Dash (2017). Natural Convection Heat Transfer From a Short or Long, Solid or Hollow Horizontal Cylinder Suspended in Air or Placed on Ground. *Journal of Heat Transfer 139*(7), 072501. *(p. xxi, 97, 98, 129)*

Aghalayam, P., P.-a. Bui, and D. G. Vlachos (1998). The role of radical wall quenching in flame stability and wall heat flux : hydrogen-air mixtures. *Combustion Theory and Modelling 2*(4), 515–530. *(p. 32, 37)*

Al-Arabi, M., M. Khamis, and M. Abd-Ul-Aziz (1991). Heat transfer by natural convection from the inside surface of a uniformly heated tube at different angles of inclination. *International Journal of Heat and Mass Transfer 34*(4-5), 1019–1025. *(p. 98)*

Bai, B., Z. Chen, H. Zhang, and S. Chen (2013). Flame propagation in a tube with wall quenching of radicals. *Combustion and Flame 160*(12), 2810 – 2819. *(p. xvi, 33, 34, 35, 36, 80)*

Bang, C. U., Y. C. Hong, S. C. Cho, H. S. Uhm, and W. J. Yi (2006). Methane-augmented microwave plasma burner. *IEEE Transactions on Plasma Science 34*(5 I), 1751–1756. *(p. 185)*

Bao, A., Y. G. Utkin, S. Keshav, and I. V. Adamovich (2007). Methanol and Ethanol Ignition by Repetitively Pulsed , Nanosecond Pulse Duration Plasma 1. (January 2006), 1–16. *(p. 182)*

Barbi, E., J. R. Mahan, W. O'Brien, and T. Wagner (1989). Operating characteristics of a hydrogen-argon plasma torch for supersonic combustion applications. *Journal of Propulsion and Power 5*(2), 129–133. *(p. 182)*

Barbosa, S., G. Pilla, D. A. Lacoste, P. Scouflaire, S. Ducruix, C. O. Laux, and D. Veynante (2015). Influence of nanosecond repetitively pulsed discharges on the stability of a swirled propane/air burner representative of an aeronautical combustor. *Philosophical Transactions of the Royal Society A : Mathematical, Physical and Engineering Sciences 373*(2048). *(p. 182)*

Billah, M. M., M. M. Rahman, U. M. Sharif, N. A. Rahim, R. Saidur, and M. Hasanuzzaman (2011). Numerical analysis of fluid flow due to mixed convection in a lid-driven cavity having a heated circular hollow cylinder. *International Communications in Heat and Mass Transfer 38*(8), 1093–

1103. *(p. 99)*

Bioche, K., A. Pieyre, G. Ribert, F. Richecoeur, and L. Vervisch (2019). The role of gravity in the asymmetry of flames in narrow combustion chambers. *Combustion and Flame 203*, 238–246. *(p. 130)*

Bioche, K., L. Vervisch, and G. Ribert (2018). Premixed flame-wall interaction in a narrow channel : Impact of wall thermal conductivity and heat losses. *J. Fluid Mech. 856*, 5–35. *(p. 130, 132)*

Bouheraoua, L., P. Domingo, and G. Ribert (2017). Large-eddy simulation of a supersonic lifted jet flame : Analysis of the turbulent flame base. *Combust. Flame 179*, 199–218. *(p. 131)*

Brandenburg, R., A. Bogaerts, W. Bongers, A. Fridman, G. Fridman, B. R. Locke, V. Miller, S. Reuter, M. Schiorlin, T. Verreycken, and K. K. Ostrikov (2018). White paper on the future of plasma science in environment, for gas conversion and agriculture. *Plasma Processes and Polymers* (April), 1–18. *(p. 182)*

Brübach, J., A. Dreizler, and J. Janicka (2007). Gas compositional and pressure effects on thermographic phosphor thermometry. *Measurement Science and Technology 18*(3), 764–770. *(p. 66)*

Brübach, J., J. P. Feist, and A. Dreizler (2008). Characterization of manganese-activated magnesium fluorogermanate with regards to thermographic phosphor thermometry. *Measurement Science and Technology 19*(2). *(p. 66, 69)*

Brübach, J., J. Janicka, and A. Dreizler (2009). An algorithm for the characterisation of multi-exponential decay curves. *47*, 75–79. *(p. xix, 67, 68, 71, 72)*

Brübach, J., C. Pflitsch, A. Dreizler, and B. Atakan (2012). On surface temperature measurements with thermographic phosphors : A review. *Progress in Energy and Combustion Science 39*(1), 37–60. *(p. 56, 57, 69)*

Candel, S., T. Schmitt, and N. Darabiha (2011). Progress in transcritical combustion. *23rd ICDERS*. *(p. 103)*

Castela, M. (2016). *Modelling plasma-assisted combustion in quiescent and turbulent flow conditions*. Ph. D. thesis, Université Paris-Saclay, CentraleSupélec. *(p. 196)*

Castela, M., B. Fiorina, A. Coussement, O. Gicquel, N. Darabiha, and C. O. Laux (2016). Modelling the impact of non-equilibrium discharges on reactive mixtures for simulations of plasma-assisted ignition in turbulent flows. *166*, 133–147. *(p. xxviii, 196, 197, 198)*

Chang, C. L. (2008). Numerical simulation for natural convection of micropolar fluids flow along slender hollow circular cylinder with wall conduction effect. *Communications in Nonlinear Science and Numerical Simulation 13*(3), 624–636. *(p. 99)*

Chao, C. Y. H., K. S. Hui, W. Kong, P. Cheng, and J. H. Wang (2007). Analytical and experimental study of premixed methane-air flame pro-

pagation in narrow channels. *International Journal of Heat and Mass Transfer 50*(7-8), 1302–1313. *(p. 14)*

Chen, Z., M. P. Burke, and Y. Ju (2009). Effects of Lewis number and ignition energy on the determination of laminar flame speed using propagating spherical flames. *Proceedings of the Combustion Institute 32 I*(1), 1253–1260. *(p. 184)*

Chen, Z. and Y. Ju (2007). Theoretical analysis of the evolution from ignition kernel to flame ball and planar flame. *Combustion Theory and Modelling 11*(3), 427–453. *(p. 184)*

Childs, P. R., J. R. Greenwood, and C. A. Long (2000). Review of temperature measurement. *Review of Scientific Instruments 71*(8), 2959–2978. *(p. 54)*

Churchill, S. W. and H. H. S. Chu (1975). Correlating equations for laminar and turbulent free convection from a horizontal cylinder. *International Journal of Heat and Mass Transfer 18*(9), 1049–1053. *(p. 95, 100)*

Churchill, S.W. and Usagi, R. (1972). A general expression for the correlation of rates od transfer and other phenomena. *AIChE Journal 18*(6), 1121–1129. *(p. 95)*

Clavin, P., P. Pelcé, and L. He (1990). One-dimensional vibratory instability of planar flames propagating in tubes. *J. Fluid Mech. 216*, 299–322. *(p. 129)*

Clavin, P. and G. Searby (2016). *Combustion Waves and Fronts in Flows*. Cambridge : Cambridge University Press. *(p. 136)*

Coche, P., V. Guerra, and L. L. Alves (2016, may). Microwave air plasmas in capillaries at low pressure i. self-consistent modeling. *Journal of Physics D : Applied Physics 49*(23), 235207. *(p. 188)*

Curtiss, C. F. and J. O. Hirschfelder (1949). Transport properties of multicomponent gas mixtures. *J. Chem. Phys. 17*(6), 550–555. *(p. 131)*

Daou, J. and M. Matalon (2002). Influence of conductive heat-losses on the propagation of premixed flames in channels. *Combustion and Flame 128*(4), 321–339. *(p. 8, 19, 22, 87)*

Darrieus, G. (1938). Propagation d'un front de flamme. *La Technique Moderne 30*, 18. *(p. 129)*

Dasan, B. G., T. Yildirim, and I. H. Boyaci (2018). Surface decontamination of eggshells by using non-thermal atmospheric plasma. *International Journal of Food Microbiology 266*(July 2017), 267–273. *(p. 182)*

Degenève, A., P. Jourdaine, C. Mirat, R. Vicquelin, and T. Schuller (2018). Optimisation de la mesure de température de paroi par thermographie de luminophore appliquée à la combustion. *CFTL*. *(p. 67)*

Dejoan, A. and V. N. Kurdyumov (2018). Thermal expansion effect on the propagation of premixed flames in narrow channels of circular cross-section : Multiplicity of solutions, axisymmetry and non-axisymmetry. *Proceedings of the Combustion Institute 000*, 1–9. *(p. 13)*

Di Stazio, A., C. Chauveau, G. Dayma, and P. Dagaut (2015). Combustion in micro-channels with a controlled temperature gradient. *Experimental Thermal and Fluid Science*. *(p. xvi, 14, 15, 130)*

Di Stazio, A., C. Chauveau, G. Dayma, and P. Dagaut (2016). Oscillating flames in micro-combustion. *Combustion and Flame 167*(Supplement C), 392–394. *(p. 18)*

Dogwiler, U., J. Mantzaras, P. Benz, B. Kaeppeli, R. Bombach, and A. Arnold (1998). Homogeneous ignition of methane-air mixtures over platinum : Comparison of measurements and detailed numerical predictions. *Symposium (International) on Combustion 27*(2), 2275–2282. *(p. xvi, 16, 17)*

Domingo, P. and L. Vervisch (2017). Dns and approximate deconvolution as a tool to analyse one-dimensional filtered flame sub-grid scale modeling. *Combust. Flame 177*, 109–122. *(p. 131)*

Domingo, P., L. Vervisch, and D. Veynante (2008). Large-eddy simulation of a lifted methane-air jet flame in a vitiated coflow. *Combust. Flame 152*(3), 415–432. *(p. 131)*

Douglas, Jr, J. (1955). On the numerical integration of $\partial^2 u/\partial x^2+\partial^2 u/\partial y^2=\partial u/\partial t$ by implicit methods. *J. Soc. Ind. App. Math. 3*(1), 42–65. *(p. 131)*

Duboc, B., G. Ribert, and P. Domingo (2018). Evaluation of chemistry models on methane/air edge flame simulation. *Proc. Comb. Inst.*. *(p. 131)*

Duchaine, F., A. Corpron, L. Pons, V. Moureau, F. Nicoud, and T. Poinsot (2009). Development and assessment of a coupled strategy for conjugate heat transfer with large eddy simulation : application to a cooled turbine blade. *Int. J. Heat Fluid Flow 30*(6), 1129–1141. *(p. 131)*

Ducros, F., V. Ferrand, F. Nicoud, C. Weber, D. Darracq, C. Gacherieu, and T. Poinsot (1999). Large-eddy simulation of the shock/turbulence interaction. *J. Comput. Phys. 152*(2), 517–549. *(p. 131)*

Dunn-Rankin, D., E. M. Leal, and D. C. Walther (2005). Personal power systems. *Progress in Energy and Combustion Science 31*(5-6), 422–465. *(p. 3)*

Ekkad, S. V. and J.-c. Han (2000). A transient liquid crystal thermography technique for gas turbine heat transfer measurements. *11*, 957–968. *(p. 55)*

Esakov, I., L. Grachev, K. Khodataev, and D. Van Wie (2004). Experiments on Propane Ignition in High-Speed Airflow Using a Deeply Undercritical Microwave Discharge. *42nd AIAA Aerospace Sciences Meeting and Exhibit* (January), 1–7. *(p. 182)*

Evans, C. J. and D. C. Kyritsis (2009). Operational regimes of rich methane and propane/oxygen flames in mesoscale non-adiabatic ducts. *Proceedings of the Combustion Institute 32*(2), 3107–3114. *(p. 14)*

Farouk, B. (1981). Natural convection from a horizontal cylinder - laminar regime. *Journal of Heat Transfer 103*(August), 522–527. *(p. xx, 95, 96)*

Federici, J. A. and D. G. Vlachos (2008). A computational fluid dynamics study of propane/air microflame stability in a heat recirculation reactor. *Combustion and Flame 153*(1-2), 258–269. *(p. xvi, 14, 15)*

Feist, J. (2001). *Development of phosphor thermometry for gas turbines*. Ph. D. thesis, Department of Mechanical Engineering, Imperial College, London. *(p. 66)*

Fernández-Galisteo, D., C. Jiménez, M. Sánchez-Sanz, and V. N. Kurdyumov (2014). The differential diffusion effect of the intermediate species on the stability of premixed flames propagating in microchannels. *Combustion Theory and Modelling 18*(March), 582–605. *(p. 13)*

Fernández-Galisteo, D., C. Jiménez, M. Sánchez-Sanz, and V. N. Kurdyumov (2017). Effects of stoichiometry on premixed flames propagating in narrow channels : symmetry-breaking bifurcations. *Combustion Theory and Modelling 21*(6), 1050–1065. *(p. 13)*

Fernández-Galisteo, D. and V. N. Kurdyumov (2018). Impact of the gravity field on stability of premixed flames propagating between two closely spaced parallel plates. *Proceedings of the Combustion Institute 000*, 1–7. *(p. 20, 123, 124)*

Fernandez-Pello, A. C. (2002). Micropower generation using combustion : Issues and approaches. *Proceedings of the Combustion Institute*. *(p. 4)*

Frenklach, M., H. Wang, C.-L. Yu, M. Goldenberg, C. T. Bowman, R. K. Hanson, D. F. Davidson, E. J. Chang, G. P. Smith, D. M. Golden, W. C. Gardiner, and V. Lissianski (1995). Gri-mech—an optimized detailed chemical reaction mechanism for methane combustion. Technical report, Gas Research Institute, Chicago, IL. Report No. GRI-95/0058. *(p. 132)*

Fuhrmann, N., J. Brübach, and A. Dreizler (2013). Phosphor thermometry : A comparison of the luminescence lifetime and the intensity ratio approach. *Proceedings of the Combustion Institute 34*(2), 3611–3618. *(p. 56)*

Guiberti, T. F., P. Scouflaire, and T. Schuller (2014). La Phosphorescence Induite par Laser pour la Mesure de Température des Surfaces d'une Chambre de Combustion. *14eme Congrès Francophone de Techniques Laser (CFTL)*. *(p. 67)*

Guirguis, R. H., A. K. Oppenheimt, and I. Karasaloj (1981). Thermochemistry of Methane Ignition. *Combustion in Reactive Systems*, 134–153. *(p. 30)*

Hackert, C. L., J. L. Ellzey, and O. A. Ezekoye (1998). Effects of thermal boundary conditions on flame shape and quenching in ducts. *Combustion and Flame 112*(1-2), 73–84. *(p. 8, 19)*

Hammack, S., T. Lee, and C. Carter (2012). Microwave plasma enhancement

of various flame geometries at atmospheric pressure. *IEEE Transactions on Plasma Science 40*(12), 3139–3146. *(p. 185)*

Hammack, S., X. Rao, T. Lee, and C. Carter (2011). Direct-coupled plasma-assisted combustion using a microwave waveguide torch. *IEEE Transactions on Plasma Science 39*(12 PART 1), 3300–3306. *(p. xxvii, 185, 187)*

Hemawan, K. W., C. L. Romel, S. Zuo, I. S. Wichman, T. A. Grotjohn, and J. Asmussen (2006). Microwave plasma-assisted premixed flame combustion. *Applied Physics Letters 89*(14). *(p. 185)*

Hemawan, K. W., I. S. Wichman, T. Lee, T. A. Grotjohn, and J. Asmussen (2009). Compact microwave re-entrant cavity applicator for plasma-assisted combustion. *Review of Scientific Instruments 80*(5). *(p. xxvii, 185, 186)*

Heraeus. Heraeus : Quartz glass for optics data and properties. *(p. xxi, 106)*

Heyes, A. L., S. Seefeldt, and J. P. Feist (2006). Two-colour phosphor thermometry for surface temperature measurement. *Optics and Laser Technology 38*(4-6), 257–265. *(p. 56)*

Hong, Y. C. and H. S. Uhm (2006). Properties of plasma flames sustained by microwaves and burning hydrocarbon fuels. *Physics of Plasmas 13*(11). *(p. 185)*

Huang, W., S. Vosen, and R. Greif (1988). Heat transfer during laminar flame quenching : Effect of fuels. *Symposium (International) on Combustion 21*(1), 1853 – 1860. Twenty-First Symposuim (International on Combustion). *(p. 103)*

ICCD (2018). International center for diffraction data (icdd), www.icdd.com. *(p. 48)*

Ishiwada, N., E. Fujii, and T. Yokomori (2018). Evaluation of Dy-doped phosphors (YAG :Dy, Al2O3 :Dy, and Y2SiO5 :Dy) as thermographic phosphors. *Journal of Luminescence 196*(October 2017), 492–497. *(p. 57)*

Jackson, T. L., J. Buckmaster, Z. Lu, D. C. Kyritsis, and L. Massa (2007). Flames in narrow circular tubes. *Proceedings of the Combustion Institute 31 I*(1), 955–962. *(p. 22, 87)*

Jacobsen, L. S., C. D. Carter, R. A. Baurle, T. A. Jackson, S. Williams, D. Bivolaru, S. Kuo, J. Barnett, and C.-J. Tam (2008). Plasma-Assisted Ignition in Scramjets. *Journal of Propulsion and Power 24*(4), 641–654. *(p. 182)*

Jaouen, N., L. Vervisch, P. Domingo, and G. Ribert (2017). Automatic reduction and optimisation of chemistry for turbulent combustion modelling : Impact of the canonical problem. *Combust. Flame 175*, 60–79. *(p. 132)*

Jiménez, C., D. Fernández-Galisteo, and V. N. Kurdyumov (2015). DNS study of the propagation and flashback conditions of lean hydrogen-air flames in narrow channels : Symmetric and non-symmetric solutions. *International Journal of Hydrogen Energy 40*(36), 12541–12549. *(p. 13, 129, 130)*

Jordan, J. and D. A. Rothamer (2013). Pr : YAG temperature imaging in gas-phase flows. pp. 285–291. *(p. 50)*

Jovicic, G., L. Zigan, S. Will, and A. Leipertz (2015). Luminescence Properties of the Thermographic Phosphors Dy3+ :YAG and Tm3+ :YAG for the Application in High Temperature Systems. *Zeitschrift Fur Physikalische Chemie-International Journal of Research in Physical Chemistry & Chemical Physics 229*(6, SI), 977–997. *(p. 57)*

Ju, Y. and C. W. Choi (2003). An analysis of sub-limit flame dynamics using opposite propagating flames in mesoscale channels. *Combustion and Flame 133*(4), 483–493. *(p. 14)*

Ju, Y. and K. Maruta (2011). Microscale combustion : Technology development and fundamental research. *Progress in Energy and Combustion Science 37*(6), 669–715. *(p. xv, 4, 5)*

Ju, Y. and W. Sun (2015a). Plasma assisted combustion : Dynamics and chemistry. *Progress in Energy and Combustion Science 48*, 21–83. *(p. xxvii, 181)*

Ju, Y. and W. Sun (2015b). Plasma assisted combustion : Progress, challenges, and opportunities. *(p. xxvii, 184)*

Ju, Y. and B. Xu (2005). Theoretical and experimental studies on mesoscale flame propagation and extinction. *Proceedings of the Combustion Institute 30 II*, 2445–2453. *(p. 9, 10)*

Ju, Y. and B. Xu (2006a). Effects of channel width and lewis number on the multiple flame regimes and propagation limits in mesoscale. *Combustion Science and Technology 178*(10-11), 1723–1753. *(p. 14, 19, 129)*

Ju, Y. and B. Xu (2006b). Studies of the effects of radical quenching and flame stretch on mesoscale combustion. *44th AIAA Aerospace Sciences Meeting and Exhibit* (January), 1–6. *(p. 32, 35)*

Kaisare, N. S. and D. G. Vlachos (2012). A review on microcombustion : Fundamentals, devices and applications. *Progress in Energy and Combustion Science 38*(3), 321–359. *(p. xv, xvi, 5, 15, 16)*

Kazakov, K. A. (2012). Analytical study in the mechanism of flame movement in horizontal tubes. *Phys. Fluids 24*(2), 022108. *(p. 130, 135, 140)*

Khalid, A. H. and K. Kontis (2009). 2D surface thermal imaging using rise-time analysis from laser-induced luminescence phosphor thermometry. *Measurement Science and Technology 20*(2). *(p. 65)*

Kim, K. T., D. H. Lee, and S. Kwon (2006). Effects of thermal and chemical surface-flame interaction on flame quenching. *Combustion and Flame 146*(1-2), 19–28. *(p. xvii, 33, 34, 36, 37)*

Kim, N. I. and K. Maruta (2006). A numerical study on propagation of premixed flames in small tubes. *Combustion and Flame 146*(1-2), 283–301. *(p. 9)*

Kim, W., M. Godfrey Mungal, and M. A. Cappelli (2010). The role of in situ

reforming in plasma enhanced ultra lean premixed methane/air flames. *Combustion and Flame 157*(2), 374–383. *(p. 182)*

Kim, W., M. Mungal, and M. Cappelli (2005). Flame stabilization using a plasma discharge in a lifted jet flame. *43rd AIAA Aerospace Sciences Meeting and Exhibit* (January), 10–13. *(p. 182)*

Kissel, T., E. Baum, A. Dreizler, and J. Br??bach (2009). Two-dimensional thermographic phosphor thermometry using a CMOS high speed camera system. *Applied Physics B : Lasers and Optics 96*(4), 731–734. *(p. 65)*

Knappe, C., P. Andersson, M. Algotsson, M. Richter, J. Linden, M. Alden, M. Tuner, and B. Johansson (2011). Laser-Induced Phosphorescence and the Impact of Phosphor Coating Thickness on Crank-Angle Resolved Cylinder Wall Temperatures. *SAE International Journal of Engines 4*(1), 2011–01–1292. *(p. 56)*

Kong, D., R. K. Eckhoff, and F. Alfert (1995). Auto-ignition of CH4 air, C3H8 air, CH4/C3H8/air and CH4/CO2/air using a 11 ignition bomb. *Journal of Hazardous Materials 40*(1), 69–84. *(p. 30)*

Koren, C. (2016). *Modélisation des transferts de chaleur couplés pour la simulation multi-physique des chambres de combustion*. Ph. D. thesis, Université Paris-Saclay. *(p. 132)*

Kosarev, I. N., N. L. Aleksandrov, S. V. Kindysheva, S. M. Starikovskaia, and A. Y. Starikovskii (2008). Kinetic mechanism of plasma-assisted ignition of hydrocarbons. *Journal of Physics D : Applied Physics 41*(3). *(p. 182)*

Kuehn, T. and R. Goldstein (1976). Correlating equations for natural convection heat transfer between horizontal circular cylinders. *International Journal of Heat and Mass Transfer 19*(10), 1127–1134. *(p. 95, 101)*

Kumar, S., K. Maruta, and S. Minaev (2007). On the formation of multiple rotating Pelton-like flame structures in radial microchannels with lean methane–air mixtures. *Proceedings of the Combustion Institute 31*(2), 3261–3268. *(p. 18)*

Kurdyumov, V. N. (2011). Lewis number effect on the propagation of premixed flames in narrow adiabatic channels : Symmetric and non-symmetric flames and their linear stability analysis. *Combustion and Flame 158*(7), 1307–1317. *(p. 12, 13, 19, 129)*

Kurdyumov, V. N. and E. Fernández-Tarrazo (2002). Lewis number effect on the propagation of premixed laminar flames in narrow open ducts. *Combustion and Flame 128*(4), 382–394. *(p. 8, 13, 19)*

Kurdyumov, V. N. and C. Jiménez (2014). Propagation of symmetric and non-symmetric premixed flames in narrow channels : Influence of conductive heat-losses. *Combustion and Flame 161*(4), 927–936. *(p. 12)*

Kurdyumov, V. N. and C. Jiménez (2016). Structure and stability of premixed flames propagating in narrow channels of circular cross-section : Non-axisymmetric, pulsating and rotating flames. *Combustion and Flame 0*, 1–15. *(p. 12)*

Kurdyumov, V. N., G. Pizza, C. E. Frouzakis, and J. Mantzaras (2009). Dynamics of premixed flames in a narrow channel with a step-wise wall temperature. *Combustion and Flame 156*(11), 2190–2200. *(p. 12, 18)*

Landau, L. (1944). On the theory of slow combustion. *Acta Phys. 19*, 77–85. *(p. 129)*

Lee, S. T. and C. H. Tsai (1994). Numerical investigation of steady laminar flame propagation in a circular tube. *Combustion and Flame 99*(3-4), 484–490. *(p. xv, xvi, 8, 9, 19, 20, 123)*

Li, J., S. K. Chou, Z. W. Li, and W. M. Yang (2008). A comparative study of H2-air premixed flame in micro combustors with different physical and boundary conditions. *Combustion Theory and Modelling 12*(2), 325–347. *(p. 9, 10)*

Li, J., S. K. Chou, W. M. Yang, and Z. W. Li (2009). A numerical study on premixed micro-combustion of CH4-air mixture : Effects of combustor size, geometry and boundary conditions on flame temperature. *Chemical Engineering Journal 150*(1), 213–222. *(p. xv, 9, 10)*

Liu, T. (2011). Pressure and Temperature-Sensitive Paints. *Encyclopedia of Aerospace Engineering*, 1–11. *(p. 55)*

Lord, R. (1900). Investigation of the character of the equilibrium of an incompressible heavy fluid of variable density. *Sci. Papers*, 200–207. *(p. 124)*

Maruta, K. (2011). Micro and mesoscale combustion. *Proceedings of the Combustion Institute 33*(1), 125–150. *(p. xv, 4, 6)*

Maruta, K., T. Kataoka, N. I. Kim, S. Minaev, and R. Fursenko (2005). Characteristics of combustion in a narrow channel with a temperature gradient. *Proceedings of the Combustion Institute 30 II*(2), 2429–2436. *(p. xvi, 14, 18, 19, 80)*

Maruta, K., J. K. Parc, K. C. Oh, T. Fujimori, S. S. Minaev, and R. V. Fursenko (2004). Characteristics of microscale combustion in a narrow heated channel. *Combustion, Explosion and Shock Waves 40*(5), 516–523. *(p. 14, 18, 80)*

Maruta, K., K. Takeda, J. Ahn, K. Borer, L. Sitzki, and P. D. Ronney (2002). Extinction Limits of Catalytic Combustion in Microchannels Extinction Limits of Catalytic Combustion in Micro-channels. *Proceedings of the Combustion Institute 29*, 957–963. *(p. 16)*

Merkin, J. H. (1977). Free Convection Boundary Layers on Cylinders of Elliptic Cross Section. *Journal of Heat Transfer 99*(3), 453–457. *(p. 95)*

Miesse, C. M., R. I. Masel, C. D. Jensen, M. A. Shannon, and M. Short (2004). Submillimeter-scale combustion. *AIChE Journal 50*(12), 3206–3214. *(p. 31, 35, 36)*

Mikami, M., Y. Maeda, K. Matsui, T. Seo, and L. Yuliati (2013). Combustion of gaseous and liquid fuels in meso-scale tubes with wire mesh. *Proceedings of the Combustion Institute 34*(2), 3387–3394. *(p. xvi, 17, 18)*

Milcarek, R. J. and J. Ahn (2019). Micro-tubular flame-assisted fuel cells running methane, propane and butane : On soot, efficiency and power density. *Energy 169*, 776–782. *(p. 208)*

Milcarek, R. J., H. Nakamura, T. Tezuka, K. Maruta, and J. Ahn (2019). Microcombustion for micro-tubular flame-assisted fuel cell power and heat cogeneration. *Journal of Power Sources 413*(October 2018), 191–197. *(p. 208)*

Minaev, S., K. Maruta, and R. Fursenko (2007). Nonlinear dynamics of flame in a narrow channel with a temperature gradient. *Combustion Theory and Modelling 11*(2), 187–203. *(p. 18)*

Minkowycz, W. and E. Sparrow (1974). Local nonsimilar solutions for natural convection on a vertical cylinder. *Journal of Heat Transfer 96*(2), 178–183. *(p. 98)*

Moisan, M., J. Barbeau, S. Moreau, J. Pelletier, M. Tabrizian, and L. Yahia (2001). Low-temperature sterilization using gas plasmas : A review of the experiments and an analysis of the inactivation mechanisms. *International Journal of Pharmaceutics 226*(1-2), 1–21. *(p. 182)*

Moisan, M., C. Beaudry, and P. Leprince (1974). A New Hf Device for the Production of Long Plasma Columns At A High Electron Density. *50*(2), 125–126. *(p. 185)*

Moisan, M., R. Pantel, J. Hubert, E. Bloyet, P. Leprince, J. Marec, and A. Ricard (1979). Production and Applications of Microwave Surface-Wave Plasma at Atmospheric-Pressure. *Journal of Microwave Power and Electromagnetic Energy 14*(1), 57–61. *(p. 185)*

Momentive, P. M. I. (2017). Thermal properties of fused quartz. *(p. 132)*

Munir, F. A. and M. Mikami (2015). A numerical study of propane-air combustion in meso-scale tube combustors with concentric rings. *Journal of Thermal Science and Technology 10*(1), JTST0008–JTST0008. *(p. 17)*

Na, T. Y. (1995). Effect of wall conduction on natural convection over a vertical slender hollow circular cylinder. *Applied Scientific Research 54*(1), 39–50. *(p. 98)*

Nakamura, H., A. Fan, S. Minaev, E. Sereshchenko, R. Fursenko, Y. Tsuboi, and K. Maruta (2012). Bifurcations and negative propagation speeds of methane/air premixed flames with repetitive extinction and ignition in a heated microchannel. *Combustion and Flame*. *(p. xvi, 14, 15, 18)*

Norton, D. G. and D. G. Vlachos (2004). A CFD study of propane/air microflame stability. *Combustion and Flame 138*(1-2), 97–107. *(p. 19)*

Ombrello, T. and Y. Ju (2008). Kinetic ignition enhancement of H2 versus fuel-blended air diffusion flames using nonequilibrium plasma. *IEEE Transactions on Plasma Science 36*(6), 2924–2932. *(p. 182)*

Ombrello, T., Y. Ju, and A. Fridman (2008). Kinetic Ignition Enhancement of Diffusion Flames by Nonequilibrium Magnetic Gliding Arc Plasma. *AIAA Journal 46*(10), 2424–2433. *(p. 182, 183)*

Ombrello, T., X. Qin, Y. Ju, A. Gutsol, A. Fridman, and C. Carter (2006). Combustion Enhancement via Stabilized Piecewise Nonequilibrium Gliding Arc Plasma Discharge. *AIAA Journal 44*(1), 142–150. *(p. 182)*

Ombrello, T., S. H. Won, Y. Ju, and S. Williams (2010). Flame propagation enhancement by plasma excitation of oxygen. Part I : Effects of O3. *Combustion and Flame 157*(10), 1906–1915. *(p. 182, 183)*

Omrane, A., F. Ossler, and M. Alde (2002). Two-Dimensional Surface Temperature Measurements. *29*, 2653–2659. *(p. 65)*

Pancheshnyi, S. V., D. A. Lacoste, A. Bourdon, and C. O. Laux (2006). Ignition of propane-air mixtures by a repetitively pulsed nanosecond discharge. *IEEE Transactions on Plasma Science 34*(6), 2478–2487. *(p. 182)*

Pilla, G., D. Galley, D. A. Lacoste, F. Lacas, D. Veynante, and C. O. Laux (2006). Stabilization of a Turbulent Premixed Flame Using a Nanosecond Repetitively Pulsed Plasma. *IEEE Transactions on Plasma Science 34*, 2471–2477. *(p. xxvii, 182, 183)*

Pizza, G., C. E. Frouzakis, J. Mantzaras, A. G. Tomboulides, and K. Boulouchos (2007). Dynamics of premixed hydrogen/air flames in microchannels. *Combustion and Flame 152*, 433–450. *(p. 11)*

Pizza, G., C. E. Frouzakis, J. Mantzaras, A. G. Tomboulides, and K. Boulouchos (2008). Dynamics of premixed hydrogen/air flames in mesoscale channels. *Combustion and Flame 155*(1-2), 2–20. *(p. 11, 19)*

Pizza, G., C. E. Frouzakis, J. Mantzaras, A. G. Tomboulides, and K. Boulouchos (2010). Three-dimensional simulations of premixed hydrogen/air flames in microtubes. *J. Fluid Mech. 658*, 463–491. *(p. 129)*

Poinsot, T. J. and S. K. Lele (1992). Boundary conditions for direct simulations of compressible viscous flows. *J. Comput. Phys. 101*(1), 104–129. *(p. 131)*

Raimondeau, S., D. Norton, D. Vlachos, and R. Masel (2002). Modeling of high-temperature microburners. *Proceedings of the Combustion Institute 29*(1), 901–907. *(p. xvii, 9, 10, 31, 32, 34, 35, 36)*

Rani, H. P. and G. J. Reddy (2012). Conjugate Transient Free Convective Heat Transfer from a Vertical Slender Hollow Cylinder with Heat Generation Effect. *Journal Applied Mathematics 1*(2), 90–98. *(p. 99)*

Ranson, R. M., C. B. Thomas, and M. R. Craven (1998). A thin film coating for phosphor thermography. *Measurement Science and Technology 9*(12), 1947–1950. *(p. 52, 66)*

Rao, X., S. Hammack, C. Carter, T. Grotjohn, J. Asmussen, and T. Lee (2011). Microwave-plasma-coupled re-ignition of methane-and-oxygen mixture under auto-ignition temperature. *IEEE Transactions on Plasma Science 39*(12 PART 1), 3307–3313. *(p. 185)*

Reymond, O., D. B. Murray, and T. S. O'Donovan (2008). Natural convection

heat transfer from two horizontal cylinders. *Experimental Thermal and Fluid Science 32*(8), 1702–1709. *(p. 96)*

Richecoeur, F. and D. C. Kyritsis (2005). Experimental study of flame stabilization in low Reynolds and Dean number flows in curved mesoscale ducts. *Proceedings of the Combustion Institute 30*(2), 2419–2427. *(p. 18)*

Rodrigues, P. (2018). *Modélisation multiphysique de flammes turbulentes suitées avec la prise en compte des transferts radiatifs et des transferts de chaleur pariétaux*. Ph. D. thesis, CentraleSupélec, Laboratory EM2C. *(p. 106)*

Rodrigues, P., O. Gicquel, N. Darabiha, K. P. Geigle, and R. Vicquelin (2018). Assessment of External Heat Transfer Modeling of a Laboratory-Scale Combustor Inside a Pressure-Housing Environment. (c), 1–14. *(p. 106)*

Ronney, P. D. (2003). Analysis of non-adiabatic heat-recirculating combustors. *Combustion and Flame 135*(4), 421–439. *(p. 14)*

Ruetsch, G., L. Vervisch, and A. Liñán (1995). Effects of heat release on triple flame. *Phys. Fluids 6*(7), 1447–1454. *(p. 132)*

Saffman, P. G. and F. S. G. Taylor (1988). The penetration of a fluid into a porous medium or hele-shaw cell containing a more viscous liquid. In *Dynamics of Curved Fronts*, pp. 155–174. Elsevier. *(p. 129)*

Saiki, Y. and Y. Suzuki (2013). Effect of wall surface reaction on a methane-air premixed flame in narrow channels with different wall materials. *Proceedings of the Combustion Institute 34*(2), 3395–3402. *(p. 35, 36)*

Saitoh, T., T. Sajiki, and K. Maruhara (1993). Bench mark solutions to natural convection heat transfer problem around a horizontal circular cylinder. *International Journal of Heat and Mass Transfer 36*(5), 1251–1259. *(p. xxi, 95, 96, 129)*

Sánchez-Sanz, M. (2012). Premixed flame extinction in narrow channels with and without heat recirculation. *Combust. Flame 159*(10), 3158–3167. *(p. 14)*

Sánchez-Sanz, M., D. Fernández-Galisteo, and V. N. Kurdyumov (2014, may). Effect of the equivalence ratio, Damköhler number, Lewis number and heat release on the stability of laminar premixed flames in microchannels. *Combustion and Flame 161*(5), 1282–1293. *(p. 19)*

Sandra K. S. Boetcher (2014). *Natural convection from circular cylinders*. *(p. 95, 98, 102)*

Saville, D. A. and S. W. Churchill (1967). Laminar free convection in boundary layers near horizontal cylinders and vertical axisymmetric bodies. *Journal of Fluid Mechanics 29*(2), 391–399. *(p. 95)*

Shionoya, S., W. Yen, and H. Yamamoto (Eds.) (2012). *Phosphor handbook* (2nd edition ed.). Boca Raton : CRC Press. *(p. 56)*

Shirsat, V. and A. K. Gupta (2011). A review of progress in heat recirculating meso-scale combustors. *Applied Energy 88*(12), 4294–4309. *(p. 32)*

Sieder, E. N. and G. E. Tate (1936). Heat Transfer and Pressure Drop of Liquids in Tubes. *Industrial and Engineering Chemistry 28*(12), 1429–1435. *(p. 94)*

Smith, G. P., D. M. Golden, M. Frenklach, B. Eiteener, M. Goldenberg, C. T. Bowman, R. K. Hanson, W. C. Gardiner, V. V. Lissianski, and Z. W. Qin (2011). *http ://www.me.berkeley.edu/gri_mech*. *(p. 110)*

Smyth, S. A. and D. C. Kyritsis (2012). Experimental determination of the structure of catalytic micro-combustion flows over small-scale flat plates for methane and propane fuel. *Combustion and Flame 159*(2), 802–816. *(p. 16)*

Song, Z., J. Liao, X. Ding, X. Liu, and Q. Liu (2013). Synthesis of YAG phosphor particles with excellent morphology by solid state reaction. *Journal of Crystal Growth 365*, 24–28. *(p. 49)*

Song, Z. B., X. W. Ding, J. L. Yu, and Y. Z. Chen (2006). Propagation and quenching of premixed flames in narrow channels. *Combustion, Explosion and Shock Waves 42*(3), 268–276. *(p. 9)*

Sosman, R. (1927). The properties of silica. *Journal of American Chemical Society*. *(p. xxi, 106, 107)*

Spalding, D. B. (1957). A Theory of Inflammability Limits and Flame-Quenching. *Proceedings of the Royal Society A : Mathematical, Physical and Engineering Sciences 240*(1220), 83–100. *(p. 31)*

Sparrow EM, G. J. (1956). Laminar-free-convection heat transfer from the outer surface of a vertical circular cylinder. *Trans ASME 78*, 1823–1829. *(p. 98)*

Stancu, G. D., O. Leroy, P. Coche, K. Gadonna, V. Guerra, T. Minea, and L. L. Alves (2016). Microwave air plasmas in capillaries at low pressure II. Experimental investigation. *Journal of Physics D : Applied Physics 49*(43). *(p. 188)*

Starikovskii, A. Y., N. B. Anikin, I. N. Kosarev, E. I. Mintoussov, S. M. Starikovskaia, and V. P. Zhukov (2006). Plasma-assisted combustion. *Pure and Applied Chemistry 78*(6), 1265–1298. *(p. 182)*

Stockman, E. S., S. H. Zaidi, R. B. Miles, C. D. Carter, and M. D. Ryan (2009). Measurements of combustion properties in a microwave enhanced flame. *Combustion and Flame 156*(7), 1453–1461. *(p. 185)*

Stockman, E. S., S. H. Zaidi, R. B. Miles, and I. Introduction (2007). Pulsed Microwave Enhancement of Laminar and Turbulent Hydrocarbon Flames. *Aerospace* (January), 1–9. *(p. 182)*

Takita, K., K. Murakami, H. Nakane, and G. Masuya (2005). A novel design of a plasma jet torch igniter in a scramjet combustor. *Proceedings of the Combustion Institute 30 II*(2), 2843–2849. *(p. 182)*

Taylor, G. I. (1950). The instability of liquid surfaces when accelerated in a direction perpendicular to their planes. i. *Proc. R. Soc. Lond. A 201*(1065), 192–196. *(p. 124)*

Technology, P. (2018). Phosphor technology. *(p. 47, 57, 66)*

Tsai, C. H. (2008). The asymmetric behavior of steady laminar flame propagation in ducts. *Combustion Science and Technology 180*(3), 533–545. *(p. xv, xvi, 11, 19, 20, 123, 124)*

Tsubouchi, T. and H. Masuda (1967). Heat transfer by natural convection from horizontal cylinders at low rayleigh numbers. *Rep. Inst. of High Speed Mechanics*, 205–219. *(p. 95, 100)*

Versaevel, P. (1996). *Combustion laminaire diphasique : Etude théorique et expérimentale*. Ph. D. thesis, Ecole Centrale Paris. *(p. 109)*

Von Karman, T. and G. Millan (1953). Theoretical and Experimental Studies on Laminar Combustion and Detonation Waves. *Proceedings of the Combustion Institute*, 173–177. *(p. 8)*

Wan, J., A. Fan, Y. Liu, H. Yao, W. Liu, X. Gou, and D. Zhao (2015). Experimental investigation and numerical analysis on flame stabilization of CH4/air mixture in a mesoscale channel with wall cavities. *Combustion and Flame 162*(4), 1035–1045. *(p. 22)*

Wang, F., J. B. Liu, J. Sinibaldi, C. Brophy, A. Kuthi, C. Jiang, P. Ronney, and M. A. Gundersen (2005). Transient plasma ignition of quiescent and flowing air/fuel mixtures. *IEEE Transactions on Plasma Science 33*(2 II), 844–849. *(p. 182)*

Wang, P., R. Kahawita, and D. L. Nguyen (1991). Transient laminar natural convection from horizontal cylinders. *Int. J. Heat Mass Transf. 34*(6), 1429–1442. *(p. 129)*

Wang, P., R. Kahawita, and T. H. Nguyen (1990). Numerical computation of the natural convection flow about a horizontal cylinder using splines. *Numerical Heat Transfer ; Part A : Applications 17*(2), 191–215. *(p. 95)*

Wolk, B., A. DeFilippo, J. Y. Chen, R. Dibble, A. Nishiyama, and Y. Ikeda (2013). Enhancement of flame development by microwave-assisted spark ignition in constant volume combustion chamber. *Combustion and Flame 160*(7), 1225–1234. *(p. 183, 184)*

Wu, W., C. A. Fuh, and C. Wang (2015). Plasma-Enhanced Ignition and Flame Stabilization in Microwave Plasma-Assisted Combustion of Premixed Methane/Oxygen/Argon Mixtures. *IEEE Transactions on Plasma Science 43*(12), 3986–3994. *(p. xxvii, 186, 188, 192)*

Yang, H., Y. Feng, Y. Wu, X. Wang, L. Jiang, D. Zhao, and H. Yamashita (2011). A surface analysis-based investigation of the effect of wall materials on flame quenching. *Combustion Science and Technology 183*(5), 444–458. *(p. 35)*

Ye, L., Y. Pan, J. Jiang, and W. Zhang (2014). A numerical study of the auto-ignition temperatures of CH4-Air, C3H8-Air, CH4-C3H8-Air and CH4-CO2-Air mixtures. *Journal of Loss Prevention in the Process Industries 29*(1), 85–91. *(p. 30)*

Zamashchikov, V. V. (2004). Some features of gas-flame propagation in narrow tubes. *Combustion, Explosion and Shock Waves 40*(5), 545–552. *(p. 129)*

université PARIS-SACLAY

ÉCOLE DOCTORALE
Sciences mécaniques et énergétiques, matériaux et géosciences (SMEMAG)

Titre : Stabilisation et propagation de flammes pauvres prémélangées dans des conduits de petites dimensions en interaction forte avec les parois.

Mots clés : combustion en méso-échelle, conduit étroit, expérimental, simulation numérique 1-D, interactions flamme-paroi, méthane/air

Résumé : Les besoins en systèmes d'énergie de quelques dizaines de Watts grandissent à mesure que la demande pour des outils portables de petite dimension augmente. La conversion d'énergie par combustion reste le procédé le plus efficace par kilogramme transporté. Seulement, la stabilisation de flammes de faible puissance dans des environnements confinés reste un défi car les échanges thermiques entre la flamme et l'extérieur sont très importants par rapport à la puissance de la flamme et conditionnent la capacité du système à produire de l'énergie de façon continue et stable. Le travail de thèse proposé étudie les propriétés et les échanges de chaleur d'une flamme de méthane dans un tube de 5 mm de diamètre. On montre expérimentalement à l'aide de diagnostics innovants et numériquement que sous certaines conditions, la flamme perd sa symétrie et que sa position dépend des échanges de chaleur. Ce travail explore aussi la possibilité d'assister la flamme en la couplant à un plasma micro-onde.

Title : Stabilization and propagation of lean premixed flames in small dimensions conducts in strong thermal interaction with the walls

Keywords : mesoscale combustion, narrow channel, experiments, numerical simulation 1-D, flame-wall interactions, methane/air

Abstract : The energy system needs of a few tens of Watts grow as the demand for reduced-size portable devices grows. Combustion energy conversion remains the most efficient process per kilogram transported. However, the stabilization of low-power flames in confined environments remains a challenge because the thermal exchanges between the flame and the outside are very important compared to the power of the flame and condition the capacity of the system to produce energy in a continuous and stable way. The thesis work proposed here studies the properties of a methane flame in a 5 mm diameter tube and the heat exchanges with the environment. It is shown experimentally using innovative diagnostics and numerically that under certain conditions, the flame loses its symmetry and can move according to heat exchanges. This work also explores the possibility of assisting the flame by coupling it to a microwave plasma.